

Neuroscience Bulletin

The Official Journal of The Chinese Neuroscience Society

神经科学通报

Volume 36
Number 1
January 2020



MAPK

circadian rhythm



 SIBS  Springer
www.neurosci.cn

About the Cover

Rapid antidepressant therapy has been shown to be related to the circadian rhythm, but the specific molecular pathways have not been clarified. Accumulating evidence shows that the mitogen-activated protein kinase (MAPK) pathway is involved in the mechanism of action of antidepressants, and can simultaneously modulate the circadian system. Wang *et al.* propose that the MAPK pathway is a common route through which various rapid antidepressants regulate circadian genes. In the cover image, the rat in the depressive-like state (left) has a disturbed circadian rhythm. In contrast, when the circadian rhythm is normalized *via* the MAPK pathway (right), the rat rapidly returns to a relatively normal mood state. See pages 66–76. (Cover image provided by Xin-Ling Wang).

Volume 36 Number 1
January 2020



Original Articles

1 Inhibition of Muscular Nociceptive Afferents *via* the Activation of Cutaneous Nociceptors in a Rat Model of Inflammatory Muscle Pain

Yehong Fang · Jie Zhu · Wanru Duan · Yikuan Xie · Chao Ma

11 *SCN9A* Epileptic Encephalopathy Mutations Display a Gain-of-function Phenotype and Distinct Sensitivity to Oxcarbazepine

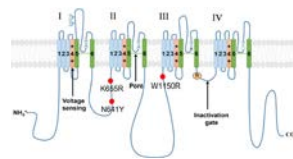
Shuzhang Zhang · Zhiping Zhang · Yuan Shen · Yudan Zhu · Kun Du · Jingkang Guo · Yonghua Ji · Jie Tao

25 Regional Metabolic Patterns of Abnormal Postoperative Behavioral Performance in Aged Mice Assessed by ¹H-NMR Dynamic Mapping Method

Taotao Liu · Zhengqian Li · Jindan He · Ning Yang · Dengyang Han · Yue Li · Xuebi Tian · Huili Liu · Anne Manyande · Hongbing Xiang · Fuqiang Xu · Jie Wang · Xiangyang Guo

39 Dependence of Generation of Hippocampal CA1 Slow Oscillations on Electrical Synapses

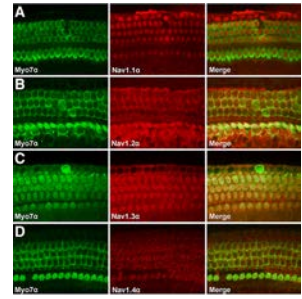
Yuan Xu · Feng-Yan Shen · Yu-Zhang Liu · Lidan Wang · Ying-Wei Wang · Zhiru Wang



p 14

49 Distribution and Functional Characteristics of Voltage-Gated Sodium Channels in Immature Cochlear Hair Cells

You Zhou · Chenchen Xia · Manli Yin · Xueling Wang · Hao Wu · Yonghua Ji



p 56

Reviews

66 Regulation of Circadian Genes by the MAPK Pathway: Implications for Rapid Antidepressant Action

Xin-Ling Wang · Kai Yuan · Wen Zhang · Su-Xia Li · George Fu Gao · Lin Lu

77 Connections Between Insomnia and Cognitive Aging

Claire E Sexton · Konstantina Sykara · Elissaios Karageorgiou · Jenny Zitser · Talita Rosa · Kristine Yaffe · Yue Leng

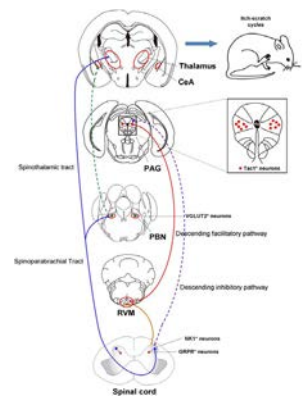
Research Highlights

85 More than Scratching the Surface: Recent Progress in Brain Mechanisms Underlying Itch and Scratch

Xu Liu · Xiu-Hua Miao · Tong Liu

89 Plasma Replacement Therapy for Alzheimer's Disease

Xu-long Ding · Peng Lei



p 87

Insight

91 Gut Microbiota and Short Chain Fatty Acids: Influence on the Autonomic Nervous System

Jessica Bruning · Andrew Chapp · Gregory A. Kaurala · Renjun Wang · Stephen Techtmann · Qing-Hui Chen



Inhibition of Muscular Nociceptive Afferents *via* the Activation of Cutaneous Nociceptors in a Rat Model of Inflammatory Muscle Pain

Yehong Fang^{1,2} · Jie Zhu^{1,3} · Wanru Duan⁴ · Yikuan Xie¹ · Chao Ma¹

Received: 22 November 2018 / Accepted: 13 January 2019 / Published online: 22 June 2019
© Shanghai Institutes for Biological Sciences, CAS 2019

Abstract Topical irritants such as capsaicin (CAP), peppermint oil (PO), and mustard oil (MO) are effective in relieving inflammatory muscle pain. We investigated the effects of topical irritants in a rat model of inflammatory muscle pain produced by injecting complete Freund's adjuvant (CFA) into the tibialis anterior muscle. CFA-induced mechanical hypersensitivity and the spontaneous activity of muscular nociceptive afferents, and decreased weight-bearing of the hindlimb were relieved by topical application of CAP, PO, or MO on the skin overlying the inflamed muscle. The effects of topical irritants were abolished when applied to the skin on the ipsilateral plantar region or on the contralateral leg, or when the relevant cutaneous nerve or dorsal root was transected. Our results demonstrated that topical irritants may alleviate inflammatory muscle pain *via* activating cutaneous nociceptors and

subsequently inhibiting the abnormal activity of muscular nociceptive neurons.

Keywords Inflammatory muscle pain · Muscular nociceptor · Cutaneous nociceptor · Capsaicin

Introduction

Muscle pain is a common medical issue worldwide that can interfere with patients' motor control [1, 2]. Besides genetic factors in diseases such as Duchenne's syndrome and fibromyalgia [3–5], most muscle pain can be attributed to muscle strain, damage, and ischemia [6, 7]. For example, low back pain, which is a common complaint in patients with muscle strain or occupational muscle damage, can last for a long time and greatly impair the quality of life [8, 9].

However, most of our knowledge about pain is based on studies of cutaneous tissue and relatively less is known about muscle pain. In contrast to cutaneous pain, which is stabbing, tolerable, and well localized, muscle pain is more likely to be tearing, intolerable, and poorly localized and has a marked tendency of referred pain [1]. Previous studies have revealed that muscle nociceptors can respond to mechanical, thermal, and chemical stimuli, leading to muscle spasm and inflammatory muscle pain [10–13]. But almost all these results are based on muscular nerve filament recordings in rodent models, or the visual analogue pain scale in human subjects, so the electrophysiological characteristics of muscle nociceptors remain unclear.

In medical practice, topical application of irritant chemicals such as capsaicin (CAP) is effective in relieving many kinds of pain, including neuropathic pain, arthritis pain, neck pain, cluster headache, and post-mastectomy

Yehong Fang and Jie Zhu have contributed equally to the work and share first authorship.

✉ Chao Ma
machao@ibms.cams.cn

¹ Institute of Basic Medical Sciences, Department of Human Anatomy, Histology and Embryology, Neuroscience Center, Chinese Academy of Medical Sciences, School of Basic Medicine, Peking Union Medical College, Beijing 100005, China

² Joint Laboratory of Anesthesia and Pain, Peking Union Medical College, Beijing 100730, China

³ Department of Radiation Oncology, Sichuan Cancer Hospital and Institute, Sichuan Cancer Center, School of Medicine, University of Electronic Science and Technology of China, Chengdu 610054, China

⁴ Department of Neurosurgery, Xuanwu Hospital, Capital Medical University, Beijing 100053, China

pain syndrome [14, 15]. Studies on transdermal absorption have revealed that the most concentrated topical drugs cannot penetrate the epidermis, suggesting an important role of cutaneous afferents in the analgesic effect of topical CAP [16]. Previously, we showed that topical analgesics might inhibit inflammatory muscle pain *via* the activation of cutaneous nociceptors in a rat model [17]. According to diffuse noxious inhibitory control theory [18], noxious stimulation from one location may be inhibited by another stimulus from a different location through convergent dorsal horn neurons. However, it is not clear whether the activity of muscle nociceptive neurons is inhibited by noxious stimuli to the skin, and whether this inhibition is associated with the activation of specific types of cutaneous nociceptors. In this study, we set out to answer the above questions with *in vivo* electrophysiological recordings from single muscle nociceptors in a rat model of inflammatory muscle pain.

Materials and Methods

Animals

Adult female Sprague-Dawley rats (specific pathogen free, 180 g–220 g, provided by the National Institutes for Food and Drug Control, Beijing, China) were randomly assigned to subgroups. All rats were housed at $23\text{ }^{\circ}\text{C} \pm 2\text{ }^{\circ}\text{C}$ and a 12/12 h light/dark cycle-controlled room with free access to rodent chow and water. This study was approved by the Institutional Animal Care and Use Committees of the Chinese Academy of Medical Sciences and the Institute of Basic Medical Sciences (Approval Number: #211–2014).

Complete Freund's Adjuvant (CFA) Injection

Under anesthesia (sodium pentobarbital, 50 mg/kg, i.p., Sigma Aldrich, St. Louis, MO, USA), the tibialis anterior muscle of the right (experimental) hindlimb was injected with 100 μL of CFA (#F5881, Sigma Aldrich) composed of inactivated and dried mycobacteria. The CFA was injected slowly into the muscle and no leakage was observed. The left (control) tibialis anterior muscle received 100 μL sterile saline. A total of 61 rats received CFA injections.

Surgery

Denervation of the Skin Over the Tibialis Anterior Muscle

Skin denervation surgery in 13 rats was conducted 3 days before injection of CFA. Under anesthesia (sodium pentobarbital, 50 mg/kg, i.p.), a longitudinal incision was made on the skin over the tibialis anterior. The lateral cutaneous

branches of the superficial peroneal nerve were bluntly separated and transected. The day after surgery, failure to respond to a nociceptive pinch of the skin over tibialis anterior indicated successful denervation (see a previous report for detailed surgical procedures [17]). Transection of the cutaneous branches of the superficial peroneal nerve only causes loss of sensation in the corresponding receptive field but does not cause neuropathic pain, as previously reported in both rat models [19] and humans [20].

L4 Dorsal Rhizotomy

Three days before CFA injection, an L4 dorsal rhizotomy was performed in 2 rats. Under anesthesia (sodium pentobarbital, 50 mg/kg, i.p.), a skin incision was made in the midline L3–L5 region and muscles attached to the right L4 vertebra were removed. A hemilaminectomy was conducted with the dura matter and arachnoid membrane removed, then the L4 dorsal root was transected $\sim 3\text{ mm}$ proximal to the L4 dorsal root ganglion (DRG). Damage to the L4 DRG and spinal cord was carefully avoided.

Assessment of CFA-Induced Inflammatory Muscle Pain

Hindlimb Perimeter Measurement

Rats ($n = 5$) were placed in the prone position. The two ends of the tibia were labeled on the skin, then the perimeter of limb was measured at the middle of the tibia.

Weight-Bearing Measurement

Rats ($n = 47$) were positioned with the hindlimbs on force plates in an Incapacitance Tester (Institute of Biomedical Engineering, Chinese Academy of Medical Sciences and Peking Union Medical College, Beijing, China). When the animal was immobile and stable, the weight bearing capacity (g) of each hindlimb in 10 s was automatically averaged. The difference score (g) was defined as weight-bearing on the right (experimental) minus that on the left (control). The final difference score was determined as the average of 3 measurements.

Evan's Blue Extravasation

A total of 4 rats were used in this experiment. Two days after CFA injection, 2 mL Evans blue (1%, i.v., Sigma Aldrich) was injected into the caudal vein. Transcardiac perfusion was conducted with 0.1 mol/L phosphate-buffered saline (PBS) 30 min later. After transcardial perfusion, the bilateral tibialis anterior muscles were

harvested. Evan's blue extravasation was measured as previously reported [21, 22].

Application of Topical Irritants

CAP, mustard oil (MO), and peppermint oil (PO) are known to activate cutaneous nociceptors [23–26]. Two days after CFA injection, hair was removed from the skin on the hindlimb and smeared with 0.5 mL 0.3% CAP, 50% MO, or 80% PO. Ethanol (ET) was used as vehicle control.

Immunofluorescent Staining

Six rats were used in this experiment. Under anesthesia (sodium pentobarbital, 50 mg/kg, i.p.), 100 μ L of the fluorescent dye 1,1'-dioctadecyl-3,3,3',3'-tetramethylindocarbocyanine perchlorate (DiI) (200 μ g/mL, Sigma Aldrich) was slowly and carefully injected to the right tibialis anterior, and no obvious DiI leakage was observed. Immunofluorescent staining was conducted 8 days later. Briefly, isotonic saline was pumped into the left ventricle and flowed from the right atrial appendage to remove the blood, and then 4% paraformaldehyde was perfused to fix the tissue. The ipsilateral L2–L6 DRGs were collected and fixed in 4% paraformaldehyde overnight at 4 °C, followed by dehydration in 30% sucrose. The DRGs were then embedded and cut at 15 μ m on a cryostat for immunofluorescent staining. After soaking in 0.2% Triton X-100 in PBS for 15 min and blocking in 10% normal donkey serum for 1 h at room temperature, sections of DRGs were incubated overnight at 4 °C in 10% normal donkey serum in PBS containing primary antibodies against PGP9.5, a ubiquitin hydrolase specifically expressed in neuronal tissue. The section was then incubated with secondary antibodies for 1 h. Finally, slides were washed in PBS and coverslipped with Vectashield mounting medium with DAPI. Images were captured using a confocal laser scanning microscope FV1000 (Olympus, Tokyo, Japan) and Olympus FluoView software. Positive neurons in each DRG were counted and then categorized into small (< 30 μ m diameter), medium (30 μ m–45 μ m), and large (> 45 μ m) neurons [27].

In Vivo Electrophysiological Recording

In vivo extracellular electrophysiological recordings from DRG neurons were performed in 67 DiI-labeled rats. Detailed information on the surgical exposure and extracellular recording from the L4 DRG was as in a previous report [28]. Briefly, under pentobarbital anesthesia (initial dose of 50 mg/kg i.p. followed by supplementary doses of 20 mg/kg i.p. whenever needed), the L5 transverse process

was removed to expose the L4 DRG, and a laminectomy was made from L1 to L6. Oxygenated artificial cerebrospinal fluid at 35 °C was dripped onto the surface of the DRG during surgery and recording. Under a dissecting microscope, the perineurium and epineurium were carefully removed, the rat was transferred to the recording platform, and a pool was formed by attaching the skin to a metal ring. The receptive field of a DRG neuron was identified by exploring the tibialis anterior using a von Frey filament with the fixed tip diameter (1 mm) or a blunt probe. To ensure that the receptive field was in the muscle (not on the skin), the same mechanical stimuli were also applied to the skin. Von Frey filaments were applied to the tibialis anterior at different forces (40 mN, 80 mN, 100 mN, 200 mN, and 280 mN) and the mechanical threshold to evoke an action potential (AP) was repeatedly measured for 10 min. Spontaneous activity (SA) was defined as a continuous discharge lasting for 3 min without any external stimulus. Any electrical activity lasting < 3 s or induced by an external stimulus was excluded. Once SA was identified, the irritant was smeared on the skin and then SA was recorded continuously for at least 30 min.

Statistical Analysis

All data are presented as the mean and its standard error (mean \pm SEM). Differences between two groups were analyzed using Student's *t*-test. Differences among multiple groups were analyzed using one-way analysis of variance (ANOVA) followed by the Bonferroni post hoc test. Two-way (time and group) ANOVA with Bonferroni the post hoc test was used to compare repeated measurements at different time points among groups. A statistically significant difference was defined as a two-sided *P* value < 0.05. IBM SPSS Statistics for Windows (version 21.0, Armonk, NY, USA) was used for statistical analysis.

Results

CFA-Induced Inflammatory Muscle Pain

Two days after CFA injection into the right tibialis anterior muscle, the right hindlimb swelled (Fig. 1A) and Evans blue extravasation, an indicator of inflammation, was evident ($n = 4$, $P < 0.01$, Fig. 1B). The perimeter of the right hindlimb at the middle of the tibia peaked at 1 day after CFA injection ($n = 5$, $P < 0.01$) and then decreased gradually in the following days (Fig. 1C). The difference score for weight-bearing declined markedly with a minimum at 1 day after CFA injection ($n = 6$, $P < 0.01$), and recovered 7 days later (Fig. 1D).

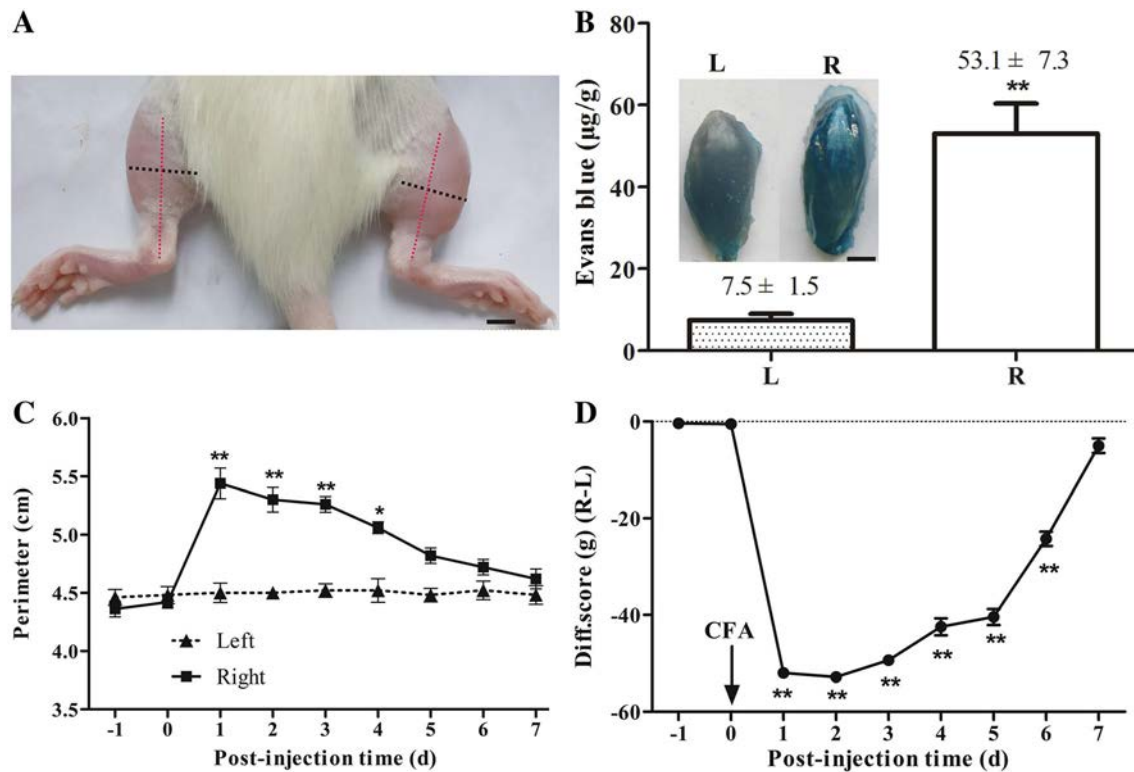


Fig. 1 Complete Freund's adjuvant (CFA)-induced inflammatory muscle pain. **A** Representative photograph showing the swollen right hindlimb 2 days after CFA injection. Red and black dotted lines indicate the position of the tibia and the perimeter at the middle of the tibia, respectively. scale bar, 5 mm. **B** Evans blue extravasation from the ipsilateral (R) tibialis anterior 2 days after CFA injection; contralateral side (L) with injection of isotonic saline as control ($n = 5$).

C Perimeter of the ipsilateral hindlimb at the middle of the tibia peaked 1 day after CFA injection and then declined ($n = 5$). **D** Difference scores in weight-bearing (ipsilateral–contralateral) reached a minimum 1 day after CFA injection and was significantly reduced for 6 days ($n = 6$). * $P < 0.05$, ** $P < 0.01$; ipsilateral vs contralateral in **B** and **C**, post-injection vs pre-injection –1 day in **D**.

Primary Sensory Neurons Innervating Tibialis Anterior Muscle

DiI-labeling and immunofluorescent staining with PGP9.5 in 6 rats demonstrated that the majority of primary sensory neurons specifically innervating tibialis anterior were in the L3, L4, and L5 DRGs (Fig. 2A, B). The majority of DiI-positive neurons were small- and medium-sized, and the L4 DRG contained the largest number of small DiI-positive neurons (Fig. 2C). Therefore the L4 DRG was chosen for recording the electrophysiological activity of muscular nociceptive C-neurons.

CFA-Induced Mechanical Hypersensitivity in Muscular Nociceptive Neurons and Inhibitory Effects of Topical Irritants

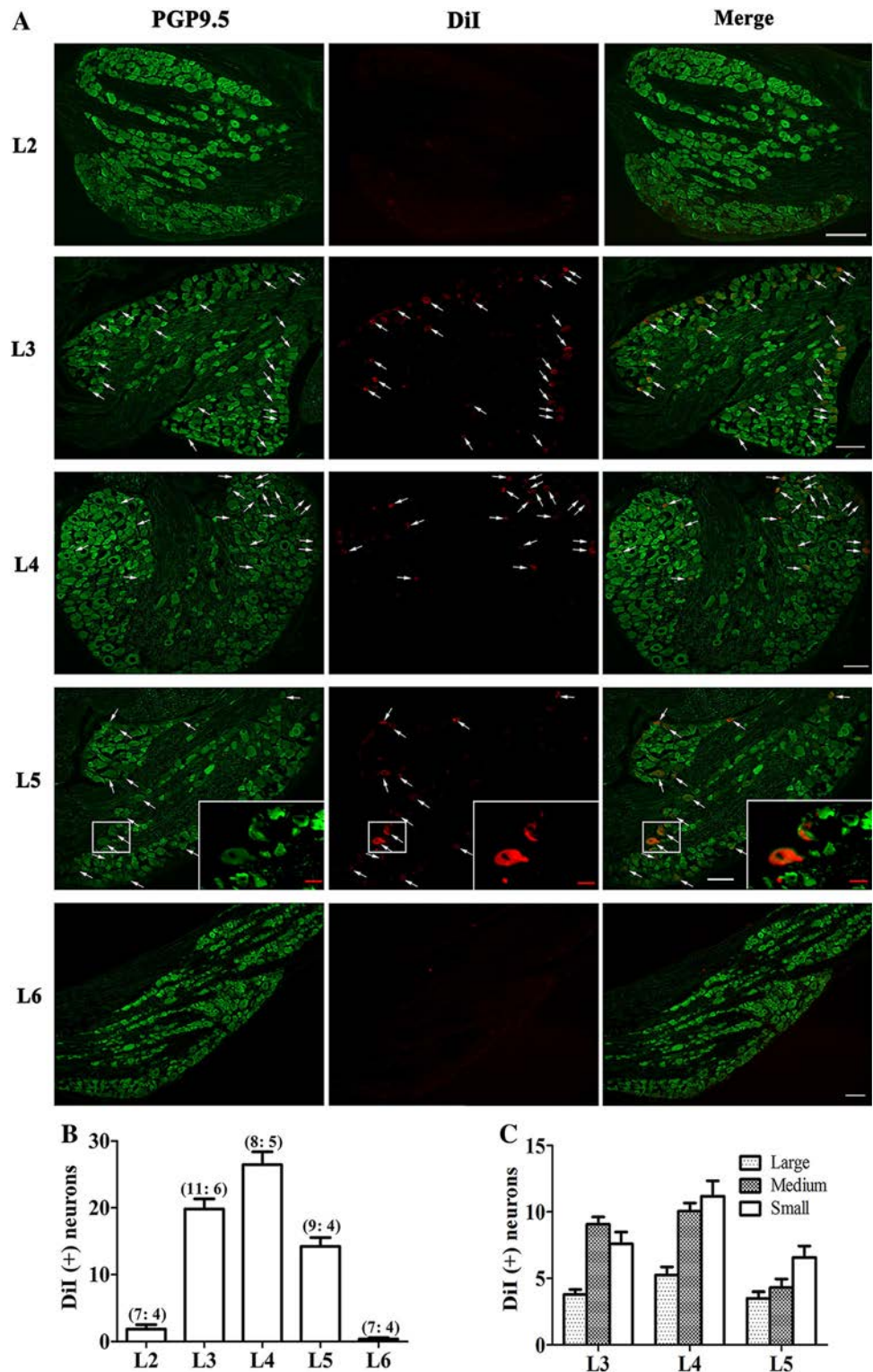
A total of 216 DiI-labeled L4 DRG neurons were recorded from 61 CFA-injected and 6 control (naïve) rats. Among the 185 neurons recorded from the CFA-injected rats, 60 were C-neurons and 2 were A -neurons (all small-diameter)

responding to localized mechanical stimuli to tibialis anterior (Fig. 3A–D); 102 were muscle spindles (69 large, 21 medium, and 11 small neurons); and the receptive fields of the remaining 17 (7 large, 2 medium, and 8 small neurons) could not be found. Among the 31 neurons recorded from naïve rats, 7 were C-type muscular nociceptive neurons (all small-diameter), 24 were muscle spindles (10 large, 4 medium, and 10 small neurons) and the receptive fields of the remaining 4 (2 large, 1 medium, and 1 small neurons) could not be found.

Muscular nociceptive neurons in CFA-injected rats showed enhanced responses to mechanical stimuli (Fig. 3E, F). Compared with the naïve rats ($n = 6$), the action potential discharge rates evoked by mechanical stimuli in CFA-injected rats ($n = 11$) increased significantly (80 mN, 7.82 ± 2.0 vs 1.25 ± 1.53 , $P < 0.01$; 100 mN, 13.27 ± 2.16 vs 5.25 ± 1.92 , $P < 0.01$; 200 mN, 20.36 ± 1.18 vs 14.62 ± 1.73 , $P < 0.05$), indicating mechanical hypersensitivity in CFA-inflamed muscle.

After topical irritants (CAP, $n = 11$; MO, $n = 6$; PO, $n = 6$) were smeared on the skin over the inflamed muscle in

Fig. 2 Anterograde labelling of primary sensory neurons innervating tibialis anterior. **A** Immunofluorescent staining of L2–L6 dorsal root ganglia (DRGs) with the neuronal marker PGP9.5 showing primary sensory neurons in the L3–L5 DRGs innervating tibialis anterior anterogradely labeled with DiI (arrows). Inset, enlarged image of labeled neurons in L5 DRG. Scale bars, 100 μ m (white); 20 μ m (red). **B** Numbers of neurons labeled by DiI in L2–L6 DRGs (number of DRGs and rats in each group listed in brackets). **C** Numbers of large (> 40 μ m), medium (30 μ m–40 μ m), and small (< 30 μ m) neurons labeled in L3–L5 DRGs. DiI, 1,1'-dioctadecyl-3,3,3',3'-tetramethylindocarbocyanine perchlorate.



CFA-injected rats, the responses of muscular nociceptive neurons to mechanical stimuli started to decrease in 5 min–10 min (Fig. 3G). When the same series of mechanical stimuli were given, the average discharge rate for all 3

irritants dropped significantly. The most dramatic change occurred after the application of CAP, suggesting a strong analgesic effect (Fig. 3H–J).

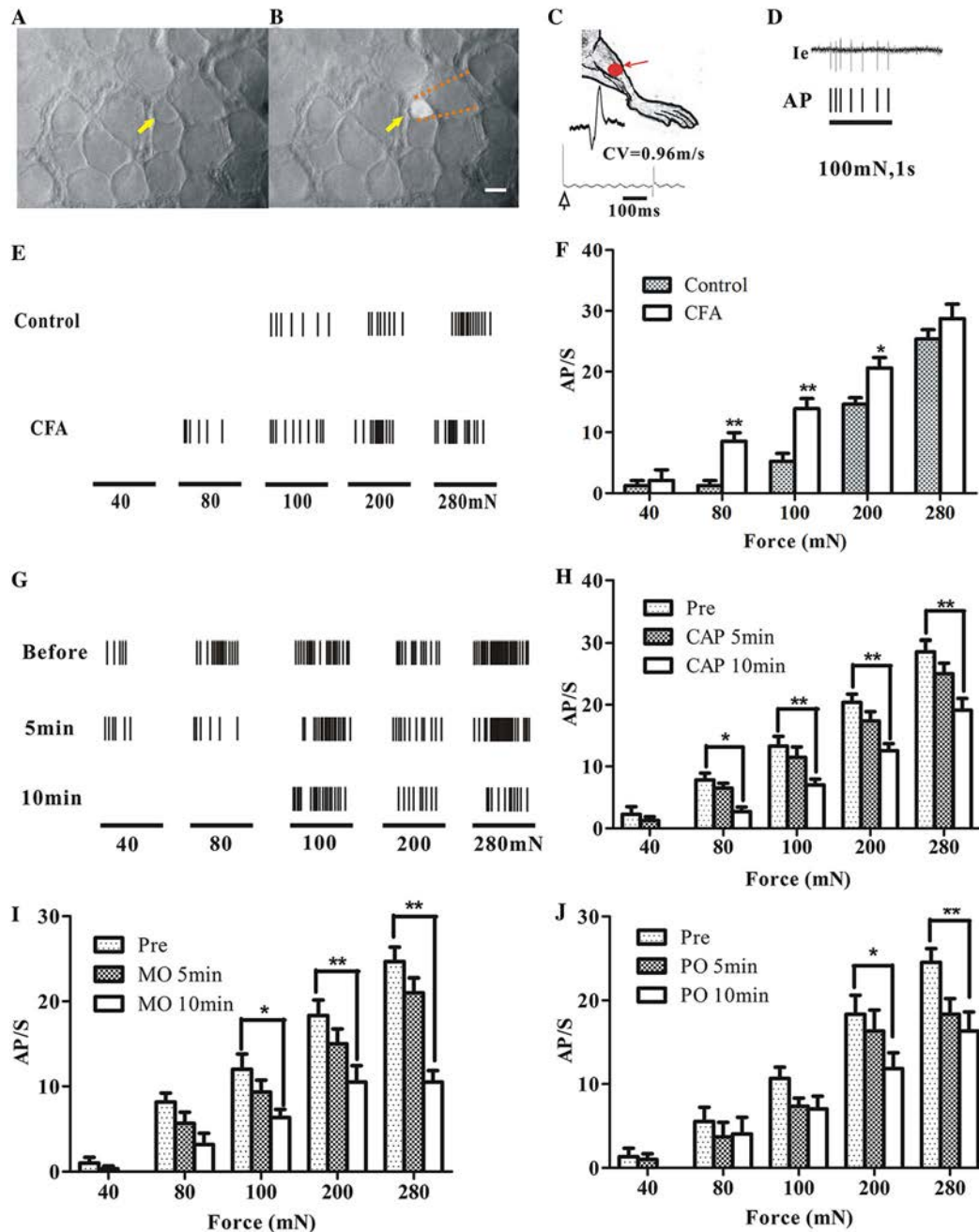


Fig. 3 Mechanical thresholds of muscular C-nociceptive neurons in rat dorsal root ganglion (DRG). **A** Bright-field image of the surface of an L4 DRG; arrow indicates a small neuron. **B** Fluorescent image of the same cell body recorded by an extracellular glass micropipette (dotted lines). Scale bar, 20 μ m. **C** Cartoon of measurement of conduction velocity of the sciatic nerve. Receptive field in tibialis anterior labeled by a red spot. **D** Single-neuron extracellular recording of a typical response of a fluorescence-labeled small neuron to 100 mN mechanical stimulation. Action potentials (APs) in the original recording trace (Ie) are presented as corresponding ticks below. **E** Responses of muscle nociceptive C-neurons to von Frey filaments of several forces (40 mN, 80 mN, 100 mN, 200 mN, and 280 mN) in

CFA-injected and control rats. **F** Action potential discharge rates (AP/s) of muscular nociceptive C-neurons evoked by mechanical stimuli in complete Freund's adjuvant (CFA)-injected ($n = 11$) and control rats ($n = 6$). **G** Typical recordings of the responses of a muscular C-nociceptive neuron from a CFA-injected rat to different forces applied to the receptive field in tibialis anterior before and after topical capsaicin (CAP) application. **H–J** Summary of responses (AP/s) of muscular C-nociceptive neurons to different forces before and after topical application of CAP ($n = 11$ in **H**), mustard oil (MO, $n = 6$ in **I**), and peppermint oil (PO, $n = 6$ in **J**) on the skin over tibialis anterior in CFA-injected rats. * $P < 0.05$, ** $P < 0.01$; CFA vs control (**F**), post- vs pre-application (**H–J**).

CFA-Induced Spontaneous Activity (SA) in Muscular Nociceptive Neurons and Inhibitory Effects of Topical Irritants

Out of the 62 muscular nociceptive DRG neurons recorded from the CFA-injected rats, SA was recorded from 30 (all were C-type and small-diameter). In contrast, none of the 7 muscular nociceptive neurons from the naïve rats showed SA. The average discharge rate of these muscular nociceptive neurons was 0.75 Hz (0.33 to 1.7 Hz). The SA was inhibited by intramuscular injection of 10 μ L lidocaine (0.02 g/mL) (Fig. 4A).

After topical application of the irritants CAP ($n = 10$), MO ($n = 6$), or PO ($n = 6$) to the skin over the inflamed muscle in CFA-injected rats, the discharge rate of SA declined significantly within a few minutes in all groups (Fig. 4B). No significant change occurred in the ET group (vehicle control) ($n = 8$) ($P > 0.05$). The application of CAP induced a stronger early response while both MO and CAP completely blocked SA within 30 min (Fig. 4B, C).

In contrast, no significant change was found in the SA frequency of muscular nociceptive neurons after topical application of CAP to the ipsilateral plantar skin ($n = 6$), or the skin over the contralateral tibialis anterior ($n = 5$), or when the skin was denervated ($n = 6$) or after an ipsilateral L4 dorsal rhizotomy ($n = 2$) ($P > 0.05$) (Fig. 4D).

Inhibitory Effect of Irritants on Unbalanced Weight-Bearing

Two days after CFA injection, the difference score (ipsilateral–contralateral) for weight-bearing decreased from 0 to about -50 g. Following the application of irritants, the weight-bearing was monitored periodically for up to 24 h. In the CAP group ($n = 4$), the difference score started to recover as early as 1 h after application and lasted for ~ 12 h, with a peak at ~ 4 h (Fig. 5A). The changes in weight-bearing were less in the MO ($n = 4$) and PO ($n = 4$) groups and lasted for only ~ 6 h (Fig. 5A). No significant change was found in the ET group ($n = 4$, $P > 0.05$).

Similarly, there was no significant change in the weight-bearing scores of CFA-injected rats after application of CAP to the ipsilateral plantar skin ($n = 6$), or the skin over the contralateral tibialis anterior ($n = 6$), or when the skin was denervated ($n = 7$, $P > 0.05$) (Fig. 5B).

Discussion

In clinical practice, muscle pain is a frequent complaint in patients with muscle strain, muscle damage, or ischemia. Topical analgesics such as capsaicin cream are effective for the relief of inflammatory muscle pain, possibly through

the activation of cutaneous nociceptors, but without a clear understanding of the mechanism [17]. In this study, inflammatory muscle pain was successfully induced by CFA, as indicated by intolerable weight-bearing, massive Evans blue extravasation, mechanical hypersensitivity and SA of muscular nociceptive neurons. Nociceptive irritants applied to the skin over the inflamed muscle, but not to remote skin, were able to relieve muscle inflammation. No analgesic effect was found either after transection of the L4 dorsal root or denervation of the skin over the inflamed muscle. These findings provided strong evidence that the activation of cutaneous nociceptors by topical irritants inhibit the mechanical hypersensitivity and abnormal spontaneous activity of muscular nociceptive neurons, and thus alleviate inflammatory muscle pain.

Distinct from cutaneous pain, muscle pain is more tearing and diffuse, and often accompanied by an extended area of referred pain [29]. Compared with cutaneous sensory neurons, muscular sensory neurons have different actions on pain signal conduction and central sensitization [30], and vary in their response to peripheral nerve injury [31]. All these differences indicate the need to explore the characteristics of muscular nociceptive neurons. The electrophysiological characteristics of cutaneous nociceptive neurons have been reported in many studies, but the characteristics of muscular nociceptive neurons are barely understood because of the complexity and difficulty of *in vivo* single-neuron electrophysiological recording. In this study, the fluorescent dye DiI was used to track primary sensory neurons, allowing us to record from nociceptive neurons specifically innervating the inflamed muscle. To our knowledge, this study is the first to successfully record the electrophysiological properties of single muscular nociceptive neurons in the rat model, and this might help to better understand the mechanisms underlying muscle pain.

SA in primary nociceptive neurons is considered to be an indicator of spontaneous pain and an important factor in neuropathic pain [32]. In this study, robust SA was recorded from the nociceptive neurons innervating the inflamed muscle, and was blocked by the application of irritants to the skin over the inflamed muscle. The CFA-induced mechanical hypersensitivity of the muscular nociceptive neurons was also alleviated by these topical irritants. These effects could not be induced by mechanical stimuli or innocuous stimuli such as light touch or wiping with a Q-tip (data not shown). In traditional Chinese medicine, noxious stimuli that may irritate cutaneous nociceptors such as scraping, cupping, and certain plasters were widely used to relieve muscle pain. In modern medicine, the burning sensation of CAP and other chemical irritants is also used to treat various pains, including neuropathic pain and joint pain [14, 15].

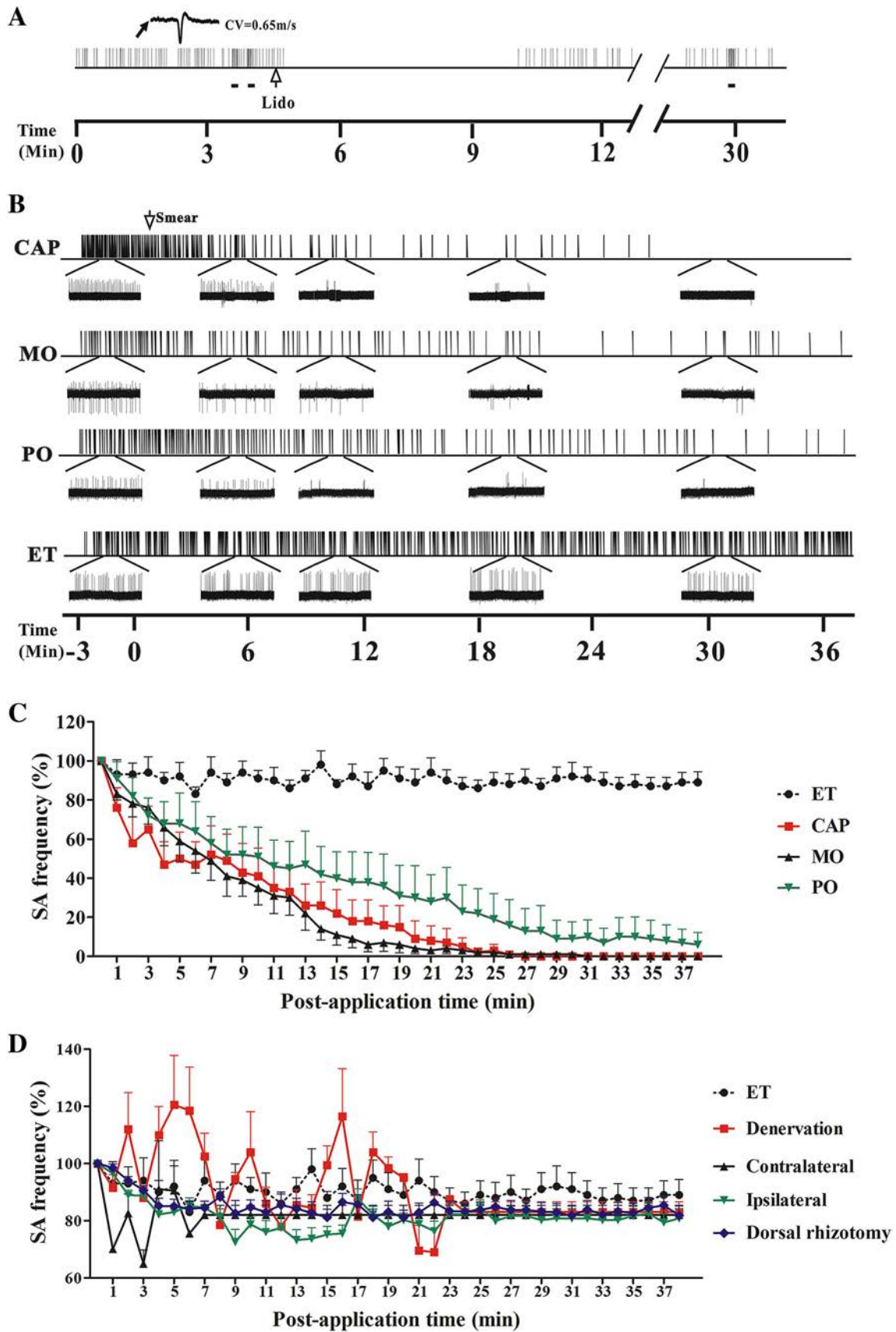


Fig. 4 Spontaneous activity (SA) of muscular nociceptive C-neurons recorded in L4 dorsal root ganglion (DRG) neurons after applying irritants in rats injected with complete Freund's adjuvant (CFA). **A** Representative recording of SA in a muscular C-nociceptive neuron (conduction velocity [CV] = 0.65 m/s) 2 days after CFA injection. The SA was blocked within 1 min after intramuscular injection of lidocaine (Lido, 10 μ L, blank arrow) into the receptive field, and then recovered \sim 6 min later. Horizontal bars below recording indicate mechanical stimuli (100 mN) to the receptive field. **B** Examples of SA in muscular nociceptive C-neurons that was gradually inhibited by capsaicin (CAP), mustard oil (MO), and peppermint oil (PO) on the skin overlying the inflamed muscle in CFA-injected rats. Ethanol (ET) was used as control. Insets below, expanded traces at different time points. **C** Statistics of SA frequency after applying CAP ($n = 10$), MO ($n = 6$), PO ($n = 6$), and ET ($n = 8$) on the skin overlying the inflamed muscle in CFA-injected rats. The average SA frequency within 3 min before irritant application was defined as 100%. CAP, MO and PO *vs* ET; CAP group: $P < 0.05$ at 5 min post-application and later; MO and PO groups: $P < 0.05$ at 12 min post-application and later. **D** Statistics of SA frequency after applying CAP to the skin overlying the inflamed muscle after cutaneous denervation ($n = 6$) or L4 dorsal rhizotomy ($n = 2$); the skin overlying the contralateral tibialis anterior (Contralateral) ($n = 5$); and the ipsilateral plantar skin (Ipsilateral) ($n = 6$) in CFA-injected rats. Denervation, L4 dorsal rhizotomy, Contralateral and Ipsilateral *vs* ET ($n = 8$); $P > 0.05$ at all tested time points.

It is worth noting that there were discrepancies in our behavioral and electrophysiological findings. For example, although the inhibitory effect of MO in electrophysiology studies was stronger than that after CAP, the analgesia induced by MO was less than that induced by CAP in behavioral tests. This discrepancy might be due to the difference in the durations of the behavioral and electrophysiological recordings. In the behavioral experiments, we found that the strongest analgesic effect occurred a few hours after applying the irritants. In the electrophysiological recordings, we were only able to record the discharges of primary neurons for as long as 40 min after the skin was smeared with irritant. Although the recordings were

conducted with great care, the activity of DRG neurons tends to attenuate after prolonged recording. This technical limitation might be the reason for the discrepancies between the behavioral and electrophysiological results, and will be further explored in future studies.

CAP, MO, and PO evoke pain sensation in the skin by activating different subtypes of nociceptive neuronal ending through different receptors (TRPV1, TRPM8, and TRPA1, respectively) [33]. We believe that the inhibitory effect on the evoked and spontaneous activity of muscular DRG neurons by these topical irritants may be attributed to the activation of small-diameter nociceptive cutaneous afferents, regardless of the subtypes of these neurons. So far, the mechanism of this inhibitory effect of cutaneous nociceptors on muscular nociceptors has not been fully clarified. Using behavioral and *in vivo* electrophysiological methods, we first confirmed a previous finding that application of the analgesic CAP to the skin over the inflamed muscle alleviates inflammatory muscle pain [17]. Furthermore, the analgesic effects disappeared when the sensory input was blocked by dorsal rhizotomy or skin denervation, or when the irritants were applied to remote skin. These results suggest that activated cutaneous nociceptive afferents inhibit muscular nociceptive neurons through an inhibitory interaction in the same spinal segment. This potential mechanism might be different from the theory of diffuse noxious inhibitory control [18]. We speculate that activated cutaneous nociceptive afferents inhibit the dorsal root reflex [34] of adjacent nociceptive fibers innervating the inflamed muscle, thus reducing the antidromic discharge of muscular C-fibers and the release of inflammatory mediators in the peripheral nerve terminals. The hypothesis involving spinal mechanisms needs to be further investigated in future experiments.

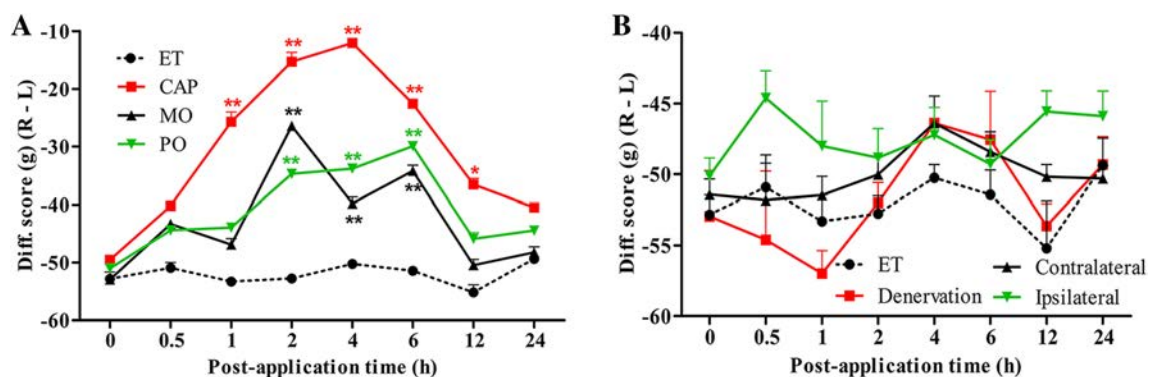


Fig. 5 Weight-bearing after application of topical irritants in CFA-injected rats. **A** Difference scores for weight-bearing (ipsilateral-contralateral) increased after the application of capsaicin (CAP) ($n = 4$), mustard oil (MO) ($n = 4$), peppermint oil (PO) ($n = 4$), and ethanol (ET) ($n = 4$) to the skin over the ipsilateral tibialis anterior. **B** Difference score for weight-bearing remained unchanged following the application of CAP to the denervated skin over the ipsilateral

tibialis anterior (Denervation) ($n = 7$), skin over the contralateral tibialis anterior (Contralateral) ($n = 6$), and the ipsilateral plantar skin (Ipsilateral) ($n = 6$). ET on the skin overlying the inflamed muscle was taken as control in both **A** and **B**. $*P < 0.05$, $**P < 0.01$; CAP, MO and PO *vs* ET (**A**); Denervation, Contralateral and Ipsilateral *vs* ET (**B**).

We studied the electrophysiological characteristics of muscular nociceptive neurons in a rat model of inflammatory muscle pain. The topical irritants CAP, MO, and PO, applied to the skin over the inflamed muscle inhibited muscular nociceptive neurons and alleviated muscle pain *via* the activation of cutaneous nociceptors. Our findings suggest novel therapeutic strategies for the treatment of inflammatory muscle pain.

Acknowledgements We thank Bo Yuan and Tao Wang from the Institute of Basic Medical Sciences, Chinese Academy of Medical Sciences, Beijing, China, for technical assistance. This work was supported by the National Natural Science Foundation of China (81771205 and 91632113), the Natural Science Foundation and Major Basic Research Program of Shanghai Municipality, China (16JC1420500 and 16JC1420502), the Chinese Academy of Medical Sciences Innovation Fund for Medical Sciences (2017-I2M-3-008), and the National Natural Science Foundation for Young Scientists of China (81600956).

Conflict of interest All authors claim that there are no conflicts of interest.

References

- Harden RN. Muscle pain syndromes. *Am J Phys Med Rehabil* 2007, 86: S47–S58.
- Staud R. Future perspectives: pathogenesis of chronic muscle pain. *Best Pract Res Clin Rheumatol* 2007, 21: 581–596.
- Sumpton JE, Moulin DE. Fibromyalgia. *Handb Clin Neurol* 2014, 119: 513–527.
- Borg-Stein J, Iaccarino MA. Myofascial pain syndrome treatments. *Phys Med Rehabil Clin N Am* 2014, 25: 357–374.
- Segal LS, Odgers R, Carpentieri D, Shrader MW. Back pain in Duchenne muscular dystrophy: steroids are not always the culprit. *J Pediatr Orthop B* 2016, 25: 81–85.
- Mense S. Muscle pain: mechanisms and clinical significance. *Dtsch Arztebl Int* 2008, 105: 214–219.
- Graven-Nielsen T, Arendt-Nielsen L. Induction and assessment of muscle pain, referred pain, and muscular hyperalgesia. *Curr Pain Headache Rep* 2003, 7: 443–451.
- Salzberg L. The physiology of low back pain. *Prim Care* 2012, 39: 487–498.
- Golob AL, Wipf JE. Low back pain. *Med Clin North Am* 2014, 98: 405–428.
- Ambalavanar R, Moritani M, Haines A, Hilton T, Dessem D. Chemical phenotypes of muscle and cutaneous afferent neurons in the rat trigeminal ganglion. *J Comp Neurol* 2003, 460: 167–179.
- Hoheisel U, Reinohl J, Unger T, Mense S. Acidic pH and capsaicin activate mechanosensitive group IV muscle receptors in the rat. *Pain* 2004, 110: 149–157.
- Hoheisel U, Unger T, Mense S. Excitatory and modulatory effects of inflammatory cytokines and neurotrophins on mechanosensitive group IV muscle afferents in the rat. *Pain* 2005, 114: 168–176.
- Kirilova I, Rausch VH, Tode J, Baron R, Janig W. Mechano- and thermosensitivity of injured muscle afferents. *J Neurophysiol* 2011, 105: 2058–2073.
- Hautkappe M, Roizen MF, Toledano A, Roth S, Jeffries JA, Ostermeier AM. Review of the effectiveness of capsaicin for painful cutaneous disorders and neural dysfunction. *Clin J Pain* 1998, 14: 97–106.
- Sawynok J. Topical analgesics in neuropathic pain. *Curr Pharm Des* 2005, 11: 2995–3004.
- Cal K. Skin disposition of menthol after its application in the presence of drug substances. *Biopharm Drug Dispos* 2008, 29: 449–454.
- Duan WR, Lu J, Xie YK. Mechanisms of topical analgesics in relieving pain in an animal model of muscular inflammation. *Pain Med* 2013, 14: 1381–1387.
- Le Bars D, Dickenson AH, Besson JM. Diffuse noxious inhibitory controls (DNIC). II. Lack of effect on non-convergent neurones, supraspinal involvement and theoretical implications. *Pain* 1979, 6: 305–327.
- Zhou LJ, Ren WJ, Zhong Y, Yang T, Wei XH, Xin WJ, *et al.* Limited BDNF contributes to the failure of injury to skin afferents to produce a neuropathic pain condition. *Pain* 2010, 148: 148–157.
- Ijpm FF, Nicolai JP, Meek MF. Sural nerve donor-site morbidity: thirty-four years of follow-up. *Ann Plast Surg* 2006, 57: 391–395.
- Cooksey CJ. Quirks of dye nomenclature. 1. Evans blue. *Biotech Histochem* 2014, 89: 111–113.
- Donelan J, Boucher W, Papadopoulou N, Lytinas M, Papaliodis D, Dobner P, *et al.* Corticotropin-releasing hormone induces skin vascular permeability through a neurotensin-dependent process. *Proc Natl Acad Sci USA* 2006, 103: 7759–7764.
- Inoue H, Asaka T, Nagata N, Koshihara Y. Mechanism of mustard oil-induced skin inflammation in mice. *Eur J Pharmacol* 1997, 333: 231–240.
- Banvolgyi A, Pozsgai G, Brain SD, Helyes ZS, Szolcsanyi J, Ghosh M, *et al.* Mustard oil induces a transient receptor potential vanilloid 1 receptor-independent neurogenic inflammation and a non-neurogenic cellular inflammatory component in mice. *Neuroscience* 2004, 125: 449–459.
- Elsaie LT, El Mohsen AM, Ibrahim IM, Mohey-Eddin MH, Elsaie ML. Effectiveness of topical peppermint oil on symptomatic treatment of chronic pruritus. *Clin Cosmet Investig Dermatol* 2016, 9: 333–338.
- Argoff CE. Topical analgesics in the management of acute and chronic pain. *Mayo Clin Proc* 2013, 88: 195–205.
- Tandrup T. Unbiased estimates of number and size of rat dorsal root ganglion cells in studies of structure and cell survival. *J Neurocytol* 2004, 33: 173–192.
- Ma C, LaMotte RH. Multiple sites for generation of ectopic spontaneous activity in neurons of the chronically compressed dorsal root ganglion. *J Neurosci* 2007, 27: 14059–14068.
- Arendt-Nielsen L, Graven-Nielsen T. Muscle pain: sensory implications and interaction with motor control. *Clin J Pain* 2008, 24: 291–298.
- Andersen OK, Graven-Nielsen T, Matre D, Arendt-Nielsen L, Schomburg ED. Interaction between cutaneous and muscle afferent activity in polysynaptic reflex pathways: a human experimental study. *Pain* 2000, 84: 29–36.
- Hu P, McLachlan EM. Selective reactions of cutaneous and muscle afferent neurons to peripheral nerve transection in rats. *J Neurosci* 2003, 23: 10559–10567.
- Djouhri L, Koutsikou S, Fang X, McMullan S, Lawson SN. Spontaneous pain, both neuropathic and inflammatory, is related to frequency of spontaneous firing in intact C-fiber nociceptors. *J Neurosci* 2006, 26: 1281–1292.
- Moore C, Gupta R, Jordt SE, Chen Y, Liedtke WB. Regulation of pain and itch by TRP channels. *Neurosci Bull* 2018, 34: 120–142.
- Lin Q, Wu J, Willis WD. Dorsal root reflexes and cutaneous neurogenic inflammation after intradermal injection of capsaicin in rats. *J Neurophysiol* 1999, 82: 2602–2611.



SCN9A Epileptic Encephalopathy Mutations Display a Gain-of-function Phenotype and Distinct Sensitivity to Oxcarbazepine

Shuzhang Zhang¹ · Zhiping Zhang¹ · Yuan Shen² · Yudan Zhu² · Kun Du³ ·
Jingkang Guo¹ · Yonghua Ji^{1,4} · Jie Tao^{2,5}

Received: 12 December 2018 / Accepted: 12 April 2019 / Published online: 1 August 2019
© Shanghai Institutes for Biological Sciences, CAS 2019

Abstract Genetic mutants of voltage-gated sodium channels (VGSCs) are considered to be responsible for the increasing number of epilepsy syndromes. Previous research has indicated that mutations of one of the VGSC genes, *SCN9A* (Nav1.7), result in febrile seizures and Dravet syndrome in humans. Despite these recent efforts, the electrophysiological basis of *SCN9A* mutations remains unclear. Here, we performed a genetic screen of patients with febrile seizures and identified a novel missense mutation of *SCN9A* (W1150R). Electrophysiological characterization of different *SCN9A* mutants in HEK293T cells, the previously-reported N641Y and K655R variants, as well as the newly-found W1150R variant, revealed that the current density of the W1150R and N641Y variants was significantly larger than that of the wild-type (WT) channel. The time constants of recovery from fast inactivation of the N641Y and K655R variants were markedly

lower than in the WT channel. The W1150R variant caused a negative shift of the G–V curve in the voltage dependence of steady-state activation. All mutants displayed persistent currents larger than the WT channel. In addition, we found that oxcarbazepine (OXC), one of the antiepileptic drugs targeting VGSCs, caused a significant shift to more negative potential for the activation and inactivation in WT and mutant channels. OXC-induced inhibition of currents was weaker in the W1150R variant than in the WT. Furthermore, with administering OXC the time constant of the N641Y variant was longer than those of the other two *SCN9A* mutants. In all, our results indicated that the point mutation W1150R resulted in a novel gain-of-function variant. These findings indicated that *SCN9A* mutants contribute to an increase in seizure, and show distinct sensitivity to OXC.

Keywords Voltage-gated sodium channel · *SCN9A* · Epilepsy · Electrophysiological function · Oxcarbazepine · Sensitivity

✉ Yonghua Ji
yhji@staff.shu.edu.cn

✉ Jie Tao
jietao_putuo@foxmail.com

¹ Institute of Biomembrane and Biopharmaceutics, Shanghai University, Shanghai 200444, China

² Central Laboratory and Department of Neurology, Putuo Hospital, Shanghai University of Traditional Chinese Medicine, Shanghai 200062, China

³ Department of Clinical Laboratory, Xin Hua Hospital Affiliated to Shanghai Jiao Tong University School of Medicine, Shanghai 202150, China

⁴ Xinhua Translational Institute for Cancer Pain, Xinhua Hospital Chongming Branch, Shanghai 202150, China

⁵ Putuo Clinical Medical School, Anhui Medical University, Shanghai 200062, China

Introduction

The voltage-gated sodium channel (VGSC) plays a notable role in the generation and propagation of the action potentials in neurons [1]. It has been reported that VGSCs are genetically mutated in epileptic patients as well as animal models [2–5]. The VGSC subtype Nav1.7 is encoded by *SCN9A*, which is well known to be involved in the generation, development, and maintenance of pain responses [6, 7]. Nav1.7 is preferentially expressed in the peripheral nervous system [8–10] and dynamically expressed in the central nervous system, including the cerebral cortex and hippocampus [11]. Furthermore, it has

been determined that the gain-of-function mutants of *SCN9A* are involved in neuropathic pain, such as in inherited erythromelalgia, paroxysmal extreme pain disorder, and fibrotic neuropathy, whereas the loss-of-function mutants of *SCN9A* can lead to an indifference to pain [12–14]. One noteworthy finding showed *SCN9A* mutants in 21 individuals in a family suffering from febrile seizures [15]. A missense mutation of *SCN9A* (N641Y), a conserved amino-acid residue located at the intracellular loop between domains I and II of the VGSC protein, was detected in a pedigree with febrile seizures and regarded as a gain-of-function mutation. Mice carrying the *SCN9A*-N641Y mutation are more susceptible to clonic and tonic seizures induced by electrical stimulation [16]. When *SCN9A* was sequenced in 92 unrelated patients with childhood seizures occurring during febrile illness, an associated missense mutation (K655R) was found [17]. In addition, in an analysis of a cohort of 109 patients with Dravet syndrome, nine were identified with eight different *SCN9A* mutations, including K655R [16]. Collectively, these data confirm that *SCN9A* missense mutations are disease-causing for febrile seizures and Dravet syndrome. Interestingly, several *SCN9A* mutants either act as modifiers in the presence of stronger mutants or cause mild seizures by themselves, some of which also harbor splice site or missense mutations in *SCN1A* [17]. Interestingly, a few of the pathogenic *SCN9A* mutants with or without *SCN1A* mutations have been identified in epileptic patients [18, 19]. It is thus worthwhile to delve into the molecular mechanism by which *SCN9A* variants induce epileptic seizures.

Oxcarbazepine (OXC) is one of the novel anti-epileptic drugs used to control tonic-clonic seizures. It is generally well-tolerated and has a more predictable dose-response relationship than carbamazepine. One report indicates that OXC most likely has a greater effect than carbamazepine in reducing serum Na^+ levels, particularly at higher doses [20]. Moreover, it has been reported that OXC inhibits abnormal neuronal firing by targeting of voltage-dependent Na^+ channels, and reduces the excitatory synaptic transmission [21].

In this study, we set out to investigate the molecular mechanism of *SCN9A* in the generation of epilepsy. To do so, we performed a genetic screen of children with febrile seizures, and identified a novel *SCN9A* missense variant: W1150R. We then determined the electrophysiological characteristics of the variants W1150R, N641Y, and K655R and also tested the sensitivity of three gain-of-function *SCN9A* variants to OXC.

Materials and Methods

Mutation Screening

Genomic DNA was extracted from peripheral blood with kit (DP348, Tiangen, Beijing, China). The samples were assessed by Shanghai Biotechnology Corp., China. *SCN9A* variants were examined in children with febrile seizures by whole-exome sequencing. This study was approved by the Institutional Review Board at Putuo District Center Hospital, Shanghai (Putuo Hospital, Shanghai University of Traditional Chinese Medicine). And informed consent was given by the parent or guardian.

Site-Directed Mutagenesis of *SCN9A* (hNav1.7)

Plasmids

Three individual point-mutations (N641Y, K655R, and W1150R) were constructed. Each amino-acid substitution was introduced into the pEZ-Lv206-hNav1.7 plasmid using a Hieff MutTM Site-Directed Mutagenesis Kit (11004ES10, Yeasen, Shanghai, China) according to the manufacturer's protocol. The constructs were verified by resequencing before transfection into HEK293T cells.

Homology Modelling

An alignment of the top 48 sequences most similar to *SCN9A* was conducted using PSI-BLAST (Discovery Studio 2017 R2, Neotrident, Shanghai, China). The cryo-EM structure of the electric eel Nav1.4 (PDB ID 5XSY) [22] served as the structural template to construct wild-type and W1150R homology models of hNav1.7, using the MODELER. MODELER selected the optimal model based on probability density function (PDF) or discrete optimized protein energy (DOPE) values. When the PDF of the total energy of a structural model is the same, the DOPE score, based on the atomic statistical potential energy, can be used as a basis for measuring the quality of the model.

Cell Transfection

HEK293T cells were grown in a humidified atmosphere of 5% CO_2 and 95% air at 37 °C in Dulbecco's modified Eagle's medium (Invitrogen, CA) supplemented with 10% fetal bovine serum (Invitrogen), then seeded in 24-well plates 24 h before transfection. Wild-type pEZ-Lv206-hNav1.7 plasmids or mutants were transfected into HEK293T cells together with pIRES-EGFP-h β 1 using Lipofectamine 3000 (Invitrogen) with 4 μg of plasmids and 1 μg pIRES-EGFP-h β 1 according to the manufacturer's

instructions. Electrophysiological recordings from fluorescent cells were made 48 h after transfection.

Chemicals and Solutions

OXC from Sigma (Poole, UK) was dissolved in extracellular solution containing 1% dimethyl sulfoxide at 120 $\mu\text{mol/L}$ [23, 24].

Electrophysiological Recording

The patch clamp recordings were performed at room temperature using EPC-10USB (HEKA Elektronik, Germany). Data were acquired and analyzed using Patchmaster (HEKA Elektronik). Cells recognized by the marker genes Cherry (pEZ-Lv206-hNav1.7) and GFP (pIRES-EGFP-h β 1) were chosen for patch clamp recording. The solutions used for whole-cell voltage clamp recording were: extracellular solution (in mmol/L): 140 NaCl, 2 CaCl₂, 2 MgCl₂, 10 HEPES, and 10 D-glucose, pH 7.3 with NaOH (320 mOsm adjusted with D-glucose); and intracellular solution (in mmol/L): 140 CsF, 10 CsCl, 2 MgCl₂, 10 EGTA, 10 HEPES, pH 7.3 with CsOH, osmolality adjusted to 310 mOsm with D-glucose. The patch pipettes had resistances of 2 M Ω –5 M Ω when filled with pipette solution. Cells were held at -120 mV in all experiments. When voltage errors were used with 80% series resistance compensation, this cell can be used for data statistics.

The peak currents were determined using 100-ms pulses from -100 mV to $+75$ mV in 5-mV steps from a holding potential of -120 mV at 5-s intervals. The peak current was normalized for cell capacitance, and plotted against voltage to generate the peak current density–voltage relationship. Conductance as a function of voltage was obtained from the current–voltage relationship: $G(V) = I(V)/(V - E_{\text{Na}})$ and fitted by the Boltzmann function: $G = I/(1 + \exp[(V - V_{1/2})/K])$ to determine the voltage midpoint ($V_{1/2}$) and slope factor (K). For steady-state inactivation, cells were held at -140 mV and the test potential was from -140 mV to 20 mV for 600 ms at 10-mV increments. A second pulse to -10 mV for 50 ms was used to assess channel availability. The normalized current was plotted against voltage, and steady-state inactivation curves were also fitted with the Boltzmann equation as above to determine the voltage midpoint ($V_{1/2}$) and slope factor K . To generate fast inactivation curves, cells were stepped to inactivating potentials from -140 mV to 20 mV for 60 ms followed by a 50-ms step to -10 mV as the second pulse. The fast inactivation peak current was normalized by maximum current amplitude, and fitted by Boltzmann function as above to determine the voltage midpoint ($V_{1/2}$) and slope factor K . For recovery from inactivation, cells were held at -120 mV and

depolarized to a test potential of 0 mV for 50 ms to inactivate Na⁺ channels. Recovery was determined at times between 2 ms and 40 ms with a test potential of -140 mV. A 50-ms pulse to -10 mV was subsequently applied to assess the extent of channel recovery. Peak current was normalized by maximum current amplitude and fitted with a single exponential function: $I/I_{\text{max}} = A [1 - \exp(-t/\tau_{\text{rec}})]$ to determine the time constant τ .

For experiments including the testing of OXC, electrophysiological protocols under control, drug-free conditions were obtained before bath application of OXC (120 $\mu\text{mol/L}$, 5 min).

Statistical Analysis

Data were analyzed with OriginPro 8.5 (OriginLab, CA), Excel 2016 (Microsoft, WA) and Prism 6 (GraphPad software, San Diego, CA). Data are presented as the mean \pm standard error of the mean (SEM). Student's *t*-test or one-way ANOVA was used to assess the statistical significance of differences. When $P < 0.05$, differences were accepted as significant.

Results

Identification of an Identical *De Novo* Variant in *SCN9A* (hNav1.7) from a Patient with Febrile Seizures

We identified a novel variant c3488T > C [p.(W1150R)] in a patient with febrile seizures. The patient presented at age 2 with complex focal seizures with secondary generalization. The patient's first seizure (generalized tonic-clonic seizure for 5 min) developed with fever (38.6 °C). The EEG showed high-potential spike activity, paroxysmal release, and δ frequency power enhancement. At age 3, seizures occurred 4 times with fever (38 °C–39.5 °C), the longest lasting 10 min. The patient had no pain or malnutrition. Growth and mental development were the same as his peers. His grandfather had a history of febrile seizures but there was no additional family history of epilepsy.

We determined that the location of amino-acid W1150 was in the domain II/III cytoplasmic linker of Nav1.7 (Fig. 1A). A previous study already reported that two mutants (N641Y and K655R) are located in the domain I/II cytoplasmic linker of Nav1.7 [16] (Fig. 1A). Therefore, we constructed three plasmids: *SCN9A*-N641Y, *SCN9A*-K655R, and *SCN9A*-W1150R (Fig. 1B).

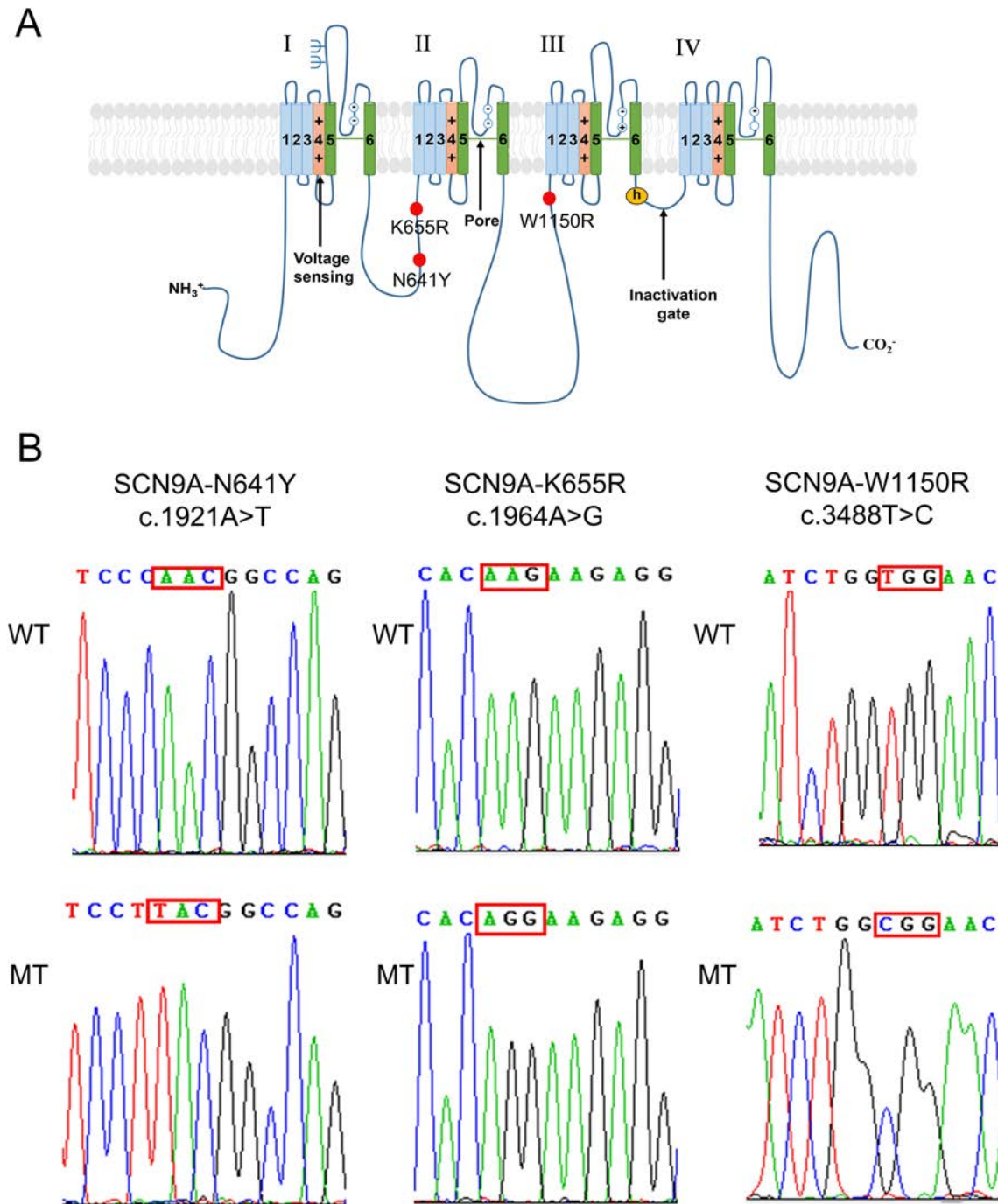


Fig. 1 Location and sequencing of the *SCN9A* variants. **A** Predicted transmembrane topology of *SCN9A* depicting the location of the variants. The S4 segments are voltage sensors and marked with plus

signs. **B** DNA sequencing identified the mutations in the constructed pEZ-Lv206-hNav1.7 plasmid. The mutation sites are marked by a red squares.

Activation Properties of hNav1.7 Variants

Homology modeling revealed that the hNav1.7 mutation W1150R altered the α -helix of the S1 segment in domain III (Fig. 2). Representative currents of hNav1.7 and variants co-expressed with h β 1 subunits in HEK293T cells are illustrated in Fig. 3A. The average peak current

density–voltage relationships were measured from cells transiently expressing mutants or hNav1.7 (Fig. 3B). We measured the peak current densities of the three variants and found that those of the W1150R and N641Y variants were significantly larger than that of the WT channel (WT, -109.5 ± 10.4 pA/pF, $n = 11$; N641Y, -183.4 ± 16.9 pA/pF, $n = 16$, $P < 0.01$; W1150R, -159.1 ± 15.1 pA/pF,

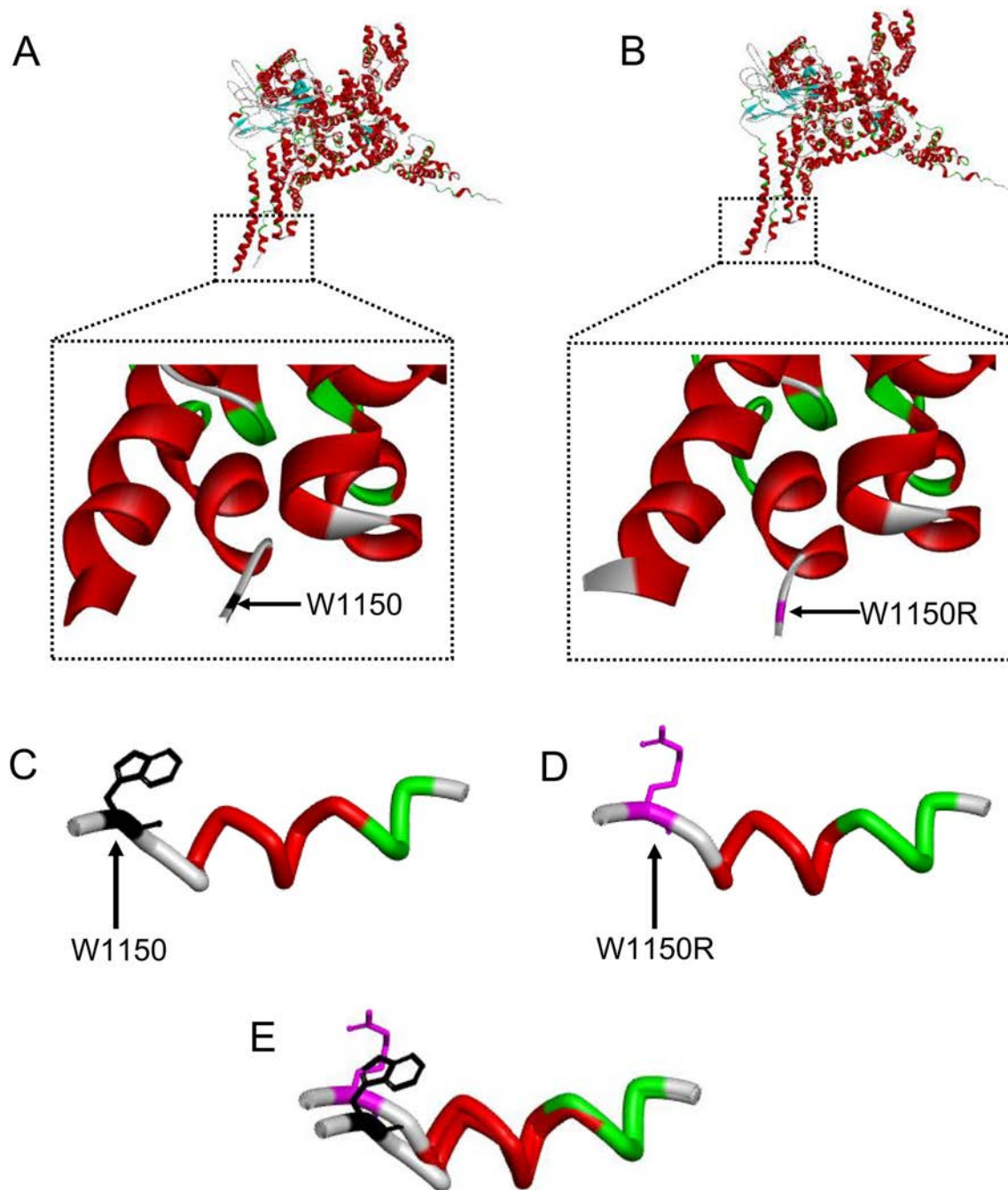


Fig. 2 W1150R mutation affects the α -helix of the S1 segment in domain III. **A, B** Schematics of the backbone structure of the wild-type and mutated domains. **C–E** Stick diagrams of the S1 segment of domain III of the wild-type and W1150R mutant. Black, W1150; magenta, W1150R.

$n = 8$, $P < 0.05$; Table 1). However, the current density of the K655R variant did not significantly differ from WT channels (K655R, -134.4 ± 12.2 pA/pF, $n = 10$; Table 1). Using statistical analysis, we also found a large hyperpolarizing shift of the G - V curve for the voltage-dependence of steady-state activation that occurred in the W1150R variant ($V_{1/2}$ by -4.3 mV; $n = 12$, $P < 0.05$; Fig. 3C, D, Table 1). On the contrary, the N641Y and K655R variants presented a marked depolarizing shift of the G - V curve (Fig. 3C, D). The

$V_{1/2}$ values for the N641Y and K655R variants were -15.0 ± 0.6 mV and -16.0 ± 1.8 mV, respectively (Table 1). There was no difference in the slope factor (K) for any of the mutants when compared with the control group (Fig. 3E, Table 1). The transition from the open to the inactivated state was delayed in the W1150R variant at depolarizing voltages ranging $+20$ mV and $+70$ mV (Fig. 3F), but in the K655R variant the transition was delayed between $+20$ mV and $+40$ mV. As for the

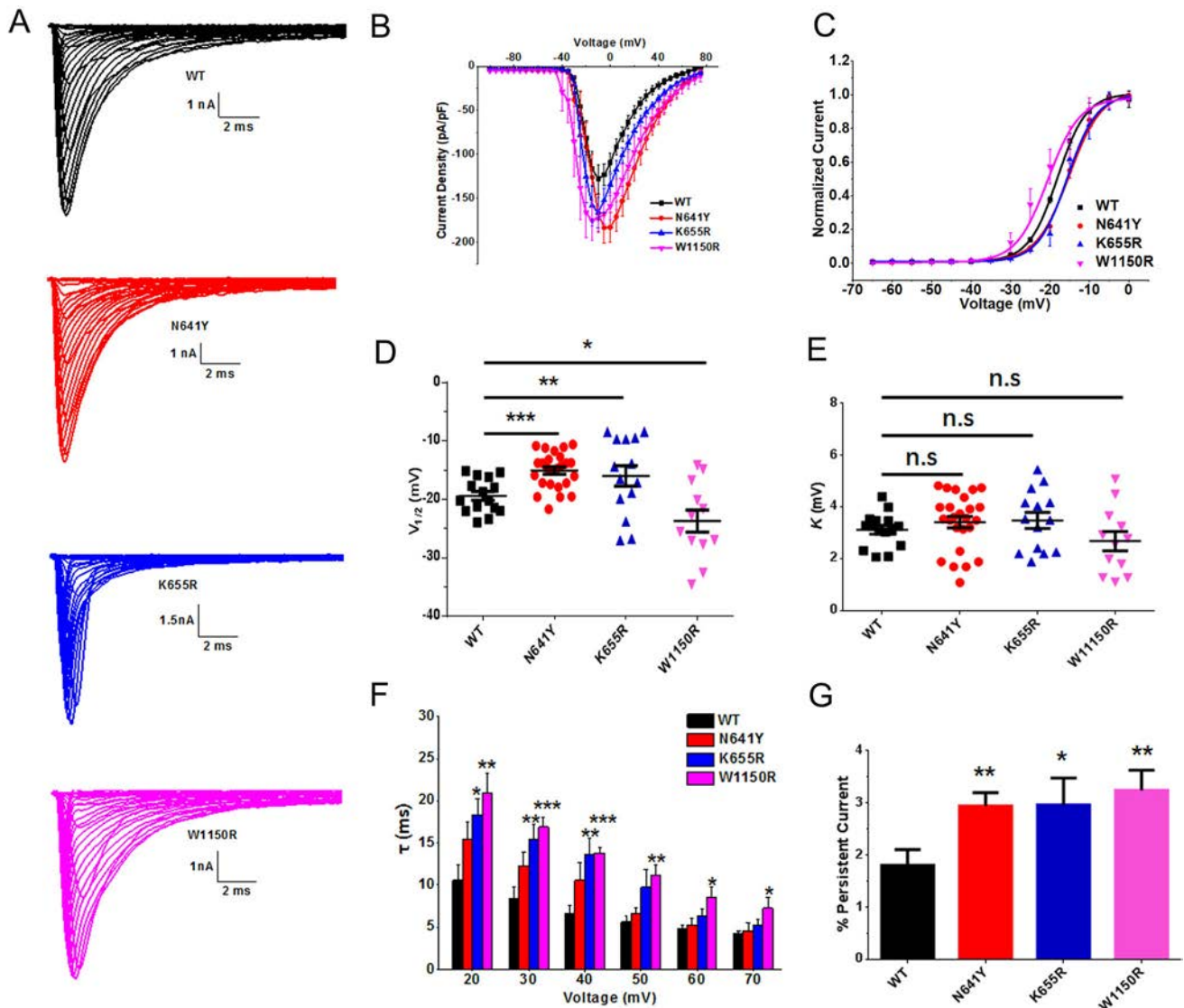


Fig. 3 Steady-state activation of *SCN9A* variants and hNav1.7. **A** Average Na^+ current traces recorded from HEK293T cells co-expressing pEZ-Lv206-hNav1.7 and pIRES-EGFP-h β 1 plasmids. **B** Average current density–voltage relationship. Peak currents were normalized to cell capacitance. **C** Voltage-dependence of steady-state activation of WT and variants. Curves are Boltzmann fits of the data. **D** Scatter plots of voltage at half-maximal steady-state activation ($V_{1/2}$

for WT and variants. **E** Scatter plots of the slope factor of activation (K). **F** Average fast time constants (τ) from single exponential fits to macroscopic current decays as a function of voltage. **G** Magnitude of persistent current as a percentage of the peak current at -10 mV. Data are the mean \pm SEM. * $P < 0.05$, ** $P < 0.01$, *** $P < 0.001$. Black, WT; red, N641Y; blue, K655R; magenta, W1150R.

N641Y variant, the open time was unchanged. The persistent current generated by the three variants was greater than that of the WT channel, measured as a percentage of the peak current (N641Y = $2.9\% \pm 0.2\%$, $n = 16$, $P < 0.01$; K665R = $3.0\% \pm 0.5\%$, $n = 9$, $P < 0.05$; W1150R = $3.2\% \pm 0.4\%$, $n = 13$, $P < 0.01$; WT = $1.8\% \pm 0.3\%$, $n = 15$; Fig. 3G).

Characterization of the Inactivation of hNav1.7 Variants

To assess the voltage-dependence of steady-state inactivation and fast inactivation, cells expressing the WT and variants were tested. Compared to WT channels, there was no significant difference in any of the mutants regarding the half-maximal voltage-dependence of steady-state inactivation (WT: $V_{1/2} = -67.0 \pm 0.5$ mV, $n = 16$; N641Y: $V_{1/2} = -64.3 \pm 1.3$ mV, $n = 20$; K655R: $V_{1/2} = -66.1 \pm 0.8$ mV, $n = 18$; W1150R: $V_{1/2} =$

Table 1 Biophysical properties of mutant and WT channels.

	Steady-state activation		Steady-state inactivation		Fast inactivation		Recovery from fast inactivation		Current density (0 mV)			
	$V_{1/2}$ (mV)	K	n	$V_{1/2}$ (mV)	K	n	$V_{1/2}$ (mV)	K	n	τ (ms)	n	pA/pF
WT	-19.4 ± 0.8	3.1 ± 0.2	15	-67.0 ± 0.5	5.4 ± 0.2	16	-34.8 ± 0.7	8.2 ± 0.4	24	1.9 ± 0.2	10	-109.5 ± 10.4
N641Y	-15.0 ± 0.6***	3.4 ± 0.2	25	-64.3 ± 1.3	6.2 ± 0.2*	20	-33.0 ± 1.0	7.2 ± 0.4	20	1.3 ± 0.1*	8	-183.4 ± 16.9**
K655R	-16.0 ± 1.8**	3.5 ± 0.3	14	-66.1 ± 0.8	5.2 ± 0.2	18	-33.7 ± 1.0	8.1 ± 0.5	26	1.4 ± 0.1*	17	-134.4 ± 12.2
W1150R	-23.7 ± 1.9*	2.7 ± 0.4	12	-65.4 ± 1.1	5.1 ± 0.2	14	-33.5 ± 1.3	7.6 ± 0.7	17	2.1 ± 0.2	12	-159.1 ± 15.1*

$V_{1/2}$, voltage midpoint activation or inactivation; K , slope factor; n , number of cells; τ , time constant.

Values represent the mean ± SEM.

* $P < 0.05$, ** $P < 0.01$, *** $P < 0.001$, unpaired Student's t -test.

Table 2 Oxcarbazepine (OXC; 120 μ mol/L) modulated the biophysical properties of mutant and WT channels.

	Activation		Steady inactivation		Fast inactivation		Recovery from fast inactivation			
	$V_{1/2}$ (mV)	K	n	$V_{1/2}$ (mV)	K	n	$V_{1/2}$ (mV)	K	n	τ (ms)
WT	-19.5 ± 0.7	3.3 ± 0.1	8	-66.3 ± 0.6	5.6 ± 0.3	9	-38.0 ± 0.4	8.5 ± 0.3	7	1.7 ± 0.3
WT + OXC	-23.6 ± 1.2**	3.7 ± 0.2	8	-71.7 ± 1.5**	5.8 ± 0.2	9	-46.1 ± 1.5***	8.8 ± 0.5	7	2.5 ± 0.2**
N641Y	-17.0 ± 0.8	3.6 ± 0.4	6	-62.7 ± 1.1	6.5 ± 0.1	14	-37.1 ± 0.9	5.5 ± 0.3	9	1.3 ± 0.1
N641Y + OXC	-24.6 ± 0.6***	3.7 ± 0.2	6	-69.1 ± 1.4**	6.7 ± 0.4	14	-46.4 ± 2.1***	4.9 ± 0.8	9	2.8 ± 0.3***
K655R	-17.8 ± 1.8	3.5 ± 0.3	9	-67.9 ± 0.3	5.1 ± 0.2	11	-37.0 ± 0.9	8.1 ± 0.5	13	1.4 ± 0.1
K655R + OXC	-24.3 ± 0.7*	3.6 ± 0.4	12	-71.3 ± 0.7***	6.1 ± 0.2**	11	-41.5 ± 1.2**	8.5 ± 0.5	13	1.8 ± 0.1**
W1150R	-23.7 ± 1.9	2.8 ± 0.3	12	-64.5 ± 0.5	5.6 ± 0.2	10	-37.5 ± 1.3	8.9 ± 1.3	9	2.4 ± 0.2
W1150R + OXC	-31.2 ± 2.5*	2.9 ± 0.4	12	-73.1 ± 2.0***	6.1 ± 0.3	10	-50.3 ± 2.3***	8.9 ± 1.0	9	3.2 ± 0.3*

$V_{1/2}$, voltage midpoint activation or inactivation; K , slope factor; n , number of cells; τ , time constant.

Values represent the mean ± SEM.

* $P < 0.05$, ** $P < 0.01$, *** $P < 0.001$, unpaired Student's t -test.

– 65.4 ± 1.1 mV, $n = 14$; Fig. 4A, B, Table 1). Notably, only the slope factor of the N641Y variant was increased ($n = 20$, $P < 0.05$; Fig. 4C, Table 1). There were no statistical differences in the average fits for fast inactivation for the variants compared to the WT channels (WT: $V_{1/2} = -34.8 \pm 0.7$ mV, $K = 8.2 \pm 0.4$, $n = 24$; N641Y: $V_{1/2} = -33.0 \pm 1.0$ mV, $K = 7.2 \pm 0.4$, $n = 20$; K655R: $V_{1/2} = -33.7 \pm 1.0$ mV, $K = 8.1 \pm 0.5$, $n = 26$; W1150R:

$V_{1/2} = -33.5 \pm 1.3$ mV, $K = 7.6 \pm 0.7$, $n = 17$; Fig. 4D–F, Table 1).

Recovery Properties of hNav1.7 Variants

We also examined the kinetic correlations between the recovery and inactivation of the WT and variants. The time constant of recovery from inactivation for the W1150R variant (2.1 ± 0.2 ms, $n = 12$) was similar to that of the

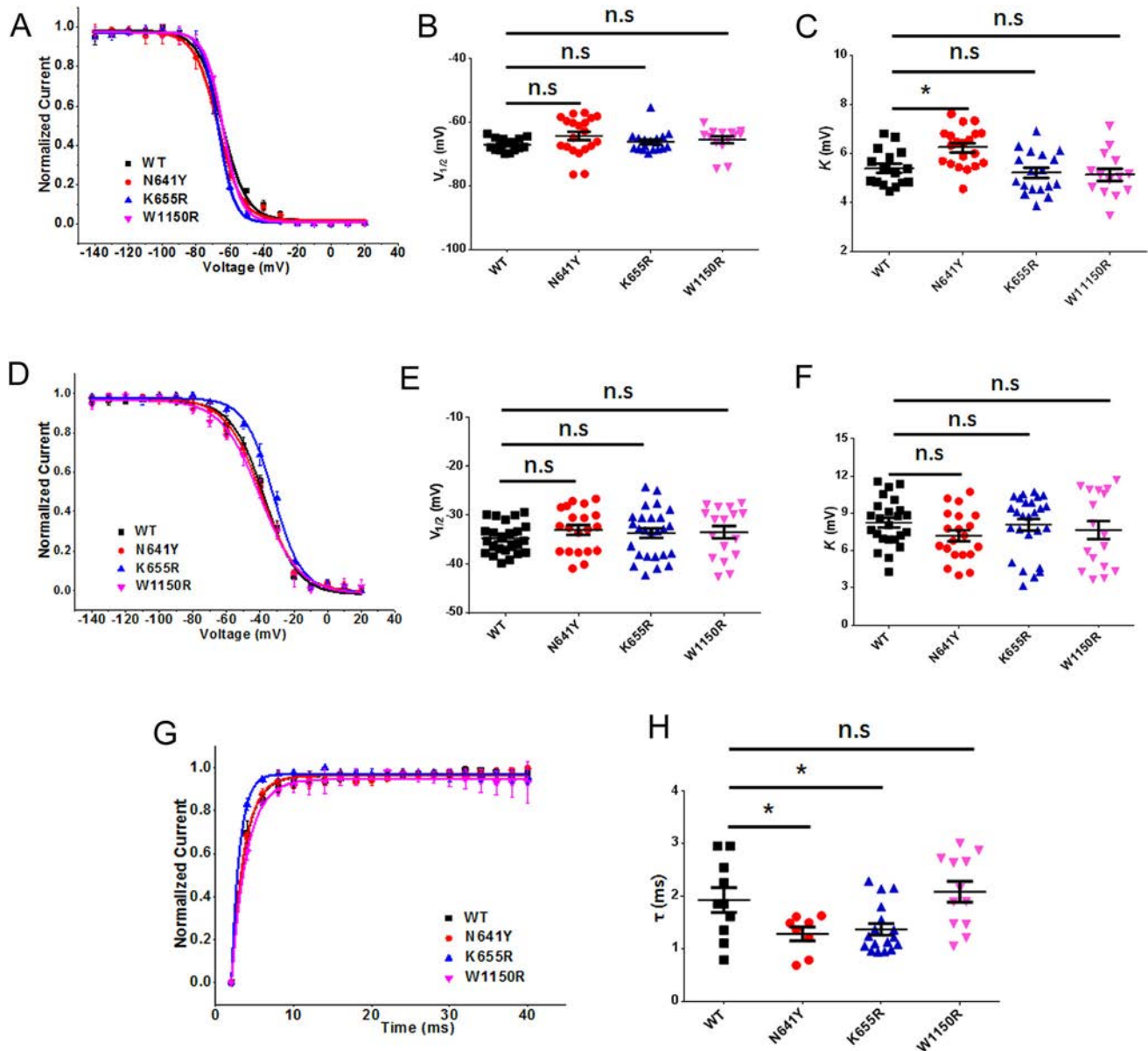


Fig. 4 Inactivation and recovery from inactivation of *SCN9A* variants and hNav1.7. **A** Voltage-dependence of steady-state inactivation of WT and variants. Curves are Boltzmann fits of the data. **B** Scatter plots of voltage at half-maximal steady-state inactivation ($V_{1/2}$) for WT and variants. **C** Scatter plots of the slope factor of steady-state inactivation (K). **D** Voltage-dependence of fast inactivation of WT and variants. Curves are Boltzmann fits. **E** Scatter plots of $V_{1/2}$ for

WT and variants. **F** Scatter plots of K . **G** Voltage dependence of recovery from inactivation of WT and variants. Curves are single exponential fits of the data. **H** Scatter plots of the time constant of recovery from inactivation of WT and variants. Data are the mean \pm SEM. * $P < 0.05$, ** $P < 0.01$. Black, WT; red, N641Y; blue, K655R; magenta, W1150R.

WT channel (1.8 ± 0.2 ms, $n = 10$). The values for the other variants were significantly lower (N641Y: 1.3 ± 0.1 ms, $n = 8$, $P < 0.05$; K655R: 1.4 ± 0.1 ms, $n = 17$, $P < 0.05$) (Fig. 4G, H and Table 1).

Influence of Temperature on the Activation of hNav1.7 and the W1150R Variant

We determined the effects of temperature on the activation of hNav1.7 and the W1150R variant. The $V_{1/2}$ for the WT channel did not differ from the room temperature group [WT (25 °C): $V_{1/2} = -19.36 \pm 1.567$ mV, $n = 15$; WT (38 °C): $V_{1/2} = -21.42 \pm 1.072$ mV, $n = 19$; Fig. 5A, B]. The W1150R variant had a large hyperpolarizing shift of the G - V curve for the voltage-dependence of steady-state activation when the temperature was raised ($V_{1/2}$ by -4.7 mV; $n = 7$, $P < 0.05$; Fig. 5C, D).

Effects of OXC on the Activation of hNav1.7 Variants

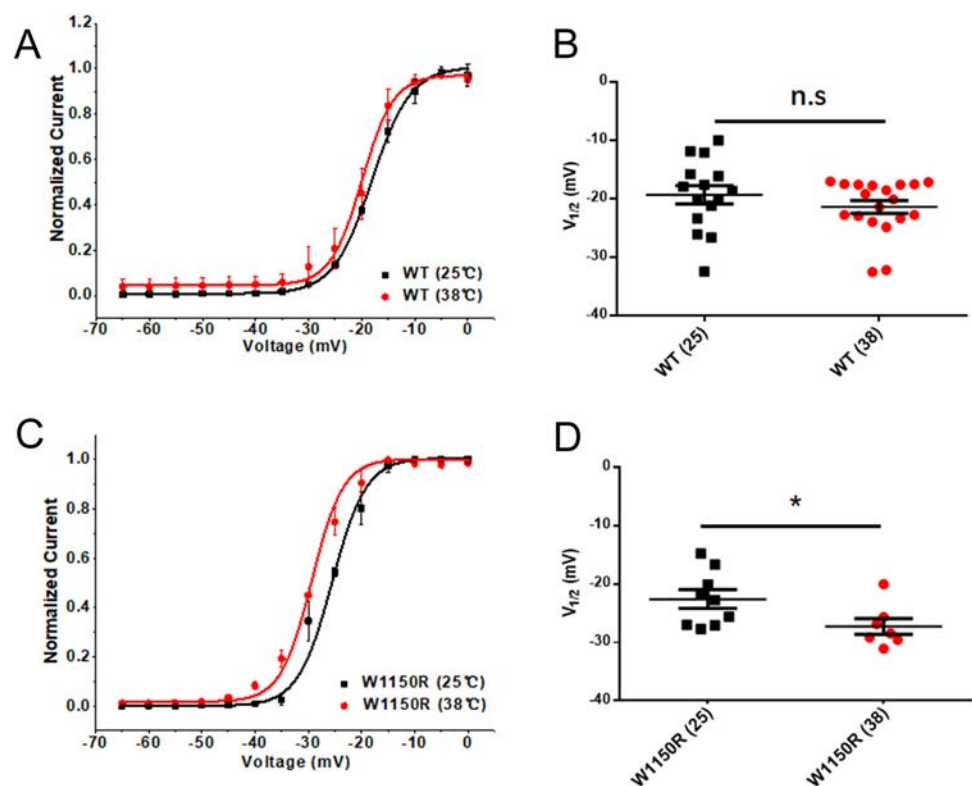
Representative currents from steady-state activation and those after treatment with OXC are shown in Fig. 6A. At 120 $\mu\text{mol/L}$, tonic block by OXC was significantly greater for the K655R ($66.55\% \pm 3.4\%$; $n = 7$) than for the WT currents ($55.23\% \pm 3.4\%$, $n = 12$, $P < 0.05$) (Fig. 6B). That of the N641Y variant ($56.26\% \pm 3.5\%$, $n = 10$) was similar to the WT channel. However, the tonic block by

OXC was significantly weaker for the W1150R ($41.38\% \pm 3.2\%$; $n = 10$, $P < 0.01$) than for the WT currents. With the use of OXC (120 $\mu\text{mol/L}$), a tendency of negative shift for the G - V curve of steady-state activation occurred in the WT and variants. The difference between the half-maximal voltage values before and after OXC was significant in the N641Y variant compared to the others ($V_{1/2}$ by -7.6 mV, $P < 0.001$) (Fig. 6C–F). The slope (K) was constant for all variants (Table 2). There was an apparent shortening in the time from the open to the inactivation state in the N641Y variant at depolarizing voltages ranging $+20$ mV and $+40$ mV (Fig. 7B), but this occurred in the K655R variant only at $+20$ mV (Fig. 7C), while the open time for the W1150R variant was unchanged (Fig. 7D).

Effects of OXC on the Inactivation of hNav1.7 Variants

As for the steady-state inactivation, the $V_{1/2}$ of the N641Y, K665R, and W1150R variants was negatively shifted by OXC (by -6.4 mV, $n = 14$, $P < 0.01$; by -3.4 mV, $n = 11$, $P < 0.001$; by -8.6 mV, $n = 10$, $P < 0.001$; respectively; Fig. 8A–D and Table 2). Treatment with OXC (120 $\mu\text{mol/L}$) also induced a hyperpolarizing shift in the voltage-dependence of the fast inactivation in the variants (N641Y $V_{1/2}$ by -9.3 mV, $n = 9$, $P < 0.001$; K655R $V_{1/2}$ by -4.5 mV, $n = 13$, $P < 0.01$; W1150R $V_{1/2}$

Fig. 5 Influence of temperature on the steady-state activation of hNav1.7 and the W1150R variant. **A, C** Voltage-dependence of steady-state activation at 25 °C and 38 °C for hNav1.7 (A) and the W1150R variant (C). Curves are Boltzmann fits. **B** Scatter plots of voltage at half-maximal steady-state activation ($V_{1/2}$) for the WT at 25 °C and 38 °C (25 °C: -19.36 ± 1.567 , $n = 15$; 38 °C: -21.42 ± 1.072 , $n = 19$). **D** Scatter plots of $V_{1/2}$ for W1150R at 25 °C and 38 °C (25 °C: -22.57 ± 1.568 , $n = 9$; 38 °C: -27.24 ± 1.376 , $n = 7$). Data are the mean \pm SEM. * $P < 0.05$; black, 25 °C; red, 38 °C.



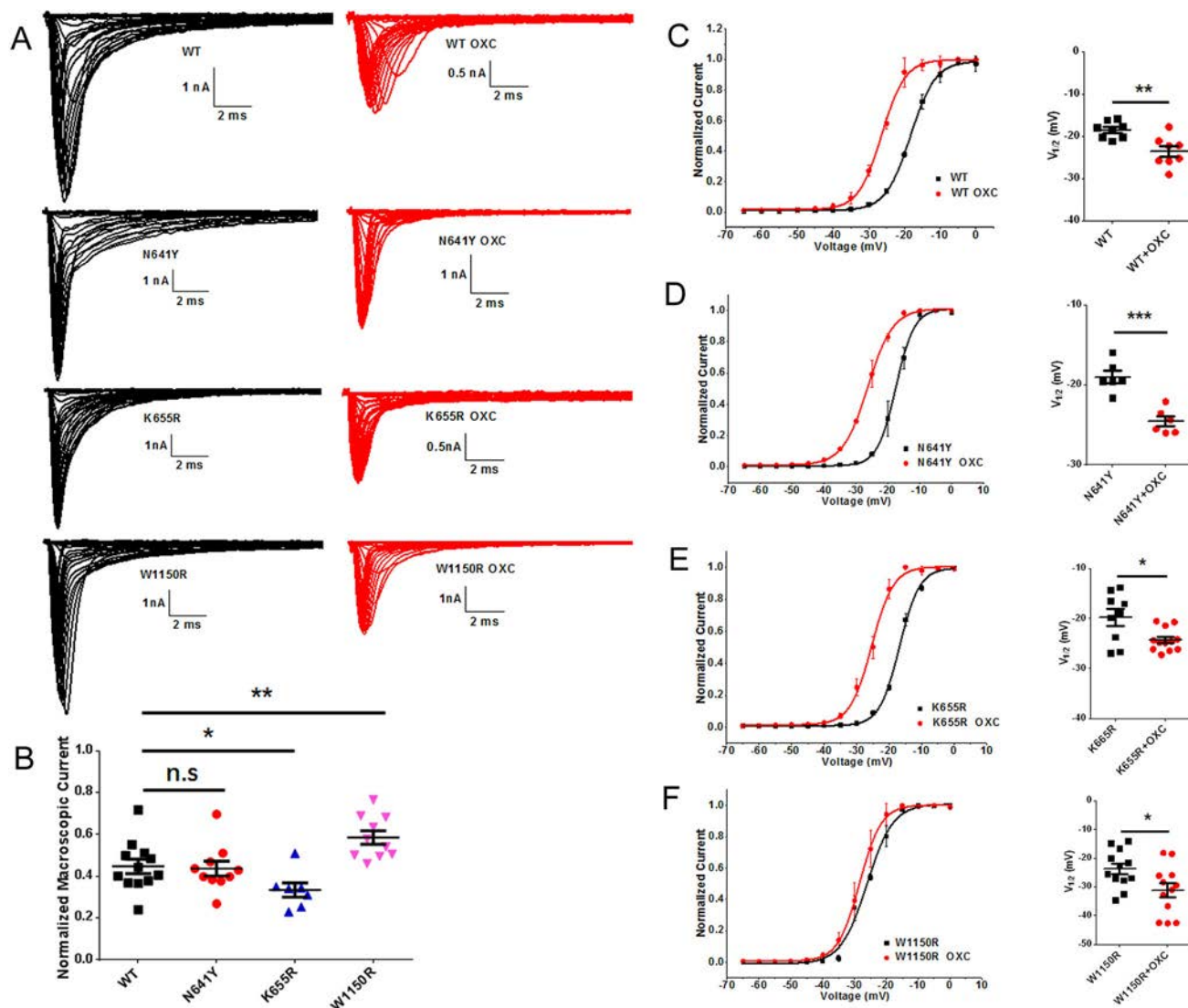


Fig. 6 Oxcarbazepine (OXC) inhibited Na^+ channel currents of hNav1.7 and *SCN9A* variants and modulates the steady-state activation. **A** Average Na^+ current traces recorded from HEK293T cells co-expressing pEZ-Lv206-hNav1.7 and pIRES-EGFP-h β 1 plasmids and treated with OXC. **B** Scatter plots showing the normalized macroscopic current amplitude remaining after blockade by OXC (120 $\mu\text{mol/L}$). **C–F** Left, shifts in the voltage-dependence of

steady-state activation for WT (**C**), N641Y (**D**), K655R (**E**), and W1150R (**F**) following treatment with OXC (120 $\mu\text{mol/L}$). Curves are Boltzmann fits. Right, scatter plots of voltage at half-maximal steady-state inactivation ($V_{1/2}$). Data are the mean \pm SEM. * $P < 0.05$, ** $P < 0.01$, *** $P < 0.001$. Black, no drug treatment; red, treated with OXC.

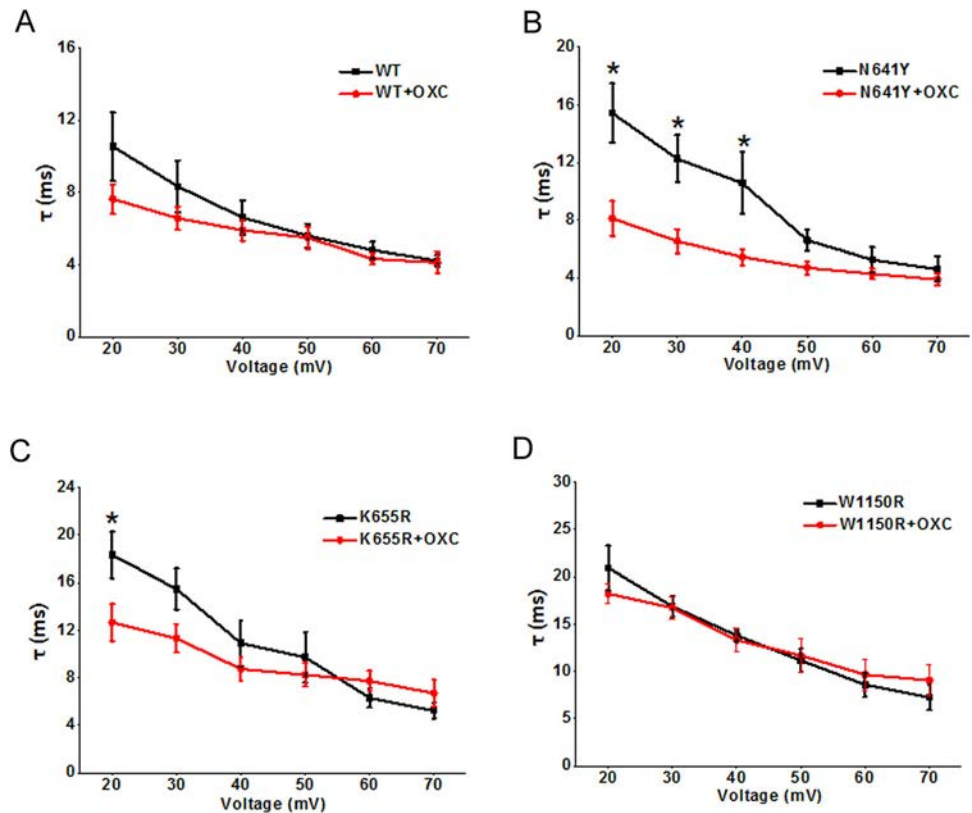
by -12.8 mV, $n = 9$, $P < 0.001$; Fig. F, G, H, respectively). After treatment with OXC, the voltage sensitivity (slope factor, K) was unchanged for both steady-state inactivation and fast inactivation (Table 2).

Effects of OXC on the Recovery of hNav1.7 Variants

The time constant of recovery underlying each of the hNav1.7 variants was increased in the presence of 120 $\mu\text{mol/L}$ OXC, (WT by 0.8 ms, $n = 17$, $P < 0.01$; N641Y by 1.5 ms, $n = 8$, $P < 0.001$; K655R by 0.4 ms, $n = 16$, $P < 0.01$; W1150R by 0.8 ms, $n = 11$, $P < 0.05$;

Fig. 9A–D and Table 2). The percentage recovery in the WT and variants decreased in the presence of 120 $\mu\text{mol/L}$ OXC from 0.90 ± 0.006 for Control ($n = 8$) to 0.73 ± 0.007 for WT ($n = 7$, $P < 0.05$), 0.69 ± 0.04 for N641Y ($n = 7$, $P < 0.0001$), 0.77 ± 0.02 for K655R ($n = 12$, $P < 0.01$), and 0.63 ± 0.06 for W1150R ($n = 8$, $P < 0.01$; Fig. 9E).

Fig. 7 Oxcarbazepine (OXC) modulates the fast time constants of hNav1.7 and *SCN9A* variants. **A–D** Average fast time constants of WT hNav1.7 channels (**A**), average fast time constants of p.(N641Y) mutant hNav1.7 channels (**B**), average fast time constant of p.(K655R) mutant hNav1.7 channels (**C**), and average fast time constant of p.(W1150R) mutant hNav1.7 channels (**D**) with 120 $\mu\text{mol/L}$ OXC *versus* membrane potential. Data are the mean \pm SEM. $*P < 0.05$.



Discussion

To date, among the myriad epilepsy-associated Na^+ channel mutations described, Nav1.7 mutants have been detected in patients suffering from generalized epilepsy, temporal lobe epilepsy, febrile seizures plus, and febrile seizures [15, 16, 18, 25]. In this study, the novel *SCN9A* mutant W1150R was identified in a patient with febrile seizures. Electrophysiological characterization of W1150R suggested that the mutant is a gain-of-function variant that notably alters the kinetic properties of hNav1.7. The presence of W1150R not only leads to a significant increase in current density, but also shortens the channel activation time and markedly shifts the G - V curve to negative potentials. Close attention was paid to the voltage-dependent inactivation parameters of W1150R, which were constant. This implied that the window currents of the W1150R variant were increased. Increments of the window currents have been shown to reduce the action potential threshold and cause hyperexcitation [26, 27]. In addition, the W1150R variant could enhance Na^+ currents by increasing persistent currents as well as significantly prolonging the open time of hNav1.7. Several studies have supported the notion that persistent Na^+ currents also drive intrinsic neuronal excitability [28, 29]. Several epilepsy-associated Nav1.1 mutations have been found to enhance persistent currents [30–32]. Transgenic mice expressing

mutant Nav1.2 channels that generate increased persistent currents display a severe epileptic phenotype [33]. Our results allow us to speculate that the generalized epilepsy induced by gain-of-function mutations in VGSC genes could be related to the facilitation of channel activation of as well as the enhancement of peak and persistent Na^+ currents.

The other hNav1.7 variants found in febrile seizure patients, N641Y and K655R, are also regarded as gain-of-function variants [16, 17]. The phenotype of these two variants in steady-state activation differs from that of W1150R. In the N641Y and K655R variants, the G - V curve of activation was shifted towards depolarization, and the time constant of recovery was significantly reduced. However, none of the three variants affected the inactivation. It has been shown that many mutant Na^+ channels associated with epilepsy exhibit delayed inactivation as well as increased persistent Na^+ currents [30–32]. As is generally known, a larger persistent current accentuates subthreshold depolarizations and facilitates the generation of the action potential, so we compared this property between the WT and variants, and ultimately found that the variants displayed larger persistent currents than WT channels. The above data suggested that hyperexcitability might be associated with an increased persistent current and rapid recovery of the inactivated channel to the resting

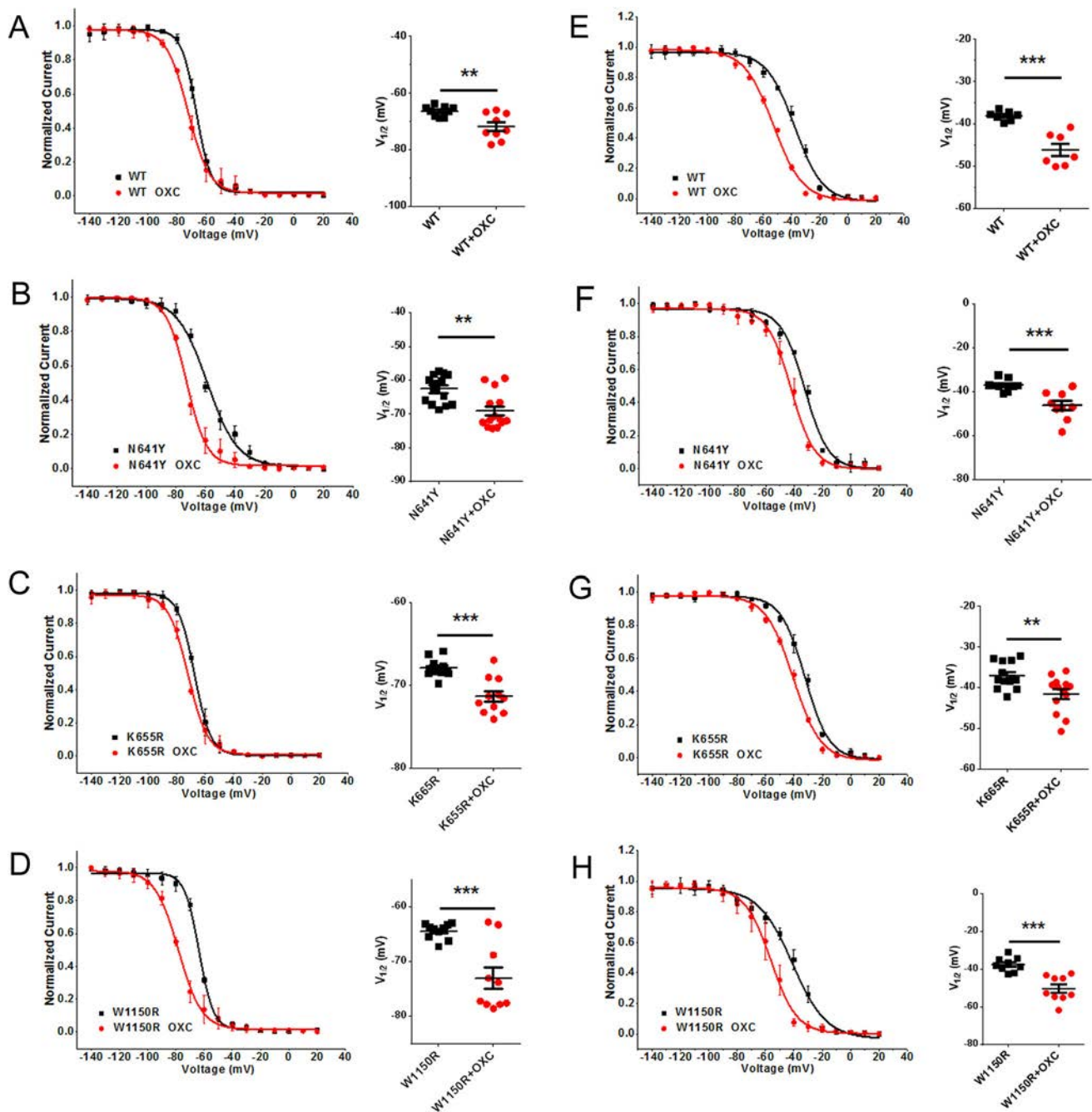


Fig. 8 Oxcarbazepine (OXC) modulated the inactivation of hNav1.7 and *SCN9A* variants. **A–D** Left, shift in the voltage-dependence of steady-state inactivation in the WT (**A**), N641Y (**B**), K655R (**C**), and W1150R (**D**) after treatment with 120 μmol/L OXC. Curves are Boltzmann fits. Right, scatter plots of voltage at half-maximal steady-

state inactivation ($V_{1/2}$). **E–H** Left, shift in the voltage dependence of fast inactivation for WT (**E**), N641Y (**F**), K655R (**G**), and W1150R (**H**) after treatment with 120 μmol/L OXC. Curves are Boltzmann fits. Right, scatter plots of $V_{1/2}$. Data are the mean ± SEM. ** $P < 0.01$, *** $P < 0.001$. Black, no drug treatment; red, with OXC.

state, thereby increasing the probability that the open state of Na^+ channels was configured for longer periods.

The pharmacological data in this study revealed that treatment of both the N641Y and K655R variants with 120 μmol/L OXC resulted in a marked reduction in Na^+ currents and a shortening of the opening time. This may correspond with the capacity of OXC to inhibit abnormal

neuronal firing and reduce excitatory synaptic transmission [21]. Our results implicate OXC as an effective treatment for epileptic patients with N641Y and K655R variants. However, we did find that the Na^+ currents of the W1150R variant were not significantly inhibited by OXC. At the molecular level, this could explain, in part, why patients

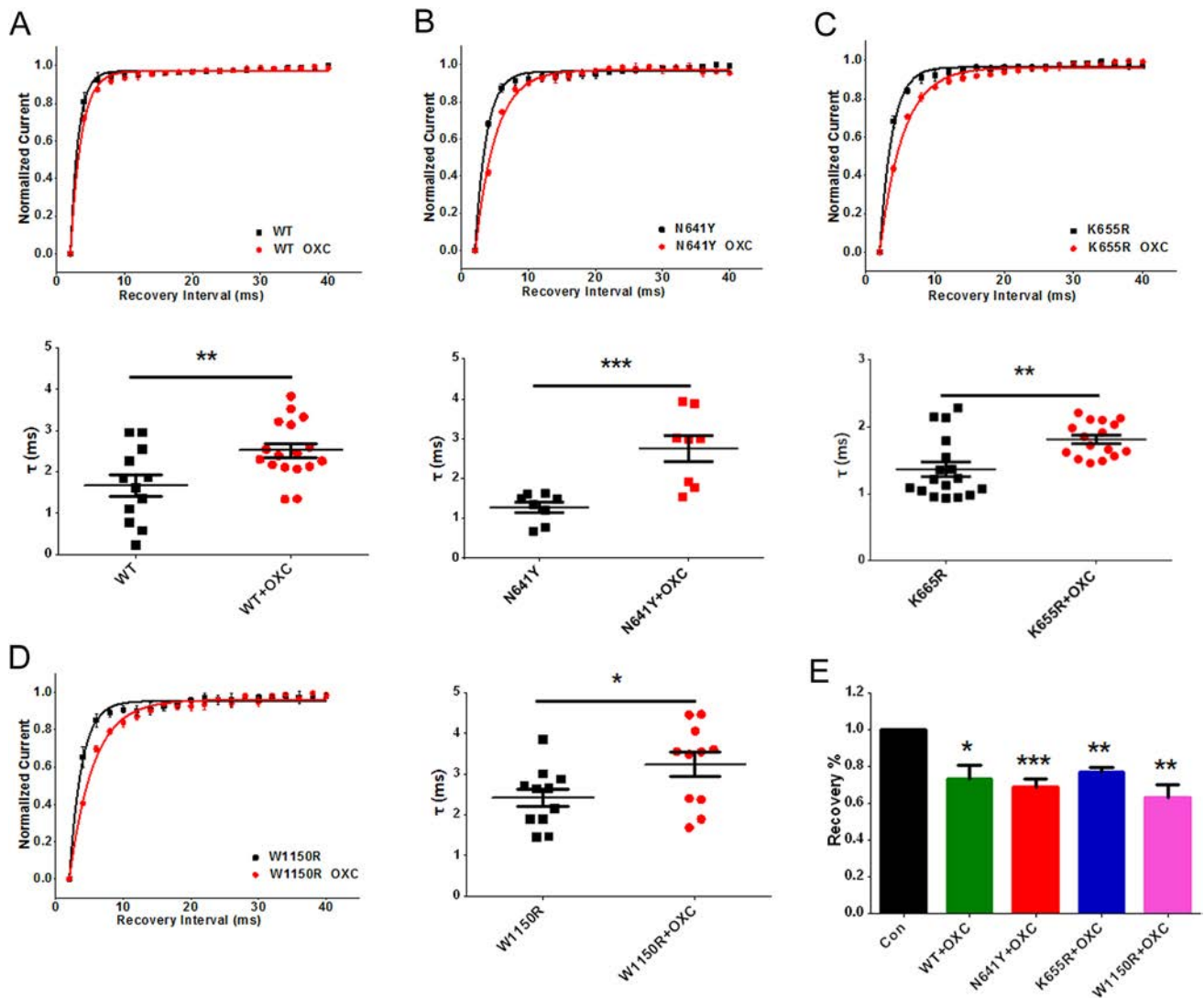


Fig. 9 Oxcarbazepine (OXC) modulated recovery from inactivation in hNav1.7 and *SCN9A* variants. **A–D** Shifts in the voltage-dependence of recovery from inactivation in the WT (A), N641Y (B), K655R (C), and W1150R (D) after treatment with 120 $\mu\text{mol/L}$

OXC (curves are single exponential fits) and scatter plots of the time constant of recovery from inactivation. **E** Percentage recovery of ion channels treated with 120 $\mu\text{mol/L}$ OXC. Data are the mean \pm SEM. * $P < 0.05$, ** $P < 0.01$, *** $P < 0.001$.

with some Nav channel mutations are not sensitive to OXC.

In summary, we have identified a novel *SCN9A* mutant (W1150R) in a patient with febrile seizures. Examination of the gain-of-function hNav1.7 mutants, N641Y, K655R, and W1150R led us to the conclusion that two of the variants are sensitive, while the W1150R variant is insensitive to OXC.

Acknowledgements We are grateful to Prof. Ren Lai and Shilong Yang (Kunming Institute of Zoology, Chinese Academy of Sciences) for providing the pEZ-Lv206-hNav1.7 plasmid. This work was supported by the National Natural Science Foundation of China (81603410, 31571032, and 31771191), the Shanghai Municipal Commission of Health and Family Planning Foundation (20184Y0086), Innovation Program of Shanghai Municipal Education

Commission (15ZZ063), the Research Project of Putuo Hospital, Shanghai University of Traditional Chinese Medicine (2016102A and 2016208A), and a Project for Capacity Promotion of Putuo District Clinical Special Disease.

Conflict of interest The authors declare that they have no conflict of interest.

References

- Cooper DC, Chung S, Spruston N. Output-mode transitions are controlled by prolonged inactivation of sodium channels in pyramidal neurons of subiculum. *PLoS Biol* 2005, 3: e175.
- Vreugdenhil M, Hoogland G, van Veelen CW, Wadman WJ. Persistent sodium current in subicular neurons isolated from patients with temporal lobe epilepsy. *Eur J Neurosci* 2004, 19: 2769–2778.

3. Banerjee J, Fischer CC, Wedegaertner PB. The amino acid motif L/IIxxFE defines a novel actin-binding sequence in PDZ-RhoGEF. *Biochemistry* 2009, 48: 8032–8043.
4. Blumenfeld H, Lampert A, Klein JP, Mission J, Chen MC, Rivera M, *et al.* Role of hippocampal sodium channel Nav1.6 in kindling epileptogenesis. *Epilepsia* 2009, 50: 44–55.
5. Hargus NJ, Merrick EC, Nigam A, Kalmar CL, Baheti AR, Bertram EH, 3rd, *et al.* Temporal lobe epilepsy induces intrinsic alterations in Na channel gating in layer II medial entorhinal cortex neurons. *Neurobiol Dis* 2011, 41: 361–376.
6. Bang S, Yoo J, Gong X, Liu D, Han Q, Luo X, *et al.* Differential inhibition of Nav1.7 and neuropathic pain by hybridoma-produced and recombinant monoclonal antibodies that target Nav1.7: differential activities of Nav1.7-targeting monoclonal antibodies. *Neurosci Bull* 2018, 34: 22–41.
7. Chang W, Berta T, Kim YH, Lee S, Lee SY, Ji RR. Expression and role of voltage-gated sodium channels in human dorsal root ganglion neurons with special focus on Nav1.7, species differences, and regulation by paclitaxel. *Neurosci Bull* 2018, 34: 4–12.
8. Toledo-Aral JJ, Moss BL, He ZJ, Koszowski AG, Whisenand T, Levinson SR, *et al.* Identification of PN1, a predominant voltage-dependent sodium channel expressed principally in peripheral neurons. *Proc Natl Acad Sci USA* 1997, 94: 1527–1532.
9. Rush AM, Dib-Hajj SD, Liu S, Cummins TR, Black JA, Waxman SG. A single sodium channel mutation produces hyper- or hypoexcitability in different types of neurons. *Proc Natl Acad Sci USA* 2006, 103: 8245–8250.
10. Ahn HS, Black JA, Zhao P, Tyrrell L, Waxman SG, Dib-Hajj SD. Nav1.7 is the predominant sodium channel in rodent olfactory sensory neurons. *Mol Pain* 2011, 7: 32.
11. Mechaly I, Scamps F, Chabbert C, Sans A, Valmier J. Molecular diversity of voltage-gated sodium channel alpha subunits expressed in neuronal and non-neuronal excitable cells. *Neuroscience* 2005, 130: 389–396.
12. Dib-Hajj SD, Cummins TR, Black JA, Waxman SG. Sodium channels in normal and pathological pain. *Annu Rev Neurosci* 2010, 33: 325–347.
13. Cox JJ, Reimann F, Nicholas AK, Thornton G, Roberts E, Springell K, *et al.* An SCN9A channelopathy causes congenital inability to experience pain. *Nature* 2006, 444: 894–898.
14. Fertleman CR, Baker MD, Parker KA, Moffatt S, Elmslie FV, Abrahamsen B, *et al.* SCN9A mutations in paroxysmal extreme pain disorder: allelic variants underlie distinct channel defects and phenotypes. *Neuron* 2006, 52: 767–774.
15. Peiffer A, Thompson J, Charlier C, Otterud B, Varvil T, Pappas C, *et al.* A locus for febrile seizures (FEB3) maps to chromosome 2q23–24. *Ann Neurol* 1999, 46: 671–678.
16. Singh NA, Pappas C, Dahle EJ, Claes LR, Pruess TH, De Jonghe P, *et al.* A role of SCN9A in human epilepsies, as a cause of febrile seizures and as a potential modifier of Dravet syndrome. *PLoS Genet* 2009, 5: e1000649.
17. Doty CN. SCN9A: another sodium channel excited to play a role in human epilepsies. *Clin Genet* 2010, 77: 326–328.
18. Cen Z, Lou Y, Guo Y, Wang J, Feng J. Q10R mutation in SCN9A gene is associated with generalized epilepsy with febrile seizures plus. *Seizure* 2017, 50: 186–188.
19. Yang C, Hua Y, Zhang W, Xu J, Xu L, Gao F, *et al.* Variable epilepsy phenotypes associated with heterozygous mutation in the SCN9A gene: report of two cases. *Neurol Sci* 2018, 39: 1113–1115.
20. Dong X, Leppik IE, White J, Rarick J. Hyponatremia from oxcarbazepine and carbamazepine. *Neurology* 2005, 65: 1976–1978.
21. Kwan P, Sills GJ, Brodie MJ. The mechanisms of action of commonly used antiepileptic drugs. *Pharmacol Ther* 2001, 90: 21–34.
22. Yan Z, Zhou Q, Wang L, Wu J, Zhao Y, Huang G, *et al.* Structure of the Nav1.4-beta1 complex from electric eel. *Cell* 2017, 170: 470–482.e411.
23. Lee CY, Lai HY, Chiu A, Chan SH, Hsiao LP, Lee ST. The effects of antiepileptic drugs on the growth of glioblastoma cell lines. *J Neurooncol* 2016, 127: 445–453.
24. Booker SA, Pires N, Cobb S, Soares-da-Silva P, Vida I. Carbamazepine and oxcarbazepine, but not eslicarbazepine, enhance excitatory synaptic transmission onto hippocampal CA1 pyramidal cells through an antagonist action at adenosine A1 receptors. *Neuropharmacology* 2015, 93: 103–115.
25. Scheffer IE, Wallace RH, Mulley JC, Berkovic SF. Locus for febrile seizures. *Ann Neurol* 2000, 47: 840–841.
26. Ellerkmann RK, Remy S, Chen J, Sochivko D, Elger CE, Urban BW, *et al.* Molecular and functional changes in voltage-dependent Na(+) channels following pilocarpine-induced status epilepticus in rat dentate granule cells. *Neuroscience* 2003, 119: 323–333.
27. Ketelaars SO, Gorter JA, van Vliet EA, Lopes da Silva FH, Wadman WJ. Sodium currents in isolated rat CA1 pyramidal and dentate granule neurones in the post-status epilepticus model of epilepsy. *Neuroscience* 2001, 105: 109–120.
28. Alzheimer C, Schwindt PC, Crill WE. Modal gating of Na⁺ channels as a mechanism of persistent Na⁺ current in pyramidal neurons from rat and cat sensorimotor cortex. *J Neurosci* 1993, 13: 660–673.
29. Baker MD, Chandra SY, Ding Y, Waxman SG, Wood JN. GTP-induced tetrodotoxin-resistant Na⁺ current regulates excitability in mouse and rat small diameter sensory neurones. *J Physiol* 2003, 548: 373–382.
30. Holland KD, Kearney JA, Glauser TA, Buck G, Keddache M, Blankston JR, *et al.* Mutation of sodium channel SCN3A in a patient with cryptogenic pediatric partial epilepsy. *Neurosci Lett* 2008, 433: 65–70.
31. Kahlig KM, Rhodes TH, Pusch M, Freilinger T, Pereira-Monteiro JM, Ferrari MD, *et al.* Divergent sodium channel defects in familial hemiplegic migraine. *Proc Natl Acad Sci USA* 2008, 105: 9799–9804.
32. Spanpanato J, Kearney JA, de Haan G, McEwen DP, Escayg A, Aradi I, *et al.* A novel epilepsy mutation in the sodium channel SCN1A identifies a cytoplasmic domain for beta subunit interaction. *J Neurosci* 2004, 24: 10022–10034.
33. Kearney JA, Plummer NW, Smith MR, Kapur J, Cummins TR, Waxman SG, *et al.* A gain-of-function mutation in the sodium channel gene Scn2a results in seizures and behavioral abnormalities. *Neuroscience* 2001, 102: 307–317.



Regional Metabolic Patterns of Abnormal Postoperative Behavioral Performance in Aged Mice Assessed by $^1\text{H-NMR}$ Dynamic Mapping Method

Taotao Liu^{1,2} · Zhengqian Li¹ · Jindan He¹ · Ning Yang¹ · Dengyang Han¹ · Yue Li¹ · Xuebi Tian³ · Huili Liu² · Anne Manyande⁴ · Hongbing Xiang³ · Fuqiang Xu^{2,5} · Jie Wang^{2,5,6} · Xiangyang Guo¹

Received: 22 December 2018 / Accepted: 14 May 2019 / Published online: 2 August 2019
© Shanghai Institutes for Biological Sciences, CAS 2019

Abstract Abnormal postoperative neurobehavioral performance (APNP) is a common phenomenon in the early postoperative period. The disturbed homeostatic status of metabolites in the brain after anesthesia and surgery might make a significant contribution to APNP. The dynamic changes of metabolites in different brain regions after anesthesia and surgery, as well as their potential association with APNP are still not well understood. Here, we used a battery of behavioral tests to assess the effects of laparotomy under isoflurane anesthesia in aged mice, and investigated the metabolites in 12 different sub-regions of

the brain at different time points using proton nuclear magnetic resonance ($^1\text{H-NMR}$) spectroscopy. The abnormal neurobehavioral performance occurred at 6 h and/or 9 h, and recovered at 24 h after anesthesia/surgery. Compared with the control group, the altered metabolite of the model group at 6 h was aspartate (Asp), and the difference was mainly displayed in the cortex; while significant changes at 9 h occurred predominantly in the cortex and hippocampus, and the corresponding metabolites were Asp and glutamate (Glu). All changes returned to baseline at 24 h. The altered metabolic changes could have occurred as a result of the acute APNP, and the metabolites Asp and Glu in the cortex and hippocampus could provide preliminary evidence for understanding the APNP process.

Electronic supplementary material The online version of this article (<https://doi.org/10.1007/s12264-019-00414-4>) contains supplementary material, which is available to authorized users.

✉ Jie Wang
jie.wang@wipm.ac.cn

✉ Xiangyang Guo
guoxiangyangmzk@163.com

- ¹ Department of Anesthesiology, Peking University Third Hospital, Beijing 100191, China
- ² Key Laboratory of Magnetic Resonance in Biological Systems, State Key Laboratory of Magnetic Resonance and Atomic and Molecular Physics, Wuhan Institute of Physics and Mathematics, Chinese Academy of Sciences, Wuhan 430071, China
- ³ Department of Anesthesiology and Pain Medicine, Tongji Hospital, Tongji Medical College, Huazhong University of Science and Technology, Wuhan 430030, China
- ⁴ School of Human and Social Sciences, University of West London, Middlesex TW89GA, UK
- ⁵ University of Chinese Academy of Sciences, Beijing 100049, China
- ⁶ The Second Hospital of Shijiazhuang, Shijiazhuang 050051, China

Keywords Abnormal postoperative neurobehavioral performance · $^1\text{H-NMR}$ · Metabolite · Aspartate · Glutamate

Introduction

Emerging evidence indicates that surgery/anesthesia can generate many complications such as neurocognitive disorders during the perioperative period, especially in the elderly [1, 2]. Homeostasis of cerebral metabolism is essential for neurobehavioral functioning. Disturbance of metabolites in the brain after anesthesia and surgery might contribute significantly to postoperative neurobehavioral disorders. Unfortunately, the dynamic changes of metabolites in the aging brain during the early postoperative period, as well as the potential role of these changes in the pathophysiology of abnormal postoperative neurobehavioral performance (APNP) in the frail brain remain unknown. Previous reports have suggested that several metabolites serve as biomarkers of neurobehavioral

disorders, such as glutamate (Glu), N-acetyl-aspartate (NAA), creatine, gamma-aminobutyric acid (GABA), and aspartate (Asp) in humans and rodents [3–5]. However, the association between different presentations of APNP and the corresponding metabolites is still not well documented in the aging brain.

As an ionizing radiation-free technique, *in vivo* magnetic resonance spectroscopy (^1H -MRS) can provide information on tissue chemicals, including NAA, an indicator of viable neuronal tissue density [6]; creatine, an essential molecule in energy homeostasis of the central nervous system (CNS) [7]; choline, a marker for the rate of membrane turnover [8]; Glu, the main primary excitatory neurotransmitter in the CNS [9, 10]; and GABA, the most prevalent inhibitory neurotransmitter in the CNS [11, 12]. However, there are still several limitations of its application, such as low spectral resolution, limited metabolites, and quantification of the metabolites. *In-vitro* ^1H -NMR ideally resolves these problems by optimizing the homogeneity of the magnetic field and the extracted sample without the interference of macromolecules and lipids. With much higher spectral resolution, more metabolites can be identified using this method [13]. Combined with different metabolism quenching methods, it has been extensively applied in neuroscience studies [5, 14, 15], and the metabolic mapping techniques have been extensively used to explore the variation of metabolites in various brain disorders [16, 17]. Thus, it presents a promising method for analyzing the dynamic metabolic changes in different brain regions following anesthesia and surgery, shedding light on the basic profile of APNP.

The purpose of this study was to assess the effects of anesthesia/surgery on neurobehavioral performance in aged mice during the early postoperative period and to explore the metabolic mechanisms *via* an ^1H -NMR-based method to provide a dynamic map of metabolic information of aging brains following anesthesia/surgery and advance our understanding of the APNP in the early postoperative period.

Materials and Methods

Animals

The experimental protocol was approved by the Animal Care and Use Committee of Peking University (Beijing, China, Certification number LA201413). Female C57Bl/6 mice (16 months old, 25–30 g) were purchased from the Experimental Animal Center of Hubei Provincial Academy of Prevention. All animals were housed in plastic cages (4/ cage) and maintained on a 12-h light/dark cycle (lights on 07:00–19:00), with food and water available *ad libitum*. In

order to accustom the animals to human interaction and minimize stress, the mice were handled daily for a week before the experimental day, by grasping the animal, mildly touching its skin/hair, and scratching for ~ 1 min.

Anesthesia and Surgery

Mice were randomly assigned into either the surgery plus anesthesia group ($n = 40$, 9–1 each at 0, 6, 9, and 24 h) or the control group ($n = 13$). The experimental procedure was based on previous reports with minor modifications [18, 19]. Specifically, each mouse was initially anesthetized with 1.4%–2.0% isoflurane (in 100% oxygen) in a transparent chamber (RWD Life Science, Shenzhen, China). Fifteen minutes after induction, the mouse was removed from the induction chamber, and a face mask was used to maintain the anesthesia with a 16-gauge sensor monitoring the isoflurane concentration. Then a longitudinal midline incision was made from the xiphoid to the pubic symphysis, cutting through the skin, abdominal muscles, and peritoneum. Then, the incision was sutured layer-by-layer with 5–0 Vicryl. At the end of the procedure, EMLA cream (2.5% lidocaine and 2.5% procaine) was applied to the wound area every 8 h to minimize the pain and stress from the surgery. After the surgery, the mouse was returned to the anesthesia chamber for up to 2 h to receive the rest of the 1.4%–2.0% isoflurane in 100% oxygen. The body temperature was maintained with a heating pad during the anesthesia/surgery. The mice in the control group were placed in their home cage with 100% oxygen for 2 h. To minimize the impact of circadian rhythms, anesthesia/surgery began at 08:00 am each day.

Behavioral Tests

The buried food test, open field test, and Y maze were used to measure the abnormal neurobehavioral performance in different periods after surgery. All animals received these three tests before surgery, and the results were set as the baseline for further behavioral analysis. Then all mice in the control and experimental groups performed all three tests again at 6, 9, and 24 h after anesthesia/surgery. The protocols of these tests were based on previous studies with slight modifications [18, 20]. The animals in the experimental groups at 6, 9, and 24 h were euthanized using the microwave irradiation approach under isoflurane anesthesia just after the behavioral tests.

To help habituation, all mice were moved to the behavioral testing room 1 h before the tests. Four mice from each group were tested on each day, and all tests were finished within 1 h, to minimize the impact of circadian rhythms. To avoid the influence of odor, all the equipment was cleaned with 70% ethanol after every trial. All the

behavioral data were analyzed with an animal tracking system (Smart 3.0, RWD Life Science Co., Ltd, China). The details of the experimental steps are described in the supplementary Materials and Methods.

Brain Sample Preparation for NMR Study

To minimize the impact of post-mortem changes in brain metabolites, each mouse was euthanized using the microwave method as fully described in our previous work [5]. After euthanasia, the brain was removed and dissected into 12 regions: olfactory bulb (OB), frontal cortex (FC), parietal cortex (PC), occipital cortex (OC), temporal cortex (TC), striatum (STR), hippocampus (HP), thalamus (THA), hypothalamus (HYP), midbrain (MID), medulla-pons (MED-PONS), and cerebellum (CE). Separation of the regions was made according to the Allen Brain Atlas and previous publications [21, 22] (further details in supplemental material; Fig. S1). The tissues were immediately weighed and stored at $-80\text{ }^{\circ}\text{C}$ for further processing.

The protocol for tissue extraction was the same as that in our previous study [5]. Briefly, HCl/methanol (0.1 mol/L, 100 μL) was added to the frozen tissue and homogenized for 1.5 min at 20 Hz (Tissuelyser II, Qiagen, Germany). Ice-cold 60% ethanol (800 μL) was further added and the mixture homogenized again, before centrifugation at 14,000 g for 10 min. The supernatant was then collected. The extraction steps were repeated twice with 800 μL 60% ethanol to extract the metabolites remaining in the sediment. All the supernatants were collected and desiccated in a centrifugal drying apparatus (Thermo Scientific 2010, Germany) and freezing vacuum dryer (Thermo Scientific). The dried product was preserved for further NMR studies.

The dried product was successively dissolved in 60 μL D_2O (containing the inner standard, 3-(trimethylsilyl) propionic—2, 2, 3, 3- d_4 acid sodium salt (TSP, 120 mg/L; 269913-1G, Sigma-Aldrich)) and 540 μL phosphate buffer (pH 7.2). The solution was mixed in a high-speed vortex and centrifuged at 14,000 g for 15 min, and the supernatant was withdrawn and transferred to an NMR tube.

Acquisition of NMR Spectra

^1H -NMR spectra were acquired as in previous studies [5, 23]. The extracted samples were measured with a Bruker Avance III 600 MHz NMR spectrometer (298 K) equipped with an inverse cryogenic probe (Bruker BioSpin, Germany). The spectra were acquired with a standard Watergate pulse sequence [24]. The following acquisition parameters were set for every sample: p1 (90° pulse), 8.35 μs ; number of scans, 256; spectral width, 20 ppm;

dummy scans, 8; number of free-induction decay points, 32 K.

NMR Data Processing

All ^1H -NMR spectra were processed and analyzed with TopSpin (Version 2.1, Bruker BioSpin) and a home-made software NMRSpec [25]. First, the phase correction and baseline distortion were manually completed in TopSpin. Then the corrected spectra were imported into NMRSpec for spectrum alignment, peak extraction, spectral integration, and the integration of chemical-related peaks. This software has been used in several metabolomics studies [5, 26, 27].

The chemical shifts of major amino-acids were distributed in the range of 1.20–4.46 ppm, so this gap was extracted for further analysis. First of all, the areas of all peaks (area under the curve) in this gap were automatically calculated for further statistical analysis [5]. To compensate for the different concentrations, each peak area was normalized to the sum of all the peak areas in this gap of its own spectrum prior to the discriminant analysis [21, 23, 28].

Furthermore, the absolute concentrations ($\mu\text{mol/g}$ wet weight) of the identified metabolites were calculated with the related peak areas in spectra from the samples, information on the internal standards (TSP, such as concentration and proton number), and specimen weight. The calculation was as follows:

$$C_{met} = \frac{A_{met}/(R_{met} * N_H)}{A_{TSP}} * (C_{TSP} * V_{TSP}) * 9/Wt \quad (1)$$

where A_{met} and A_{TSP} are the relative areas of the peaks of the detected metabolites and TSP, and R_{met} is a constant for a specific metabolite calculated as the ratio between the partial NMR signal of the standard metabolite in selected regions (almost pure chemical signal) in a real sample and the whole proton signal in the standard spectrum; N_H is the number of protons of the metabolite within the area A_{met} ; C_{TSP} and V_{TSP} are the concentration and volume of TSP standard solution added to the NMR tube; Wt is the total weight of the wet specimen and 9 is the number of protons in the TSP.

Statistical Analysis

In the behavioral tests, the baseline for each mouse served as the reference for abnormal neurobehavioral performance. The relative values for behavior at each time point (6, 9, and 24 h postoperatively) are presented as a percentage relative to baseline. The repeated behavioral tests of limited duration could influence the performance, thus only the control group and the 24-h group, both of

which received behavioral tests 3 times (6, 9, and 24 h), were used to assess the change in neurobehavioral performance. Values for performance were compared using the Wilcoxon Mann–Whitney U test.

To discriminate the different metabolic patterns among the control and anesthesia/surgery groups, we applied orthogonal partial least-squares discriminant analysis (OPLS-DA). Twelve brain regions were involved. For clarity, the metabolic spectra and statistical analysis of the FC region are presented as a typical example to show the efficiency of the OPLS-DA method. To determine the significant differences in the corresponding metabolite levels in the whole brain, we used one-way analyses of variance (ANOVA), followed by Turkey's *post-hoc* test to analyze differences in the concentrations of metabolites in each brain region between the control and different anesthesia/surgery groups. To calculate the main effects of the time-points on the regional metabolites (12 regions), we used two-way ANOVA followed by Turkey's *post-hoc* test. The criterion for statistical significance was set at a probability value of 0.05. All data are presented as the mean \pm SEM.

Results

Anesthesia/Surgery Increased the Latency to Find Food in a Time-Associated Manner

To assess the effects of anesthesia/surgery on the natural habits of mice, we used the buried food test (Fig. 1A1–A3). Compared with the control group, the latency to find food in the anesthesia/surgery group was longer at both 6 h ($114.0\% \pm 15.0\%$ versus $69.7\% \pm 12.8\%$, $Z = -2.098$, $P = 0.036$, Fig. 1A1) and 9 h ($171.0\% \pm 29.6\%$ vs $81.2\% \pm 12.1\%$, $Z = -2.342$, $P = 0.019$, Fig. 1A2). However, we found no significant difference in the latency at 24 h after the operation when compared with controls (Fig. 1A3). Taken together, these data suggested that the abdominal surgery plus isoflurane anesthesia undermines

the natural ability of mice to find food and this process is time-associated.

Anesthesia/Surgery Decreased the Time Spent in the Center of the Open Field Box in a Time-Associated Manner

The open field test was used to evaluate whether anesthesia/surgery affected the emotional state of mice (Fig. 2). The anesthesia/surgery decreased the time spent in the center region at both 6 h ($39.0\% \pm 8.9\%$ vs $122.0\% \pm 32.6\%$, $Z = -2.075$, $P = 0.038$, Fig. 2A1) and 9 h ($21.1\% \pm 6.9\%$ vs $139.0\% \pm 49.1\%$, $Z = -2.532$, $P = 0.011$, Fig. 2A2), but not at 24 h (Fig. 2A3). This indicates that the anesthesia/surgery had an adverse effect on the emotional state of mice in a time-associated manner. Furthermore, other parameters (latency to the center and total traveling distance) did not show significant difference between the two groups at any time point (Fig. 2B1–C3), suggesting that anesthesia/surgery does not cause motor dysfunction. Taken together, the results of these behavioral tests were consistent with our hypothesis that anesthesia/surgery causes neurobehavioral disorder in a time-associated manner in aged mice.

Anesthesia/Surgery Decreased the Exploration in the Novel Arm of the Y-Maze in a Time-Associated Manner

The spontaneous Y-maze test was introduced to evaluate spatial learning and memory in the mice (Fig. 3). Compared with the control group, anesthesia/surgery shortened the time spent in the novel arm at 6 h ($81.0\% \pm 11.7\%$ vs $116.0\% \pm 10.0\%$, $Z = -2.203$, $P = 0.028$, Fig. 3A1) after the intervention, but not at 9 h (Fig. 3A2) and 24 h (Fig. 3A3). Furthermore, the entries to the novel arm in the anesthesia/surgery group were significantly fewer than those in the control group at both 6 h ($81.7\% \pm 4.1\%$ vs $105.0\% \pm 3.8\%$, $Z = -2.950$, $P = 0.003$, Fig. 3B1) and 9 h ($84.7\% \pm 7.3\%$ vs $107.0\% \pm 6.4\%$, $Z = -2.061$,

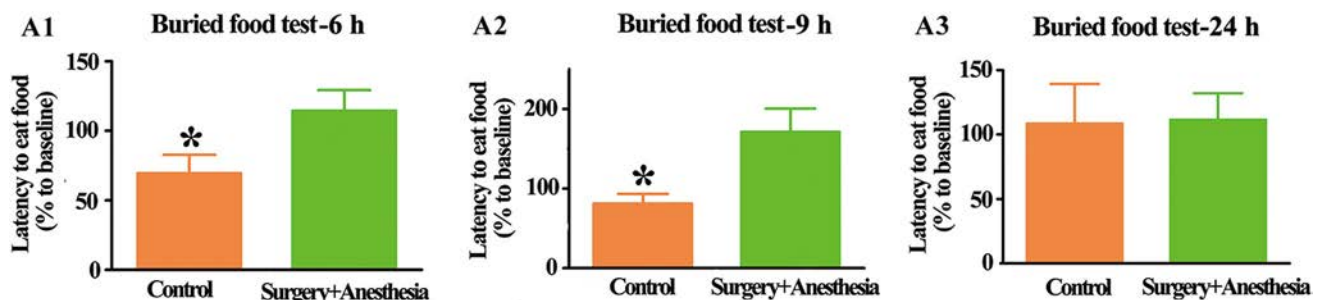


Fig. 1 Impact at 6, 9, and 24 h of anesthesia/surgery on mouse behaviors assessed by the buried food test. Data are presented as the mean \pm SEM. * $P < 0.05$, Mann–Whitney U test.

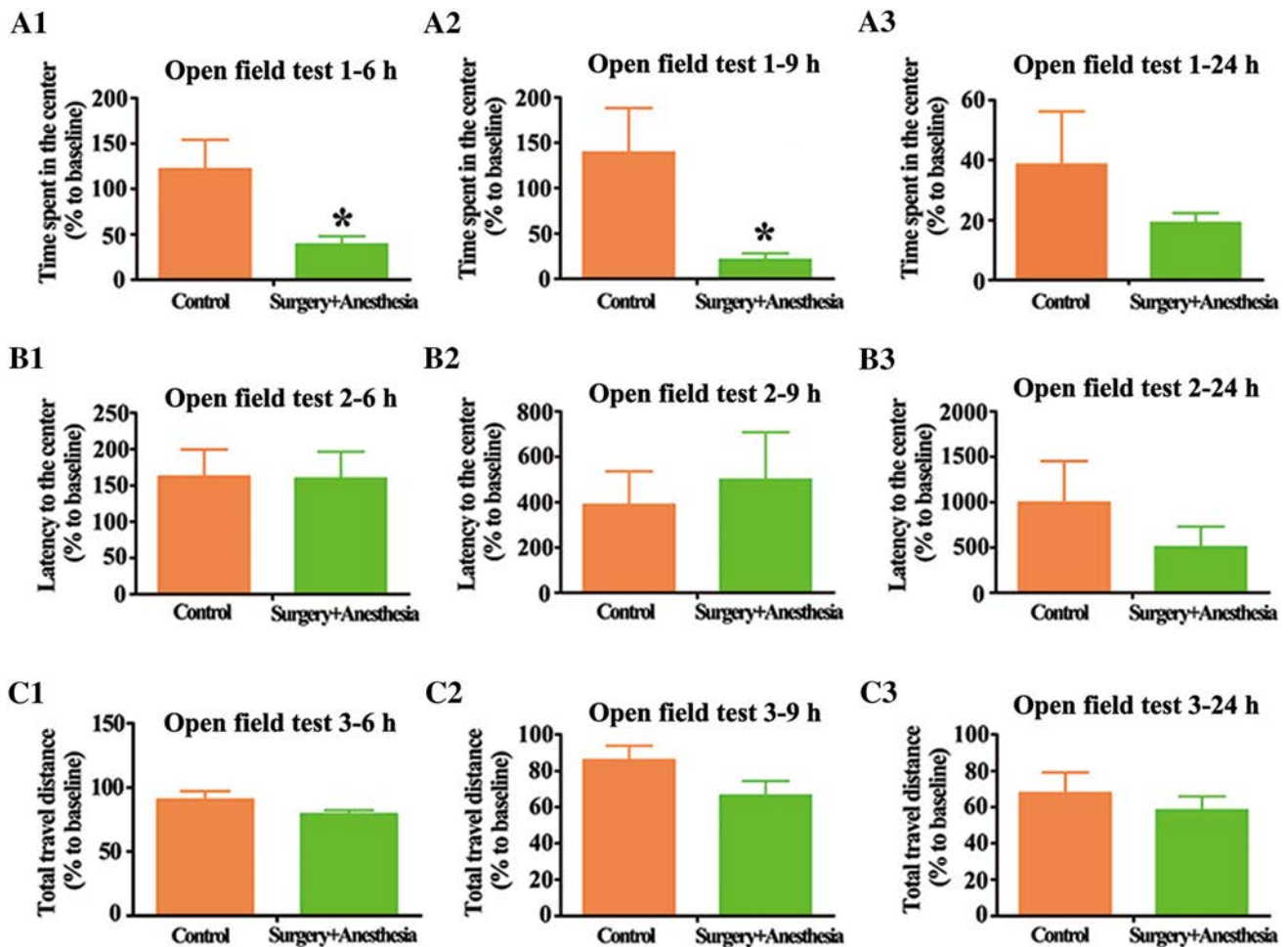


Fig. 2 Impact at 6 h, 9 h and 24 h of anesthesia/surgery on mouse behaviors assessed by the open field test. **A1–A3** Time spent in the center. **B1–B3** Latency to the center. **C1–C3** Total traveling distance. Data are presented as the mean \pm SEM. * $P < 0.05$, Mann–Whitney U test.

$P = 0.039$, Fig. 3B2), but not at 24 h (Fig. 3B3). In addition, the total entries to the three arms and total traveling distance showed no significant difference at any time point (Fig. S2). These results demonstrate that anesthesia/surgery impairs spatial learning and memory in mice in both a time-associated and motor-independent manner.

¹H-NMR-Based Metabolic Information for the Aged Brain at Different Postoperative Time Points

To document the dynamic changes in the concentrations of metabolites that may be related to the abnormal neurobehavioral performance and anesthesia/surgery, we selected four time points (0, 6, 9, and 24 h after anesthesia/surgery) to analyze the information on metabolites in the ¹H-NMR spectra [an example region (FC) at different time points is

illustrated in Fig. 4]. The average normalized spectra of the different groups and the basic metabolic information, including the metabolite name and the related chemical shift are shown in Fig. 4. It can be seen that group at 0 h had the minimum spectral heights of Asp and Glu; and the maximum spectral height of alanine (Ala). However, without statistical analysis, it was difficult to compare the significance of differences among the different groups, so further analysis is necessary.

Metabolic Patterns in Different Brain Regions after Anesthesia/Surgery

The contents of metabolites in the control group were set as the baseline and variations were investigated and identified. The significant changes in metabolites are listed in Table 1 and S1. The levels of metabolites in almost every region exhibited time-associated patterns (maximum variation at 0 h, returned to normal levels at 24 h). Most of metabolites

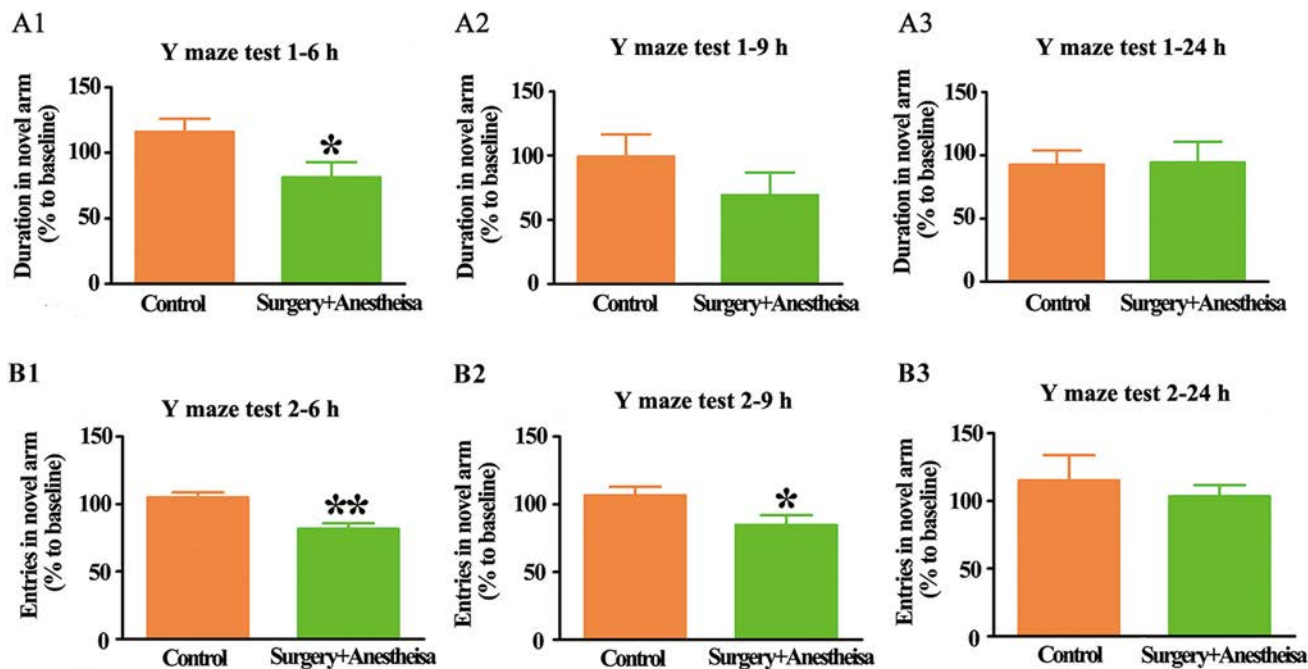


Fig. 3 Impact at 6, 9, and 24 h of anesthesia/surgery on mouse behaviors assessed by the Y-maze test. **A1–A3** Duration in the novel arm. **B1–B3** Entries into the novel arm. Data are presented as the mean \pm SEM. * $P < 0.05$, ** $P < 0.01$, Mann–Whitney U test.

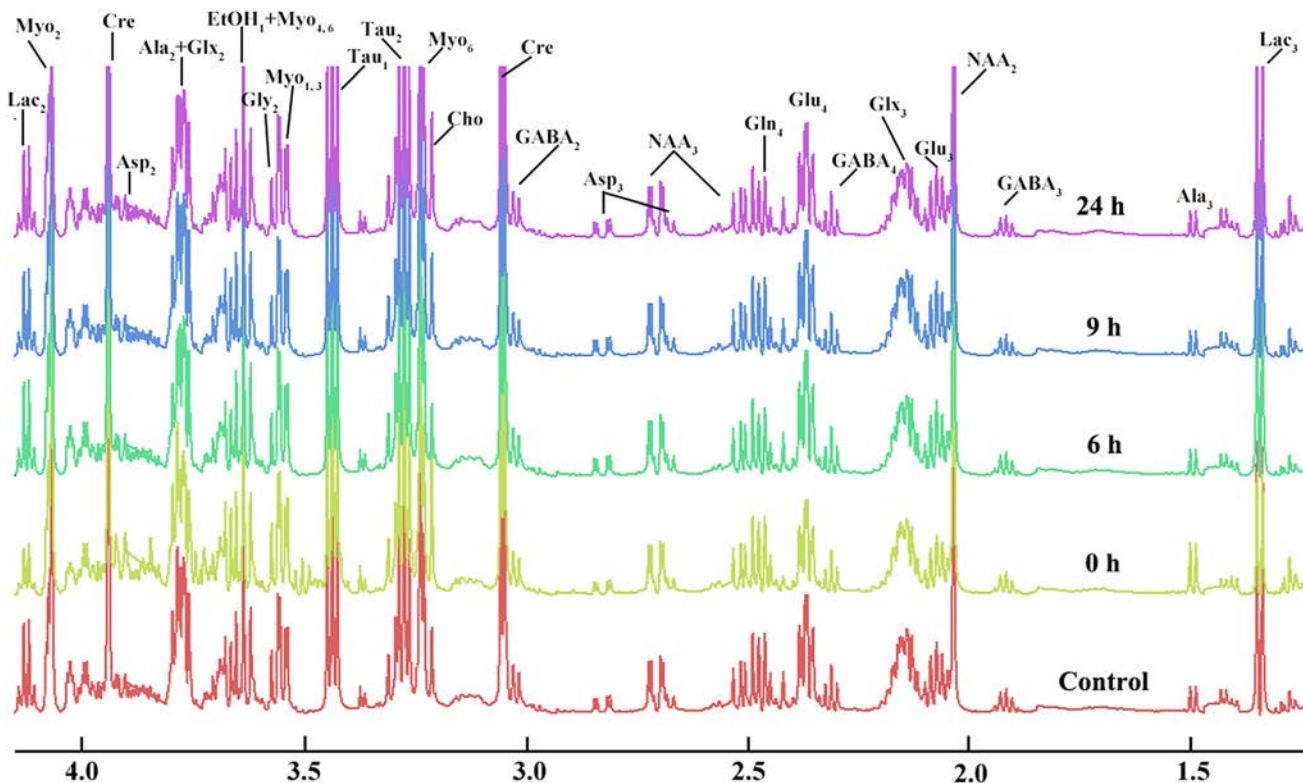


Fig. 4 Normalized average ¹H-NMR spectra for the frontal cortex samples in the control and model groups at 0, 6, 9, and 24 h after anesthesia/surgery. Horizontal axis, chemical shift of the spectrum. Lower-case, carbon position connected with the hydrogen signal; Lac,

lactate; Myo, myo-inositol; Cre, creatine; Ala, alanine; Glx, glutamine + glutamate; Gly, glycine; Asp, aspartate; EtOH, ethanol; Tau, taurine; GABA, gamma-aminobutyric acid; NAA, N-acetyl aspartate.

Table 1 Metabolite changes in the whole brain classified by region.

	0 h	6 h	9 h	24 h
OB	Myo -14.3%↑ ($P = 0.009$) Glu -39.6%↓ ($P < 0.001$) Ala -76.9%↑ ($P < 0.001$)			
FC	Asp -22.2%↓ ($P = 0.001$) Glu -20.2%↓ ($P < 0.001$) Ala -89.9%↑ ($P < 0.001$) Lac -56%↑ ($P < 0.001$)	Asp -13.0%↑ ($P = 0.046$)	Asp -16.6%↑ ($P = 0.009$)	
PC	Tau -8.74%↑ ($P = 0.031$) Glu -17.8%↓ ($P < 0.001$) Ala -65.4↑ ($P < 0.001$) GABA -13.4↓ ($P = 0.020$)	Asp -15.8%↑ ($P = 0.011$)	Asp -13.1%↑ ($P = 0.069$)	
OC	Cre -18.6%↓ ($P = 0.039$) Glu -20.1↓ ($P < 0.001$) Ala -67.7↑ ($P < 0.001$)	Asp -15.5%↑ ($P = 0.044$)	Asp -15.8%↑ ($P = 0.053$)	
TC	Asp -19.6%↓ ($P = 0.007$) Glu -14.1%↓ ($P < 0.001$) Ala -76.6%↑ ($P < 0.001$)			
STR	Tau -7.3%↑ ($P = 0.047$) Glu -22.0%↓ ($P < 0.001$) Ala -89.0%↑ ($P < 0.001$)			
HP	Tau -8.8%↑ ($P = 0.027$) Glu -18.2%↓ ($P < 0.001$) Ala -70.6%↑ ($P < 0.001$)		Glu -6.1%↑ ($P = 0.029$)	
THA	Tau -12.0%↑ ($P = 0.045$) Glu -23.9%↓ ($P < 0.001$) Ala -63.7%↑ ($P = 0.005$)			
HYP	Glu -19.1%↓ ($P = 0.007$) Ala -56.0%↑ ($P = 0.003$)			
MID	Ala -71.9%↑ ($P = 0.005$)			
MED	Asp -36.8%↓ ($P < 0.001$)			
CE	Gly -15.9%↓ ($P = 0.030$) Asp -34.0%↓ ($P = 0.003$) Ala -30.2%↑ ($P = 0.029$) Gln -45.9%↓ ($P = 0.015$)			

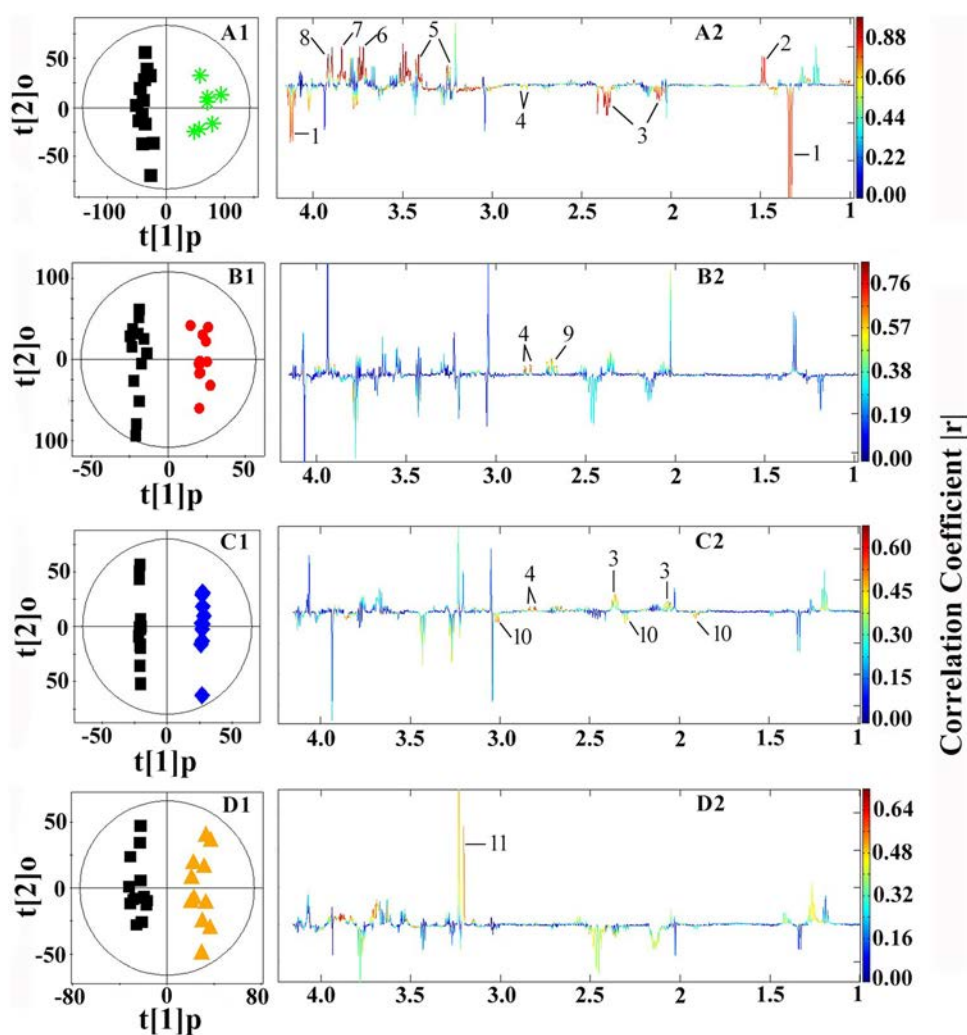
Variation of metabolites in distinct brain regions at different periods after anesthesia/surgery. Statistically significant differences among groups were assessed by one-way ANOVA followed by Turkey's *post-hoc* multiple comparison test.

dramatically decreased in most regions (except for the MID) after anesthesia/surgery, except for Ala that increased in the 0 h group. The metabolites in most regions fully recovered to normal (baseline) levels after 6 h except in the cortex. Eight regions (FC, PC, OC, TC, STR, HP, THA, and MID) were involved after 9 h, and most metabolites returned to baseline after 24 h except in the OB, FC, TC, and CE.

Discriminant Analysis Between the Control and Anesthesia/Surgery Groups

The OPLS-DA method was used to select the dominant metabolite changes caused by anesthesia/surgery and to visually discriminate the samples in different groups. Among the 12 regions, the metabolites in the FC region changed throughout the period. It was therefore selected as an example to illustrate the results of OPLS-DA (Fig. 5). The significantly different metabolites corresponding to anesthesia/surgery treatment were screened out with

Fig. 5 OPLS-DA scores and coefficient-coded loading plots for the models in the frontal cortex at different time points. **A1–D1** OPLS-DA scores at 0, 6, 9, and 24 h after anesthesia/surgery; **A2–D2** Coefficient-coded loading plots at 0, 6, 9, and 24 h after anesthesia/surgery. $t[1]_p$, first predictive component; $t[2]_o$, orthogonal principal component score; 1, Lac; 2, Ala; 3, Glu; 4, Asp; 5, taurine; 6, ethanol + myo-inositol; 7, Ala + Glu + Gln; 8, creatine; 9, N-acetyl Asp; 10, gamma-aminobutyric acid; 11, choline.



correlation coefficients of the OPLS-DA method ($r > 0.4329$, $P < 0.05$, $F = 19$).

Compared with the control group, the anesthesia/surgery group showed multiple significant changes at 0 h (Fig. 5A2). For instance, there was a decrease in Glu and Asp accompanied by an increase in Ala. There was also an increase in Asp both at 6 h (Fig. 5B2) and 9 h (Fig. 5C2); but an increase in Glu and a decrease in GABA only occurred at 9 h (Fig. 5C2). In addition, there was a tendency for choline to increase and for Glu to decrease 24 h postoperatively (Fig. 5D2).

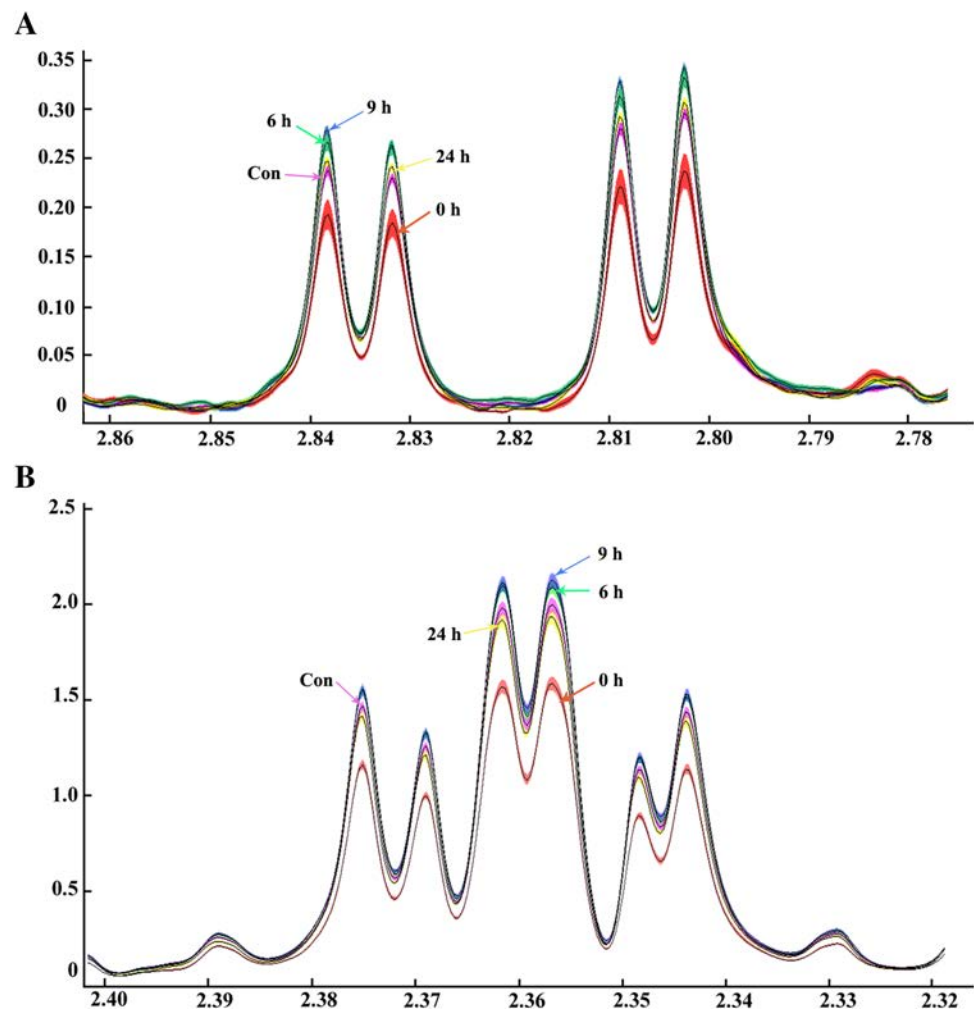
Considering the vital function of excitatory amino-acids in the brain, the dynamic changes in Glu and Asp were further investigated (Figs. S3 and S4). Dynamic changes of Glu and Asp in FC are illustrated in Fig. 6A. Our results demonstrated that anesthesia/surgery sharply reduced the level of Asp at 0 h, and there was a gradual reversal of the trend at 6 h and 9 h (blue line), but the level returned close to baseline after 24 h. The other excitatory amino-acid Glu presented a variation tendency similar to Asp (Fig. 6B).

Tendency of Glutamate and Aspartate to Change in the Whole Brain After Anesthesia/Surgery

To further assess the effects of anesthesia/surgery on Glu and Asp in the whole brain, their absolute concentrations were calculated and compared (Figs. 7, 8). The effects of anesthesia/surgery on Asp were mainly reflected in the cortex (FC, PC, OC, and TC) at 0, 6, and 9 h, and its variation tendency was similar. Furthermore, the variation tendency of Glu caused by anesthesia/surgery mostly occurred in the FC, TC, STR, HP, and THA (Fig. 8) at 0 and 9 h.

Collectively, these results suggested that anesthesia/surgery could cause a neurobehavioral disorder in a time-associated manner in aged mice. The anesthesia/surgery also altered the dynamics of some metabolites (Glu, GABA, Ala, Asp, choline, NAA, Gln, and Gly), and the variations in some metabolites (Glu and Asp) were consistent with the dynamic changes of the abnormal

Fig. 6 Normalized average ^1H -NMR spectra of selected metabolites in the frontal cortex at different times after anesthesia/surgery (mean \pm SEM). Horizontal axis, chemical shift of the spectrum. **A** Asp; **B** Glu. Pink, control; red, 0 h; green, 6 h; blue, 9 h; yellow, 24 h.



behavior performance. The changes in metabolites also occurred in a time-associated manner.

Effects of Time and Region on Asp and Glu After Anesthesia/Surgery

To determine whether time and region affected Asp and Glu after anesthesia/surgery, we compared their concentrations in the 12 regions at 0, 6, 9, and 24 h using two-way ANOVA. Both Asp ($F_{\text{time}} = 35.853$, $P < 0.001$; $F_{\text{regions}} = -115.439$, $P < 0.001$) and Glu ($F_{\text{time}} = 91.425$, $P < 0.001$; $F_{\text{regions}} = 98.057$, $P < 0.001$) were associated with time and region during recovery (Tables S2–S5).

Longitudinal Changes in the Metabolites and Behavioral Performance

To investigate the association between the metabolic changes and neurobehavioral abnormalities, we analyzed the correlations between the longitudinal neurobehavioral changes and the significantly altered metabolites (Glu and

Asp). The FC region was selected as it showed the most metabolic changes (Figs. 9, 10). The concentrations of Asp and Glu were positively correlated with the latency to food, especially for Asp (Fig. 9). However, they were negatively correlated with the other behaviors, such as duration in the center, duration in the novel arm, and entries into the novel arm (Figs. 9, 10). Among these relationships, the concentrations of Asp were significantly negatively correlated with the duration ($P = 0.041$) and entries into the novel arm ($P = 0.028$) (Fig. S5).

Discussion

The principal findings of this study were as follows: (1) A series of neurobehavioral changes, including inattention, learning/memory dysfunction, and emotional dysregulation (anxiety), were found in aged mice following surgery under isoflurane anesthesia. (2) Compared with the control group, the altered metabolite in the experimental group at 6 h was Asp, and the differences mainly occurred in the cortex;

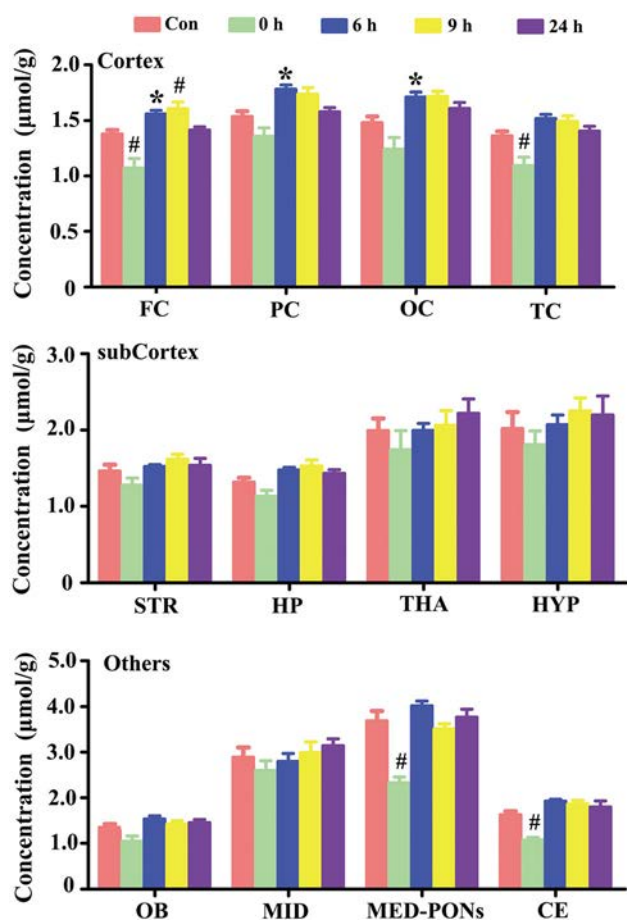


Fig. 7 Concentrations of aspartate in distinct brain regions at different time points after anesthesia/surgery. Statistically significant differences between groups were assessed by one-way ANOVA followed by Turkey's *post-hoc* multiple comparison test ($*P < 0.05$, $\#P < 0.01$). FC, frontal cortex; PC, parietal cortex; OC, occipital cortex; TC, temporal cortex; STR, striatum; HP, hippocampus; THA, thalamus; HYP, hypothalamus; OB, olfactory bulb; MID, midbrain; MED-PONs, medulla-pons; CE, cerebellum.

while significant changes in Asp and Glu at 9 h occurred predominantly in the cortex and hippocampus. (3) We found correlations between longitudinal changes in the metabolites and behavioral performance. (4) Both Asp and Glu were associated with time and region during recovery.

Application of *In-Vitro* Nuclear Magnetic Resonance Spectroscopy

Two magnetic resonance spectra methods can be used to analyze changes of the metabolites in animal models—*in vivo* MRS and *in vitro* NMR. Generally, the *in vivo* MRS method provides more accurate region-specific information due to its high spatial resolution, ability to longitudinally monitor the changes of metabolites, and reduce the animal numbers in most studies. Moreover, it has direct potential for clinical translation. The most fundamental requirement

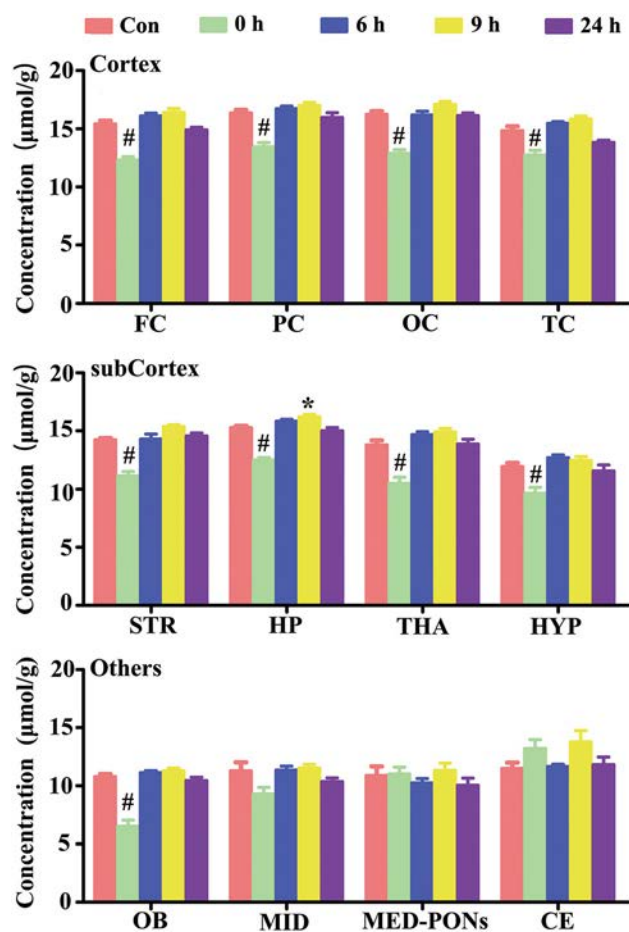


Fig. 8 Concentrations of glutamate in distinct brain regions at different periods after anesthesia/surgery. Statistically significant differences among groups were assessed by one-way ANOVA followed by Turkey's *post-hoc* multiple comparison test ($*P < 0.05$, $\#P < 0.01$). The full names of the regions are as in Fig. 7.

for ^1H -MRS testing is to keep the animal immobile during the whole data collection process, and there are only two ways to keep an animal immobile—continuous anesthesia or an apparatus to restrict movement. Given that our APNP model was constructed by isoflurane plus surgery, which meant anesthesia was likely an important factor in facilitating changes in behavior and/or metabolites, we did not use ^1H -MRS. The *in-vitro* NMR also involved anesthesia, but the dose and duration were far less than that required for ^1H -MRS. In addition, MRS only tested one specific region in each trial. To screen the regional metabolic patterns during APNP, the mouse brain was divided into 12 regions for NMR measurement.

Abnormal Neurobehavioral Performance in Aged Mice After Anesthesia/Surgery

All the behavioral tests were closely dependent on the movement ability of mice. The results showed that the

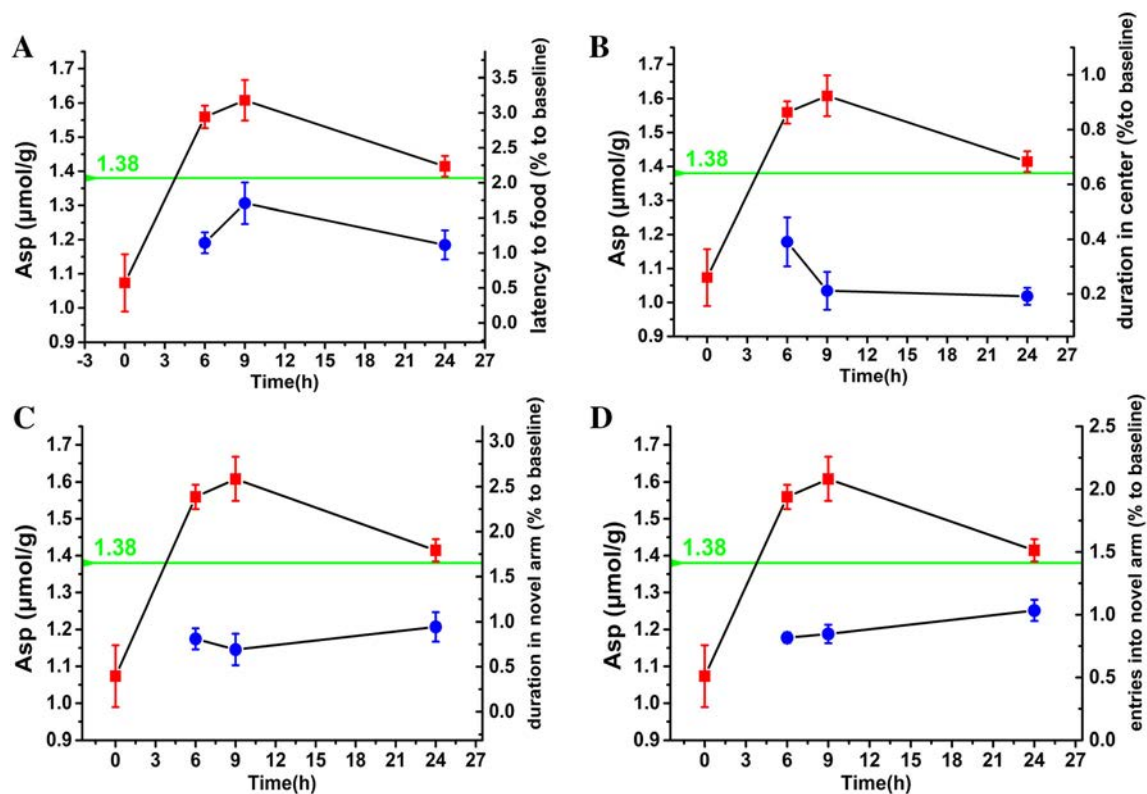


Fig. 9 Longitudinal changes in Asp and different kinds of neurobehavioral performance after anesthesia/surgery. Red, metabolite concentrations; blue, different kinds of neurobehavioral performance;

green: metabolite concentrations in the control group. Data are shown as the mean \pm SEM.

locomotor activity was not significantly impaired at any time, suggesting that the abnormal neurobehavioral performance at 6 h or 9 h was not related to motor functions. Although there may be other confounders, such as the effect of olfaction on the buried food test [29], each element of intact attention, unsubsided consciousness, normal emotion, and organized thinking was indispensable normal performance.

Our results are not exactly the same as those from a previous study [18], in which there was no significant difference in the latency to eat food at 6 h and the time spent in the center at 9 h. This discrepancy is probably due to the difference in research subjects (16-month-old *vs* 4-month-old mice), which is consistent with the consensus that aging is an independent risk factor for postoperative neurobehavioral disorders [30].

Brain Regions Affected After Anesthesia/Surgery

Our results showed that the most severely-affected regions were all in the four areas of cortex and the HP. These regions play distinct and complementary roles in the processing of normal neurobehavioral function (*e.g.* learning and memory, emotion regulation) [31, 32]. APNP may occur when the FC and HP are simultaneously directly

impaired or their mutual complementary effect is abnormal [33–35].

Our results are also consistent with recent clinical imaging work. It has been reported that several regions are involved in the pathology of neurobehavioral dysfunction after anesthesia/surgery, including cortex and the HP. These were obtained using diverse technologies such as single-photon emission computed tomography and the xenon-enhanced computed tomography to investigate changes in cerebral blood flow [36, 37], diffusion tensor imaging to analyze neuronal connections [38], and the blood-oxygen-level-dependent signal to measure functional connectivity [39]. Thus, regions of the cortex and HP could play key roles in the pathology of neurobehavioral disorders after anesthesia/surgery.

Metabolic Variation After Anesthesia/Surgery

Many metabolites in the whole brain fluctuated significantly following anesthesia/surgery, including Myo, Asp, Glu, Gln, GABA, Tau, and Ala. The general tendency was that the concentration of excitatory amino-acids decreased (*e.g.* Asp and Glu) and the concentration of inhibitory amino acids (*e.g.* GABA and Tau) increased, indicating that anesthesia/surgery disturbs the balance of excitatory

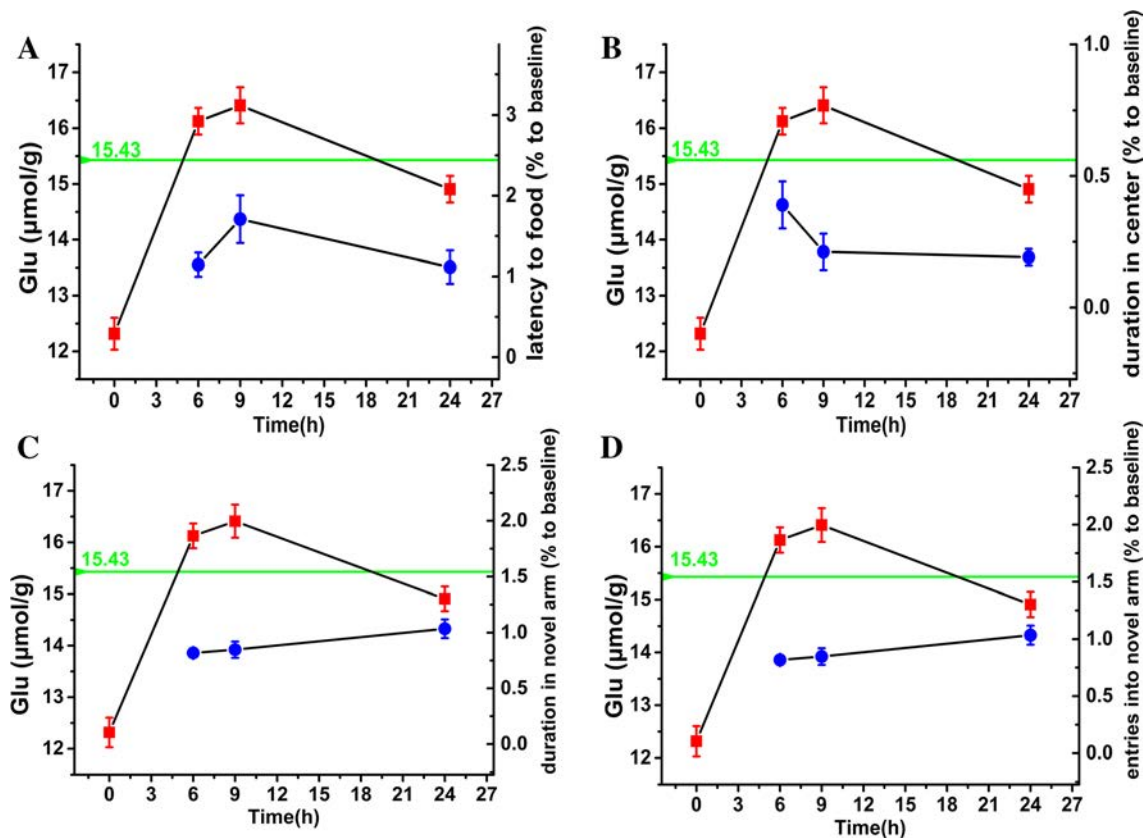


Fig. 10 Longitudinal changes in Glu and different kinds of neurobehavioral performance after anesthesia/surgery. Red, metabolite concentrations; blue, different kinds of neurobehavioral performance;

green, metabolite concentrations in the control group. Data are shown as the mean \pm SEM.

and inhibitory functions in the brain. Most of these metabolic alterations had almost disappeared and the neurobehavioral performance returned to normal after 24 h.

The tendency of Asp to be elevated in the cortex at 6 h and 9 h accompanied by evident neurobehavioral disorders is supported by a previous study, in which an increment of Asp was accompanied by impairment of neurobehavioral performance [4]. There are two isomers of Asp, L-Asp and D-Asp. The latter triggers glutamate transmission and is able to activate the N-methyl-D-aspartate receptor [40]; while the former is a critical building block of proteins and can be converted to the latter with the aid of D-Asp racemase [41]. Published data indicate that the application of exogenous D-Asp not only alleviates the cognitive impairment induced by neuropathic pain [42], but also enhances long-term potentiation and improves cognition in aged mice [43]. We therefore concluded that there may be a positive correlation between the content of D-Asp and cognition. However, it has been reported that D-Asp is low and it accounts for $< 1\%$ of the total Asp in adults, while the content of L-Asp is relatively high [44]. This suggests that the metabolic changes detected in our study were

mainly L-Asp, and there might have been more D-Asp due to conversion from the L type. The possible explanations of the increased Asp and the decline in cognition are as follows: (1) The effects of D-Asp on cognition might be associated with an individual's age, as reported by a previous study [45]. (2) Excess D-Asp generated D-Asp excitotoxicity as a surplus of the excitatory neurotransmitter Glu. (3) The increase of Asp was a result of compensatory feedback from the decreased D-asp. Nevertheless, the exact content of D-Asp needs to be determined in future studies.

Imbalance of Glu is strongly linked with both acute and chronic neurodegeneration, which can lead to excitotoxicity by disturbing the steady state of calcium, energy balance, and normal neuronal death pathways [46]. In the current study, the excess Glu at 9 h may be excitotoxic and impair cognition-related cerebral regions, such as the HP. This speculation is supported by an animal study, in which increased Glu was associated with cognitive dysfunction [4]. However, Kroll *et al.* reported that reduced Glu might also be related to the impairment of cognition in asthma patients [47]. This paradoxical evidence might be due to the different species as well as the time-course of the

investigations. In the former study, an acute rat model was investigated over a period < 24 h, while the latter study was a clinical observation for the possible association of Glu and cognitive decline in asthma patients, a common chronic disease of the respiratory system.

Limitations and Perspective

This study aimed to explore the metabolic patterns of APNP associated with surgical treatment; and several potential metabolites were preliminarily screened out using a dynamic mapping technique. Regrettably, we cannot identify the concrete cause (anesthesia or surgery) of APNP due to the lack of an anesthesia-alone group. An ¹H-MRS study has demonstrated that isoflurane anesthesia indeed alters the brain metabolites of mice immediately after anesthesia [48]. But whether (or how) the anesthesia alone affects APNP in the aged brain needs to be explored in a further study.

Conclusions

By means of the ¹H-NMR method, we explored APNP after anesthesia/surgery from a metabolic perspective. Both neurobehavioral performance and the concentrations of metabolites exhibited a parallel pattern in a time-associated manner. The metabolites that fluctuated most in the various cerebral regions were two critical excitatory amino-acids, Asp and Glu. Our results provide a dynamic map of metabolite alterations associated with the neurobehavioral disorders following anesthesia/surgery, which may be conducive to ultimately revealing the metabolic mechanism of postoperative neurobehavioral disorders.

Acknowledgements We would like to express our gratitude to Mrs. Pingping An (Wuhan Institute of Physics and Mathematics, Chinese Academy of Sciences) for her help in housing the animals. This work was supported by grants from the National Natural Science Foundation of China (8187051484, 8157050329, and 81600933), the Interdisciplinary Medicine Seed Fund of Peking University (BMU2017MC006), and the Youth Innovation Promotion Association of the Chinese Academy of Sciences, China (Y6Y0021004).

Conflict of interest The authors declare no competing financial interests.

References

1. Pinho C, Cruz S, Santos A, Abelha FJ. Postoperative delirium: age and low functional reserve as independent risk factors. *J Clin Anesth* 2016, 33: 507–513.
2. Pendlebury ST, Lovett NG, Smith SC, Dutta N, Bendon C, Lloyd-Lavery A, *et al.* Observational, longitudinal study of delirium in consecutive unselected acute medical admissions: age-specific rates and associated factors, mortality and re-admission. *BMJ Open* 2015, 5: e007808.
3. Allaili N, Valabregue R, Auerbach EJ, Guillemot V, Yahia-Cherif L, Bardinet E, *et al.* Single-voxel H-1 spectroscopy in the human hippocampus at 3 T using the LASER sequence: characterization of neurochemical profile and reproducibility. *NMR Biomed* 2015, 28: 1209–1217.
4. Cui B, Wu MG, She XJ, Liu HT. Impulse noise exposure in rats causes cognitive deficits and changes in hippocampal neurotransmitter signaling and tau phosphorylation. *Brain Res* 2012, 1427: 35–43.
5. Liu TT, He ZG, Tian XB, Kamal GM, Li ZX, Liu ZY, *et al.* Specific patterns of spinal metabolites underlying alpha-Me-5-HT-evoked pruritus compared with histamine and capsaicin assessed by proton nuclear magnetic resonance spectroscopy. *Biochim Biophys Acta-Mol Basis Dis* 2017, 1863: 1222–1230.
6. Meyerhoff DJ, MacKay S, Bachman L, Poole N, Dillon WP, Weiner MW, *et al.* Reduced brain N-acetylaspartate suggests neuronal loss in cognitively impaired human immunodeficiency virus-seropositive individuals: *in vivo* ¹H magnetic resonance spectroscopic imaging. *Neurology* 1993, 43: 509–515.
7. Andres RH, Ducray AD, Schlattner U, Wallimann T, Widmer HR. Functions and effects of creatine in the central nervous system. *Brain Res Bull* 2008, 76: 329–343.
8. Boulanger Y, Labelle M, Khiat A. Role of phospholipase A(2) on the variations of the choline signal intensity observed by ¹H magnetic resonance spectroscopy in brain diseases. *Brain Res Brain Res Rev* 2000, 33: 380–389.
9. Niciu MJ, Kelmendi B, Sanacora G. Overview of glutamatergic neurotransmission in the nervous system. *Pharmacol Biochem Behav* 2012, 100: 656–664.
10. Wang XF, Zhao TY, Su RB, Wu N, Li J. Agmatine prevents adaptation of the hippocampal glutamate system in chronic morphine-treated rats. *Neurosci Bull* 2016, 32: 523–530.
11. Maddock RJ, Buonocore MH. MR spectroscopic studies of the brain in psychiatric disorders. *Curr Top Behav Neurosci* 2012, 11: 199–251.
12. Shi J, Li Q, Wen T. Dendritic cell factor 1-knockout results in visual deficit through the GABA system in mouse primary visual cortex. *Neurosci Bull* 2018, 34: 465–475.
13. Govindaraju V, Young K, Maudsley AA. Proton NMR chemical shifts and coupling constants for brain metabolites. *NMR Biomed* 2000, 13: 129–153.
14. Wang J, Du H, Jiang L, Ma X, de Graaf RA, Behar KL, *et al.* Oxidation of ethanol in the rat brain and effects associated with chronic ethanol exposure. *Proc Natl Acad Sci U S A* 2013, 110: 14444–14449.
15. Gonzalez-Riano C, Garcia A, Barbas C. Metabolomics studies in brain tissue: a review. *J Pharm Biomed Anal* 2016, 130: 141–168.
16. Clausen MR, Edelenbos M, Bertram HC. Mapping the variation of the carrot metabolome using H-1 NMR spectroscopy and consensus PCA. *J Agric Food Chem* 2014, 62: 4392–4398.
17. Peng JN, Patil SM, Keire DA, Chen K. Chemical structure and composition of major glycans covalently linked to therapeutic monoclonal antibodies by middle-down nuclear magnetic resonance. *Anal Chem* 2018, 90: 11016–11024.
18. Peng M, Zhang C, Dong Y, Zhang Y, Nakazawa H, Kaneki M, *et al.* Battery of behavioral tests in mice to study postoperative delirium. *Sci Rep* 2016, 6: 29874.
19. Yang SM, Gu CP, Mandeville ET, Dong YL, Esposito E, Zhang YY, *et al.* Anesthesia and surgery impair blood-brain barrier and cognitive function in mice. *Front Immunol* 2017, 8: 902.
20. Nathan BP, Yost J, Litherland MT, Struble RG, Switzer PV. Olfactory function in apoE knockout mice. *Behav Brain Res* 2004, 150: 1–7.

21. Wang J, Zeng HL, Du H, Liu Z, Cheng J, Liu T, *et al.* Evaluation of metabolites extraction strategies for identifying different brain regions and their relationship with alcohol preference and gender difference using NMR metabolomics. *Talanta* 2018, 179: 369–376.
22. Wang J, Du H, Ma X, Pittman B, Castracane L, Li TK, *et al.* Metabolic products of [2-(13) C]ethanol in the rat brain after chronic ethanol exposure. *J Neurochem* 2013, 127: 353–364.
23. Du H, Fu J, Wang S, Liu H, Zeng Y, Yang J, *et al.* ¹H-NMR metabolomics analysis of nutritional components from two kinds of freshwater fish brain extracts. *RSC Adv* 2018, 8: 19470–19478.
24. Liu ML, Mao XA, Ye CH, Huang H, Nicholson JK, Lindon JC. Improved WATERGATE pulse sequences for solvent suppression in NMR spectroscopy. *J Magn Reson* 1998, 132: 125–129.
25. Liu Y, Cheng J, Liu HL, Deng YH, Wang J, Xu FQ. NMRSpec: an integrated software package for processing and analyzing one dimensional nuclear magnetic resonance spectra. *Chemom Intell Lab Syst* 2017, 162: 142–148.
26. Kamal GM, Wang XH, Yuan B, Wang J, Sun P, Zhang X, *et al.* Compositional differences among Chinese soy sauce types studied by C-13 NMR spectroscopy coupled with multivariate statistical analysis. *Talanta* 2016, 158: 89–99.
27. Kamal GM, Yuan B, Hussain AI, Wang J, Jiang B, Zhang X, *et al.* C-13-NMR-based metabolomic profiling of typical Asian soy sauces. *Molecules* 2016, 21: 1168.
28. Zhang LM, Wang LM, Hu YL, Liu ZG, Tian Y, Wu XC, *et al.* Selective metabolic effects of gold nanorods on normal and cancer cells and their application in anticancer drug screening. *Biomaterials* 2013, 34: 7117–7126.
29. Lehmkuhl AM, Dirr ER, Fleming SM. Olfactory assays for mouse models of neurodegenerative disease. *J Vis Exp* 2014, 90: e51804.
30. Maldonado JR. Delirium pathophysiology: an updated hypothesis of the etiology of acute brain failure. *Int J Geriatr Psychiatry* 2017, 33: 1428–1457.
31. Frank LM, Brown EN, Wilson M. Trajectory encoding in the hippocampus and entorhinal cortex. *Neuron* 2000, 27: 169–178.
32. Bannerman DM, Rawlins JNP, McHugh SB, Deacon RMJ, Yee BK, Bast T, *et al.* Regional dissociations within the hippocampus—memory and anxiety. *Neurosci Biobehav Rev* 2004, 28: 273–283.
33. Chang RYK, Nouwens AS, Dodd PR, Etheridge N. The synaptic proteome in Alzheimer’s disease. *Alzheimers Dement* 2013, 9: 499–511.
34. Kang MG, Byun K, Kim JH, Park NH, Heinsen H, Ravid R, *et al.* Proteogenomics of the human hippocampus: the road ahead. *BBA-Proteins Proteom* 2015, 1854: 788–797.
35. Focking M, Lopez LM, English JA, Dicker P, Wolff A, Brindley E, *et al.* Proteomic and genomic evidence implicates the postsynaptic density in schizophrenia. *Mol Psychiatr* 2015, 20: 424–432.
36. Fong TG, Bogardus ST, Daftary A, Auerbach E, Blumenfeld H, Modur S, *et al.* Cerebral perfusion changes in older delirious patients using 99mTc HMPAO SPECT. *J Gerontol A-Biol Sci Med Sci* 2006, 61: 1294–1299.
37. Yokota H, Ogawa S, Kurokawa A, Yamamoto Y. Regional cerebral blood flow in delirium patients. *Psychiatr Clin Neurosci* 2003, 57: 337–339.
38. Cavallari M, Dai WY, Guttmann CRG, Meier DS, Ngo LH, Hshieh TT, *et al.* Neural substrates of vulnerability to postsurgical delirium as revealed by presurgical diffusion MRI. *Brain* 2016, 139: 1282–1294.
39. Choi SH, Lee H, Chung TS, Park KM, Jung YC, Kim SI, *et al.* Neural network functional connectivity during and after an episode of delirium. *Am J Psychiatry* 2012, 169: 498–507.
40. D’Aniello G, Tolino A, D’Aniello A, Errico F, Fisher GH, Di Fiore MM. The role of D-aspartic acid and N-methyl-D-aspartic acid in the regulation of prolactin release. *Endocrinology* 2000, 141: 3862–3870.
41. D’Aniello S, Somorjai I, Garcia-Fernandez J, Topo E, D’Aniello A. D-aspartic acid is a novel endogenous neurotransmitter. *FASEB J* 2011, 25: 1014–1027.
42. Palazzo E, Luongo L, Guida F, Marabese I, Romano R, Iannotta M, *et al.* D-aspartate drinking solution alleviates pain and cognitive impairment in neuropathic mice. *Amino Acids* 2016, 48: 1553–1567.
43. Errico F, Nistico R, Napolitano F, Mazzola C, Astone D, Pisapia T, *et al.* Increased D-aspartate brain content rescues hippocampal age-related synaptic plasticity deterioration of mice. *Neurobiol Aging* 2011, 32: 2229–2243.
44. Dunlop DS, Neidle A, Mchale D, Dunlop DM, Lajtha A. The presence of free D-aspartic acid in rodents and man. *Biochem Biophys Res Commun* 1986, 141: 27–32.
45. Errico F, Nistico R, Napolitano F, Oliva AB, Romano R, Barbieri F, *et al.* Persistent increase of D-aspartate in D-aspartate oxidase mutant mice induces a precocious hippocampal age-dependent synaptic plasticity and spatial memory decay. *Neurobiol Aging* 2011, 32: 2061–2074.
46. Benarroch EE. Glutamate transporters diversity, function, and involvement in neurologic disease. *Neurology* 2010, 74: 259–264.
47. Kroll JL, Steele AM, Pinkham AE, Choi C, Khan DA, Patel SV, *et al.* Hippocampal metabolites in asthma and their implications for cognitive function. *Neuroimage Clin* 2018, 19: 213–221.
48. Boretius S, Tammer R, Michaelis T, Brockmoller J, Frahm J. Halogenated volatile anesthetics alter brain metabolism as revealed by proton magnetic resonance spectroscopy of mice *in vivo*. *Neuroimage* 2013, 69: 244–255.



Dependence of Generation of Hippocampal CA1 Slow Oscillations on Electrical Synapses

Yuan Xu¹ · Feng-Yan Shen² · Yu-Zhang Liu¹ · Lidan Wang¹ · Ying-Wei Wang² · Zhiru Wang¹

Received: 29 December 2018 / Accepted: 26 May 2019 / Published online: 29 August 2019
© Shanghai Institutes for Biological Sciences, CAS 2019

Abstract Neuronal oscillations in the hippocampus are critical for many brain functions including learning and memory. The underlying mechanism of oscillation generation has been extensively investigated in terms of chemical synapses and ion channels. Recently, electrical synapses have also been indicated to play important roles, as reported in various brain areas *in vivo* and in brain slices. However, this issue remains to be further clarified, including in hippocampal networks. Here, using the completely isolated hippocampus, we investigated *in vitro* the effect of electrical synapses on slow CA1 oscillations (0.5 Hz–1.5 Hz) generated intrinsically by the hippocampus. We found that these oscillations were totally abolished by bath application of a general blocker of gap junctions (carbenoxolone) or a specific blocker of electrical synapses (mefloquine), as determined by whole-cell recordings in both CA1 pyramidal cells and fast-spiking cells. Our findings indicate that electrical synapses are required for the hippocampal generation of slow CA1 oscillations.

Keywords Electrical synapse · Hippocampus · Oscillation · CA1 · Mefloquine · Carbenoxolone

Introduction

Hippocampus-dependent brain functions rely on neuronal oscillations in hippocampal networks [1–4]. To understand the neural mechanism underlying the generation of oscillation, previous studies have extensively investigated the roles of various types of chemical synapses and ion channels [5–9]. More recently, growing attention has also been paid to the contribution of electrical synapses, i.e., Cx36 (connexin 36) gap junctions, which bridge neuronal membranes and allow electrical coupling and the transfer of small molecules between neurons [10]. Using a specific blocker of Cx36 gap junctions, the general blocker of gap junctions containing Cx36 and other connexins (e.g., Cx43 between glial cells), as well as Cx36-knockout mice, numerous studies have demonstrated the contribution of electrical synapses to neuronal oscillations in different brain regions including the hippocampus [11, 12]. In studies carried out in brain slices to assess neuronal oscillations induced by artificial stimulation (e.g., drug treatment), as well as in the brain *in vivo* to assess oscillations generated intrinsically by neural circuits, transmission at Cx36 gap junctions or Cx36-containing gap junctions has been commonly found to be capable of enhancing neuronal oscillations at relatively low frequencies, in particularly, theta (5 Hz–10 Hz) [13–16] and gamma (30 Hz–80 Hz) oscillations [17–21]. Moreover, it has been shown that network activity in the theta or gamma bands can be synchronized by transmission at Cx36 gap junctions or Cx36-containing gap junctions [12, 18, 21, 22]. In addition to theta and gamma

Yuan Xu and Feng-Yan Shen have contributed equally to this work.

Electronic supplementary material The online version of this article (<https://doi.org/10.1007/s12264-019-00419-z>) contains supplementary material, which is available to authorized users.

✉ Zhiru Wang
zrwang@brain.ecnu.edu.cn

¹ Institute and Key Laboratory of Brain Functional Genomics of The Chinese Ministry of Education, Shanghai Key Laboratory of Brain Functional Genomics, School of Life Sciences, East China Normal University, Shanghai 200062, China

² Department of Anesthesiology, Huashan Hospital, Fudan University, Shanghai 200040, China

oscillations, a few studies have also suggested an effect of Cx36 gap junctions on high-frequency oscillations (>100 Hz) [23–25]. Although electrical synapses have been indicated to be important for the generation of neuronal oscillations in various brain areas including the hippocampus, the functional role remains to be further investigated. A better understanding of this issue might be obtained from more direct pharmacological studies of the contribution of electrical synapses to network oscillations, given that in previous *in vivo* studies, electrical synapses or gap junctions may not have been totally blocked by drug treatment (e.g., with i.p. injection to avoid animal death) or be totally inactivated in Cx36-knockouts (due to possible compensatory factors), and in brain slices, neuronal oscillations cannot usually be generated by a local network and are induced by artificial stimulation (drug application [15, 16]).

In our previous report in the completely-isolated hippocampal formation *in vitro*, we showed that CA1 oscillations at a low frequency (0.5 Hz–1.5 Hz) can be intrinsically generated (i.e., with no artificial stimulation) [26]. In this study, by taking advantage of the completely isolated hippocampus, which allows more direct pharmacological manipulation (compared with *in vivo* experiments), we have investigated the effect of hippocampal electrical synapses on the generation of CA1 oscillations.

Materials and Methods

Electrophysiological Recording in the Isolated Hippocampus

All animal procedures were performed in accordance with the Animal Care and Use Committee of East China Normal University (reference number: AR201404015). As described previously [26], we used Sprague-Dawley rats from postnatal day 14 (P14) to P18. To isolate the hippocampal formation, animals were anaesthetized with pentobarbital (i.p., 80 mg/kg; unless otherwise specified), and after decapitation the brain was rapidly removed and placed in ice-cold artificial cerebrospinal fluid (aCSF), which contained (in mmol/L) 119 NaCl, 2.5 KCl, 2.5 CaCl₂, 1.3 MgSO₄, 1 NaH₂PO₄, 26.2 NaHCO₃, and 11 glucose. One minute later, the brain was transferred to a cold plate, and the hemispheres were separated with a razor blade. The cerebellum, brain stem, and thalamus were moved aside to expose the hippocampal formation. The hippocampus was then completely isolated from the surrounding cortical issue with a small metal hook. This procedure was completed within 0.5 min–1 min. The entire hippocampus was then incubated in aCSF at room temperature for >1 h before electrophysiological recording.

The recording temperature in the submerged chamber was maintained at 28 °C–30 °C. Neurons were visualized under an Olympus microscope (DX50WI, Tokyo, Japan). Perforated whole-cell recordings with amphotericin B were made as described previously [26]. Patch pipettes with a 2.5 μm–3.0 μm tip were pulled from borosilicate glass tubing (Kimble Glass Inc., Queretaro, Mexico); they had a resistance of 3.0 MΩ–4.5 MΩ. The internal solution contained (in mmol/L) 136.5 K-gluconate, 17.5 KCl, 9.0 NaCl, 1.0 MgCl₂, 10.0 HEPES, 0.2 EGTA, and amphotericin B (0.3 mg/mL). A small amount (0.5 mg/mL–0.8 mg/mL) of glass beads (5 μm–15 μm in diameter; Polysciences, Inc., Warrington, UK) were included in the internal solution to maintain precipitate-free solution in the pipette tip [27]. The recording pipette was advanced into the hippocampus with a motor-driven manipulator (Siskiyou MMX7630, Siskiyou Corp., OR). Signals were acquired with patch-clamp amplifiers (Axopatch 700B, Axon Instruments, CA) and sampled at 5 kHz by a data acquisition card (Digidata 1440, Axon Instruments), with a 2 or 5 kHz low-pass filter. Liquid junction potentials (–13 mV) were corrected. Recordings with resting potentials between –65 mV and –75 mV were included for further analysis. The series resistance (not compensated for recording) was 48 ± 15 MΩ (mean \pm SD). Unless otherwise specified, no holding currents were applied during current-clamp recording.

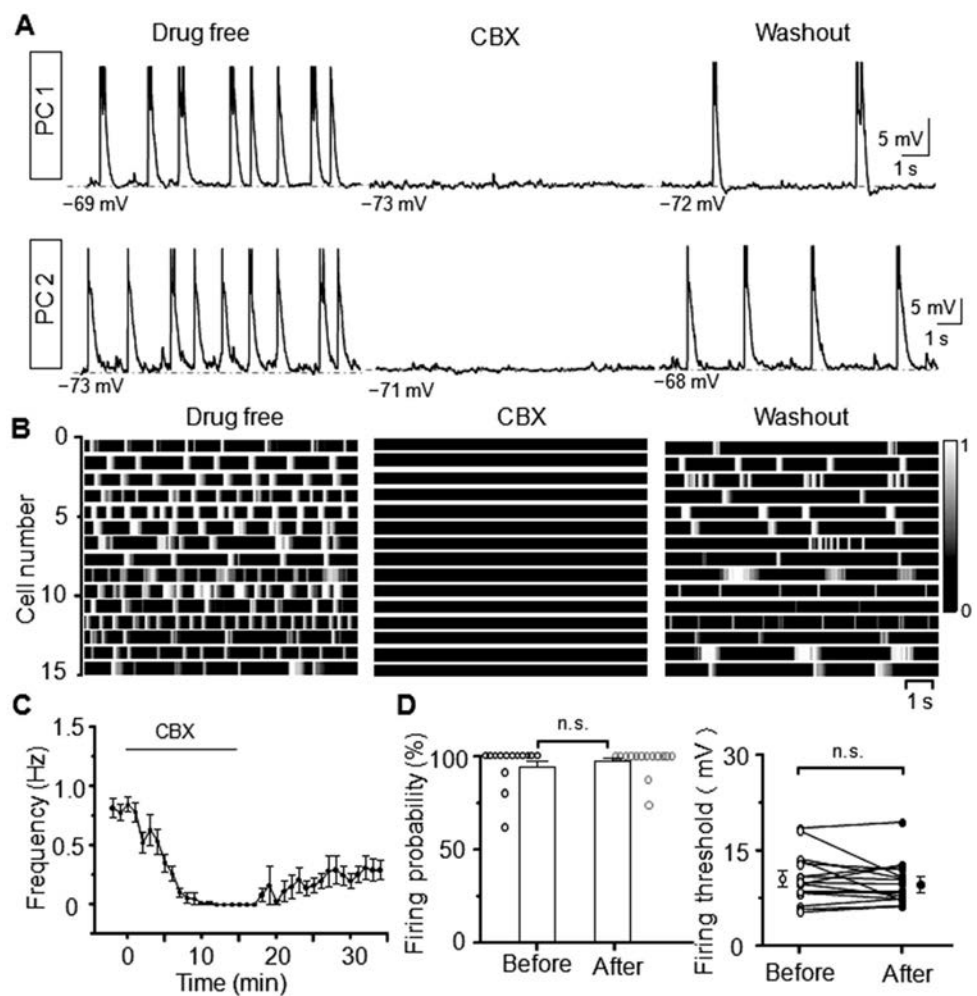
CA1 pyramidal cells (PCs) were recorded from the cell layer, and CA1 fast-spiking (FS) cells were recorded from the stratum oriens. To determine the cell type (PCs or FS cells), we evaluated the firing properties at depolarizing potentials (i.e., low firing rates with adaptation in PCs and sustained firing at high rates in FS cells) as well as spike half-widths (PCs, 3.2 ± 0.8 ms; FS cells, 1.7 ± 0.5 ms), as described in our previous report [26]. In further analysis of randomly-selected recordings, we found that putative CA1 PCs had a spike threshold (absolute value) of -53.6 ± 6.0 mV ($n = 35$) and spike amplitude (from spike threshold) of 54.2 ± 8.1 mV, both of which were significantly different from those found in putative FS cells ($n = 24$; spike threshold, -49.0 ± 5.4 mV, $P = 0.021$ unpaired *t*-test; spike amplitude, 41.0 ± 5.7 mV, $P = 0.041$).

Local field potentials (LFPs) were recorded in CA1 100 μm distal to the cell layer (in the stratum radiatum), using patch pipettes filled with aCSF, and signal acquisition was similar to whole-cell recording.

Electrophysiological Recording in Hippocampal Slices

Young rats (the same age as those for the isolated hippocampus) were initially anaesthetized with sodium pentobarbital (i.p., 80 mg/kg;). After decapitation, the

Fig. 1 CBX abolished V_m oscillations in CA1 PCs. **A** Two example PCs (from different hippocampal formations) showing V_m oscillations recorded in the absence and presence of CBX (action potentials were partially truncated; dashed lines, resting potentials). **B, C** Summary of all experiments as illustrated in **A** ($n = 15$), with V_m amplitudes normalized to the firing threshold of each cell and indicated by the gray scale (action potentials omitted in **B**; right, recordings 10–15 min after drug washout), and with time course plot (**C**) for the changes in oscillation frequencies (averaged across population data) induced by CBX (starting at time 0) and drug washout. **D** For the data shown in **B** and **C**. Left, firing probability of V_m oscillations (circles, individual data; bars, mean \pm SEM); right, firing thresholds (from resting potential) (for data points at right: dots connected by lines, data from the same cell; dots with bars, mean \pm SEM) recorded before and 10–15 min after CBX treatment. n.s., not significant.



brain was rapidly removed and placed in ice-cold aCSF (as used for the isolated hippocampus). Coronal slices (400 μm thick) containing the dorsal hippocampus were cut on a vibratome (Leica, VT1000 S, Wetzlar, Germany), and were then incubated at room temperature for >1 h before electrophysiological recording. The temperature in the submerged recording chamber was maintained at 28 $^{\circ}\text{C}$ –30 $^{\circ}\text{C}$, and perforated whole-cell recordings from CA1 PCs were conducted similar to that described for the isolated hippocampus. Bipolar tungsten electrodes were placed in the stratum radiatum for stimulation, which was produced by a pulse generator (Master-8; A.M.P.I., Jerusalem, Israel) through a stimulus isolator (ISO-Flex; A.M.P.I.). Inhibitory postsynaptic currents (IPSCs, recorded at -65 mV in voltage-clamp mode) were evoked at 0.07 Hz in the presence of bath-applied 6,7-dinitroquinoxaline-2,3-dione (DNQX, 40 $\mu\text{mol/L}$) and D-2-amino-5-phosphonopentanoate (D-AP5, 50 $\mu\text{mol/L}$) to prevent excitatory synaptic transmission.

Data Analysis and Statistics

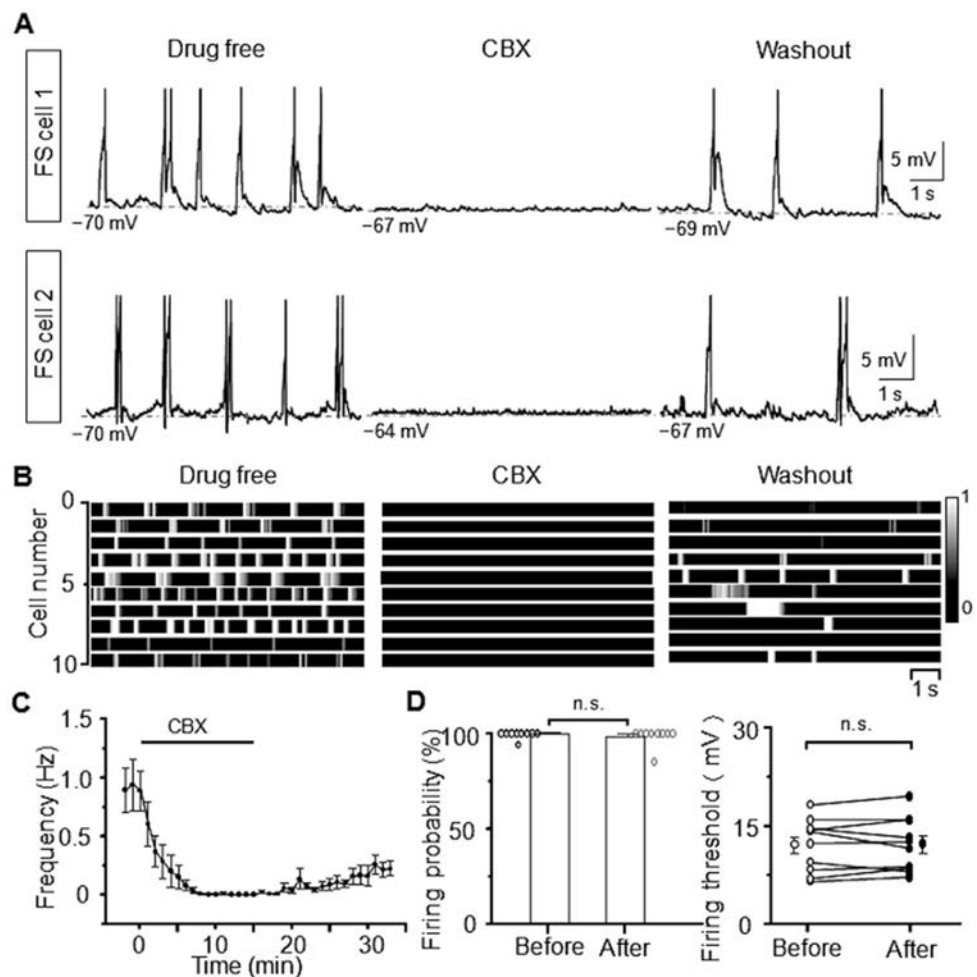
Firing thresholds were defined as the membrane potential (V_m) value at which $dV/dt > 10$ V/s. Fourier power spectra of LFPs were calculated from randomly-selected 2-min recordings using MatLab (MathWorks Inc., MA). Unless otherwise specified, statistical significance was determined using the paired Student's *t*-test (for recordings before and after drug treatment), and average values are presented as the mean \pm SEM.

Results

General Blocker of Cx36-Containing Gap Junctions Abolished CA1 Oscillations

As demonstrated in our recent report [26], spontaneous oscillations that were generated intrinsically at a low frequency (0.5 Hz–1.5 Hz) occur in CA1 neurons in the completely isolated hippocampal formation as used in the

Fig. 2 CBX abolished V_m oscillations in CA1 FS cells. **A–D** Data as in Fig. 1, but for FS cells ($n = 10$).



present study. In such an *in vitro* complete hippocampal formation, our whole-cell recordings show that such spontaneous CA1 oscillations consist primarily of membrane-potential (V_m) depolarizations, which are usually suprathreshold for generating neuronal firing, as shown in our previous study [26] and below in this study.

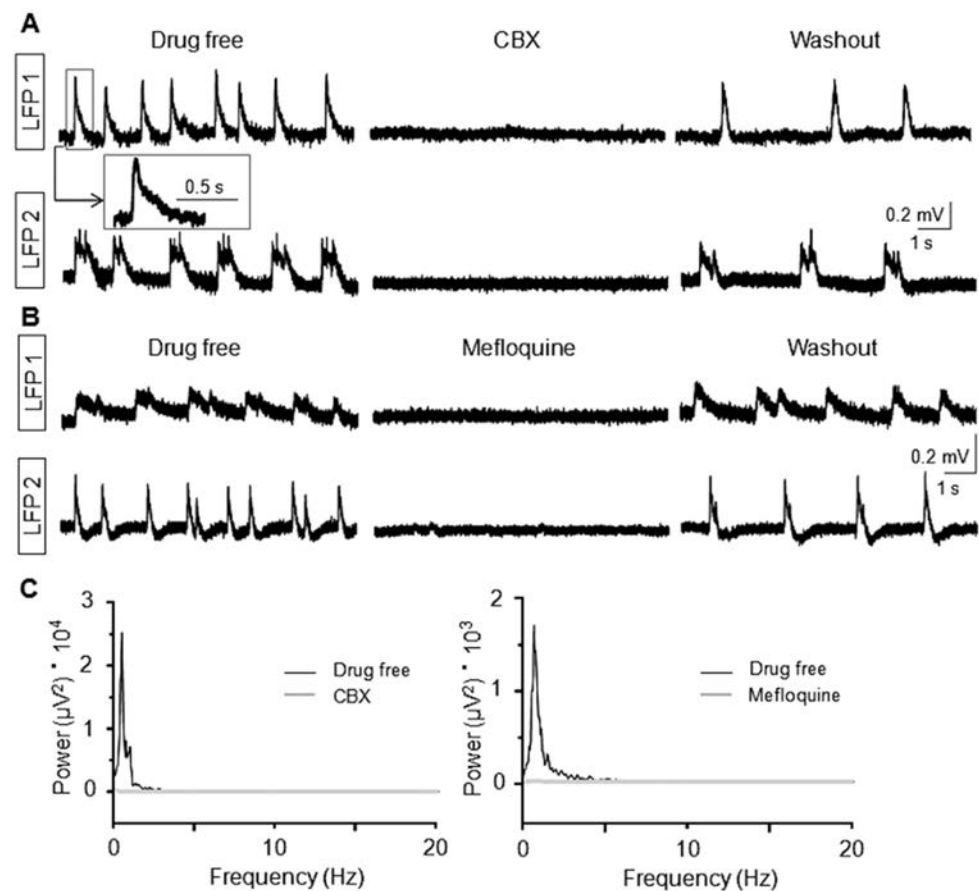
To examine the possible effect of electrical synapse-mediated activity on the intrinsically produced CA1 oscillations, we first recorded from CA1 PCs and used the general blocker of gap junctions carbenoxolone (CBX) to prevent transmission at electrical synapses (i.e., Cx36) as well as connexins between glial cells (e.g., Cx43) [28, 29]. We found in all CA1 PCs ($n = 15$; recorded in current-clamp mode without holding currents) that V_m oscillations were completely blocked when CBX (150 $\mu\text{mol/L}$) was applied in the bath (Fig. 1).

Our previous studies have shown that V_m oscillations of CA1 PCs are synchronized with CA1 interneurons and suggest an interneuron-based mechanism for the hippocampal generation of CA1 oscillations [26]. We then determined whether V_m oscillations of CA1 interneurons were also susceptible to the blocking effect of CBX. In another

group of experiments, current-clamp recordings were made from CA1 FS cells in the stratum oriens, in which we again found that V_m oscillations of all FS cells recorded disappeared during CBX treatment (Fig. 2), similar to the findings from PCs (Fig. 1). The absence of V_m oscillations in both CA1 PCs and FS cells after CBX application was consistent with our LFP recordings from CA1 (<100 μm distal to the cell layer), in which spontaneous LFP oscillations were totally blocked by CBX (Fig. 3).

In the above experiments from PCs and FS cells, we further found that after drug washout, the V_m oscillations of CA1 neurons gradually re-emerged, suggesting the capacity of the hippocampus to regenerate CA1 oscillations in the absence of external stimulation. However, the frequency of these re-emerging oscillations did not recover to the baseline level (before drug application), even 20 min after drug washout (Figs. 1C, 2C), possibly because the regeneration required a longer period for recovery, and/or CBX was difficult to thoroughly wash out, as previously reported [30]. Nonetheless, the partially-regenerated V_m oscillations were usually suprathreshold, and both the firing probabilities of V_m oscillations and firing thresholds were

Fig. 3 No CA1 oscillations occurred in LFP recordings during CBX or mefloquine treatment. **A, B** Example LFP recordings showing the absence of CA1 oscillations during CBX (**A**; inset, LFP at higher temporal resolution) or mefloquine application (**B**). **C** Fourier power spectra of LFPs recorded before and after CBX or mefloquine application, calculated from data shown in **A** and **B**.



unchanged, as compared with the recordings before CBX treatment (Figs. 1D, 2D).

Selective Blocker of Cx36 Electrical Synapses Abolished CA1 Oscillations

The findings with CBX treatment suggested that the CA1 oscillation in PCs (Fig. 1) and FS cells (Fig. 2) required transmission at Cx36-containing gap junctions. In the subsequent experiments, we used a selective Cx36 blocker (mefloquine) [31] to assess more directly the contribution of electrical synapses to CA1 oscillations. In such experiments, we also found that bath application of mefloquine (25 $\mu\text{mol/L}$) totally blocked the V_m oscillations of CA1 neurons in all recordings from PCs (Fig. 4) and FS cells (Fig. 5), as well as in LFP recordings in CA1 (Fig. 3). These results provided more direct evidence for the essential role of electrical synapses in the hippocampal generation of CA1 oscillations.

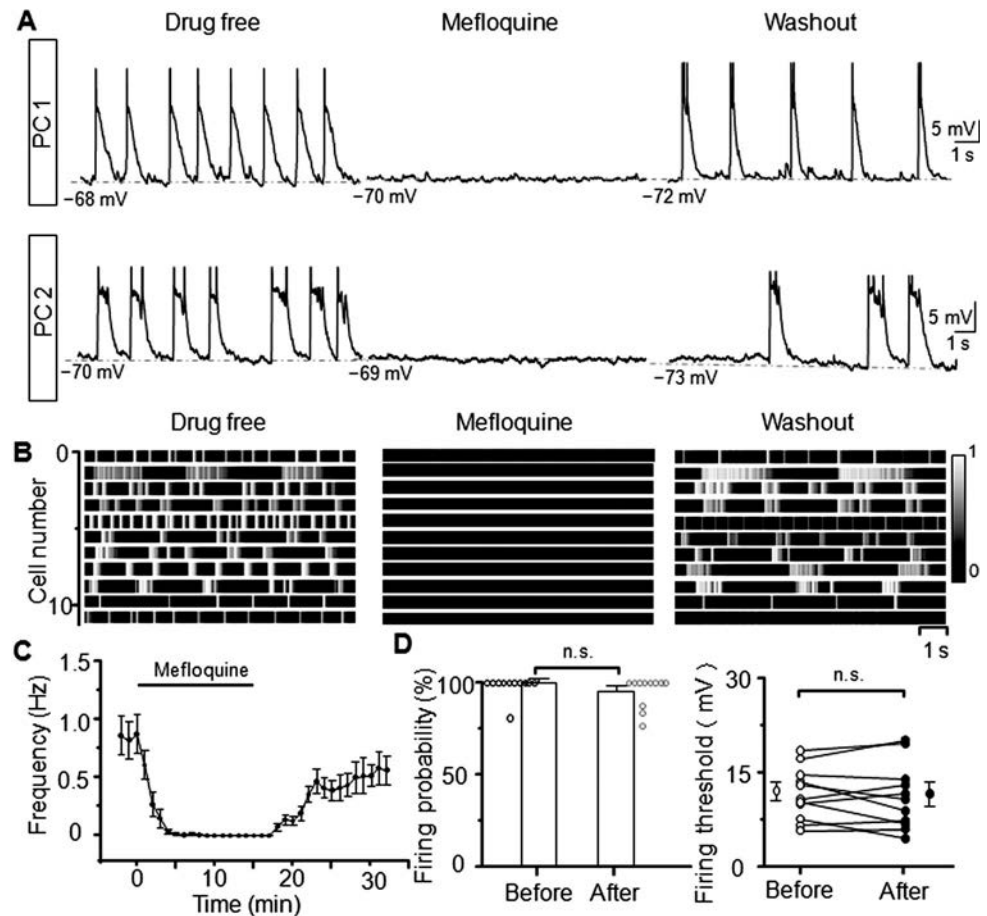
In addition, similar to the findings with CBX treatment, V_m oscillations regenerated after mefloquine washout (Figs. 4, 5), and the frequency did not recover to the baseline level within 20 min after washout. Also, such partially-regenerated V_m oscillations (in both PCs and FS

cells) were usually suprathreshold and had a firing probability and firing threshold similar to those recorded before drug application (Figs. 4D, 5D).

Synchronization of Partially-Regenerated CA1 V_m Oscillations After Drug Washout

We have reported that CA1 V_m oscillations in the completely isolated hippocampus are strongly synchronized among neurons [26]. In the present study, the recordings after drug washout showed a gradual re-emergence of CA1 V_m oscillations, although the frequency (within 20 min after washout) was significantly lower than that before drug application. We next asked whether the partially-regenerated V_m oscillations were also synchronized between CA1 neurons. To answer this, we made paired whole-cell recordings from CA1 neurons (mainly PCs, because the probability of achieving paired recordings from FS cells was low, and we had already shown that CA1 V_m oscillations are highly synchronized between PCs and FS cells [26]), and found that after drug (CBX or mefloquine) treatment, the regenerated CA1 V_m oscillations were highly synchronized between various neurons within 15 min after washout, similar to that before drug

Fig. 4 Mefloquine abolished V_m oscillations in CA1 PCs. **A–D** Data are displayed as in Fig. 1, for recordings from CA1 PCs but with mefloquine treatment ($n = 11$).



application (Fig. 6). These results indicated that the gradually-regenerating CA1 oscillations were synchronized in CA1 networks, and this synchronization could in turn be responsible for further regenerating CA1 oscillations.

No Effect of CBX or Mefloquine on Inhibitory Synaptic Transmission

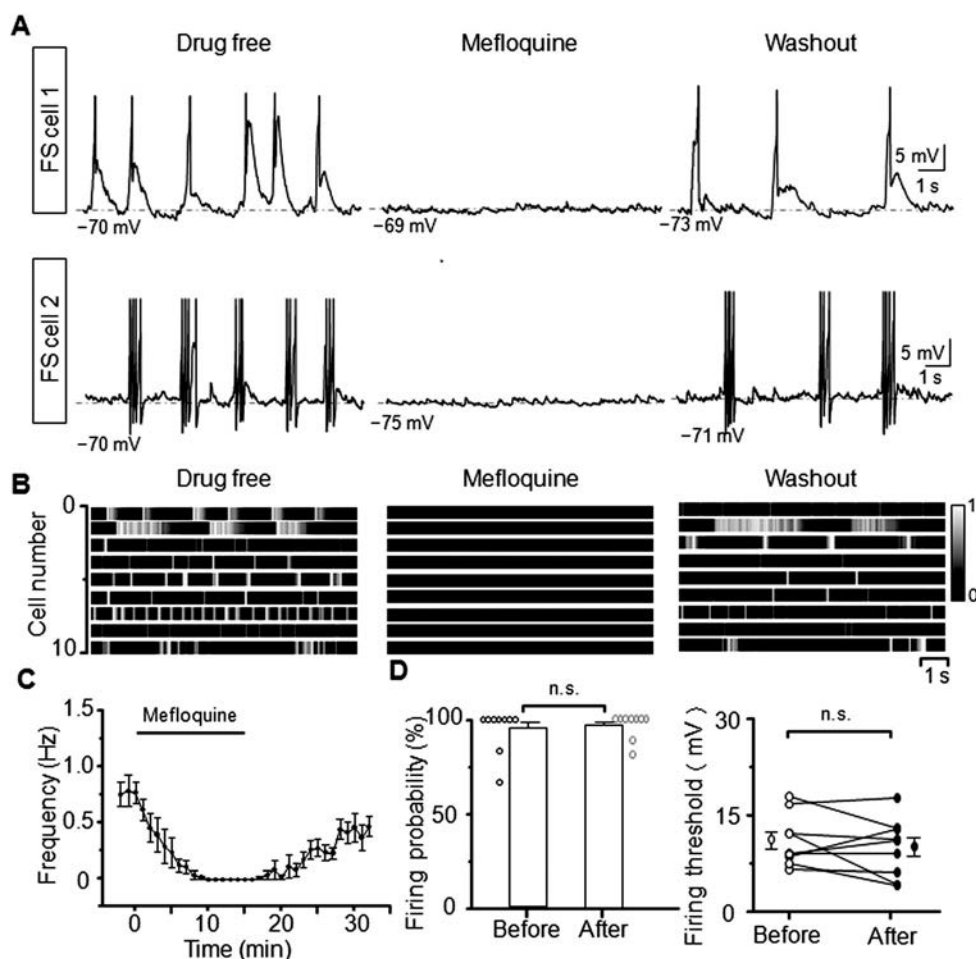
Our previous report in the completely isolated hippocampus has shown that the intrinsically generated CA1 oscillations are largely dependent on GABAergic synaptic transmission in the hippocampus [26]. In this study, with the findings of the blocking effects of CBX and mefloquine on CA1 oscillations, we further determined whether such drug treatment influenced GABAergic synaptic transmission in CA1 neurons. We therefore made perforated whole-cell recordings from CA1 PCs in hippocampal slices to measure the inhibitory postsynaptic currents (IPSCs) evoked by Schaffer collateral stimulation (recordings at -65 mV in voltage-clamp mode, with 40 $\mu\text{mol/L}$ DNQX and 50 $\mu\text{mol/L}$ D-AP5 in the bath solution). We found no change in the stimulation-evoked IPSCs of CA1 PCs after applying CBX or mefloquine (Fig. 7).

Discussion

In the completely isolated hippocampus, we investigated the role of electrical synapses in the hippocampal generation of low-frequency CA1 oscillations. We found that the V_m oscillations of both CA1 PCs and FS cells were totally abolished when Cx36 and astrocyte connexins were blocked by CBX, or when Cx36 was specifically blocked by mefloquine. These findings suggest an electrical synapse-based mechanism for the hippocampal generation of CA1 neuronal oscillations.

Three major types of neuronal oscillation occur in the *in vivo* hippocampus, as commonly demonstrated by LFP recording [11, 32, 33]: theta rhythms (~ 5 Hz– 10 Hz, also suggested to have a broader range of 3 Hz– 12 Hz), gamma rhythms (~ 30 Hz– 80 Hz), and sharp wave–ripples (~ 110 Hz– 250 Hz). In the completely isolated hippocampus, we found spontaneous CA1 oscillations (in both LFPs and V_m changes) at 0.5 Hz– 1.5 Hz, considerably slower than those found *in vivo* (e.g., compared with theta bands). The clearly slowed CA1 oscillations recorded in our experiments may be attributed to a largely impaired capacity of the *in vitro* hippocampus to produce network activity, for example, due to the absence of extra-

Fig. 5 Mefloquine abolished V_m oscillations in CA1 FS cells. **A–D** Data are displayed as in Fig. 4, but for recordings from FS cells with mefloquine treatment ($n = 9$).



hippocampal inputs as well as other *in vivo* machinery or conditions for oscillation generation. However, these *in vitro* CA1 oscillations may be analogous to theta oscillations, because V_m changes occurring at theta bands measured by *in vivo* whole-cell recording from CA1 PCs have also been found to consist primarily of large-amplitude V_m depolarizations (often able to generate neuronal firing) [34–36], which are similar to the slow CA1 oscillations shown in this study (Fig. 1).

No other CA1 oscillations (e.g., at higher frequencies comparable to gamma or ripple bands) were found in the isolated hippocampus, as indicated by the power spectra of CA1 LFP activity. On the other hand, our analysis of whole-cell recording data detected oscillatory spike activity that occurred at a periodicity similar to that of V_m changes (Fig. S1), consistent with the high probability of oscillatory V_m depolarizations for generating neuronal firing (Figs. 1D, 2D, 4D, 5D).

In the hippocampus and other brain areas, the effects of electrical synapses on the generation of neuronal oscillations have been investigated in both *in vivo* brains and slices. However, this issue remains to be further clarified, for example, given that in *in vivo* experiments drug

treatment may not be sufficient to completely block electrical synapses or gap junctions, and in *in vitro* experiments neuronal oscillations are usually produced by artificial stimulation but not intrinsically by a neural network [15, 16]. In our experiments in the completely isolated hippocampus, we have shown the presence of slow (0.5 Hz–1.5 Hz) V_m oscillations that were generated intrinsically in CA1 neurons. In addition, such a slow CA1 oscillation occurred when animals were anaesthetized with different drugs, such as pentobarbital and ketamine (Fig. S2A), and even occurred in hippocampus isolated from adult animals (Fig. S2B). We adopted the complete hippocampus isolated from young rats to evaluate the contribution of electrical synapses to hippocampal neuronal oscillations. With drug treatment in such *in vitro* recordings, surprisingly we found that the slow CA1 oscillations (in V_m changes, LFPs, and neuronal firing) were totally abolished by blocking electrical synapses or gap junctions with mefloquine or carbenoxolone. These results indicate that electrical synapses are necessary rather than partially responsible for generating these slow oscillations, a neuronal mechanism of neuronal oscillations for which little previous evidence is available.

Fig. 6 Partially-regenerated CA1 oscillations after drug washout were highly synchronized. **A, B** Paired whole-cell recordings from CA1 neurons showing highly synchronized V_m oscillations before and within 10–15 min after CBX (A) or mefloquine treatment (B). **C** Cross-correlograms between V_m oscillations recorded before (left) and within 10–15 min after (right) CBX treatment ($n = 4$ pairs) or mefloquine treatment ($n = 4$ pairs) (grey, results of all individual neuronal pairs; black, results averaged across all data from both CBX and mefloquine experiments). **D** Summary of the peak values of cross-correlograms for the data shown in C (circles, CBX; squares, mefloquine). In the data shown in C and D, 1 PC and 1 FS cell were recorded in two of the neuronal pairs, and all other paired recordings were from PCs.

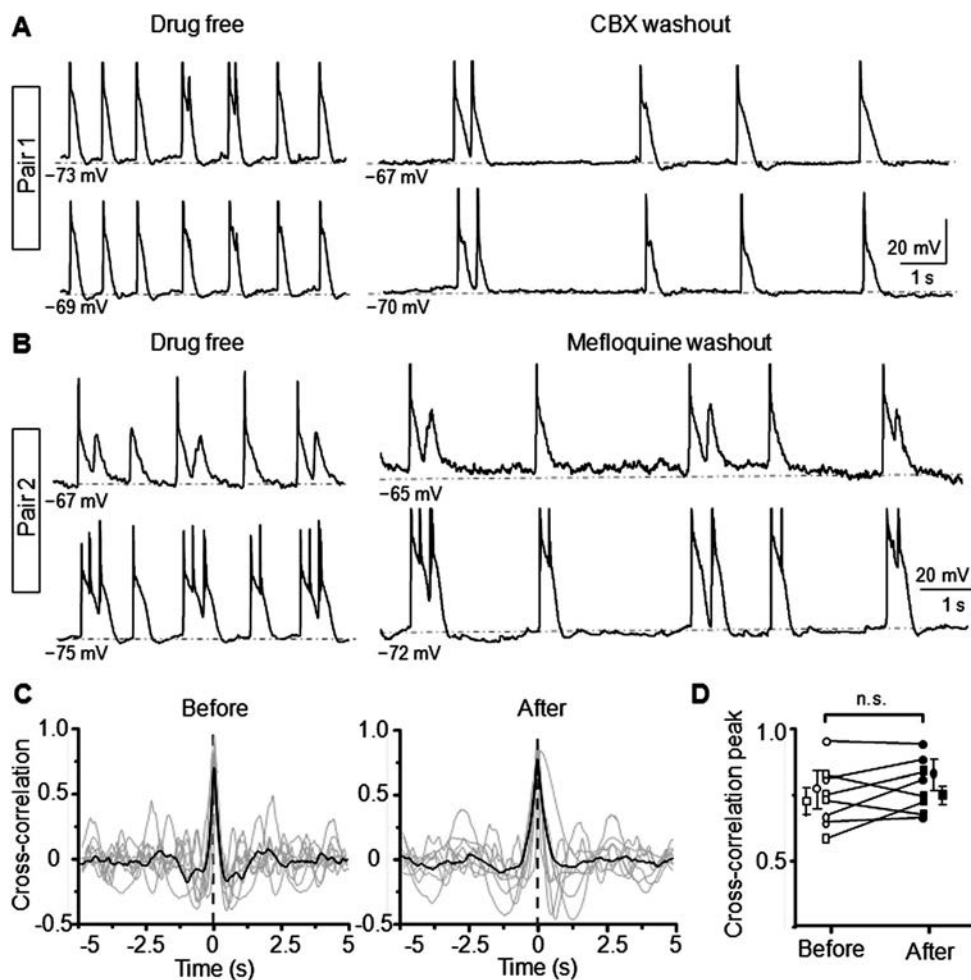
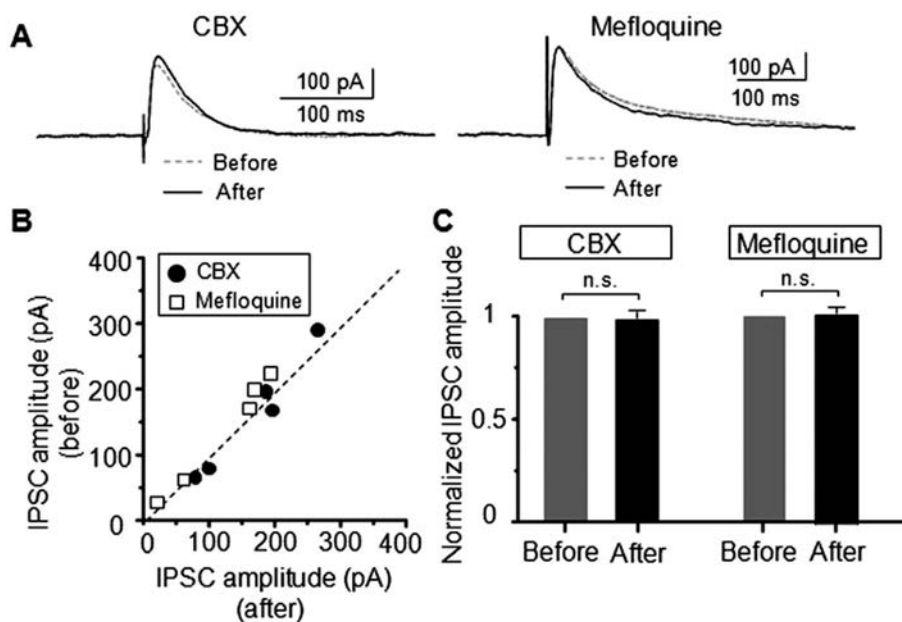


Fig. 7 No change in IPSCs after CBX or mefloquine treatment. **A** Two examples of CA1 PCs recording in hippocampal slices (with bath application of 40 $\mu\text{mol/L}$ DNQX and 50 $\mu\text{mol/L}$ D-AP5) showing the average IPSCs evoked by Schaffer collateral stimulation in the absence (gray dashed lines) and presence (black solid lines) of CBX (left) or mefloquine (right). **B, C** Summary of all experiments as in A ($n = 5/\text{group}$), with IPSC amplitude before drug application plotted against the values after drug application (B), and IPSC amplitudes (normalized to the values before drug application in individual data) averaged over population data (C).



Mefloquine has been reported to be a specific blocker of Cx36 gap junctions (i.e., electrical synapses between neurons). On the other hand, there are some non-specific

blocking effects of mefloquine on certain ion channels, such as L-type Ca^{2+} channels, delayed rectifier channels, and ATP-sensitive K^{+} channels, but the IC_{50} values for

blocking these channels are 3- to 15-fold higher than those required for Cx36 blockade [31, 37–39]. In our study, a dose of 25 $\mu\text{mol/L}$ mefloquine was used to block Cx36; this has been reported to exert only weak effects on ion channels [31]. As for chemical synapses, although we found no effect on GABAergic synaptic transmission (Fig. 7), previous reports have indicated that this concentration can result in small changes of excitatory synaptic transmission in brain slices as a slight ($< 5\%$) reduction of evoked field excitatory postsynaptic potentials [31]. However, although some weak non-specific effects may be exerted on excitatory chemical synapses as well as some ion channels in our recordings with the use of 25 $\mu\text{mol/L}$ mefloquine, our other findings suggest that such effects may not be able to cause the disappearance of CA1 oscillations. First, in a recent report in the completely isolated hippocampus [26], we have examined the dependence of CA1 V_m oscillations at the level of hippocampal network excitation by partially blocking AMPA receptors with a low dose of DNQX, and showed that CA1 V_m oscillations are still generated even with a 35%–45% reduction of AMPA receptor-mediated EPSPs. Second, in an unpublished study in this *in vitro* hippocampal formation, we also found little change in CA1 V_m oscillations when hyperpolarization-activated (I_h) channels are blocked. Moreover, the disappearance of CA1 oscillations in the presence of CBX, a drug that blocks transmission at Cx36 and other gap junctions [28, 40] but without the same non-specific actions of mefloquine on chemical synapses and ion channels, further reduces the possibility that the blocking effects of mefloquine on CA1 oscillations resulted from its non-specific effects. Nonetheless, the specificity of the contribution of electrical synapses to neuronal oscillations remains to be further examined, for example, using Cx36-knockout mice.

One explanation of the dependence of the CA1 oscillation on Cx36 electrical synapses is the requirement of electrical coupling between interneurons for oscillation generation. It is known that Cx36 is highly expressed in interneurons [21, 41, 42]. In addition, both *in vivo* and *in vitro* studies have demonstrated that interneurons in a local network are critical for producing neuronal oscillations [5, 6, 43–46]. In the completely isolated hippocampus, we have also found that GABAergic transmission is required for the intrinsically-generated CA1 oscillations [26]. Thus, we propose that electrical transmission at Cx36 electrical synapses between interneurons may be essential for the hippocampal generation of neuronal oscillations.

Also, we suggest that Cx36 between hippocampal PCs is also likely involved in the hippocampal generation of CA1 oscillations, given the presence of Cx36 in PCs reported in more recent studies [41, 42, 47]. In addition, the interaction of activity in PCs and interneurons has been reported to be

critical for producing neuronal oscillations, including in the hippocampal circuit [43, 48, 49].

Previous studies *in vivo* and in brain slices have demonstrated the contribution of electrical synapses to oscillation generation in various brain regions including the hippocampus, particularly with respect to theta and gamma oscillations [11, 12]. In this study, we further addressed this issue by taking advantage of the *in vitro* complete hippocampus, in which neuronal oscillations can be intrinsically generated. Our pharmacological and electrophysiological experiments indicate the requirement of electrical synapses for the hippocampus to generate a slow (0.5 Hz–1.5 Hz) V_m oscillation in both CA1 PCs and CA1 FS neurons. These findings provide new insights into the hippocampal mechanism for oscillation generation on the basis of electrical synapses, as well as hippocampus-dependent functions such as learning and memory.

Acknowledgements This work was supported by grants from the National Natural Science Foundation of China (31471078, 91132711, and 30970960), and a Key Project of Shanghai Science and Technology Commission (15JC1400102 and 19ZR1416600).

References

- Buzsaki G. Hippocampal sharp wave-ripple: A cognitive biomarker for episodic memory and planning. *Hippocampus* 2015, 25: 1073–1188.
- Marshall L, Born J. The contribution of sleep to hippocampus-dependent memory consolidation. *Trends Cogn Sci* 2007, 11: 442–450.
- Burgess N, Barry C, O’Keefe J. An oscillatory interference model of grid cell firing. *Hippocampus* 2007, 17: 801–812.
- Molle M, Born J. Slow oscillations orchestrating fast oscillations and memory consolidation. *Prog Brain Res* 2011, 193: 93–110.
- Bonifazi P, Goldin M, Picardo MA, Jorquera I, Cattani A, Bianconi G, *et al.* GABAergic hub neurons orchestrate synchrony in developing hippocampal networks. *Science* 2009, 326: 1419–1424.
- Wulff P, Ponomarenko AA, Bartos M, Korotkova TM, Fuchs EC, Bahner F, *et al.* Hippocampal theta rhythm and its coupling with gamma oscillations require fast inhibition onto parvalbumin-positive interneurons. *Proc Natl Acad Sci U S A* 2009, 106: 3561–3566.
- Alford ST, Alpert MH. A synaptic mechanism for network synchrony. *Front Cell Neurosci* 2014, 8: 290.
- Buzsaki G, Wang XJ. Mechanisms of gamma oscillations. *Annu Rev Neurosci* 2012, 35: 203–225.
- Calabrese RL, De Schutter E. Motor-pattern-generating networks in invertebrates: modeling our way toward understanding. *Trends Neurosci* 1992, 15: 439–445.
- Belluardo N, Mudo G, Trovato-Salinaro A, Le Gurun S, Charollais A, Serre-Beinier V, *et al.* Expression of connexin36 in the adult and developing rat brain. *Brain Res* 2000, 865: 121–138.
- Posluszny A. The contribution of electrical synapses to field potential oscillations in the hippocampal formation. *Front Neural Circuits* 2014, 8: 32.

12. Bennett MV, Zukin RS. Electrical coupling and neuronal synchronization in the mammalian brain. *Neuron* 2004, 41: 495–511.
13. Bissiere S, Zelikowsky M, Ponnusamy R, Jacobs NS, Blair HT, Fanselow MS. Electrical synapses control hippocampal contributions to fear learning and memory. *Science* 2011, 331: 87–91.
14. Allen K, Fuchs EC, Jaschonek H, Bannerman DM, Monyer H. Gap junctions between interneurons are required for normal spatial coding in the hippocampus and short-term spatial memory. *J Neurosci* 2011, 31: 6542–6552.
15. Konopacki J, Kowalczyk T, Golebiewski H. Electrical coupling underlies theta oscillations recorded in hippocampal formation slices. *Brain Res* 2004, 1019: 270–274.
16. Bocian R, Posluszny A, Kowalczyk T, Golebiewski H, Konopacki J. The effect of carbenoxolone on hippocampal formation theta rhythm in rats: *in vitro* and *in vivo* approaches. *Brain Res Bull* 2009, 78: 290–298.
17. Buhl DL, Harris KD, Hormuzdi SG, Monyer H, Buzsaki G. Selective impairment of hippocampal gamma oscillations in connexin-36 knock-out mouse *in vivo*. *J Neurosci* 2003, 23: 1013–1018.
18. Traub RD, Kopell N, Bibbig A, Buhl EH, LeBeau FE, Whittington MA. Gap junctions between interneuron dendrites can enhance synchrony of gamma oscillations in distributed networks. *J Neurosci* 2001, 21: 9478–9486.
19. Hormuzdi SG, Pais I, LeBeau FE, Towers SK, Rozov A, Buhl EH, *et al.* Impaired electrical signaling disrupts gamma frequency oscillations in connexin 36-deficient mice. *Neuron* 2001, 31: 487–495.
20. Pais I, Hormuzdi SG, Monyer H, Traub RD, Wood IC, Buhl EH, *et al.* Sharp wave-like activity in the hippocampus *in vitro* in mice lacking the gap junction protein connexin 36. *J Neurophysiol* 2003, 89: 2046–2054.
21. Deans MR, Gibson JR, Sellitto C, Connors BW, Paul DL. Synchronous activity of inhibitory networks in neocortex requires electrical synapses containing connexin36. *Neuron* 2001, 31: 477–485.
22. Christie JM, Bark C, Hormuzdi SG, Helbig I, Monyer H, Westbrook GL. Connexin36 mediates spike synchrony in olfactory bulb glomeruli. *Neuron* 2005, 46: 761–772.
23. Tseng SH, Tsai LY, Yeh SR. Induction of high-frequency oscillations in a junction-coupled network. *J Neurosci* 2008, 28: 7165–7173.
24. Galarreta M, Hestrin S. Spike transmission and synchrony detection in networks of GABAergic interneurons. *Science* 2001, 292: 2295–2299.
25. Draguhn A, Traub RD, Schmitz D, Jefferys JG. Electrical coupling underlies high-frequency oscillations in the hippocampus *in vitro*. *Nature* 1998, 394: 189–192.
26. Xu Y, Wang L, Liu YZ, Yang Y, Xue X, Wang Z. GABAergic interneurons are required for generation of slow CA1 oscillation in rat hippocampus. *Neurosci Bull* 2016, 32: 363–373.
27. Wang Y, Liu YZ, Wang SY, Wang Z. *In vivo* whole-cell recording with high success rate in anaesthetized and awake mammalian brains. *Mol Brain* 2016, 9: 86.
28. Roux L, Madar A, Lacroix MM, Yi C, Benchenane K, Giaume C. Astroglial connexin 43 hemichannels modulate olfactory bulb slow oscillations. *J Neurosci* 2015, 35: 15339–15352.
29. Cao R, Jiang S, Duan L, Xiong YF, Gao B, Rao ZR. Hypertonic stimulation induces synthesis and release of glutamate in cultured rat hypothalamic astrocytes and C6 cells. *Neurosci Bull* 2008, 24: 359–366.
30. Pan F, Mills SL, Massey SC. Screening of gap junction antagonists on dye coupling in the rabbit retina. *Vis Neurosci* 2007, 24: 609–618.
31. Cruikshank SJ, Hopperstad M, Younger M, Connors BW, Spray DC, Srinivas M. Potent block of Cx36 and Cx50 gap junction channels by mefloquine. *Proc Natl Acad Sci U S A* 2004, 101: 12364–12369.
32. Colgin LL. Rhythms of the hippocampal network. *Nat Rev Neurosci* 2016, 17: 239–249.
33. Zhao ZF, Li XZ, Wan Y. Mapping the information trace in local field potentials by a computational method of two-dimensional time-shifting synchronization likelihood based on graphic processing unit acceleration. *Neurosci Bull* 2017, 33: 653–663.
34. Liu YZ, Wang Y, Shen W, Wang Z. Enhancement of synchronized activity between hippocampal CA1 neurons during initial storage of associative fear memory. *J Physiol* 2017, 595: 5327–5340.
35. Grienberger C, Chen X, Konnerth A. NMDA receptor-dependent multidendrite Ca(2+) spikes required for hippocampal burst firing *in vivo*. *Neuron* 2014, 81: 1274–1281.
36. Zhan Y. Harnessing GABAergic transmission for slow oscillations. *Neurosci Bull* 2016, 32: 501–502.
37. Kang J, Chen XL, Wang L, Rampe D. Interactions of the antimalarial drug mefloquine with the human cardiac potassium channels KvLQT1/minK and HERG. *J Pharmacol Exp Ther* 2001, 299: 290–296.
38. Gribble FM, Davis TM, Higham CE, Clark A, Ashcroft FM. The antimalarial agent mefloquine inhibits ATP-sensitive K-channels. *Br J Pharmacol* 2000, 131: 756–760.
39. Maertens C, Wei L, Droogmans G, Nilius B. Inhibition of volume-regulated and calcium-activated chloride channels by the antimalarial mefloquine. *J Pharmacol Exp Ther* 2000, 295: 29–36.
40. Alvarez-Maubecin V, Garcia-Hernandez F, Williams JT, Van Bockstaele EJ. Functional coupling between neurons and glia. *J Neurosci* 2000, 20: 4091–4098.
41. Venance L, Rozov A, Blatow M, Burnashev N, Feldmeyer D, Monyer H. Connexin expression in electrically coupled postnatal rat brain neurons. *Proc Natl Acad Sci U S A* 2000, 97: 10260–10265.
42. Buzsaki G. Electrical wiring of the oscillating brain. *Neuron* 2001, 31: 342–344.
43. Cobb SR, Buhl EH, Halasy K, Paulsen O, Somogyi P. Synchronization of neuronal activity in hippocampus by individual GABAergic interneurons. *Nature* 1995, 378: 75–78.
44. Picardo MA, Guigue P, Bonifazi P, Batista-Brito R, Allene C, Ribas A, *et al.* Pioneer GABA cells comprise a subpopulation of hub neurons in the developing hippocampus. *Neuron* 2011, 71: 695–709.
45. Chang YY, Gong XW, Gong HQ, Liang PJ, Zhang PM, Lu QC. GABAA receptor activity suppresses the transition from interictal to ictal epileptiform discharges in juvenile mouse hippocampus. *Neurosci Bull* 2018, 34: 1007–1016.
46. Zhu Q, Ke W, He Q, Wang X, Zheng R, Li T, *et al.* Laminar distribution of neurochemically-identified interneurons and cellular co-expression of molecular markers in epileptic human cortex. *Neurosci Bull* 2018, 34: 992–1006.
47. Condorelli DF, Belluardo N, Trovato-Salinaro A, Mudo G. Expression of Cx36 in mammalian neurons. *Brain Res Brain Res Rev* 2000, 32: 72–85.
48. Stark E, Roux L, Eichler R, Senzai Y, Royer S, Buzsaki G. Pyramidal cell-interneuron interactions underlie hippocampal ripple oscillations. *Neuron* 2014, 83: 467–480.
49. Csicsvari J, Hirase H, Czurko A, Mamiya A, Buzsaki G. Oscillatory coupling of hippocampal pyramidal cells and interneurons in the behaving Rat. *J Neurosci* 1999, 19: 274–287.



Distribution and Functional Characteristics of Voltage-Gated Sodium Channels in Immature Cochlear Hair Cells

You Zhou^{1,2,3} · Chenchen Xia⁴ · Manli Yin⁴ · Xueling Wang^{1,2,3} · Hao Wu^{1,2,3} · Yonghua Ji^{4,5}

Received: 10 March 2019 / Accepted: 15 April 2019 / Published online: 6 August 2019
© Shanghai Institutes for Biological Sciences, CAS 2019

Abstract Voltage-gated sodium channels (VGSCs) are transiently expressed in cochlear hair cells before hearing onset and play an indispensable role in shaping spontaneous activity. In this study, we showed that Na⁺ currents shaped the spontaneous action potentials in developing mouse inner hair cells (IHCs) by decreasing the time required for the membrane potential to reach the action-potential threshold. In immature IHCs, we identified 9 known VGSC subtypes (Nav1.1 α –1.9 α), among which Nav1.7 α was the most highly expressed subtype and the main contributor to Na⁺ currents in developing hair cells. Electrophysiological recordings of two cochlea-specific Nav1.7 variants (CbmNav1.7a and CbmNav1.7b) revealed a novel loss-of-function mutation (C934R) at the extracellular linker between segments 5 and 6 of domain II. In

addition, post-transcriptional modification events, such as alternative splicing and RNA editing, amended the gating properties and kinetic features of CbmNav1.7a_(C934). These results provide molecular and functional characteristics of VGSCs in mammalian IHCs and their contributions to spontaneous physiological activity during cochlear maturation.

Keywords Cochlear hair cell · Spontaneous action potential · Voltage-gated sodium channel · Post-transcriptional modification · Gating property

Introduction

Hair cells, the primary sensory receptors of the mammalian cochlea, relay sound information to the brain *via* the coordinated release of neurotransmitters to activate spiral ganglion neurons [1]. Before the onset of hearing [at about postnatal days (P) 12–13 in most altricial rodents], inner hair cells (IHCs) cannot respond to sound but instead generate spontaneous action potentials that are sufficient to induce the release of vesicles [2]. The spontaneous activity originating from IHCs is involved in regulating a variety of cellular responses and the refinement of downstream neuronal circuits in developing auditory systems [3, 4]. Although spontaneous action potentials in premature IHCs are mainly due to interplay between an inward Ca²⁺ current and a delayed rectifier K⁺ current, they are also modulated by other transiently-expressed conductance events, such as the small-conductance Ca²⁺-sensitive K⁺ (SK2) current [5]. The SK2 channel is not required to generate spontaneous action potentials but is essential for sustaining continuous repetitive spontaneous activity in pre-hearing IHCs and for the functional maturation of IHCs

Electronic supplementary material The online version of this article (<https://doi.org/10.1007/s12264-019-00415-3>) contains supplementary material, which is available to authorized users.

✉ Hao Wu
wuhao622@sina.cn

✉ Yonghua Ji
yhji@staff.shu.edu.cn

- ¹ Department of Otolaryngology – Head and Neck Surgery, Ninth People's Hospital, Shanghai Jiaotong University School of Medicine, Shanghai 200125, China
- ² Ear Institute, Shanghai Jiaotong University School of Medicine, Shanghai 200125, China
- ³ Shanghai Key Laboratory of Translational Medicine on Ear and Nose Diseases, Shanghai 200125, China
- ⁴ Laboratory of Neuropharmacology and Neurotoxicology, Shanghai University, Shanghai 200444, China
- ⁵ Translational Institute for Cancer Pain, Xinhua Hospital Chongming Branch, Shanghai 202150, China

[6]. The Na^+ current is also transiently expressed in developing IHCs and is speculated to be involved in shaping spontaneous cochlear activity before the onset of hearing [7, 8]. In contrast, outer hair cells (OHCs) at the pre-hearing stage do not show spontaneous action potentials, but rather exhibit a single Ca^{2+} -dependent action potential following depolarizing injections of current [9]. Similar to IHCs, immature OHCs produce a repertoire of membrane currents including Na^+ currents [10]. The role of Na^+ currents in immature OHCs has not been reported to date, and it is worthwhile to investigate the functional maturation and acquisition of electromotile activity before the onset of hearing [11].

It is well known that voltage-gated Na^+ channels (VGSCs) are essential for the generation and propagation of action potentials in most excitable tissues. VGSCs are membrane protein complexes generally composed of one primary α subunit and two auxiliary β subunits [12]. To date, 9 subunit isoforms ($\text{Na}_v1.1\alpha$ – 1.9α) have been discovered in mammalian cells; $\text{Nav1.1}\alpha$, 1.2α , 1.3α , and 1.6α are predominantly expressed in the central nervous system; $\text{Nav1.7}\alpha$, 1.8α , and 1.9α are preferentially distributed in peripheral sensory neurons; and $\text{Nav1.4}\alpha$ and 1.5α are selectively expressed in skeletal muscle cells and cardiac cells, respectively [13]. The 9 VGSC subtypes are highly homologous in terms of sequence and structure; however, their gating characteristics, pharmacological properties, tissue distribution, and physiological functions are subtly diverse and specific [14]. In developing vestibular hair cells, two types of Na^+ current have been identified, namely a tetrodotoxin (TTX)-sensitive current that might be carried by $\text{Nav1.2}\alpha$ and 1.6α , and a TTX-insensitive current carried by $\text{Nav1.5}\alpha$ [15, 16]. However, the Na^+ current in developing IHCs has been shown to be highly sensitive to TTX [8, 17]. Our previous study revealed that all known subtypes of VGSCs are expressed in mouse cochlear sensory epithelia before the onset of hearing and that various VGSC splicing variants might be important to adapt to the unique physiological properties of the immature cochlea [18]. These results point to pivotal roles for VGSCs in regulating spontaneous activity in the developing cochlea.

To understand the physiological roles of VGSCs in pre-hearing hair cells, we aimed to investigate the following: (1) how the Na^+ current is involved in regulating spontaneous activity; (2) which subtype mainly contributes to the Na^+ current; and (3) whether cochlea-specific VGSC variants exhibit distinct gating properties.

Materials and Methods

Experimental Animals

C57BL6 mice [pregnant and newborn (P3–P7)] were obtained from the Shanghai Laboratory Animal Center (Chinese Academy of Sciences, Shanghai, China) and maintained under a 12/12 h light/dark cycle, with standard food and water provided *ad libitum*. The infant mice used in this work were killed by acute decapitation using dissecting scissors, and then quickly transferred into pre-cooled solution for dissection of the cochlea. The experimental procedures described here were performed in accordance with the National Institutes of Health (NIH) guidelines for the Care and Use of Laboratory Animals and were approved by the Ethics Committee and the Committee of Animal Experimentation at Shanghai University. All efforts were made to minimize the number of animals used and their suffering.

Tissue Preparation

The cochleas used for electrophysiological recording were dissected in extracellular solution composed of (in mmol/L): 135 NaCl, 5.8 KCl, 1.3 CaCl_2 , 0.9 MgCl_2 , 0.7 NaH_2PO_4 , 5.6 D-glucose, 10 Hepes-NaOH, 2 sodium pyruvate, 50× MEM amino acid solution (Invitrogen, Carlsbad, CA) and 100× MEM vitamin solution (Invitrogen) (pH 7.5, 308 mOsmol/kg). The extracellular solution was saturated with O_2 and cooled before cochlea dissection. The cochleas collected for RNA extraction and immunohistochemistry were dissected in ice-cold artificial cerebral spinal fluid (ACSF) containing the following (in mmol/L): 124 NaCl, 2.5 KCl, 1.3 CaCl_2 , 1.3 MgCl_2 , 1.25 NaH_2PO_4 , 26 NaHCO_3 , and 11 D-glucose (pH 7.4, 295 mmol/kg). The ACSF was saturated with 95% O_2 and 5% CO_2 . Intact sensory epithelia were acquired by carefully removing the stria vascularis, vestibular membrane, spiral ganglion, and tectorial membrane using fine forceps.

Whole-Cell Electrophysiological Recordings from Hair Cells

The dissected cochleas ($n = 15$ mice) were transferred into a microscope chamber and immobilized under a nylon mesh attached to a platinum steel ring. Extracellular solution was continuously perfused at ~ 30 mL/h using a peristaltic pump (BT100-2J, Longer, Baoding, Hebei, China). The extracellular solution and chamber were maintained close to body temperature (35°C – 37°C) using a dual-channel heater controller (TC-344B, Warner Instruments, Hamden, CT). The organ of Corti was viewed under

an upright infrared microscope (IX71, Olympus, Tokyo, Japan). Voltage- and current-clamp recordings were performed based on the whole-cell patch-clamp technique using an Axon 700B amplifier (Molecular Devices, Sunnyvale, CA). Patch pipettes were pulled from soda glass capillaries (Weitan Technology, Changsha, Hunan, China) using a horizontal microelectrode puller (P-1000, Sutter Instrument, Novato, CA) and the electrode resistances in extracellular solution were 3 M Ω –5 M Ω . For Na⁺ current recordings under voltage-clamp conditions, the pipette solution contained (in mmol/L): 131 CsCl, 3 MgCl₂, 1 EGTA-CsOH, 5 Na₂ATP, 5 Hepes-KOH, and 10 sodium phosphocreatine (pH 7.3, 292 mOsmol/kg). The Ca²⁺-free extracellular solution for Na⁺ current recordings contained (in mmol/L): 135 NaCl, 5.8 KCl, 3.9 MgCl₂, 0.7 NaH₂PO₄, 5.6 D-glucose, 10 Hepes-NaOH, 2 sodium pyruvate, 50 \times MEM amino acids (Invitrogen), and 100 \times MEM Vitamin solution (Invitrogen) (pH 7.5, 308 mOsmol/kg). For action potential recordings under current-clamp conditions, the pipette solution contained (in mmol/L): 131 KCl, 3 MgCl₂, 1 EGTA-KOH, 5 Na₂ATP, 5 Hepes-KOH, and 10 sodium phosphocreatine (pH 7.3, 292 mOsmol/kg). The extracellular solution for action potential recordings was the same as that used for dissection of cochleas. To investigate the function of Na⁺ current, 500 nmol/L TTX was added to the extracellular solution to block Na⁺ channels. To investigate the function of Ca²⁺ current, we used Ca²⁺-free extracellular solution in which MgCl₂ was increased to 3.9 mmol/L to maintain approximately constant membrane charge [8, 19]. The two extracellular solutions (with 1.3 mmol/L Ca²⁺ and Ca²⁺-free) for voltage- and current-clamp recordings were both saturated with O₂. Data were acquired using pClamp software with a DigiData 1440A data-acquisition board (Axon Instruments, Burlingame, CA). Voltage recordings were sampled at 5 and 50 kHz and low-pass filtered at 2.5 and 10 kHz (eight-pole Bessel). For current recordings, data were sampled at 100 kHz and low-pass filtered at 10 kHz using an eight-pole Bessel, the series resistance errors were compensated by 80%, and the leak conductance was subtracted using the P/N protocol. Data were analyzed off-line using Origin software (Origin Lab, Northampton, MA).

Quantitative RT-PCR (qPCR)

The intact cochlear sensory epithelia from 25 mice (P3–P7) were collected and total RNA was extracted using TRIzol reagent (Invitrogen) according to the manufacturer's protocol. RNA integrity was confirmed with the Agilent 2100 Bioanalyzer (Agilent Technologies, Santa Clara, CA), showing clear characteristic peaks at 28S and 18S. First-strand cDNA was synthesized from total RNA using oligo

(dT)18 and PrimeScript RTase (Cat#: RR037Q, Takara, Dalian, China). The short mRNA fragments encoding the 9 VGSC subtypes and Ca_v1.3 were then cloned by RT-PCR and the cloned fragments were sequenced to ensure the specificity of the primers (listed in Table S1). For single-cell qPCR, the intact cochlear sensory epithelia from seven P6 mice were placed in a microscope chamber and immobilized under a nylon mesh attached to a platinum-steel ring. After incubation (35 °C–37 °C) in extracellular solution with 0.625 mg/mL trypsin for 5 min, samples were washed by perfusion and cleaned using a stream of fluid from a pipette; then single IHC and OHC from the apical or basal sensory epithelium were each aspirated into a pipette filled with RNase-free extracellular solution (Recombinant RNase Inhibitor; Cat#: 2313A, Takara), and then transferred to a pre-cooled PCR tube. The synthesis of first-strand cDNA and qPCR were performed according to the manufacturer's protocol (SYBR qPCR Mix; QPS-201, Toyobo, Osaka, Japan).

Tissue Immunohistochemistry

The apical-middle coil of sensory epithelia from 40 P6 mice were dissected and fixed in 4% paraformaldehyde for 2 h at 4 °C. The cochleas were then washed three times with 0.1 mol/L phosphate buffer solution (PBS, pH 7.4) for 5 min each and incubated in 0.5% Triton X-100 containing 3% H₂O₂ for 30 min at room temperature. After washing with PBS, samples were antigen-repaired for 25 min with pepsin at 37 °C. The cochleas were then washed three times and blocked for 1 h with 5% goat albumin serum at room temperature. Primary antibodies against myosin 7 α (Abcam, Cambridge, UK; 1:100), Nav1.1 α (Abcam; 1:500), Nav1.2 α (Abcam; 1:500), Nav1.3 α (Santa Cruz, San Francisco, CA; 1:50), Nav1.4 α (Abcam; 1:500), Nav1.5 α (Abcam; 1:500), Nav1.6 α (Alomone, Jerusalem, Israel; 1:300), Nav1.7 α (Abcam; 1:300), Nav1.8 α (Abcam; 1:500), and Nav1.9 α (Abcam; 1:200) were diluted in 5% goat serum. After incubation at 4 °C for 24 h, the samples were washed three times in PBS and then incubated with the Cys- and FITC-conjugated secondary antibodies (Abcam; 1:500) at room temperature for 1 h. The sensory epithelia were dehydrated, cover-slipped, and photographed under an upright fluorescence microscope (Nikon, Sendai, Japan).

Transcriptome Analysis

The cochlear sensory epithelium was acutely dissected from 90 C57BL6 mice at P5–P7 and each detached into apical and basal sensory epithelia using a microelectrode. Three cDNA libraries of independent apical samples (Apex-1, Apex-2, and Apex-3) and three cDNA libraries

of independent basal samples (Base-1, Base-2, and Base-3) were constructed according to Illumina's instructions (Shanghai Personalbio Co., China). The mRNA was isolated using magnetic oligo (dT) beads. Fragmentation buffer was added to cleave the mRNA into short fragments, and these fragments were used as templates. Random hexamer-primers were used to synthesize first-strand cDNA. Buffer, dNTPs, RNase H, and DNA polymerase I were used to synthesize second-strand cDNA. Then, the fragments were purified using a QiaQuick PCR extraction kit (Qiagen, Hilden, Germany) and resolved with elution buffer for end repair and poly (A) addition. The resulting short fragments were then connected to sequencing adapters. Fragments with a suitable range of lengths were selected based on the results of agarose gel electrophoresis and were used as templates for library amplification. Library quantification was performed using Pico green and a fluorescence spectrophotometer (Quantifluor-ST fluorimeter, Promega; Quant-iT Pico Green dsDNA Assay Kit, Invitrogen). The library quality was confirmed using the Agilent 2100 Bioanalyzer and Agilent High Sensitivity DNA Kit (Agilent Technologies). Finally, the library was pair-end sequenced using Illumina NextSeq 500. Raw image data generated by sequencing were stored in fastq format and submitted to the National Center for Biotechnology Information Sequence Read Archive database (accession number: PRJNA505942).

Raw sequencing data were filtered to remove low-quality reads before subsequent analyses. Quality analysis by means of FastQC showed that the average quality of the filtered data was very high. Theoretical values coincided well with the measured values (Table S2). To annotate all useful reads, the clean reads were mapped to the mouse genome database; RPKM (reads per kilobase per million reads) values were used to measure the expression of each gene. The DESeq package was adopted to estimate variance-mean dependence in the count data from the Illumina sequencing assays and to test for differential expression based on a model using the negative binomial distribution in accordance with equation (1): $(1) v = s\mu + \alpha s^2\mu^2$, where μ is the expected normalized count value (estimated by the average normalized count value), s is the size factor for the sample under consideration, and α is the dispersion value for the unigene. Differentially-expressed genes were detected in the apical and basal samples based on average expression levels that differed at least 1.5-fold and P value < 0.05 when comparing apical and basal samples.

Plasmid Construction and Expression

cDNA encoding two α subunits of Nav1.7 variants (CbmNav1.7a and CbmNav1.7b) (GenBank Numbers:

KM373695.1 and KM373696.1) cloned from the developing cochlear sensory epithelia in our previous work [18] and wild-type Nav1.7 α from peripheral dorsal root ganglion (DRG) neurons (GenBank Number: NM-001290674.1) were synthesized and each cloned into the pIRES2 expression vector with an EGFP tag. To investigate the effects of different substitution/deletions of amino acid residues on channel properties which were induced by various posttranscriptional modification events, nine mutants (1–9) were generated and functionally compared. These related mutant plasmids were produced using sequential PCR (GenScript Biotech Corp., Nanjing, China). Mutant 1 was generated by replacing two codons in exon 5 (substituting 201V206D for 201L206N) of wtNav1.7; mutant 2 by deleting eleven codons in exon 11 (deletion of 11 amino acid residues) of mutant 1; mutant 3 by deleting exon 20 (deletion of 41 amino acid residues) of mutant 2; mutant 2 was used as the starting material to generate the 934R, 1037T, and 1643S variants (mutants 4–6); and CbmNav1.7a was used to generate the 934C, 1037I, and 1643F variants (mutants 7–9) (Table 1). HEK293T cells were used in all experiments (Shanghai Cell Bank of the Chinese Academy of Sciences, Shanghai, China). The cells were cultured in Dulbecco's modified Eagle's medium (Life Technologies, Grand Island, NY) supplemented with 10% heat-inactivated fetal bovine serum (Gibco, Grand Island, NY). Culture dishes were incubated at 37 °C in a humidified atmosphere containing 5% CO₂ and cultured for 2–3 days. One day before transfection, HEK293T cells were transferred into 24-well plates. At 90% confluence, the cells were transiently transfected using Lipofectamine 3000 (Invitrogen) at a ratio of 1 μ L reagent to 1 μ g total plasmid per well. Electrophysiological experiments were performed 1–2 days after transfection.

Whole-Cell Electrophysiological Recordings from HEK293T Cells

Whole-cell voltage-clamp recordings were made using an Axon Multiclamp 700B Microelectrode Amplifier (Molecular Devices) at room temperature (21 °C–25 °C). Patch pipettes were fabricated from glass capillary tubes using the PC-10 Puller (Narishige, Tokyo, Japan) with resistances of 2 M Ω –3 M Ω . Data acquisition and stimulation protocols were controlled by a Pentium III computer (Legend, Beijing, China) equipped with pCLAMP10.3 (Molecular Devices). Capacitance transients were cancelled and cells with a seal resistance < 1 G Ω were omitted. Series resistance (Rs) was compensated (80%–90%) to minimize voltage errors, and cells with an uncompensated Rs > 10 M Ω were omitted. Leak subtraction was performed using the P/N protocol. Data were

Table 1 Construction strategies of nine Nav1.7 mutants.

Mutant 1	Mutant 2	Mutant 3
wt Nav1.7 (L201V/N206D)	mutant 1 (647–657 deletion)	mutant 2 (1266–1306 deletion)
Mutant 4	Mutant 5	Mutant 6
mutant 2 (C934R)	mutant 2 (I1037T)	mutant 2 (F1643S)
Mutant 7	Mutant 8	Mutant 9
CbmNav1.7a (R934C)	CbmNav1.7a (T1037I)	CbmNav1.7a (S1634F)

Note: Mutants 1–3 were employed to analyze the substitution/deletion of amino acid residues respectively induced by three alternative splicing events. Mutants 4–6 were constructed to analyze the substitution of amino acid residues induced by three RNA editing events. Mutants 7–9 were generated for backward verification of the effects of three RNA editing events on channel properties.

sampled at 50 kHz and low-pass filtered at 10 kHz. The extracellular solution contained (in mmol/L): 140 NaCl, 3 KCl, 1 MgCl₂, 1.5 CaCl₂, 10 D-glucose, and 10 HEPES-NaOH (pH 7.4, 320 mOsmol/kg). The pipette solution contained (in mmol/L): 131 CsCl, 3 MgCl₂, 1 EGTA-CsOH, 5 Na₂ATP, 5 HEPES-CsOH, and 10 sodium phosphocreatine (pH 7.3, 292 mOsmol/kg).

Na⁺ currents were elicited by 100-ms depolarizing pulses to + 80 mV from a holding potential of – 100 mV. Mean conductance (G) was calculated from peak current-voltage relationships using equation (2) as follows: (2) $G = I/(V - V_r)$, where I is the peak current elicited by depolarization, V is the membrane potential, and V_r is the reversal potential. The voltage dependence for activation was fitted using the Boltzmann relationship as follows (equation 3): (3) $G/G_{\max} = 1/[1 + \exp(V - V_m)/k_m]$, where V_m is the voltage for half-maximum activation and k_m is the slope factor. Current decays were fitted using a double-exponential equation (4) as follows: (4) $I = A_{\text{fast}} \times \exp[-(t - K)/\tau_{\text{fast}}] + A_{\text{slow}} \times \exp[-(t - K)/\tau_{\text{slow}}] + I_{\text{SS}}$, where I is the current, A_{fast} and A_{slow} represent the percentages of channels inactivating with time constants τ_{fast} and τ_{slow} , t is the conditioning pulse duration, K is the time shift, and I_{SS} is the steady-state asymptote. The voltage-dependence of the steady-state inactivation and fast inactivation data was described using the two-state Boltzmann equation (5) as follows: $I/I_{\max} = 1/[1 + \exp(V - V_{1/2})/k]$, where V is the membrane potential of the conditioning step, $V_{1/2}$ is the membrane potential at which half-maximal inactivation is achieved, and k is the slope factor. Recovery data were fitted with a single-exponential equation (6) as follows: (6) $I/I_{\text{peak}} = 1 - A \times \exp(-t/\tau_{\text{rec}})$, where A is the relative proportion of current recovering with time constant τ_{rec} , and t is the recovery interval. Voltage-dependent deactivation kinetics was assessed by eliciting tail currents at a range of potentials after briefly activating the channels (0 mV, 0.5 ms). The averaged voltage-plot was compiled using time constants (τ_d) obtained from tail current recordings and determined by fitting each decay

component with a single-exponential equation. Ramp current generation was assayed using a slow depolarizing ramp stimulus (0.27 mV/ms, 600 ms) from – 120 mV to + 40 mV at a holding potential of – 120 mV. Inward ramp currents displayed are the result of dividing the individual traces by the peak transient Na⁺ current recorded during the I/V protocol, thus yielding the percentage of peak current for each recording.

Statistical Analysis

Data are presented as the mean \pm SEM and were analyzed using Origin 8.5 (OriginLab, Northampton, MA) and GraphPad Prism 7 (GraphPad Software, La Jolla, CA). The number of cells recorded in the electrophysiological experiments is represented by n . The paired or unpaired Student's two-tailed t -test was used for two-group comparison and one-way analysis of variance (ANOVA) followed by the *post-hoc* Bonferroni test was used for multiple comparisons. $P < 0.05$ was considered statistically significant.

Results

Sodium Currents Shape the Action Potentials of Immature IHCs

Current-clamp recordings demonstrated that the immature IHCs generated spontaneous and evoked action potentials, which were reversibly abolished by the absence of extracellular Ca²⁺ (Fig. S1). No spontaneous action potentials were detectable in developing OHCs, but single action potentials were elicited by depolarizing current injection (Fig. S2). Voltage-clamp recordings showed that typical voltage-dependent Na⁺ currents were elicited in both IHCs and OHCs following 200-ms conditioning steps to a range of potentials from – 100 mV to + 80 mV (Fig. 1A–E). To evaluate whether Na⁺ currents contribute to the action potentials, IHCs were further studied before

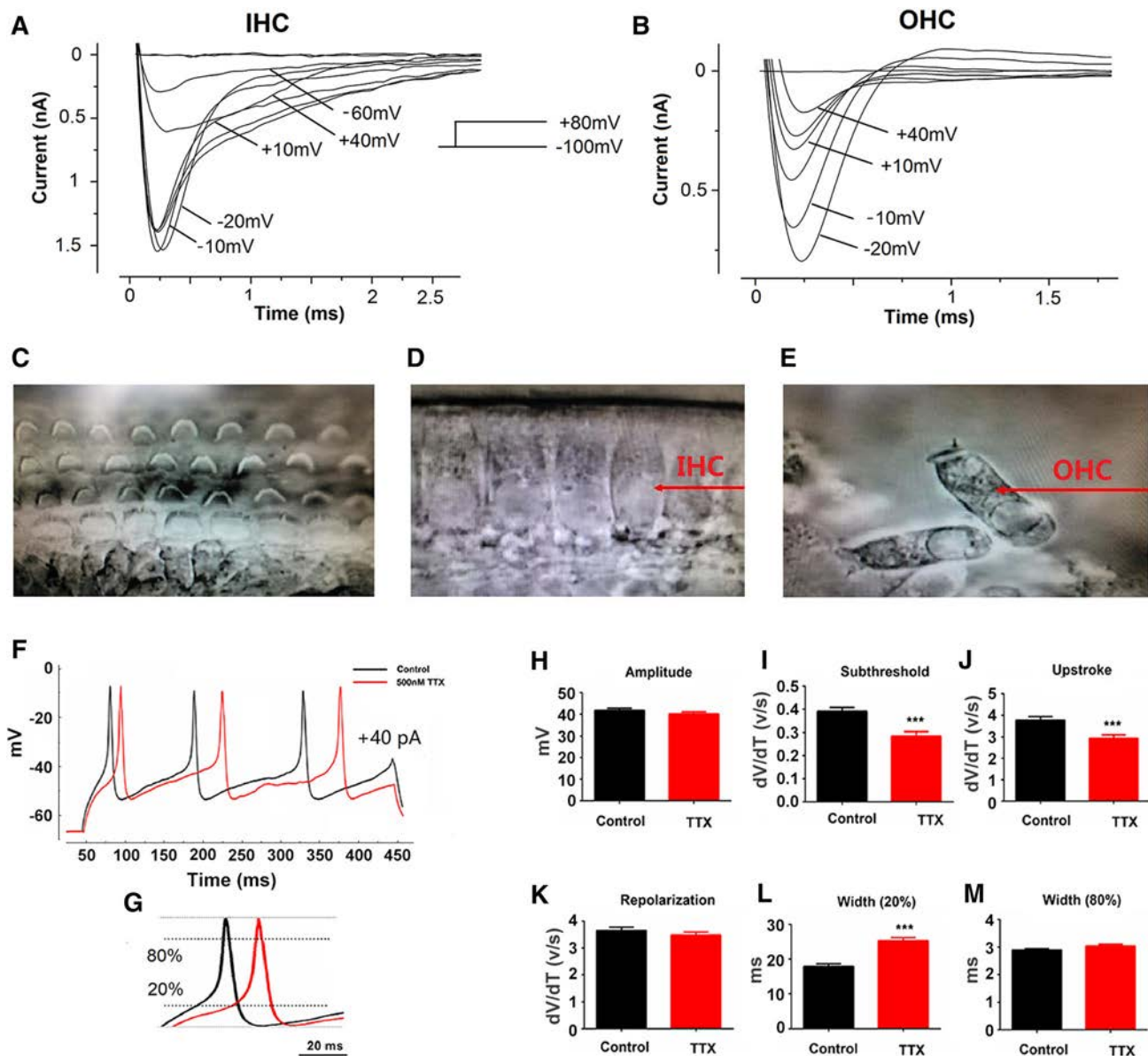


Fig. 1 Quantitative effects of TTX on action potentials in immature hair cells. **A** Na^+ current recorded from a P6 IHC (apical) by applying depolarizing voltage steps from a holding potential of -100 mV (recording conditions: $V_m = 60$ mV, $C_m = 7.83$ pF, temperature 37°C). **B** Na^+ current recorded from a P6 OHC (basal). For clarity, only some of the traces are shown and some of the potentials are shown next to them (recording conditions: $V_m = 62$ mV, $C_m = 8.79$ pF, temperature 37°C). **C–E** Three rows of OHCs with “V”-like stereocilia and one row of IHCs ($40\times$ water-immersion lens). **F** Action potentials evoked by $+40$ pA injection in a P5 IHC before (black solid line) and during superfusion (red solid line) with

500 nmol/L TTX (recording conditions: $V_m = 67$ mV, $C_m = 11.8$ pF, temperature 37°C). **G** Measurement of the width of the action potentials at the 20% and 80% labels (black dotted lines) between peak and maximum repolarization levels (dotted lines). **H–K** Amplitude of single action potentials before and during the TTX application ($n = 10$). **I–K** Rate of subthreshold depolarization (I), upstroke (J), and repolarization (K) of single action potentials before and during TTX application ($n = 10$). **L, M** Width of action potentials measured at the two levels shown in **G** ($n = 10$). *** $P < 0.001$, control versus TTX-superfusion group, paired Student’s *t*-test. Data are presented as the mean \pm SEM.

and after extracellular application of TTX. The extracellular application of 500 nmol/L TTX did not prevent the induced action potentials in immature IHCs, but affected their time course (Fig. 1F, G). In the presence of TTX, the amplitude (Fig. 1H) and repolarization rate (dV/dt) of action potentials were unchanged (Fig. 1K), but the

subthreshold depolarization rate was significantly slower ($P < 0.001$, $n = 10$) (Fig. 1I). The lack of Na^+ currents was also found to decrease the maximum rate of rise of the action potential upstroke ($P < 0.001$, $n = 10$) (Fig. 1J). In addition, we measured the width of the action potential at levels below threshold (20% of spike height) and the action

potential proper (80% of spike height). At the subthreshold level, the width of action potentials was greater in the presence of TTX ($P < 0.001$, $n = 10$) (Fig. 1L). However, the width of the actual spike did not change significantly (Fig. 1M). These results are consistent with previous studies showing that the Na^+ currents in premature IHCs play a role in shaping the action potentials mainly by reducing the time necessary for the membrane potential to reach threshold [8, 17].

Expression and Distribution of VGSC Subtypes in Immature Hair Cells

Immunolabeling experiments showed that IHCs and OHCs in the organ of Corti were specifically labeled by antibodies directed against the nine VGSC subtypes (Fig. 2A–I). Further, RT-PCR experiments revealed that all subtypes (Nav1.1 α –1.9 α) were present in developing cochlear sensory epithelia (Fig. 2J). Single-cell qPCR revealed that six of the subtypes (Nav1.2 α , 1.3 α , 1.4 α , 1.5 α , 1.7 α , and 1.9 α) were found in apical and basal IHCs, while the other three (Nav1.1 α , 1.6 α , and 1.8 α) were expressed at extremely low levels or undetectable (Fig. 2K). On the other hand, six subtypes (Nav1.2 α , 1.3 α , 1.5 α , 1.6 α , 1.7 α , and 1.9 α) were detected in apical and basal OHCs, while the other three (Nav1.1 α , 1.4 α , and 1.8 α) were only found in either apical or basal OHCs (Fig. 2L). Compared to the other eight subtypes, Nav1.7 α exhibited the highest expression in immature IHCs and OHCs from apical and basal sensory epithelia, suggesting that it might be the dominant subtype that contributed to the Na^+ currents in developing hair cells (Fig. 2K, C). Furthermore, transcriptome analyses revealed that the α subunits of the nine VGSC subtypes and four β subunits (β 1– β 4) occurred in the apical and basal sensory epithelia. Among them, Nav1.5 α was expressed at a higher level in apical sensory epithelia, whereas Nav1.1 α and β 4 were expressed at higher levels in basal sensory epithelia (differential screening criteria: fold of change ≥ 1.5 , $P < 0.05$) (Fig. 2M, N).

Functional Characterization of Nav1.7 Variants in Cochlear Sensory Epithelia

When compared to the typical wtNav1.7 variant from peripheral DRG neurons, CbmNav1.7a and CbmNav1.7b cloned from developing cochlear sensory epithelia have been characterized by distinct molecular structures produced by three alternative splicing and three RNA editing events [18] (Fig. 3A, B). In the present study, we determined that Na^+ currents were not elicited from CbmNav1.7a and 1.7b upon exogenous expression in HEK293T cells (Fig. 3C–E). To identify which amino-

acid replacement/deletion silenced these two Nav1.7 variants, 9 related mutants were constructed and functionally expressed in HEK293T cells (the mutation strategies are listed in Table 1). We found that mutants 1 and 2 generated Na^+ currents, whereas mutant 3 did not, indicating that the deletion of this segment (segment 4 and part of segment 3 in domain III attributed to alternative deletion of exon 20) might be responsible for the lack of currents associated with CbmNav1.7b (Fig. 3F–H). Na^+ currents were recorded from mutants 5 and 6, but not mutant 4 (Fig. 3I–K). In contrast, Na^+ currents were recorded from mutant 7 but not mutants 8 and 9 (Fig. 3L–N). This suggested that an amino-acid substitution (C934R) located in the extracellular linker between segments 5 and 6 of domain II might be the key factor leading to loss of currents in CbmNav1.7a and 1.7b. Furthermore, western blot and immunolabeling experiments showed that Nav1.7 protein was present in the membrane and cytosol of HEK293T cells transfected with mutant 4, suggesting that the residue replacement C934R results in complete loss-of-function of Nav1.7 (Fig. S3).

Then, we speculated that the Na^+ currents of hair cells might be attributable to functional CbmNav1.7a_(C934) (mutant 7) under physiological conditions. To test this hypothesis, we compared the biophysical properties of wtNav1.7 and CbmNav1.7a_(C934). The expression levels of the two variants were not statistically different with a current density of 384.03 ± 44.63 pA/pF for wtNav1.7 ($n = 20$) and 320.54 ± 58.2 pA/pF for CbmNav1.7a_(C934) ($n = 15$), and their peak currents were observed at -10 mV (Fig. 4A). There was no significant difference between wtNav1.7 and CbmNav1.7a_(C934) in terms of the $G(V)$ relationship and the recovery process (Fig. 4B, H and Table 2). The fast inactivation time constants in the range of depolarization (-20 mV to $+20$ mV) of CbmNav1.7a_(C934) were significantly larger ($P < 0.001$) (Fig. 4C). The midpoint of activation ($V_{1/2}$) for steady-state inactivation of CbmNav1.7a_(C934) was significantly shifted leftward ($P < 0.001$), while the slope factor (k_m) remained unchanged (Fig. 4D, Table 2). The $V_{1/2}$ of fast inactivation for CbmNav1.7a_(C934) was shifted in a hyperpolarizing direction ($P < 0.05$), whereas the k_m remained unchanged (Fig. 4E, Table 2). The time constants for deactivation of CbmNav1.7a_(C934) during potentials ranging from -100 mV to $+40$ mV were smaller ($P < 0.001$) (Fig. 4F). In addition, the peak amplitude of the ramp current of CbmNav1.7a_(C934) was significantly larger than that of wtNav1.7 ($P < 0.05$) (Fig. 4G). The recovery time constant and I_{\max} of CbmNav1.7a_(C934) were similar to those of wtNav1.7 (Fig. 4H, Table 2). These data showed that CbmNav1.7a_(C934) was associated with a slower fast-inactivation process from the open-state and a quicker deactivation process as well as a larger ramp current amplitude.

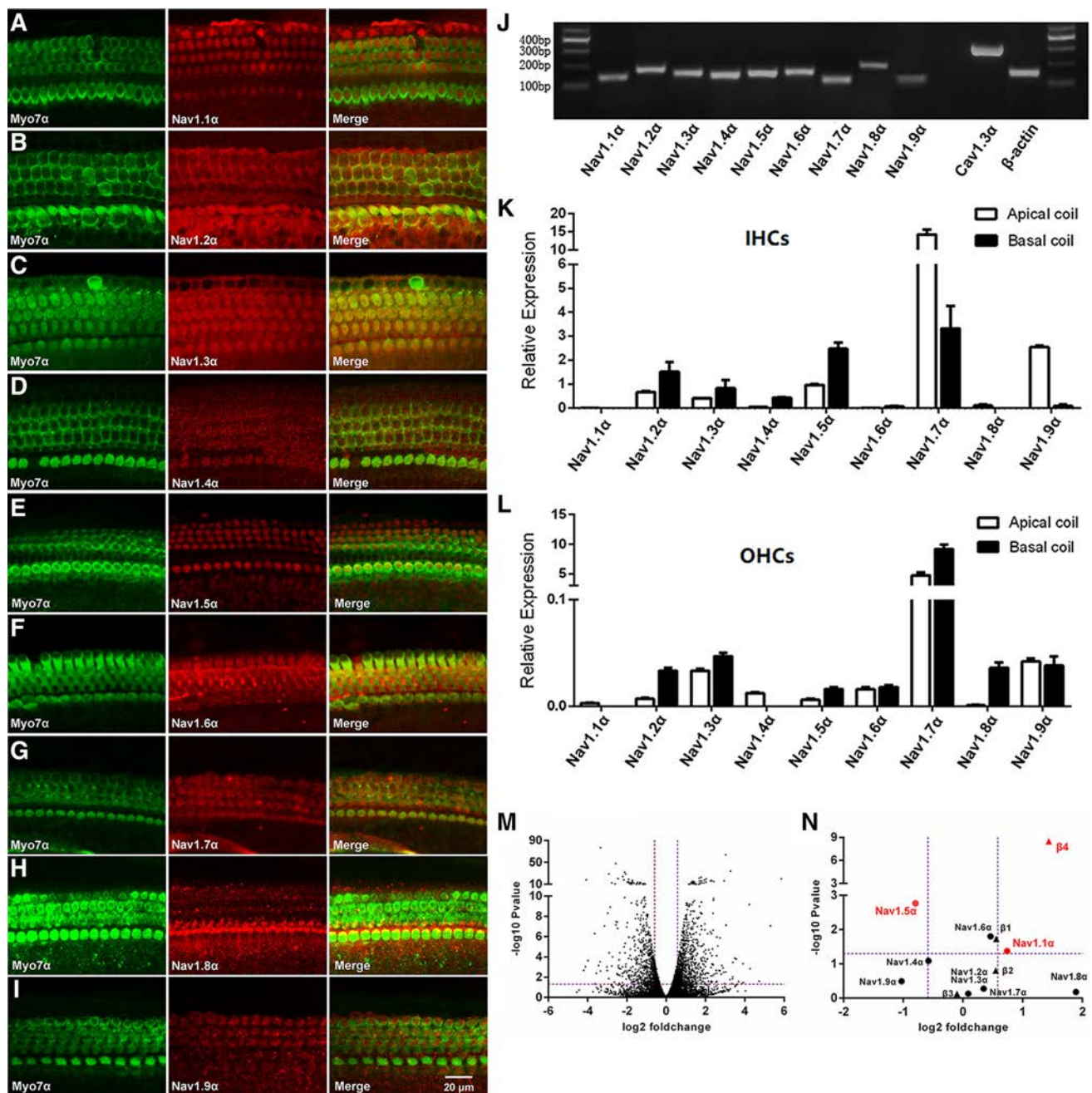


Fig. 2 Distribution and expression of VGSC subtypes in immature hair cells. **A–I** Red, VGSC subtypes (anti-Nav1.1 α –1.9 α); green, hair cell specific-marker (anti-myosin 7 α); yellow, co-labeling. **J** mRNA segments of the 9 VGSC α subunits from sensory epithelia. **K, L** mRNA expression levels of Nav1.1 α –1.9 α in single IHCs and OHCs in apical and basal sensory epithelia from P6 mice. **M** Volcano plots

of the expression levels of genes in apical and basal sensory epithelia (y-axis, \log_{10} P -value of difference; x-axis, \log_2 fold-changes; fold-change ≥ 1.5 and P -value < 0.05 were set as threshold to identify differentially-expressed genes). **N** P values vs fold-changes for the 9 α -subunits and 4 β -subunits of VGSCs; red, differentially-expressed genes (Nav1.1 α , 1.5 α , and β 4).

Alternative Splicing Events Modified the Characteristics of CbmNav1.7a_(C934)

To determine whether alternative splicing events contribute to the function of CbmNav1.7a_(C934), the biophysical properties of wtNav1.7, mutant 1, and mutant 2 were

compared. Mutant 1 did not significantly differ from wtNav1.7 in terms of I – V curve (348.25 ± 52.5 pA/pF for mutant 1 at -10 mV, $n = 10$), $G(V)$ relationship, $V_{1/2}$ and k_m of steady-state inactivation and fast inactivation, and recovery time constants (Fig. 5A, B, D, H, Table 3). Analyses of current decay showed that the τ_{fast} and τ_{slow} of

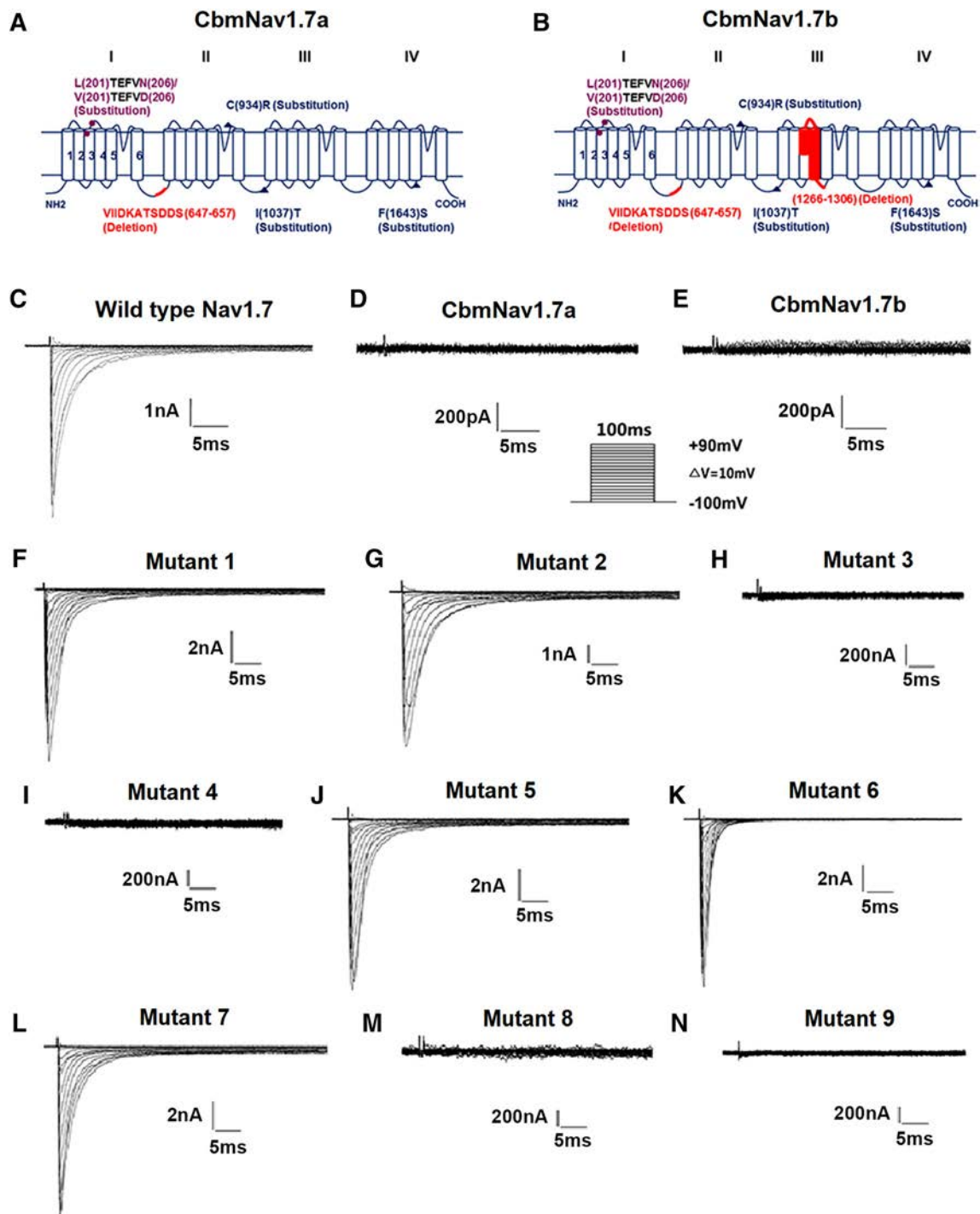


Fig. 3 Electrophysiological recordings from CbmNav1.7 variants and related mutants in HEK293T cells. **A, B** Locations of the substitution and deletion of amino-acids in CbmNav1.7a and 1.7b compared with wtNav1.7 (purple, segment replacement generated by alternative splicing of exon 5; red, segment deletion generated by alternative splicing of exon 11 or exon 20; blue, single amino-acid

residue replacement produced by three RNA editing events in exons 15, 16, and 26). **C–E** Na⁺ current recordings from wtNav1.7, CbmNav1.7a, and CbmNav1.7b exogenously expressed in HEK293T cells. **F–N** Na⁺ current recordings of nine Nav1.7 mutants exogenously expressed in HEK293T cells.

mutant 1 were both smaller than those of wtNav1.7 ($P < 0.001$ and $P < 0.01$, respectively) at high depolarizing voltages (0 mV to 20 mV), whereas τ_{fast} was markedly

larger ($P < 0.05$) at low depolarizing voltages (−20 mV to −10 mV) (Fig. 5C). Analyses of deactivation kinetics showed that the time constant of deactivation for mutant 1

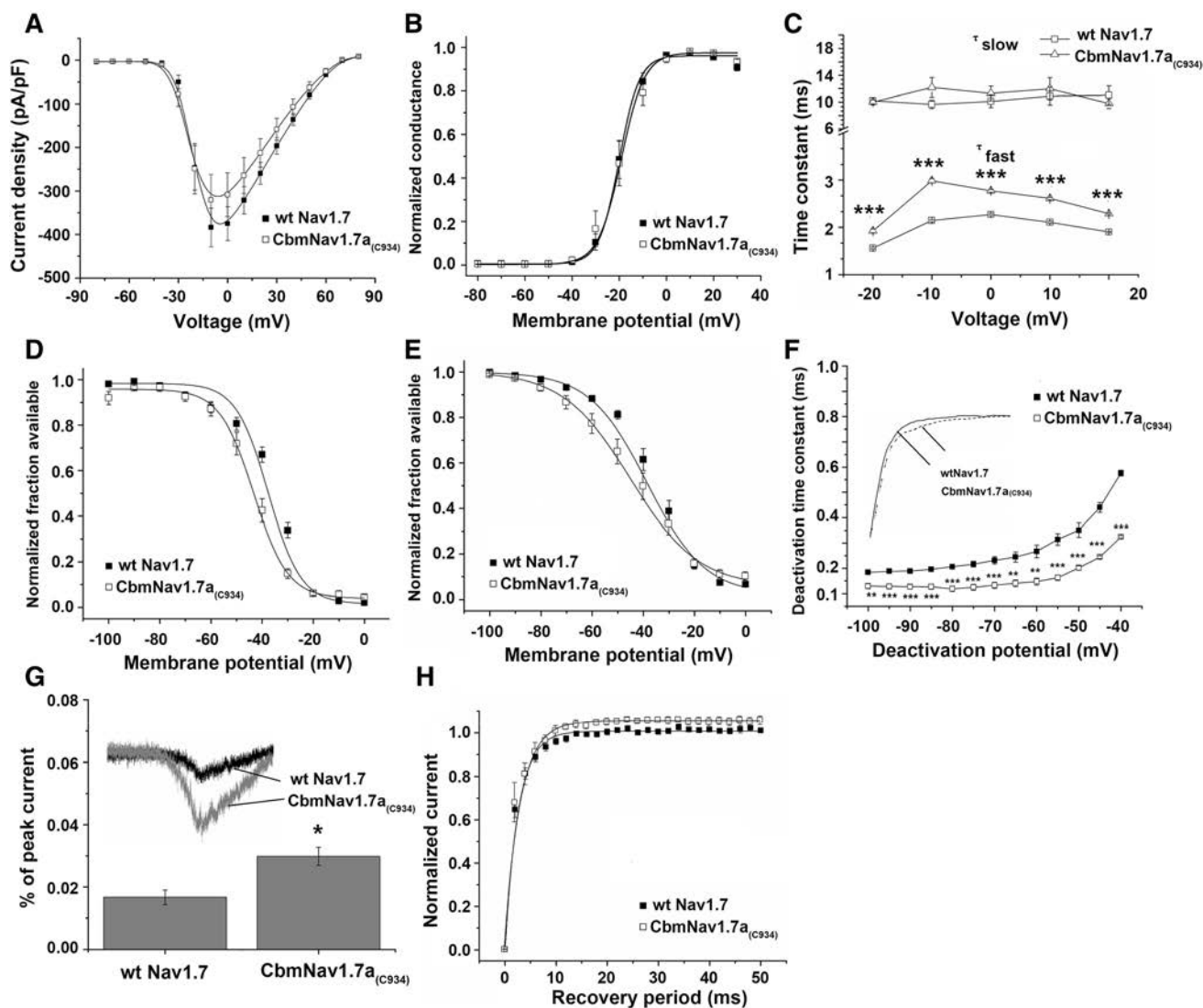


Fig. 4 Biophysical properties of CbmNav1.7a_(C934). **A** Peak current-voltage relationships for wtNav1.7 (black squares) and CbmNav1.7a_(C934) (white squares). **B** Voltage-dependence of activation of wtNav1.7 and CbmNav1.7a_(C934) fitted with a Boltzmann function. **C** Kinetics of inactivation of wtNav1.7 (white squares) and CbmNav1.7a_(C934) (white triangles) fitted with a double-exponential equation, and the time constants representing the slow (τ_{slow}) and fast (τ_{fast}) components. **D** Voltage-dependence of steady-state inactivation of wtNav1.7 (black squares) and CbmNav1.7a_(C934) (white squares) fitted with a Boltzmann function. **E** Voltage-dependence of fast inactivation of wtNav1.7 and CbmNav1.7a_(C934) fitted with a

Boltzmann function. **F** Time constant for tail current deactivation at repolarization potentials ranging from -100 to -40 mV for wtNav1.7 and CbmNav1.7a_(C934) obtained with single-exponential fits. **G** Example of ramp current traces for wtNav1.7 (black line) and CbmNav1.7a_(C934) (grey line); peak ramp currents were calculated. **H** Recovery of channel availability from fast inactivation of wtNav1.7 and CbmNav1.7a_(C934); the continuous curve is a single-exponential function fitted to the data with a time constant. * $P < 0.05$, ** $P < 0.01$, *** $P < 0.001$, wtNav1.7 vs CbmNav1.7a_(C934), unpaired Student's *t*-test. Data are presented as the mean \pm SEM.

was significantly larger ($P < 0.01$) than wtNav1.7 across a range of voltages from -100 mV to -80 mV (Fig. 5F). In addition, mutant 1 also had a larger peak value of ramp current than wtNav1.7 ($P < 0.05$) (Fig. 5G). These data signified that the alternative splicing of exon 5, leading to amino-acid replacements L201V/N206D, accelerates the fast/slow inactivation at high depolarizing voltages, retards the fast inactivation at low depolarizing voltages, slows the deactivation, and increases the ramp current.

Mutant 2 did not differ significantly from mutant 1 in terms of *I-V* curve (373.82 ± 53.6 pA/pF for mutant 2 at 0 mV, $n = 14$), *G(V)* relationship, $V_{1/2}$ and k_m of steady-state inactivation and fast inactivation, recovery time constant, and ramp current (Fig. 5A, B, D–H, Table 3). The τ_{fast} of mutant 2 was significantly larger at higher depolarizing potentials (0 mV to 20 mV) ($P < 0.001$) (Fig. 5C) and its deactivation time constant was lower for potentials ranging from -100 mV to -40 mV

Table 2 Biophysical properties of CbmNav1.7a_(C934) variant.

Mutant form	Voltage-dependent activation			Steady-state inactivation		
	$V_{1/2}$ (mV)	k_m (mV)	n	$V_{1/2}$ (mV)	k_m (mV)	n
wtNav1.7	-20.00 ± 1.64	4.23 ± 0.55	19	-37.53 ± 1.61	6.31 ± 0.82	9
CbmNav1.7a _(C934)	-19.13 ± 2.25	4.89 ± 0.90	14	$-43.26 \pm 0.85^{***}$	6.63 ± 0.52	8
Mutant form	Fast inactivation			Recovery from inactivation		
	$V_{1/2}$ (mV)	Time (ms)	n	I_{max}	Time (ms)	n
wtNav1.7	-38.45 ± 2.27	11.24 ± 1.11	9	1.00 ± 0.004	2.61 ± 0.14	8
CbmNav1.7a _(C934)	$-44.83 \pm 1.51^*$	13.22 ± 1.05	14	1.05 ± 0.002	3.02 ± 0.11	6

Note: Values are mean \pm SEM

*Significant difference ($*P < 0.05$, $***P < 0.001$) between wtNav1.7 and CbmNav1.7a_(C934) using unpaired Student's two-tailed *t*-test.

($P < 0.01$) (Fig. 5F). These data indicated that the alternative splicing of exon 11, leading to a deletion of amino-acid fragment 647–657, slows the fast inactivation at high potentials and accelerates the deactivation.

The τ_{fast} of mutant 2 across potentials from -20 mV to 20 mV was significantly larger than that of wtNav1.7 ($P < 0.05$), while the τ_{slow} at 10 mV was smaller ($P < 0.01$) (Fig. 5C). The deactivation time constant was markedly smaller than that of wtNav1.7 (-40 mV to -100 mV) ($P < 0.05$) (Fig. 5F), and the peak ramp current of mutant 2 was also larger than that of wtNav1.7 ($P < 0.05$) (Fig. 5G).

RNA Editing Events Account for the Functional Characteristics of CbmNav1.7a_(C934)

To investigate whether RNA editing events contribute to the function of CbmNav1.7a_(C934), we broadly compared its biophysical properties with those of mutants 2, 5, and 6. We found no significant differences between mutants 2 and 5 in terms of *I-V* curve (376.28 ± 84.17 pA/pF for mutant 5 at -10 mV, $n = 7$), *G(V)* relationship, $V_{1/2}$ and k_m of steady-state inactivation and fast inactivation, ramp current, and recovery (Fig. 6A, B, D, E, G, H, Table 4). Compared to mutant 2, the τ_{fast} of mutant 5 was larger for potentials from -20 mV to 20 mV ($P < 0.01$), whereas the τ_{slow} showed selective increases at some depolarizing potentials ($P < 0.01$) (Fig. 6C). The deactivation time constant of mutant 5 was higher at -40 mV and -45 mV ($P < 0.05$) (Fig. 6F). These results show that the U-to-C RNA editing at exon 16, leading to the amino-acid substitution I1037T, delays fast/slow inactivation, and deactivation.

The current density (310.54 ± 32.93 pA/pF for mutant 6 at -10 mV, $n = 11$), *G(V)* relationship, recovery, and ramp current for mutants 2 and 6 did not statistically differ

(Fig. 6A, B, G, H, Table 4). The τ_{fast} of mutant 6 was significant smaller for potentials from -20 mV to 20 mV ($P < 0.05$) (Fig. 6C). The steady-state and fast inactivation curves of mutant 6 were both shifted in a hyperpolarizing direction, and their $V_{1/2}$ values were each decreased ($P < 0.001$) (Fig. 6D, E, Table 4). In addition, the deactivation time constant was markedly larger than that of mutant 2 for potentials from -100 mV to -40 mV ($P < 0.001$) (Fig. 6F). These data indicate that the U-to-C RNA editing at exon 26, leading to the amino-acid substitution F1643S, accelerates fast inactivation, delays the transition of the channel from an inactive to an open state, and delays deactivation.

The τ_{fast} of CbmNav1.7a_(C934) was larger for potentials from -10 mV to 20 mV than mutant 2 ($P < 0.001$) (Fig. 6C). The steady-state and fast inactivation curves for CbmNav1.7a_(C934) were both shifted in a hyperpolarizing direction, and their $V_{1/2}$ values were each decreased ($P < 0.001$ and $P < 0.05$) (Fig. 6D, E and Table 4). These data suggested that the two RNA editing events cooperatively slow the fast inactivation and delay the transition from an inactive to an open state.

Discussion

Physiological Role of Sodium Currents in Pre-hearing Hair Cells

Spontaneous electrical activity is a common feature of sensory systems during early development, and has been implicated in promoting neural survival and maturation, as well as the growth and refinement of their projections to yield circuits [20–23]. In the auditory system, spontaneous electrical activity generated by cochlear hair cells before the onset of hearing has also been implicated in shaping the

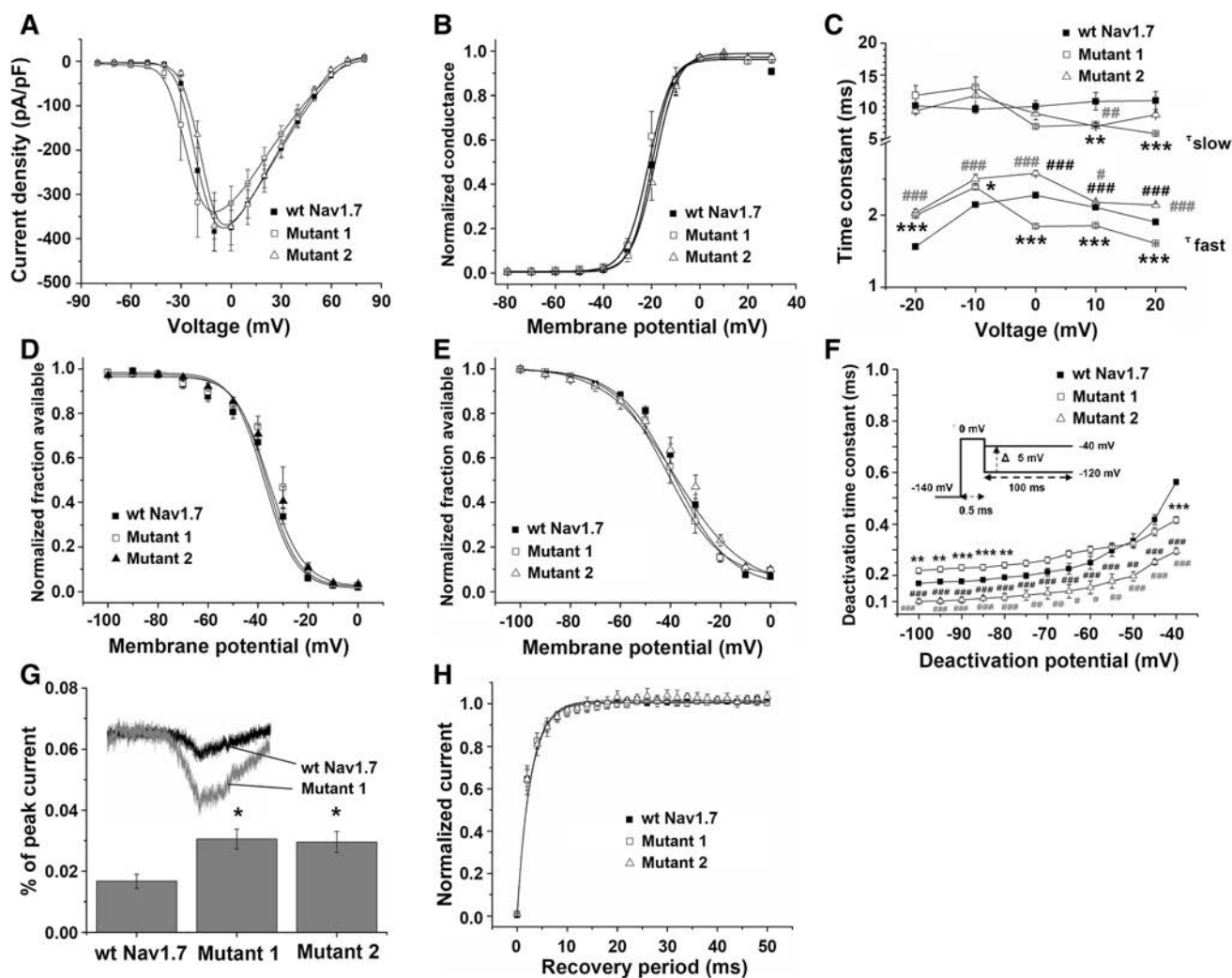


Fig. 5 Biophysical properties of alternative splicing variants of CbmNav1.7a. **A** Peak current-voltage relationships of wtNav1.7, mutant 1, and mutant 2. **B** Voltage-dependence of activation of wtNav1.7, mutant 1, and mutant 2 fitted with a Boltzmann function. **C** Kinetics of inactivation of wtNav1.7, mutant 1 and mutant 2 fitted with a double-exponential equation, and the time constants representing the slow (τ_{slow}) and fast (τ_{fast}) components. Symbols: wtNav1.7 (black squares), mutant 1 (white squares), mutant 2 (white triangles). **D** Voltage-dependence of steady-state inactivation of the 3 variants fitted with a Boltzmann function. **E** Voltage-dependence of fast inactivation of the 3 variants fitted with a Boltzmann function. **F** Time constant for tail current deactivation at repolarization potentials ranging from -100 to -40 mV for the 3 variants,

obtained from single-exponential fits. *Difference between wtNav1.7 and mutant 1; #(dark), difference between mutants 1 and 2; #(gray), difference between wtNav1.7 and mutant 2. **G** Example of ramp current traces for wtNav1.7 (black) and mutant 1 (grey); peak currents were calculated, *significant difference of mutant 1 and mutant 2 each compared with wtNav1.7. **H** Recovery of channel availability from fast inactivation of the 3 variants; continuous curve is a single-exponential function fitted to the data with a time constant. * $P < 0.05$, ** $P < 0.01$, *** $P < 0.001$, one-way ANOVA followed by a Bonferroni *post-hoc* test for multiple comparison of the wtNav1.7, mutant1 and mutant 2. Data are presented as the mean \pm SEM.

organization of nascent circuits [24, 25]. The spontaneous action potentials in premature IHCs are mainly due to the interplay between an inward Ca^{2+} current and a delayed rectifier K^{+} current and are also finely modulated by other transiently-occurring conductance events, such as small conductance Ca^{2+} -sensitive K^{+} currents [5]. In this study, we found that the spontaneous action potentials in premature IHCs were reversibly abolished by Ca^{2+} -free solution, clearly showing that spontaneous activity is Ca^{2+} -

dependent, consistent with a previous report [8]. The typical inward Na^{+} current was recorded in IHCs from P6 mice, and the biophysical characteristics were similar to those in premature rat IHCs [17]. However, although it is the main contributor to the rising phase of the action potential in most neurons [12], the Na^{+} current in immature IHCs is not necessary for the generation of action potentials, but rather regulates their frequency [8]. In the present study, we re-assessed the potential

Table 3 Biophysical properties of mutant 1 and mutant 2.

Mutant form	Voltage-dependent activation			Steady-state inactivation		
	$V_{1/2}$ (mV)	k_m (mV)	n	$V_{1/2}$ (mV)	k_m (mV)	n
wtNav1.7	-20.00 ± 1.64	4.23 ± 0.55	19	-37.53 ± 1.61	6.31 ± 0.82	9
Mutant 1	-21.28 ± 1.29	4.76 ± 0.51	11	-37.37 ± 1.78	6.65 ± 0.88	8
Mutant 2	-18.65 ± 1.22	4.69 ± 0.51	14	-35.84 ± 1.16	6.86 ± 0.62	10
Mutant form	Fast inactivation			Recovery from inactivation		
	$V_{1/2}$ (mV)	k_m (mV)	n	I_{max}	Time (ms)	n
wtNav1.7	-38.45 ± 2.27	11.24 ± 1.11	9	1.00 ± 0.004	2.61 ± 0.14	8
Mutant 1	-40.95 ± 1.61	10.83 ± 0.88	6	0.99 ± 0.002	2.70 ± 0.14	5
Mutant 2	-38.02 ± 2.81	13.76 ± 1.74	8	1.00 ± 0.004	2.71 ± 0.16	8

Note: Values are mean \pm SEM. No significant difference between wtNav1.7, mutant 1 and mutant 2 using one-way ANOVA followed by a Bonferroni *post-hoc* test.

physiological role of Na^+ current in immature IHCs and found that it shaped their action potentials by decreasing the time necessary for the membrane potential to reach a threshold. These data strongly suggest that the Na^+ current can make the generation of spontaneous action potentials in immature IHCs more robust and regulate their frequency.

On the other hand, our current recordings showed that premature OHCs did not fire spontaneous action potentials, although a single action potential was triggered by depolarizing current injection from the resting potential, in accord with a previous study [26]. Since IHCs and OHCs exhibit otherwise qualitatively similar basolateral membrane currents, the lack of repetitive action potential activity in OHCs is somewhat surprising. This might be due to the absence of the SK2 current, which plays a crucial role in sustaining repetitive action potential activity in immature IHCs, and/or different concentrations of Ca^{2+} -buffering proteins between the two cell types [27, 28]. In addition, Cav1.3 gene knockout induces the degeneration of OHCs as well as IHCs, pointing to a possible role of Ca^{2+} action potentials in the normal maturation of both immature hair cell types [29]. The typical Na^+ current was initially recorded in premature OHCs from isolated acute cochlear sensory epithelia in the present study, which verified the existence of a Na^+ current in isolated premature OHCs [10]. The Na^+ current in early developmental stage strongly suggests a noteworthy role in OHC maturation.

Composition of VGSC Subunits in Pre-hearing Hair Cells

The Na^+ currents in premature cochlear IHCs and OHCs are considered to be TTX-sensitive [8, 10]. Nav1.1 α and Nav1.6 α have been determined to be located on the

membrane of IHCs and OHCs, whereas Nav1.2 α and Nav1.7 α are located on the nerve fibers below IHCs and OHCs [17]. In the current study, we found six VGSC subtypes (Nav1.1 α , 1.2 α , 1.3 α , 1.4 α , 1.6 α , and 1.7 α) mediating TTX-sensitive currents on the membrane of IHCs and OHCs, which strongly hinted that multiple subtypes might synergistically contribute to the Na^+ currents in developing hair cells. Furthermore, three subtypes (Nav1.5 α , 1.8 α , and 1.9 α) that mediate TTX-insensitive currents were also detected in premature IHCs and OHCs. These results are consistent with previous findings identifying the full-length mRNA encoding nine VGSC subtypes in developing cochlear sensory epithelia [18]. However, it seems that the three subtypes with extremely low abundance (Nav1.5 α , 1.8 α , and 1.9 α) cannot functionally mediate the detectable TTX-insensitive currents in immature hair cells [8, 17]. Furthermore, the biophysical properties of Na^+ currents in IHCs and OHCs are similar, but their sensitivity to TTX differs (1 mmol/L TTX fully blocks the currents in IHCs, while 10 mmol/L is required for OHCs) [10, 17]. This discrepancy could be attributed to the combinational expression patterns and the expression levels of VGSC subtypes in the two types of hair cell.

Among the nine known subtypes of VGSC, the Nav1.7 subtype has been suggested to be the main carrier of Na^+ currents in premature IHCs, because of the similarity in its biophysical and pharmacological properties [8]. Nav1.7 is preferentially expressed in peripheral neurons and produces a TTX-sensitive Na^+ current with hyperpolarized steady-state activation/inactivation, and fast kinetics [30]. The interesting thing is that the biophysical properties, channel kinetic characteristics, and the pharmacological sensitivity to TTX (K_D 4.8 ± 0.6 nmol/L) of Na^+ current in immature IHCs were similar to that carried by Nav1.7 (K_D of TTX

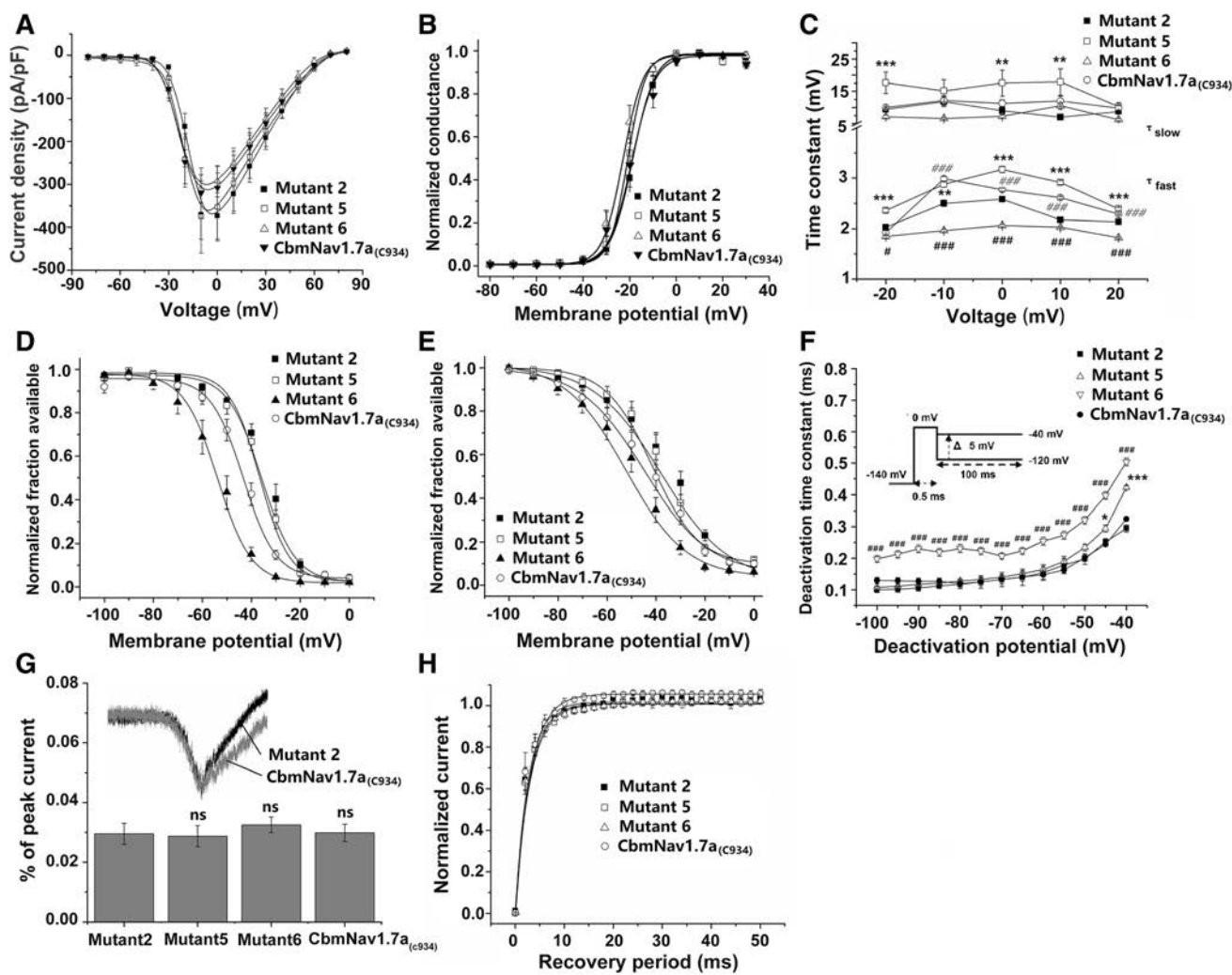


Fig. 6 Biophysical properties of RNA editing variants of CbmNav1.7a. **A** Peak current-voltage relationships of mutants 2, 5, 6, and 7 (CbmNav1.7a_(C934)). **B** Voltage-dependence of activation of the variants fitted with a Boltzmann function. **C** Kinetics of inactivation of the variants with a double-exponential equation, and the time constants representing the slow (τ_{slow}) and fast (τ_{fast}) components. *difference between mutants 2 and 5; # (dark), difference between mutants 2 and 6; # (gray), difference between mutant 2 and CbmNav1.7a_(C934). **D** Voltage-dependence of steady-state inactivation of the variants fitted with a Boltzmann function. **E** Voltage-dependence of fast inactivation of the variants fitted with a Boltzmann

function. **F** Time constants for tail current deactivation at repolarization potentials ranging from -100 to -40 mV for the variants from single-exponential fits. **G** Example of ramp current traces for mutant 2 (black) and CbmNav1.7a_(C934) (grey); the peak ramp currents were calculated. **H** Recovery of channel availability from fast inactivation of the variants; the continuous curve is a single-exponential function fitted to the data with a time constant. * $P < 0.05$, ** $P < 0.01$, *** $P < 0.001$, one-way ANOVA followed by a Bonferroni *post-hoc* test for multiple comparisons of the variants. Data are presented as the mean \pm SEM.

4.3 ± 0.92 nmol/L) [8, 17]. In the present study, we showed that Nav1.7 protein was located on the membrane of hair cells and was also the predominant Na⁺ channel transcript in single hair cells, with low abundance of other Na⁺ channel transcripts. In our previous work, Nav1.6 α mRNA was shown to have higher expression levels than the other eight subtypes in developing sensory epithelia [18]; however, the single-cell qPCR data here showed that the mRNA expression level of Nav1.6 α was markedly lower than that of Nav1.7 α in single hair cells. These inconsistent results may be due to the different

experimental material used. The cochlear sensory epithelia used in the previous study consisted of many types of cells (hair cells, supporting Deiters' cells, Hensen cells, pillar, inner phalangeal, and border cells), and Nav1.6 α might have been expressed not only in hair cells but also in other subtypes in the immature cochlea. These findings led us to hypothesize that Nav1.7 is the main contributor to the Na⁺ current in immature hair cells. In addition, Nav1.7 generates currents with slow closed-state inactivation that permits the production of ramp currents in response to small, slow depolarization near the resting membrane

Table 4 Biophysical properties of mutant 5 and mutant 6.

Mutant form	Voltage-dependent activation			Steady-state inactivation		
	$V_{1/2}$ (mV)	k_m (mV)	n	$V_{1/2}$ (mV)	k_m (mV)	n
Mutant 2	-18.65 ± 1.22	4.69 ± 0.51	14	-35.84 ± 1.16	6.86 ± 0.62	10
Mutant 5	-20.90 ± 1.55	3.77 ± 0.77	8	-36.05 ± 1.21	5.86 ± 0.64	6
Mutant 6	-21.54 ± 0.67	4.60 ± 0.25	12	$-54.99 \pm 1.01^{***}$	7.08 ± 0.46	9
CbmNav1.7a _(C934)	-19.13 ± 2.25	4.89 ± 0.90	14	$-43.26 \pm 0.85^{***}$	6.63 ± 0.52	8
Mutant form	Fast inactivation			Recovery from inactivation		
	$V_{1/2}$ (mV)	k_m (mV)	n	I_{max}	Time (ms)	n
Mutant 2	-38.02 ± 2.81	13.76 ± 1.74	8	1.00 ± 0.004	2.71 ± 0.16	8
Mutant 5	-41.63 ± 1.65	9.50 ± 0.89	8	1.01 ± 0.003	3.05 ± 0.13	4
Mutant 6	$-52.26 \pm 1.78^{***}$	12.41 ± 1.25	9	1.01 ± 0.003	2.87 ± 0.10	6
CbmNav1.7a _(C934)	$-44.83 \pm 1.51^*$	13.22 ± 1.05	14	1.05 ± 0.002	3.02 ± 0.11	6

Note: Values are mean \pm SEM.

Significant difference ($P < 0.05$, *** $P < 0.001$) of mutant 2 vs mutant 6, and mutant2 *versus* CbmNav1.7a_(C934) using one-way ANVOA followed by a Bonferroni *post-hoc* test.

potential [31]. Thus, Nav1.7 could be a threshold channel that amplifies small membrane depolarization close to the action potential threshold [32]. For example, in peripheral DRG neurons, the shape of the action potential is determined mainly by TTX-resistant Na⁺ currents, but Nav1.7 current contributes to the spike waveform by decreasing the time to reach threshold [33]. This might allow the conclusion that the Na⁺ currents mainly carried by Nav1.7 contribute to the subthreshold depolarization and regulate the frequency of spontaneous action potentials in premature hair cells.

It is known that the primary α -subunit forms the central pore of the VGSC and serves as the voltage sensor, while the auxiliary β -subunits modulate the gating kinetics and surface expression of VGSCs [34]. Here, we demonstrated that four β -subunits ($\beta 1$ – $\beta 4$) are expressed in immature sensory epithelia, the $\beta 4$ subunit being highly expressed in basal sensory epithelia. These details raise an interesting question, specifically whether α and β subunits of VGSCs assemble in a dynamic matched-paired formation in apical and basal sensory epithelia.

Post-transcriptional Regulation of VGSCs in Developing Cochlea

Transcriptional modification events such as alternative splicing and RNA editing result in a single gene encoding multiple functional proteins. VGSCs undergo extensive transcriptional modification under various physiological and pathological conditions. Our previous study has shown that two novel Nav1.7 variants (CbmNav1.7a and 1.7b) in cochlear sensory epithelia undergo various post-transcriptional modifications [18]. The interesting question is

whether the cochlea-specific modifications affect the gating properties and kinetic parameters of Nav1.7. In the present study, the Na⁺ currents of CbmNav1.7a and 1.7b could not be detected in HEK293T cells. The Na⁺ current recordings from eight Nav1.7 mutants revealed that the disappearance of CbmNav1.7a currents was attributable to an amino-acid residue replacement (C934R) located at the extracellular linker between segments 5 and 6 of domain II *via* U-to-C RNA editing in exon 15. In this case, the uncharged Cys residue was replaced by a positively-charged Arg residue, which led to the loss of the CbmNav1.7a current. If so, Cys/Arg₉₃₄ might be a novel loss-of-function mutation in Nav1.7 that occurs under physiological conditions. Moreover, the lack of segment 4 and part of segment 3 in domain III of CbmNav1.7b results in a truncated non-functional channel protein. A somewhat similar modification event has been shown in the *hNav1.6* and *CACNLIA4* genes, and this was speculated to be a “fail-safe” mechanism [35, 36]. These data suggest that the RNA editing in exon 15 and alternative splicing of exon 20 could result in “fail-safe” protection of CbmNav1.7 in premature hair cells, which might be beneficial for decreasing cellular excitability under physiological conditions.

The next question concerns which Nav1.7 variant is the main contributor to Na⁺ currents in cochlear hair cells *in vivo*. Here, we considered CbmNav1.7a_(C934) to be a potential candidate. Compared to wtNav1.7, the functional shift of CbmNav1.7a_(C934) (slower fast-inactivation from open-state, faster deactivation, and larger ramp current) could strengthen its ability to receive and amplify weak electrical signals under conditions of lower depolarized membrane voltage. These results imply that the Na⁺ currents in developing IHCs might be attributed to

Table 5 Respective contributions of transcriptional modification events for biophysical properties of CbmNav1.7a_(C934).

Location sites	Exon 5	Exon 11	Exon 5&11	Exon 16	Exon 26	Exon 16&26	Altered properties of CbmNav1.7a _(C934)
Posttranscriptional modification events	Alternative splicing	Alternative splicing		RNA editing	RNA editing		
Amino acid substitution or deletion	L201V/N206D	647–657 deletion	L201V/N206D 647–657 deletion	I1037T	F1643S	I1037T&F1643S	
Topological structure	Extracellular linker of S3 and S4 in Domain I	Intracellular linker of Domain I and II		Intracellular linker of Domain II and III	Intracellular linker of S4 and S5 in Domain IV		
Channel dynamics							
Activation							
Inactivation component	+	–	–	–	+	–	–
Steady inactivation					–	–	–
Fast inactivation					–	–	–
Deactivation	–	+	+		–		+
Ramp current	+		+				+

Note: “+” represents the process is faster or larger, “–” represents the process is slower, “empty form” represents no change.

CbmNav1.7a_(C934) *in vivo*, which is largely activated around the resting membrane potential and then involved in shaping spontaneous action potentials.

Finally, it was unclear which post-transcriptional events lead to the distinctive biophysical properties of CbmNav1.7a_(C934). The ramp current of CbmNav1.7a_(C934) was increased by (201)V(206)D (exon 5 alternative splicing) in the DI/S3–S4 linker. This result was in accord with a previous report showing that exon 5 (5N and 5A) alternative splicing of *hNav1.7* enhances the amplitude of currents in response to a slowly-depolarizing ramp stimulus [37]. The faster deactivation associated with CbmNav1.7a_(C934) was attributed to deletion of the 647–657 amino-acid fragment (exon 11 alternative splicing). In addition, F1643S (a U-to-C RNA editing event in exon 26) delayed the deactivation process, and I1037T itself had no effect on deactivation. The delayed inactivation from the open state in CbmNav1.7a_(C934) might be induced by the systemic roles of the two alternative splicing events and two RNA editing events noted above, and the accelerated deactivation of CbmNav1.7a_(C934) might be attributed to two alternative splicing events and an RNA editing event at exon 26. These results indicate that the residue replacements and fragment deficiency distributed in four functional areas can modify channel dynamics in an individual or combinational manner (Table 5).

It was also interesting that deactivation of the Nav1.7 variant was delayed by the F1643S substitution; however, when I1037T coexisted with F1643S, the deactivation was conserved. The I1037T substitution was located at the intracellular linker between DII and DIII of CbmNav1.7a_(C934), whereas the F1643S substitution was at the intracellular linker between DIV S4 and DIV S5. One remaining question is how these two modifications regulate the deactivation of CbmNav1.7a_(C934). Regardless, these results provide important clues to understanding the dynamic-functional mechanisms of VGSCs.

Conclusion

The present study demonstrated that cochlea-specific post-transcriptional modifications amend the biophysical properties of the CbmNav1.7 variant, the main contributor to Na⁺ currents involved in regulating the frequency of spontaneous action potentials in premature IHCs.

Acknowledgements We thank Prof. Lin Chen (University of Science and Technology of China) and Dr. Juanmei Yang (Eye and ENT Hospital of Fudan University) for valuable help with cochlear microscopic anatomy. This work was supported by the National Natural Science Foundation of China (31571032, 31771191, and 81730028), the National Basic Research Development Program of China (SQ2017YFSF080012), and the Postdoctoral Science Foundation of China (2018M640407).

Conflict of interest All authors claim that there are no conflicts of interest.

References

- Fettiplace R, Hackney CM. The sensory and motor roles of auditory hair cells. *Nat Rev Neurosci* 2006, 7: 19–29.
- Johnson SL, Eckrich T, Kuhn S, Zampini V, Franz C, Ranatunga KM, *et al.* Position-dependent patterning of spontaneous action potentials in immature cochlear inner hair cells. *Nat Neurosci* 2011, 14: 711–717.
- Babola TA, Li S, Gribizis A, Lee BJ, Issa JB, Wang HC, *et al.* Homeostatic control of spontaneous activity in the developing auditory system. *Neuron* 2018, 99: 511–524 e515.
- Tritsch NX, Rodriguez-Contreras A, Crins TT, Wang HC, Borst JG, Bergles DE. Calcium action potentials in hair cells pattern auditory neuron activity before hearing onset. *Nat Neurosci* 2010, 13: 1050–1052.
- Marcotti W, Johnson SL, Kros CJ. A transiently expressed SK current sustains and modulates action potential activity in immature mouse inner hair cells. *J Physiol* 2004, 560: 691–708.
- Johnson SL, Adelman JP, Marcotti W. Genetic deletion of SK2 channels in mouse inner hair cells prevents the developmental linearization in the Ca²⁺ dependence of exocytosis. *J Physiol* 2007, 583: 631–646.
- Evans MG, Fuchs PA. Tetrodotoxin-sensitive, voltage-dependent sodium currents in hair cells from the alligator cochlea. *Biophys J* 1987, 52: 649–652.
- Marcotti W, Johnson SL, Rusch A, Kros CJ. Sodium and calcium currents shape action potentials in immature mouse inner hair cells. *J Physiol* 2003, 552: 743–761.
- D OM, Hudspeth AJ. Effects of cochlear loading on the motility of active outer hair cells. *Proc Natl Acad Sci USA* 2013, 110: 5474–5479.
- Oliver D, Plinkert P, Zenner HP, Ruppertsberg JP. Sodium current expression during postnatal development of rat outer hair cells. *Pflugers Arch* 1997, 434: 772–778.
- Housley GD, Marcotti W, Navaratnam D, Yamoah EN. Hair cells—beyond the transducer. *J Membr Biol* 2006, 209: 89–118.
- Catterall WA. From ionic currents to molecular mechanisms: the structure and function of voltage-gated sodium channels. *Neuron* 2000, 26: 13–25.
- Yu FH, Yarov-Yarovsky V, Gutman GA, Catterall WA. Overview of molecular relationships in the voltage-gated ion channel superfamily. *Pharmacol Rev* 2005, 57: 387–395.
- Zhou Y, Ji Y. Voltage-gated sodium channels involve in sensory information processing. *CNS Neurol Disord Drug Targets* 2018.
- Masetto S, Bosica M, Correia MJ, Ottersen OP, Zucca G, Perin P, *et al.* Na⁺ currents in vestibular type I and type II hair cells of the embryo and adult chicken. *J Neurophysiol* 2003, 90: 1266–1278.
- Wooltorton JR, Gaboyard S, Hurley KM, Price SD, Garcia JL, Zhong M, *et al.* Developmental changes in two voltage-dependent sodium currents in utricular hair cells. *J Neurophysiol* 2007, 97: 1684–1704.
- Eckrich T, Varakina K, Johnson SL, Franz C, Singer W, Kuhn S, *et al.* Development and function of the voltage-gated sodium current in immature mammalian cochlear inner hair cells. *PLoS One* 2012, 7: e45732.
- Zhou Y, Fang FH, Liu ZR, Ji YH. Dissection of voltage-gated sodium channels in developing cochlear sensory epithelia. *Protein Cell* 2015, 6: 458–462.
- Blaustein MP, Goldman DE. The action of certain polyvalent cations on the voltage-clamped lobster axon. *J Gen Physiol* 1968, 51: 279–291.
- Blanton MG, Kriegstein AR. Spontaneous action potential activity and synaptic currents in the embryonic turtle cerebral cortex. *J Neurosci* 1991, 11: 3907–3923.
- Soto F, Ma X, Cecil JL, Vo BQ, Culican SM, Kerschensteiner D. Spontaneous activity promotes synapse formation in a cell-type-dependent manner in the developing retina. *J Neurosci* 2012, 32: 5426–5439.
- Mooney R, Penn AA, Gallego R, Shatz CJ. Thalamic relay of spontaneous retinal activity prior to vision. *Neuron* 1996, 17: 863–874.
- Murase S, Owens DF, McKay RD. In the newborn hippocampus, neurotrophin-dependent survival requires spontaneous activity and integrin signaling. *J Neurosci* 2011, 31: 7791–7800.
- Lippe WR. Rhythmic spontaneous activity in the developing avian auditory system. *J Neurosci* 1994, 14: 1486–1495.
- Johnson SL, Kuhn S, Franz C, Ingham N, Furness DN, Knipper M, *et al.* Presynaptic maturation in auditory hair cells requires a critical period of sensory-independent spiking activity. *Proc Natl Acad Sci USA* 2013, 110: 8720–8725.
- Marcotti W, Kros CJ. Developmental expression of the potassium current IK_n contributes to maturation of mouse outer hair cells. *J Physiol* 1999, 520: 653–660.
- Marcotti W, Johnson SL, Kros CJ. Effects of intracellular stores and extracellular Ca(2+) on Ca(2+)-activated K(+) currents in mature mouse inner hair cells. *J Physiol* 2004, 557: 613–633.
- Hackney CM, Mahendrasingam S, Penn A, Fettiplace R. The concentrations of calcium buffering proteins in mammalian cochlear hair cells. *J Neurosci* 2005, 25: 7867–7875.
- Dou H, Vazquez AE, Namkung Y, Chu H, Cardell EL, Nie L, *et al.* Null mutation of alpha1D Ca²⁺ channel gene results in deafness but no vestibular defect in mice. *J Assoc Res Otolaryngol* 2004, 5: 215–226.
- Sangameswaran L, Fish LM, Koch BD, Rabert DK, Delgado SG, Ilnicka M, *et al.* A novel tetrodotoxin-sensitive, voltage-gated sodium channel expressed in rat and human dorsal root ganglia. *J Biol Chem* 1997, 272: 14805–14809.
- Cummins TR, Howe JR, Waxman SG. Slow closed-state inactivation: a novel mechanism underlying ramp currents in cells expressing the hNE/PN1 sodium channel. *J Neurosci* 1998, 18: 9607–9619.
- Waxman SG. Neurobiology: a channel sets the gain on pain. *Nature* 2006, 444: 831–832.
- Blair NT, Bean BP. Roles of tetrodotoxin (TTX)-sensitive Na⁺ current, TTX-resistant Na⁺ current, and Ca²⁺ current in the action potentials of nociceptive sensory neurons. *J Neurosci* 2002, 22: 10277–10290.
- Patino GA, Isom LL. Electrophysiology and beyond: multiple roles of Na⁺ channel beta subunits in development and disease. *Neurosci Lett* 2010, 486: 53–59.
- Ophoff RA, Terwindt GM, Vergouwe MN, van Eijk R, Oefner PJ, Hoffman SM, *et al.* Familial hemiplegic migraine and episodic ataxia type-2 are caused by mutations in the Ca²⁺ channel gene CACNL1A4. *Cell* 1996, 87: 543–552.
- Plummer NW, McBurney MW, Meisler MH. Alternative splicing of the sodium channel SCN8A predicts a truncated two-domain protein in fetal brain and non-neuronal cells. *J Biol Chem* 1997, 272: 24008–24015.
- Chatelier A, Dahllund L, Eriksson A, Krupp J, Chahine M. Biophysical properties of human Nav1.7 splice variants and their regulation by protein kinase A. *J Neurophysiol* 2008, 99: 2241–2250.



REVIEW

Regulation of Circadian Genes by the MAPK Pathway: Implications for Rapid Antidepressant Action

Xin-Ling Wang¹ · Kai Yuan² · Wen Zhang³ · Su-Xia Li³ · George Fu Gao^{1,4,5} · Lin Lu^{1,2,3,6}

Received: 7 July 2018 / Accepted: 18 January 2019 / Published online: 11 March 2019
© Shanghai Institutes for Biological Sciences, CAS 2019

Abstract Accumulating evidence suggests that the circadian rhythm plays a critical role in mood regulation, and circadian disturbances are often found in patients with major depressive disorder (MDD). The mitogen-activated protein kinase (MAPK)/extracellular signal-regulated kinase (ERK) pathway is involved in mediating entrainment of the circadian system. Furthermore, the MAPK/ERK signaling pathway has been shown to be involved in the pathogenesis of MDD and the rapid onset of action of antidepressant therapies, both pharmaceutical and non-pharmaceutical. This review provides an overview of the

involvement of the MAPK/ERK pathway in modulating the circadian system in the rapid action of antidepressant therapies. This pathway holds much promise for the development of novel, rapid-onset-of-action therapeutics for MDD.

Keywords Major depressive disorder · MAPK pathway · Circadian system · Rapid antidepressant therapy

Introduction

Rapid-onset antidepressant therapies have been shown to be related to the circadian rhythm, but the specific molecular pathways have not been clarified [1–3]. The mitogen-activated protein kinase (MAPK)/extracellular signal-regulated kinase (ERK) signaling pathway is involved in major depressive disorder (MDD), but such an involvement has not been interpreted from the perspective of the circadian system [4]. The regulation of circadian genes by the MAPK/ERK pathway has been demonstrated elsewhere but not linked specifically to depression [5, 6]. In this review, we propose that rapid-onset pharmaceutical and non-pharmaceutical antidepressant therapies may modulate the circadian rhythm through the MAPK pathway.

Circadian Rhythm and Its Effect on Mood

The circadian rhythm in mammals is controlled by the suprachiasmatic nucleus (SCN), which is often referred to as the central circadian clock. It synchronizes the peripheral clock in various cells throughout the body. The molecular machinery of the circadian clock consists of

✉ Su-Xia Li
li313@bjmu.edu.cn

✉ George Fu Gao
gaof@im.ac.cn

✉ Lin Lu
linlu@bjmu.edu.cn

¹ Savaid Medical School, University of the Chinese Academy of Sciences, Beijing 101408, China

² Peking-Tsinghua Center for Life Sciences and PKU-IDG/McGovern Institute for Brain Research, Peking University, Beijing 100191, China

³ National Institute on Drug Dependence and Beijing Key Laboratory on Drug Dependence Research, Peking University, Beijing 100191, China

⁴ Key Laboratory of Pathogenic Microbiology and Immunology, Institute of Microbiology, Chinese Academy of Sciences, Beijing 100101, China

⁵ Chinese Center for Disease Control and Prevention, Beijing 102206, China

⁶ Institute of Mental Health, National Clinical Research Center for Mental Disorders, Key Laboratory of Mental Health and Peking University Sixth Hospital, Peking University, Beijing 100191, China

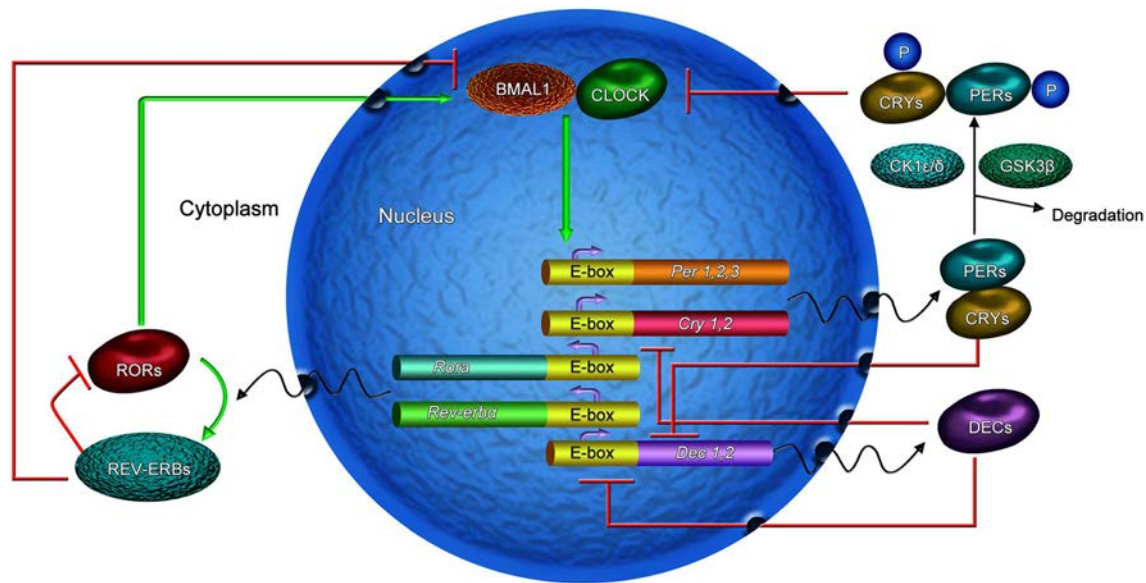


Fig. 1 Circadian feedback loops in mammalian cells. The loops contain the classical core feedback loop (including BMAL1/CLOCK and PER/CRY proteins), an REV-ERB/ROR loop, and a *Dec* loop, which interlocks with the classical core loop. CLOCK and BMAL1 form heterodimers that activate the transcription of *Cry* and *Per* genes. PER dimerizes with CRY to inhibit CLOCK–BMAL1-mediated transcription. *Rora* activates the expression of BMAL1, and *Rev-erb α* inhibits it, forming a feedback loop. The CLOCK and

BMAL1 complexes activate transcription of the *Dec1* and *Dec2* genes, whereas the PER and CRY complexes inhibit them. In addition, DECs self-regulate to inhibit the transcription of their own genes. This forms another loop. These loops are interlocked. CK1 ϵ/δ , casein kinase 1 ϵ/δ ; CRY, cryptochrome; DEC, differentiated embryo chondrocyte; E-box, enhancer-box; PER, period; ROR, retinoic acid-related orphan receptor; P, phosphorylation.

interlocked molecular feedback loops [2, 7–9]. The core circadian loop consists of positive and negative branches. The positive branch consists of circadian locomotor output cycles kaput (CLOCK) and brain and muscle ARNT-like 1 (BMAL1) proteins, which heterodimerize and bind to the Enhancer Box of the period and cryptochrome genes to activate their transcription. The period (PER) and cryptochrome (CRY) proteins then heterodimerize in the cytoplasm and are phosphorylated by glycogen synthase kinase-3 and casein kinase I ϵ . Afterward, they shuttle back into the nucleus to inhibit the transcription of *Clock* and *Bmal1* genes. Lastly, the PER and CRY proteins are degraded in the cytoplasm and release the inhibition of transcription. This process lasts about 24 h.

In addition to the core circadian feedback loop, interlocking feedback loops have also been explored with regard to their modulation of the circadian rhythm. The other feedback loop contains *Rora* and *Rev-erb α* , which regulate BMAL1 expression [10–13]. *Rora* activates the expression of BMAL1, and *Rev-erb α* inhibits it, which reinforces the oscillations. Another loop consists of *Dec1* and *Dec2*, which negatively regulate circadian rhythms [14]. The CLOCK and BMAL1 complexes activate the transcription of the *Dec1* and *Dec2* genes, whereas the PER and CRY complexes inhibit them. In addition, differentiated embryo chondrocytes self-regulate to inhibit the transcription of their own genes. They also inhibit

transcription of the *Per* and *Cry* genes [15]. These form multiple interlocked molecular feedback loops that provide stability and fine regulation of the circadian machinery (Fig. 1).

Previous studies have shown that daily rhythms are prominent in every aspect of bodily function, such as sleep/wake periods, core body temperature, blood pressure, hormone secretion, cognition, and mood [16, 17]. Disturbances of the circadian rhythm may be related to mental disorders. For example, since the 1950s, circadian disturbances have been reported in patients with mood disorders [18]. Circadian clinical manifestations in MDD patients include social activity rhythm disorder, sleep/wake cycle disorder, blood pressure rhythm disorder, and hormone secretion rhythm disorder [19]. In the late 1980s, the Social Zeitgeber Theory of mood disorders proposed that stress leads to alterations of the circadian rhythms in susceptible individuals, resulting in depressive or manic episodes [20]. Research on patients with first-episode MDD has shown disturbances in circadian rhythms of the expression of PERIOD1, PERIOD2, CRY1, BMAL1, NPAS2, and GSK-3 β , as well as abnormalities in the circadian rhythms of the secretion of melatonin, vasoactive intestinal peptide, cortisol, adrenocorticotrophic hormone, insulin growth factor-1, and growth hormone [21]. And these abnormalities are correlated with the severity of depressive symptoms. Some studies have also reported that mood symptoms are

alleviated along with the resumption of circadian rhythms with treatment [18, 19]. All therapeutic strategies that are employed for mood disorders alter or steady circadian rhythms [3]. Nevertheless, the mechanisms that underlie circadian rhythm disturbances that might induce mood alterations have not been clarified. Logan *et al.* found that chronic unpredictable mild stress (CUMS), a widely used animal model of depression, significantly reduces the rhythmic amplitude of activity and body temperature in mice [22]. These alterations of biological rhythms are directly correlated with depressive-like behaviors. Expression of the amplitude of the clock gene *per2* rhythm is decreased in the SCN and increased in the nucleus accumbens (NAc) of CUMS mice. Molecular circadian changes in the SCN and NAc are directly correlated with mood-related behaviors [22]. CUMS also causes disturbances in the circadian rhythms of plasma corticosterone, melatonin, and vasoactive intestinal peptide in rats [23]. The functions of daily rhythms of the hypothalamus-pituitary-thyroid (HPT) axis are also reduced in rats exposed to CUMS [24]. In addition, CUMS induces alterations of the *rPER2* rhythm in the rat SCN [25]. The hippocampal CLOCK protein has been shown to play an important part in the continuance of the depressive-like behaviors induced by CUMS [26].

Clock gene variants have often been associated with diurnal preference [19] and have been explored with regard to the mechanisms of mood disorders [27]. Preclinical and clinical reports suggest that mutations of both *Clock* [28, 29] and *Per* [30, 31] are associated with mood disorders. Previous research on circadian regulation has impressively exhibited its predictive value for the initiation of depression. Spulber *et al.* [32] studied the long-term behavioral changes induced by prenatal exposure to excessive glucocorticoids. They found that progressive changes in circadian entrainment precede depression. Circadian oscillations in *clock* gene mRNA expression are also diminished in skin fibroblasts before the initiation of depression. These results indicate that changes in the circadian entrainment of spontaneous activity and possibly *clock* gene expression in fibroblasts signal the development of depression. Other researchers have suggested that circadian disturbances might be the origin of mood disorders rather than their consequence [2].

Circadian rhythm disorders might be a part of the pathogenesis of mood disorders. However, detailed mechanisms, such as the cellular signaling pathways, have not been sufficiently clarified.

Regulation of the Circadian System by the MAPK Pathway

Light is known to be the strongest stimulus (zeitgeber) for entrainment of the circadian pacemaker [33, 34]. The retinohypothalamic tract (RHT) is located between the retina and the SCN in mammals. Even very dim light has been shown to entrain the circadian pacemaker [35–37]. However, non-photic stimuli have also been shown to exert weak but independent effects on the SCN. That is, other zeitgebers besides light can entrain the circadian pacemaker.

The MAPK signaling pathway may act as a critical common mediator of the circadian rhythm in the SCN, the periphery, and cultured cells, and circadian entrainment by photic and non-photic stimuli may be impacted by similar molecular mechanisms [38] (Fig. 2).

MAPK Pathway Underlies Photic Entrainment of the Circadian System

The MAPK pathway [39] in mammals consists of ERK1/2, c-Jun N-terminal kinase (JNK), p38, and ERK5. The MAPK pathway has been suggested to be involved in entrainment of the circadian clock [38]. The potential involvement of Ras, part of the MAPK signaling pathway, in modulating the circadian rhythm has been proposed in several studies [40–48]. ERKs have also been shown to play a role in photic resetting of the clock in the rodent SCN [49, 50]. The role of the SCN clock as a master pacemaker is modulated by light *via* direct excitation from the eyes. Intrinsic photosensitive retinal ganglion cells detect light through melanopsin [51] and project directly to the SCN through the RHT. The terminals of the RHT release glutamate and pituitary adenylate cyclase-activating peptide (PACAP) in the SCN [52]. They are ligands for *N*-methyl-D-aspartate receptors (NMDARs) and Pac1 receptors, respectively, at postsynaptic neurons in the SCN. The activation of NMDARs is followed by an inflow of Ca^{2+} [53, 54], which stimulates Ca^{2+} -calmodulin kinase II that successively activates cyclic adenosine monophosphate (cAMP) response element binding protein (CREB) [55, 56]. In parallel, the activation of NMDARs leads to the activation of Ras, with subsequent activation of the MAPK pathway. ERK1/2 phosphorylates p90 ribosomal S6 kinase, which successively phosphorylates CREB, which is indispensable for light-induced resetting of the circadian clock in the SCN [57, 58]. Pac1 receptors can be activated by both light and stress [59]. PACAP is a critical neurotransmitter that is released in stress transduction areas of the brain, including the paraventricular nucleus of the

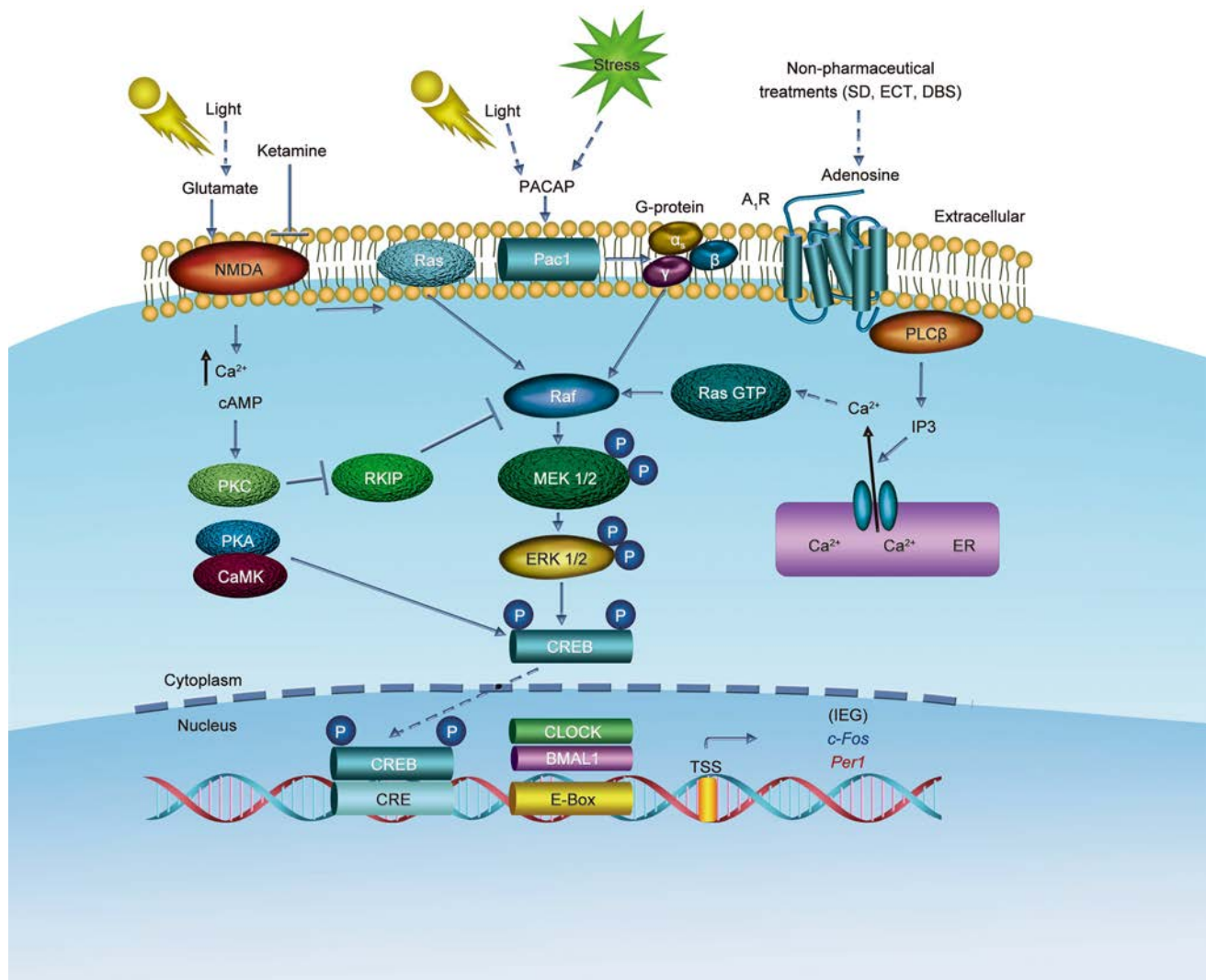


Fig. 2 Photic- and non-photic-responsive MAPK signaling pathways in the brain. In photic circadian clock entrainment, the neurotransmitters glutamate and PACAP are released onto SCN neurons *via* the eye and RHT. The activation of NMDA and Pac1 receptors in turn results in the activation of Ras and heterotrimeric G proteins, which successively activate ERK and CREB. Non-photic stimulation by SD,

ECT, or DBS leads to the activation of adenosine A₁ receptors, which leads to the activation of ERK and CREB. Phosphorylated CREB is translocated to the nucleus and activates the transcription of immediate-early genes, including *Per1*. SD, sleep deprivation; ECT, electroconvulsive therapy; DBS, deep brain stimulation; P, phosphorylation; ER, endoplasmic reticulum; TSS, transcription start site.

hypothalamus, the amygdala, extended amygdala nuclei, and the prefrontal cortex (PFC).

A previous study provided strong evidence that CREB plays a vital role as an endpoint of the MAPK pathway in the regulation of the *mPer* (*mPer1* and *mPer2*) genes [58]. Additional studies suggested that the MAPK pathway mediates the photic input which is involved in immediate-early gene (e.g., *c-fos* and *Per1*) induction in the SCN [60–62]. *Per1* is a clock gene in the negative feedback loop of the circadian system, the activation of which is thought to be an important event in modulating the clock [63]. The MAPK pathway has a series of downstream effector molecules that control the expression of related genes, including circadian genes [64] (Fig. 2). Moreover, ERK

and MAPK interact with and phosphorylate CLOCK, BMAL1, CRY1, and CRY2 in the circadian system [6].

MAPK Pathway Underlies Non-photic Entrainment of the Circadian System

In addition to light, non-photic stimuli can also impact the circadian clock [65–67]. Numerous other stimuli have been shown to increase locomotor activity or arousal in animals, including injections of triazolam [68, 69] and morphine [70], confinement to a novel wheel [71, 72], social and sexual cues [73], and sleep deprivation [74]. Some research have also revealed that the circadian clock can be reset in

humans by modulating mealtime, exercise, sleep-wake schedule, and social stimuli [75].

The intracellular biochemical cascades that underlie non-photic phase-shifts have gradually been identified. A study [76] showed that dark pulses decrease the levels of phosphorylated ERK1/2 but do not affect the levels of phosphorylated Ets-like gene 1. Another study revealed the involvement of the ERK/MAPK pathway in phase-shifts in response to 3 h of sleep deprivation initiated at midday in Syrian hamsters [67]. Cultured NIH-3T3 fibroblasts treated with tissue plasminogen activator exhibit circadian oscillations of gene expression that are restrained by a MEK inhibitor, and sustained activation of the MAPK pathway is sufficient to activate circadian gene expression [38]. These results demonstrate that the MAPK pathway acts as a critical mediator of signaling pathways that are involved in circadian entrainment by non-photic stimuli.

Research on the mechanisms that underlie physical therapy have revealed that sleep deprivation, electroconvulsive therapy (ECT), and deep brain stimulation (DBS) are associated with an increase in adenosinergic signaling [77–80]. Sleep deprivation increases the secretion of adenosine in the brain and upregulates adenosine A₁ receptors in humans and rodents [81–83]. Two physical therapies for depression, ECT and DBS, increase the levels of adenosine and stimulate A₁ receptors [77, 79, 84, 85]. Previous studies have shown that A₁ receptors regulate phospholipase C [86–89] and the ERK pathway [90, 91] in cells where they are highly expressed (e.g., neurons and smooth muscle cells). The MAPK pathway is an important component of the circadian clock [6] and mediates the regulation of the circadian rhythm. Evidence suggests that A₁ receptors mediate the circadian rhythm through the MAPK pathway and downstream CREB (Fig. 2).

To summarize, these investigations indicate that the MAPK pathway acts as a critical common mediator in the signaling pathways that regulate the circadian rhythm which is induced by both photic and non-photic stimuli. Regulation of the circadian system by the MAPK pathway may also play a critical role in depression.

MAPK Pathway in Depression

The MAPK/ERK pathway has been shown to play a critical role in MDD [92, 93] and in the actions of antidepressants [4, 94, 95]. Elements of the MAPK/ERK signaling pathway, including MEK1, MEK2, and Rap1, are reduced in the frontal cortex in MDD patients [96]. The levels of CREB cAMP and Ca²⁺ signaling also reduced in MDD [96]. Evidence also suggests decreases in ERK1/2, ERK5, MEK1, and CREB in the hippocampus [97, 98] and Rap1 activity in the PFC and hippocampus [99] in depressed

suicidal individuals. Postmortem investigations have reported that the mRNA and protein levels of ERK1/2 in prefrontal cortical areas and the hippocampus are significantly reduced in depressive suicide individuals [96, 99, 100]. MAPK-phosphatase 1 (MKP-1), a negative modulator of the MAPK pathway, is increased in the hippocampus of MDD patients [93]. The overexpression of MKP-1 is sufficient to induce depressive-like behavior in rodent models [93, 101]. The MAPK pathway has been suggested to play a vital role in the development of depression [95, 102].

Activity of the MAPK pathway is inhibited by chronic stress and restored by antidepressant treatment [103]. Inhibition of the MAPK pathway induces depressive- and anxiety-like behaviors [104]. Duman and colleagues demonstrated that inhibition of the MAPK pathway leads to depressive-like behaviors and blocks the behavioral actions of antidepressants on rodents [4]. Furthermore, depressive-like behavior is positively associated with a reduction of pERK in a rat model of depression [105]. Inhibition of the ERK pathway produces depressive-like behavior and blocks the antidepressant effects of ketamine [106]. Moreover, Pochwat *et al.* reported that ERK activation is crucial for both the short- and long-term antidepressant-like actions of NMDAR antagonists in the forced swim test in rats [107]. Recently, Labonté and colleagues reported that an increase in ERK signaling in glutamatergic pyramidal neurons in the ventromedial PFC (vmPFC) specifically increases the susceptibility of female rats to stress [108]. However, these results are in sharp contrast to those of previous studies in rodents [109–111] and postmortem human brains [96]. The study by Labonté and colleagues investigated the vmPFC, whereas most other previous studies focused on other cortical regions or the NAc. This may be the main reason for the discrepant findings. Further work is needed to illustrate why an increase in ERK signaling in the female vmPFC results in depressive-like behavior, while the same change in the male vmPFC has diverse outcomes.

In summary, abundant evidence indicates that the MAPK/ERK pathway is involved in the pathogenesis of depression and may be an attractive target for the development of new therapeutic strategies for MDD.

Regulation of the Circadian System by the MAPK Pathway: Involvement in Rapid Antidepressant Effects

Accumulating evidence suggests that MDD is a circadian-related disorder. Almost all patients with MDD suffer from alterations of diurnal rhythmicity (e.g., temperature, sleep, hormone secretion, and mood) during depressive episodes

[3]. A review showed that both low-dose ketamine and sleep deprivation therapy (SDT) modulate the circadian rhythm in humans, animals, and neuronal cells [3]. The fact that both therapies impact sleep homeostasis and the circadian rhythm indicates that the circadian and sleep-wake systems and their interactions are related to rapid antidepressant effects.

Sleep Deprivation Therapy and Other Non-pharmaceutical Treatments

The advent SDT was a major revolution when considering its rapid remission of depressive manifestations [112]. SDT generally refers to keeping patients awake for ~36 h. The mechanism underlying the effects of SDT has been investigated for many years, but no mechanism has yet been demonstrated. Bunney *et al.* proposed that abnormal circadian clock genes which control rhythms are altered by a change of the sleep-wake cycle [7, 16]. SDT responders present distinct activation of circadian genes (*Rora*, *Dec2*, and *Per1*) after SDT, whereas non-responders present notable reductions in the expression of these genes afterwards [7]. A few studies of clock genes in mice showed that a subset of circadian clock genes (e.g., *Per1* and *Per2*) appear to behave as immediate-early genes and are transcriptionally responsive within hours after sleep deprivation [113–116]. Depriving mice of sleep inhibits ~80% of rhythmic genes [114, 117].

The MAPK/ERK signaling pathway has been shown to be involved in the mechanism of action of SDT [118]. The diurnal activation of ERK in the dorsomedial SCN (i.e. the “shell”) is suppressed following sleep deprivation. A previous study indicated that adenosine A₁ receptors are important for the antidepressant effects of sleep deprivation [119, 120]. Two other rapid-onset non-pharmaceutical therapies for depression, ECT and DBS, are also associated with an increase in the release of adenosine and the activation of A₁ receptors [77, 79, 84]. Interestingly, A₁ receptors regulate the ERK pathway [90, 91]. These studies suggest that the rapid-onset non-pharmaceutical treatments for depression exert their antidepressant effects by stimulating A₁ receptor-ERK1/2 signaling (Fig. 2).

Besides, light therapy can also produce a rapid antidepressant effect. However, the parameters of light therapy varied among different clinical trials, so the results were different [121, 122]. Currently, there is no uniform procedure for light therapy. Above, we discussed the involvement of the MAPK/ERK pathway in both photic and non-photoc entrainment of the circadian system. We propose that rapid-onset-of-action non-pharmaceutical treatments for depression exert their antidepressant effects by activating MAPK/ERK signaling, which mediates

resetting of the circadian system, although no direct evidence is yet available to support our viewpoint.

Low-Dose Ketamine

Several studies indicate that the rapid antidepressant effects of low-dose ketamine are closely related to the regulation of circadian systems. Duncan *et al.* [123] found an association between the clinical antidepressant effects of ketamine and circadian timekeeping (i.e., amplitude and timing) using wrist-activity monitors in MDD patients. Bellet *et al.* [124] found that ketamine affects molecules associated with the central circadian clock. Specifically, ketamine decreases the amplitude of circadian transcription of the *Bmal1*, *Per2*, and *Cry1* genes in a dose-dependent manner. Ma *et al.* [125] reported that ketamine accelerates the differentiation of double cortin-positive adult hippocampal neural progenitors into functionally mature neurons. This process requires activation of the tyrosine kinase receptor B (TrkB)-dependent ERK pathway. TrkB-dependent neuronal differentiation is related to the sustained antidepressant effects of ketamine. Moreover, another study reported that acute inhibition of the MAPK pathway produces depressive-like behavior and blocks the antidepressant effect of ketamine [106]. Recently, Yang *et al.* found that (*R*)-ketamine significantly attenuates the decrease in ERK phosphorylation and its upstream effector MAPK/ERK in the PFC and hippocampal dentate gyrus in susceptible mice following chronic social defeat stress [126]. Based on this evidence, we speculate that low-dose ketamine produces its rapid antidepressant effects through the MAPK pathway to regulate the circadian system.

Overall, these results suggest that both SDT and ketamine act on circadian genes through the ERK/MAPK pathway, which phosphorylates CREB to produce a rapid antidepressant response. Using comparative transcriptomics analyses, Orozco-Solis *et al.* found that both SDT and ketamine act on the circadian clock *via* the MAPK/ERK pathway in the anterior cingulate cortex [127]. These findings suggest that the mediation of entrainment of the circadian system by the MAPK/ERK pathway may be involved in neuropathological processes that are associated with depression and antidepressant therapy, although further studies are needed to test this possibility (Fig. 3).

At present, most of the commonly-used first-line antidepressants target monoamine neurotransmitters, such as the selective serotonin reuptake inhibitors. Although the MAPK signaling pathway is involved in almost all of their mechanisms, they do not directly target this signaling pathway, so the onset of their action takes a relatively long

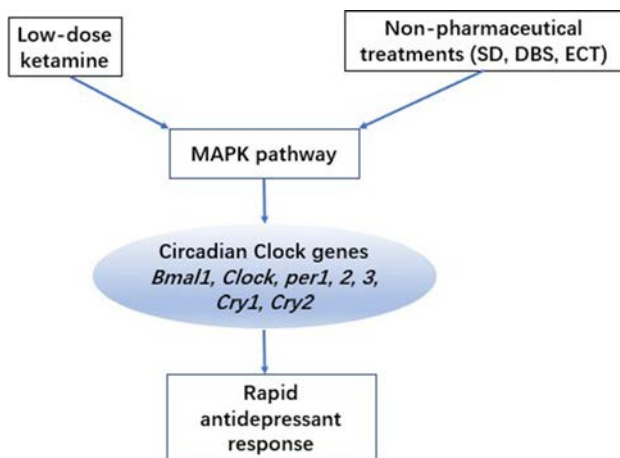


Fig. 3 Low-dose ketamine and non-pharmaceutical treatments, including SD, DBS, and ECT, regulate the circadian system through the MAPK pathway, which phosphorylates CREB to produce a rapid antidepressant response. Phosphorylated CREB directly binds to the CRE sequence of the *per1* and *per2* genes and regulates their transcription. ERK/MAPK interacts with and phosphorylates CLOCK, BMAL1, CRY1, and CRY2 in the circadian system, leading to a rapid antidepressant effect. SD, sleep deprivation; ECT, electroconvulsive therapy; DBS, deep brain stimulation.

time. Sleep deprivation can have a rapid antidepressant action but this only lasts for a short period and is easy to reverse. Depressive symptoms can recur as sleep recovers. However, the other rapid antidepressant methods, such as DBS, modified ECT, and low-dose of ketamine, whose mechanisms of action are still in the exploratory stage, are not well established. So we cannot provide the long-term outcomes of the currently available interventions targeting the MAPK pathway for antidepressant effects.

Conclusions and Future Directions

To date, accumulating evidence has indicated that the MAPK/ERK pathway is involved in the pathogenesis of depression and the mechanism of action of both pharmaceutical and non-pharmaceutical antidepressant therapies. Increasing evidence also demonstrates the mediation of entrainment of the circadian system by the MAPK/ERK pathway. However, little evidence links these systems to depression. To our knowledge, only one study has directly demonstrated such a mechanism in depression [127] using comparative transcriptomics analyses. Future studies are needed to test this hypothesis using various models, including behavioral tests, western blot, virus microinjection into specific brain areas, and conditioned intervention genes in animals.

Some basic questions still need to be answered. First, does the circadian system play an important or indispensable role in the pathogenesis of depression? Second, do

other pathways mediate entrainment of the circadian system? Third, how do these pathways interact with and affect the circadian system? These are critical questions that need to be explored. The MAPK pathway is a promising target for novel therapeutics with a rapid onset of action for the long-term treatment of severe, refractory MDD.

Based on previous studies, we propose that the regulation of circadian genes by the MAPK pathway is involved in the mechanism of depression. Nonetheless, direct evidence is needed to demonstrate that the rapid antidepressant effects of non-pharmaceutical and pharmaceutical therapies occur through entrainment of the circadian system mediated by the MAPK/ERK pathway. In fact, not all MDD patients respond to one kind of rapid antidepressant therapy, such as sleep deprivation, DBS or low-dose ketamine. This indicates that the mechanism underlying depression differs in different individuals. Nevertheless, the circadian rhythm involvement in depression and antidepressant therapy may also be complicated. Lazzarini Ospri *et al.* argued that circadian rhythms and mood could have synergistic effects but not be causally linked [128]. They proposed that mood could be affected by a comparison of the incidental properties of the output of circadian oscillators. Nevertheless, direct evidence or detailed mechanisms have not been provided. Above all, we need to explore the mechanism underlying this phenomenon. The MAPK pathway is important for mood regulation and clock entrainment, but the existing evidence cannot explain this complicated phenomenon.

In conclusion, most researchers in this field support the idea that circadian rhythm and mood are closely related, and some believe that there may be a causal link between them. However, so far there is no direct evidence of such a link. In this review, we propose that rapid-onset antidepressant therapies, both pharmaceutical and non-pharmaceutical, may regulate the circadian rhythm through the MAPK pathway. As far as we know, this is the first review to link the MAPK pathway, the circadian system, and antidepressant action, and only one report supports this link. Hence, in the future, we need use various animal models, specific gene interventions, virus microinjection into specific brain areas, or conditioned intervention genes in animals to test this hypothesis. And this may provide strong support for the Social Zeitgeber Theory of mood disorder.

Acknowledgements This review was supported by the National Basic Research Development Program of China (2015CB856400 and 2015CB553503), the National Natural Science Foundation of China (81521063), and the Natural Science Foundation of Beijing Municipality, China (7162101).

References

1. Albrecht U. Molecular mechanisms in mood regulation involving the circadian clock. *Frontiers In Neurology* 2017,8.
2. McClung CA. How might circadian rhythms control mood? Let me count the ways. *Biol Psychiatry* 2013,74:242–249.
3. Bunney BG, Li JZ, Walsh DM, Stein R, Vawter MP, Cartagena P, *et al.* Circadian dysregulation of clock genes: clues to rapid treatments in major depressive disorder. *Mol Psychiatry* 2015,20:48–55.
4. Duman CH, Schlesinger L, Kodama M, Russell DS, Duman RS. A role for MAP kinase signaling in behavioral models of depression and antidepressant treatment. *Biol Psychiatry* 2007,61:661–670.
5. Serchov T, Heumann R. Ras activity tunes the period and modulates the entrainment of the suprachiasmatic clock. *Frontiers In Neurology* 2017,8.
6. Goldsmith CS, Bell-Pedersen D. Diverse roles for MAPK signaling in circadian clocks. *Adv Genet* 2013,84:1–39.
7. Bunney BG, Bunney WE. Mechanisms of rapid antidepressant effects of sleep deprivation therapy: clock genes and circadian rhythms. *Biol Psychiatry* 2013,73:1164–1171.
8. Mohawk JA, Green CB, Takahashi JS. Central and peripheral circadian clocks in mammals. *Annu Rev Neurosci* 2012,35:445–462.
9. Zhang EE, Kay SA. Clocks not winding down: unravelling circadian networks. *Nat Rev Mol Cell Biol* 2010,11:764–776.
10. Shearman LP, Sriram S, Weaver DR, Maywood ES, Chaves I, Zheng B, *et al.* Interacting molecular loops in the mammalian circadian clock. *Science* 2000,288:1013–1019.
11. Honma S, Ikeda M, Abe H, Tanahashi Y, Namihira M, Honma K, *et al.* Circadian oscillation of BMAL1, a partner of a mammalian clock gene Clock, in rat suprachiasmatic nucleus. *Biochem Biophys Res Commun* 1998,250:83–87.
12. Sato TK, Panda S, Miraglia LJ, Reyes TM, Rudic RD, McNamara P, *et al.* A functional genomics strategy reveals Rora as a component of the mammalian circadian clock. *Neuron* 2004,43:527–537.
13. Preitner N, Damiola F, Lopez-Molina L, Zakany J, Duboule D, Albrecht U, *et al.* The orphan nuclear receptor REV-ERB α controls circadian transcription within the positive limb of the mammalian circadian oscillator. *Cell* 2002,110:251–260.
14. Honma S, Kawamoto T, Takagi Y, Fujimoto K, Sato F, Noshiro M, *et al.* Dec1 and Dec2 are regulators of the mammalian molecular clock. *Nature* 2002,419:841–844.
15. Ueda HR, Hayashi S, Chen W, Sano M, Machida M, Shigeyoshi Y, *et al.* System-level identification of transcriptional circuits underlying mammalian circadian clocks. *Nat Genet* 2005, 37:187–192.
16. Bunney WE, Bunney BG. Molecular clock genes in man and lower animals: possible implications for circadian abnormalities in depression. *Neuropsychopharmacology* 2000,22:335–345.
17. Reppert SM, Weaver DR. Molecular analysis of mammalian circadian rhythms. *Annu Rev Physiol* 2001,63:647–676.
18. Wirz-Justice A. Biological rhythm disturbances in mood disorders. *Int Clin Psychopharmacol* 2006,21 Suppl 1:S11–15.
19. McClung CA. Circadian genes, rhythms and the biology of mood disorders. *Pharmacol Ther* 2007,114:222–232.
20. Ehlers CL, Frank E, Kupfer DJ. Social zeitgebers and biological rhythms. A unified approach to understanding the etiology of depression. *Arch Gen Psychiatry* 1988,45:948–952.
21. Li SX, Liu LJ, Xu LZ, Gao L, Wang XF, Zhang JT, *et al.* Diurnal alterations in circadian genes and peptides in major depressive disorder before and after escitalopram treatment. *Psychoneuroendocrinology* 2013,38:2789–2799.
22. Logan RW, Edgar N, Gillman AG, Hoffman D, Zhu XY, McClung CA. Chronic stress induces brain region-specific alterations of molecular rhythms that correlate with depression-like behavior in mice. *Biol Psychiatry* 2015,78:249–258.
23. Zhao Y, Liu LJ, Wang C, Li SX. Swimming exercise may not alleviate the depressive-like behaviors and circadian alterations of neuroendocrine induced by chronic unpredictable mild stress in rats. *Neurol, Psychiatry Brain Res* 2012,18:202–207.
24. Guo TY, Liu LJ, Xu LZ, Zhang JC, Li SX, Chen C, *et al.* Alterations of the daily rhythms of HPT axis induced by chronic unpredicted mild stress in rats. *Endocrine* 2015,48:637–643.
25. Jiang WG, Li SX, Zhou SJ, Sun Y, Shi J, Lu L. Chronic unpredictable stress induces a reversible change of PER2 rhythm in the suprachiasmatic nucleus. *Brain Res* 2011,1399:25–32.
26. Jiang WG, Li SX, Liu JF, Sun Y, Zhou SJ, Zhu WL, *et al.* Hippocampal CLOCK protein participates in the persistence of depressive-like behavior induced by chronic unpredictable stress. *Psychopharmacology (Berl)* 2013,227:79–92.
27. Partonen T. Clock gene variants in mood and anxiety disorders. *J Neural Transm (Vienna)* 2012,119:1133–1145.
28. McClung CA. Circadian rhythms and mood regulation: insights from pre-clinical models. *Eur Neuropsychopharmacol* 2011,21 Suppl 4:S683–693.
29. Roybal K, Theobald D, Graham A, DiNieri JA, Russo SJ, Krishnan V, *et al.* Mania-like behavior induced by disruption of CLOCK. *Proc Natl Acad Sci U S A* 2007,104:6406–6411.
30. Hampp G, Albrecht U. The circadian clock and mood-related behavior. *Commun Integr Biol* 2008,1:1–3.
31. Hampp G, Ripperger JA, Houben T, Schmutz I, Blex C, Perreau-Lenz S, *et al.* Regulation of monoamine oxidase A by circadian-clock components implies clock influence on mood. *Curr Biol* 2008,18:678–683.
32. Spulber S, Conti M, DuPont C, Raciti M, Bose R, Onishchenko N, *et al.* Alterations in circadian entrainment precede the onset of depression-like behavior that does not respond to fluoxetine. *Transl Psychiatry* 2015,5:e603.
33. Wright KP, Jr., Czeisler CA. Absence of circadian phase resetting in response to bright light behind the knees. *Science* 2002,297:571.
34. Honma S. The mammalian circadian system: a hierarchical multi-oscillator structure for generating circadian rhythm. *J Physiol Sci* 2018,68:207–219.
35. Zeitzer JM, Kronauer RE, Czeisler CA. Photopic transduction implicated in human circadian entrainment. *Neurosci Lett* 1997, 232:135–138.
36. Zeitzer JM, Dijk DJ, Kronauer R, Brown E, Czeisler C. Sensitivity of the human circadian pacemaker to nocturnal light: melatonin phase resetting and suppression. *J Physiol* 2000,526 Pt 3:695–702.
37. Duffy JF, Wright KP, Jr. Entrainment of the human circadian system by light. *J Biol Rhythms* 2005,20:326–338.
38. Akashi M, Nishida E. Involvement of the MAP kinase cascade in resetting of the mammalian circadian clock. *Genes & Development* 2000,14:645–649.
39. Plotnikov A, Zehorai E, Procaccia S, Seger R. The MAPK cascades: signaling components, nuclear roles and mechanisms of nuclear translocation. *Biochim Biophys Acta* 2011, 1813:1619–1633.
40. Serchov T, Jilg A, Wolf CT, Radtke I, Stehle JH, Heumann R. Ras activity oscillates in the mouse suprachiasmatic nucleus and modulates circadian clock dynamics. *Mol Neurobiol* 2016, 53:1843–1855.
41. Butcher GQ, Lee B, Obrietan K. Temporal regulation of light-induced extracellular signal-regulated kinase activation in the suprachiasmatic nucleus. *J Neurophysiol* 2003,90:3854–3863.

42. Cheng P, He Q, He Q, Wang L, Liu Y. Regulation of the *Neurospora* circadian clock by an RNA helicase. *Genes Dev* 2005,19:234–241.
43. Eckel-Mahan KL, Phan T, Han S, Wang H, Chan GC, Scheiner ZS, *et al.* Circadian oscillation of hippocampal MAPK activity and cAMP: implications for memory persistence. *Nat Neurosci* 2008,11:1074–1082.
44. Hayashi Y, Sanada K, Fukada Y. Circadian and photic regulation of MAP kinase by Ras- and protein phosphatase-dependent pathways in the chick pineal gland. *FEBS Lett* 2001,491:71–75.
45. Relogio A, Thomas P, Medina-Perez P, Reischl S, Bervoets S, Gloc E, *et al.* Ras-mediated deregulation of the circadian clock in cancer. *PLoS Genet* 2014,10:e1004338.
46. Serchov T, Heumann R. Constitutive activation of ras in neurons: implications for the regulation of the mammalian circadian clock. *Chronobiol Int* 2006,23:191–200.
47. Tsuchiya Y, Minami I, Kadotani H, Todo T, Nishida E. Circadian clock-controlled diurnal oscillation of Ras/ERK signaling in mouse liver. *Proc Jpn Acad Ser B Phys Biol Sci* 2013,89:59–65.
48. Weber F, Hung HC, Maurer C, Kay SA. Second messenger and Ras/MAPK signalling pathways regulate CLOCK/CYCLE-dependent transcription. *J Neurochem* 2006,98:248–257.
49. Butcher GQ, Doner J, Dziema H, Collamore M, Burgoon PW, Obrietan K. The p42/44 mitogen-activated protein kinase pathway couples photic input to circadian clock entrainment. *J Biol Chem* 2002,277:29519–29525.
50. Coogan AN, Piggins HD. MAP kinases in the mammalian circadian system—key regulators of clock function. *J Neurochem* 2004,90:769–775.
51. Schmidt TM, Chen SK, Hattar S. Intrinsically photosensitive retinal ganglion cells: many subtypes, diverse functions. *Trends Neurosci* 2011,34:572–580.
52. Dibner C, Schibler U, Albrecht U. The mammalian circadian timing system: organization and coordination of central and peripheral clocks. *Annu Rev Physiol* 2010,72:517–549.
53. Tischkau SA, Gallman EA, Buchanan GF, Gillette MU. Differential cAMP gating of glutamatergic signaling regulates long-term state changes in the suprachiasmatic circadian clock. *J Neurosci* 2000,20:7830–7837.
54. Ding JM, Chen D, Weber ET, Faiman LE, Rea MA, Gillette MU. Resetting the biological clock - mediation of nocturnal circadian shifts by glutamate and No. *Science* 1994, 266:1713–1717.
55. Farnsworth CL, Freshney NW, Rosen LB, Ghosh A, Greenberg ME, Feig LA. Calcium Activation Of Ras Mediated by Neuronal Exchange Factor Ras-Grf. *Nature* 1995,376:524–527.
56. Wang JQ, Tang QS, Parelkar NK, Liu ZG, Samdani S, Choe ES, *et al.* Glutamate signaling to Ras-MAPK in striatal neurons - Mechanisms for inducible gene expression and plasticity. *Mol Neurobiol* 2004,29:1–14.
57. Butcher GQ, Lee BY, Hsieh F, Obrietan K. Light- and clock-dependent regulation of ribosomal S6 kinase activity in the suprachiasmatic nucleus. *Eur J Neurosci* 2004,19:907–915.
58. Travnickova-Bendova Z, Cermakian N, Reppert SM, Sassone-Corsi P. Bimodal regulation of mPeriod promoters by CREB-dependent signaling and CLOCK/BMAL1 activity. *Proc Natl Acad Sci U S A* 2002,99:7728–7733.
59. Eiden LE, Emery AC, Zhang LM, Smith CB. PACAP signaling in stress: insights from the chromaffin cell. *Pflugers Arch* 2018, 470:79–88.
60. Dziema H, Oatis B, Butcher GQ, Yates R, Hoyt KR, Obrietan K. The ERK/MAP kinase pathway couples light to immediate-early gene expression in the suprachiasmatic nucleus. *Eur J Neurosci* 2003,17:1617–1627.
61. Kornhauser JM, Nelson DE, Mayo KE, Takahashi JS. Photic and circadian regulation of c-fos gene expression in the hamster suprachiasmatic nucleus. *Neuron* 1990,5:127–134.
62. Abe H, Rusak B. Physiological mechanisms regulating photic induction of Fos-like protein in hamster suprachiasmatic nucleus. *Neurosci Biobehav Rev* 1994,18:531–536.
63. Tischkau SA, Mitchell JW, Tyan SH, Buchanan GF, Gillette MU. Ca²⁺/cAMP response element-binding protein (CREB)-dependent activation of Per1 is required for light-induced signaling in the suprachiasmatic nucleus circadian clock. *J Biol Chem* 2003,278:718–723.
64. Roux PP, Blenis J. ERK and p38 MAPK-activated protein kinases: a family of protein kinases with diverse biological functions. *Microbiol Mol Biol Rev* 2004,68:320–344.
65. Mrosovsky N. A non-photic gateway to the circadian clock of hamsters. *Ciba Found Symp* 1995,183:154–167; discussion 167–174.
66. Mrosovsky N. Locomotor activity and non-photic influences on circadian clocks. *Biol Rev Camb Philos Soc* 1996,71:343–372.
67. Antle MC, Tse F, Koke SJ, Sterniczuk R, Hagel K. Non-photic phase shifting of the circadian clock: role of the extracellular signal-responsive kinases I/II/mitogen-activated protein kinase pathway. *Eur J Neurosci* 2008,28:2511–2518.
68. Van Reeth O, Turek FW. Stimulated activity mediates phase shifts in the hamster circadian clock induced by dark pulses or benzodiazepines. *Nature* 1989,339:49–51.
69. Mrosovsky N, Salmon PA. Triazolam and phase-shifting acceleration re-evaluated. *Chronobiol Int* 1990,7:35–41.
70. Marchant EG, Mistlberger RE. Morphine phase-shifts circadian rhythms in mice: role of behavioural activation. *Neuroreport* 1995,7:209–212.
71. Reeb SG, Mrosovsky N. Effects of induced wheel running on the circadian activity rhythms of Syrian hamsters: entrainment and phase response curve. *J Biol Rhythms* 1989,4:39–48.
72. Wickland CR, Turek FW. Phase-shifting effects of acute increases in activity on circadian locomotor rhythms in hamsters. *Am J Physiol* 1991,261:R1109–1117.
73. Mrosovsky N. Phase response curves for social entrainment. *J Comp Physiol A* 1988,162:35–46.
74. Antle MC, Mistlberger RE. Circadian clock resetting by sleep deprivation without exercise in the Syrian hamster. *J Neurosci* 2000,20:9326–9332.
75. Mistlberger RE, Skene DJ. Nonphotic entrainment in humans? *J Biol Rhythms* 2005,20:339–352.
76. Coogan AN, Piggins HD. Dark pulse suppression of P-ERK and c-Fos in the hamster suprachiasmatic nuclei. *Eur J Neurosci* 2005,22:158–168.
77. van Calker D, Biber K. The role of glial adenosine receptors in neural resilience and the neurobiology of mood disorders. *Neurochem Res* 2005,30:1205–1217.
78. Burnstock G, Krugel U, Abbracchio MP, Illes P. Purinergic signalling: from normal behaviour to pathological brain function. *Prog Neurobiol* 2011,95:229–274.
79. Sadek AR, Knight GE, Burnstock G. Electroconvulsive therapy: a novel hypothesis for the involvement of purinergic signalling. *Purinergic Signal* 2011,7:447–452.
80. Serchov T, Heumann R, van Calker D, Biber K. Signaling pathways regulating Homer1a expression: implications for antidepressant therapy. *Biol Chem* 2016,397:207–214.
81. Basheer R, Bauer A, Elmenhorst D, Ramesh V, McCarley RW. Sleep deprivation upregulates A1 adenosine receptors in the rat basal forebrain. *Neuroreport* 2007,18:1895–1899.
82. Elmenhorst D, Basheer R, McCarley RW, Bauer A. Sleep deprivation increases A(1) adenosine receptor density in the rat brain. *Brain Res* 2009,1258:53–58.

83. Elmenhorst D, Meyer PT, Winz OH, Matusch A, Ermert J, Coenen HH, *et al.* Sleep deprivation increases A1 adenosine receptor binding in the human brain: a positron emission tomography study. *J Neurosci* 2007,27:2410–2415.
84. Bekar L, Libionka W, Tian GF, Xu Q, Torres A, Wang X, *et al.* Adenosine is crucial for deep brain stimulation-mediated attenuation of tremor. *Nat Med* 2008,14:75–80.
85. Hamani C, Diwan M, Macedo CE, Brandao ML, Shumake J, Gonzalez-Lima F, *et al.* Antidepressant-like effects of medial prefrontal cortex deep brain stimulation in rats. *Biol Psychiatry* 2010,67:117–124.
86. Biber K, Klotz KN, Berger M, Gebicke-Harter PJ, van Calker D. Adenosine A1 receptor-mediated activation of phospholipase C in cultured astrocytes depends on the level of receptor expression. *J Neurosci* 1997,17:4956–4964.
87. Rogel A, Bromberg Y, Sperling O, Zoref-Shani E. The neuroprotective adenosine-activated signal transduction pathway involves activation of phospholipase C. *Nucleosides Nucleotides Nucleic Acids* 2006,25:1283–1286.
88. Fenton RA, Shea LG, Doddi C, Dobson JG, Jr. Myocardial adenosine A(1)-receptor-mediated adenosine protection involves phospholipase C, PKC-epsilon, and p38 MAPK, but not HSP27. *Am J Physiol Heart Circ Physiol* 2010, 298:H1671–1678.
89. Robin E, Sabourin J, Benoit R, Pedretti S, Raddatz E. Adenosine A1 receptor activation is arrhythmogenic in the developing heart through NADPH oxidase/ERK- and PLC/PKC-dependent mechanisms. *J Mol Cell Cardiol* 2011,51:945–954.
90. Migita H, Kominami K, Higashida M, Maruyama R, Tsuchida N, McDonald F, *et al.* Activation of adenosine A1 receptor-induced neural stem cell proliferation via MEK/ERK and Akt signaling pathways. *J Neurosci Res* 2008,86:2820–2828.
91. Kunduri SS, Mustafa SJ, Ponnath DS, Dick GM, Nayeem MA. Adenosine A1 receptors link to smooth muscle contraction via CYP4a, protein kinase C-alpha, and ERK1/2. *J Cardiovasc Pharmacol* 2013,62:78–83.
92. Qi H, Mailliet F, Spedding M, Rocher C, Zhang X, Delagrè P, *et al.* Antidepressants reverse the attenuation of the neurotrophic MEK/MAPK cascade in frontal cortex by elevated platform stress; reversal of effects on LTP is associated with GluA1 phosphorylation. *Neuropharmacology* 2009,56:37–46.
93. Duric V, Banasr M, Licznarski P, Schmidt HD, Stockmeier CA, Simen AA, *et al.* A negative regulator of MAP kinase causes depressive behavior. *Nat Med* 2010,16:1328–1332.
94. Zhang L, Xu T, Wang S, Yu L, Liu D, Zhan R, *et al.* Curcumin produces antidepressant effects via activating MAPK/ERK-dependent brain-derived neurotrophic factor expression in the amygdala of mice. *Behav Brain Res* 2012,235:67–72.
95. Di Benedetto B, Radecke J, Schmidt MV, Rupprecht R. Acute antidepressant treatment differently modulates ERK/MAPK activation in neurons and astrocytes of the adult mouse prefrontal cortex. *Neuroscience* 2013,232:161–168.
96. Yuan P, Zhou R, Wang Y, Li X, Li J, Chen G, *et al.* Altered levels of extracellular signal-regulated kinase signaling proteins in postmortem frontal cortex of individuals with mood disorders and schizophrenia. *J Affect Disord* 2010,124:164–169.
97. Dwivedi Y, Rizavi HS, Teppen T, Sasaki N, Chen H, Zhang H, *et al.* Aberrant extracellular signal-regulated kinase (ERK) 5 signaling in hippocampus of suicide subjects. *Neuropsychopharmacology* 2007,32:2338–2350.
98. Dwivedi Y, Rizavi HS, Zhang H, Mondal AC, Roberts RC, Conley RR, *et al.* Neurotrophin receptor activation and expression in human postmortem brain: effect of suicide. *Biol Psychiatry* 2009,65:319–328.
99. Dwivedi Y, Rizavi HS, Conley RR, Pandey GN. ERK MAP kinase signaling in post-mortem brain of suicide subjects: differential regulation of upstream Raf kinases Raf-1 and B-Raf. *Mol Psychiatry* 2006,11:86–98.
100. Dwivedi Y, Rizavi HS, Roberts RC, Conley RC, Tamminga CA, Pandey GN. Reduced activation and expression of ERK1/2 MAP kinase in the post-mortem brain of depressed suicide subjects. *J Neurochem* 2001,77:916–928.
101. Barthas F, Humo M, Gilsbach R, Waltisperger E, Karatas M, Leman S, *et al.* Cingulate Overexpression of Mitogen-Activated Protein Kinase Phosphatase-1 as a Key Factor for Depression. *Biol Psychiatry* 2017,82:370–379.
102. Marsden WN. Synaptic plasticity in depression: Molecular, cellular and functional correlates. *Progress In Neuro-Psychopharmacology & Biological Psychiatry* 2013,43:168–184.
103. First M, Gil-Ad I, Taler M, Tarasenko I, Novak N, Weizman A. The effects of fluoxetine treatment in a chronic mild stress rat model on depression-related behavior, brain neurotrophins and ERK expression. *J Mol Neurosci* 2011,45:246–255.
104. Qi X, Lin W, Wang D, Pan Y, Wang W, Sun M. A role for the extracellular signal-regulated kinase signal pathway in depressive-like behavior. *Behav Brain Res* 2009,199:203–209.
105. Qi XL, Lin WJ, Li JF, Pan YQ, Wang WW. The depressive-like behaviors are correlated with decreased phosphorylation of mitogen-activated protein kinases in rat brain following chronic forced swim stress. *Behavioural Brain Research* 2006, 175:233–240.
106. Reus GZ, Vieira FG, Abelaira HM, Michels M, Tomaz DB, dos Santos MA, *et al.* MAPK signaling correlates with the antidepressant effects of ketamine. *J Psychiatr Res* 2014, 55:15–21.
107. Pochwat B, Rafalo-Ulinska A, Domin H, Misztak P, Nowak G, Szewczyk B. Involvement of extracellular signal-regulated kinase (ERK) in the short and long-lasting antidepressant-like activity of NMDA receptor antagonists (zinc and Ro 25-6981) in the forced swim test in rats. *Neuropharmacology* 2017, 125:333–342.
108. Labonte B, Engmann O, Purushothaman I, Menard C, Wang J, Tan C, *et al.* Sex-specific transcriptional signatures in human depression. *Nat Med* 2017,23:1102–1111.
109. Quan MN, Zhang N, Wang YY, Zhang T, Yang Z. Possible antidepressant effects and mechanisms of memantine in behaviors and synaptic plasticity of a depression rat model. *Neuroscience* 2011,182:88–97.
110. Covington HE, 3rd, Vialou V, Nestler EJ. From synapse to nucleus: novel targets for treating depression. *Neuropharmacology* 2010,58:683–693.
111. Mailliet F, Qi H, Rocher C, Spedding M, Svenningsson P, Jay TM. Protection of stress-induced impairment of hippocampal/prefrontal LTP through blockade of glucocorticoid receptors: implication of MEK signaling. *Exp Neurol* 2008,211:593–596.
112. Pflüg B, Tolle R. Disturbance of the 24-hour rhythm in endogenous depression and the treatment of endogenous depression by sleep deprivation. *Int Pharmacopsychiatry* 1971,6:187–196.
113. Balsalobre A, Damiola F, Schibler U. A serum shock induces circadian gene expression in mammalian tissue culture cells. *Cell* 1998,93:929–937.
114. Thompson CL, Wisor JP, Lee CK, Pathak SD, Gerashchenko D, Smith KA, *et al.* Molecular and anatomical signatures of sleep deprivation in the mouse brain. *Front Neurosci* 2010,4:165.
115. Wisor JP, Pasumarthi RK, Gerashchenko D, Thompson CL, Pathak S, Sancar A, *et al.* Sleep deprivation effects on circadian clock gene expression in the cerebral cortex parallel electroencephalographic differences among mouse strains (vol 28, pg 7193, 2008). *J Neurosci* 2008,28:7929–7929.

116. Wisorl JP, O'Hara BF, Terao A, Selby CP, Kilduff TS, Sancar A, *et al.* A role for cryptochromes in sleep regulation. *Bmc Neuroscience* 2002,3.
117. Maret S, Dorsaz S, Gurcel L, Pradervand S, Petit B, Pfister C, *et al.* Homer1a is a core brain molecular correlate of sleep loss. *Proc Natl Acad Sci U S A* 2007,104:20090–20095.
118. Zagaar M, Dao A, Levine A, Alhaider I, Alkadhi K. Regular exercise prevents sleep deprivation associated impairment of long-term memory and synaptic plasticity in the CA1 area of the hippocampus. *Sleep* 2013,36:751–761.
119. Serchov T, Clement HW, Schwarz MK, Iasevoli F, Tosh DK, Idzko M, *et al.* Increased Signaling via Adenosine A1 Receptors, Sleep Deprivation, Imipramine, and Ketamine Inhibit Depressive-like Behavior via Induction of Homer1a. *Neuron* 2015,87:549–562.
120. Hines DJ, Schmitt LI, Hines RM, Moss SJ, Haydon PG. Antidepressant effects of sleep deprivation require astrocyte-dependent adenosine mediated signaling. *Transl Psychiatry* 2013,3:e212.
121. LeGates TA, Fernandez DC, Hattar S. Light as a central modulator of circadian rhythms, sleep and affect. *Nat Rev Neurosci* 2014,15:443–454.
122. Li X, Li X. The antidepressant effect of light therapy from retinal projections. *Neurosci Bull* 2018,34:359–368.
123. Duncan WC, Jr., Slonena E, Hejazi NS, Brutsche N, Yu KC, Park L, *et al.* Motor-activity markers of circadian timekeeping are related to ketamine's rapid antidepressant properties. *Biol Psychiatry* 2017.
124. Bellet MM, Vawter MP, Bunney BG, Bunney WE, Sassone-Corsi P. Ketamine influences CLOCK:BMAL1 function leading to altered circadian gene expression. *PLoS One* 2011,6:e23982.
125. Ma Z, Zang T, Birnbaum SG, Wang Z, Johnson JE, Zhang CL, *et al.* TrkB dependent adult hippocampal progenitor differentiation mediates sustained ketamine antidepressant response. *Nat Commun* 2017,8:1668.
126. Yang C, Ren Q, Qu YG, Zhang JC, Ma M, Dong C, *et al.* Mechanistic target of rapamycin-independent antidepressant effects of (R)-Ketamine in a social defeat stress model. *Biol Psychiatry* 2018,83:18–28.
127. Orozco-Solis R, Montellier E, Aguilar-Arnal L, Sato S, Vawter MP, Bunney BG, *et al.* A circadian genomic signature common to ketamine and sleep deprivation in the anterior cingulate cortex. *Biol Psychiatry* 2017,82:351–360.
128. Lazzarini Ospri L, Prusky G, Hattar S. Mood, the circadian system, and melanopsin retinal ganglion cells. *Annu Rev Neurosci* 2017,40:539–556.



REVIEW

Connections Between Insomnia and Cognitive Aging

Claire E. Sexton^{1,2} · Konstantina Sykara³ · Elissaios Karageorgiou^{1,3} ·
Jenny Zitser¹ · Talita Rosa¹ · Kristine Yaffe⁴ · Yue Leng^{1,4}

Received: 17 December 2018 / Accepted: 19 March 2019 / Published online: 20 June 2019
© Shanghai Institutes for Biological Sciences, CAS 2019

Abstract Insomnia is a common sleep disorder among older adults, and a risk factor for poor physical and mental health. However, the relationship between insomnia and cognitive health is not well understood. Here, we review observational studies that have investigated whether insomnia is associated with deficits in objective cognitive performance and an increased risk of dementia, magnetic resonance imaging studies that have assessed grey matter volumes and white matter microstructure, and interventional studies that have explored whether the treatment of insomnia can improve cognitive outcomes. There are inconsistent findings regarding impaired performance in objective cognitive tests and reduced grey matter volumes, and limited, emerging, evidence that suggests that insomnia is associated with an increased risk of dementia and reduced white matter integrity. Although the interventional literature is still in its infancy, there is some indication that treatment may have an impact on vigilance. Well-powered studies examining sources of heterogeneity are warranted.

Keywords Insomnia · Sleep · Dementia · Cognition

Electronic supplementary material The online version of this article (<https://doi.org/10.1007/s12264-019-00401-9>) contains supplementary material, which is available to authorized users.

✉ Yue Leng
yue.leng@ucsf.edu

¹ Global Brain Health Institute, Memory and Aging Center, Department of Neurology, University of California, San Francisco, CA, USA

² Department of Psychiatry, University of Oxford, Oxford, UK

³ Neurological Institute of Athens, Athens, Greece

⁴ Department of Psychiatry, Neurology and Epidemiology, University of California, San Francisco, CA, USA

Introduction

Insomnia is a common sleep disorder among older adults, up to 50% of whom report symptoms of insomnia and, depending on the diagnostic guidelines used, up to 20% meet the criteria for insomnia disorder [1]. Symptoms of insomnia include difficulty in initiating sleep, maintaining sleep continuity, or waking up earlier than desired, despite adequate opportunity for sleep. For a clinical diagnosis of chronic insomnia disorder to be made according to the most recent guidelines, symptoms must be present at least three times a week, for at least three months, and be associated with daytime consequences [2, 3]. Insomnia is thought to stem from graded contributions of cognitive-behavioral and neurophysiologic processes, and a range of models have been proposed to explain its etiology (Table S1). Treatments span pharmacological (e.g. benzodiazepines and benzodiazepine-receptor agonists) and non-pharmacological [e.g. cognitive behavioral therapy for insomnia (CBT-I)] approaches, with evidence-based guidelines concluding that CBT-I is superior to hypnotic treatment in terms of therapeutic efficiency in both the short and long term [4]. Insomnia is an established risk factor for poor physical and mental health [5], and has also been proposed as a risk factor for poor cognitive health [6, 7]. Indeed, over the past decade, insomnia has variably been associated with deficits in objective cognitive functioning, increased risk of dementia, and reductions in grey matter volume and white matter integrity in networks essential for cognitive functioning. The possibility that successful treatment of insomnia could impact on cognitive markers is a tantalizing prospect.

Enthusiasm, however, regarding the extent to which insomnia represents a noteworthy modifiable risk factor for cognitive health in aging has been dampened by frequent

null findings. To provide an update on the research landscape, we review observational and interventional research published over the past 10 years that has explored the relationship between insomnia and cognitive health in mid- and late-life (>40 years of age), from three different perspectives. First, we summarize observational studies that have examined whether insomnia is associated with deficits in objective cognitive performance and an increased risk of dementia. Second, we review magnetic resonance imaging (MRI) studies that have assessed grey matter volumes and white matter microstructure in insomnia. Third, we present interventional studies that have investigated whether treatment of insomnia can improve cognitive outcomes. Through considering all three approaches, we aim to review whether the results are consistent within each approach, before considering whether the findings are complimentary across approaches.

Review of Evidence

Given that heterogeneity between studies may, in part, result from variations in the classification of insomnia (i.e. from the symptom to the disorder level) and small sample sizes, our review focuses on studies that used diagnostic criteria for insomnia, did not list a specific co-morbidity as an inclusion criterion, and included at least 20 participants with insomnia.

Objective Cognitive Functioning and Risk of Dementia

Table 1 provides an overview of studies of insomnia in mid- and late-life that have examined objective cognitive functioning. With regard to general cognitive function, null findings [8–10] outnumber studies that report significant deficits in insomnia [11]. With regard to specific cognitive domains, reduced performance in insomnia has been reported in individual tests spanning attention [10, 12], episodic memory [8, 10], working memory [11, 13], executive function [10], and language [10]. However, the number of null findings for individual tests is substantial [9, 14, 15]. Interestingly, while significant findings from individual cognitive tests are sporadic, pooling of measures by domain by calculating composite measures may be more sensitive in detecting group differences. Reduced performance with insomnia has been reported for composite scores for attention and episodic memory [8], as well as for working memory, verbal information processing, verbal memory, verbal fluency, and visual memory [16].

Although insomnia has typically not been included in reviews of modifiable risk factors for dementia [23, 24], an increasing number of epidemiological studies have examined the effects of insomnia on cognition in older adults. However, three systematic reviews and meta-analyses have been inconsistent in their findings [25–27]. To the best of our knowledge, only two studies have used diagnostic criteria to assess insomnia. One study of 179,738 male veterans (aged 55 years and older) from the Department of Veterans Affairs National Patient Care Database suggested that those with insomnia were 26% more likely to develop Alzheimer's disease over 8 years of follow-up, but were not significantly more likely to develop vascular dementia or Lewy body dementia [28]. Another study using Taiwan's National Health Insurance Research Database found that patients (aged 50 years and older) with insomnia and long-term use of hypnotics had more than double the risk of dementia over 3 years [29]. While these two studies both supported the idea that insomnia could be a risk factor for dementia, further confirmatory longitudinal studies from different population settings are needed.

Grey Matter Volume and White Matter Microstructure

In order to understand the biological processes that may underlie cognitive deficits in insomnia, a growing number of studies have used MRI techniques to examine differences in grey matter volumes and white matter microstructure between insomnia and control groups (Table 2). Even though certain studies indicate reduced volume of the hippocampus [16], frontal cortex [30], and pineal gland [31] in participants with insomnia compared to controls, findings are not consistent across studies, especially after full correction for multiple comparisons across space [10, 32, 33]. Two papers, which used overlapping samples, related grey matter volumes to cognitive performance. Cognitive tests scores were not significantly associated with grey matter in voxel-based morphometry analyses [10], but reduced composite measures of verbal memory, processing, and fluency scores were associated with atrophy of the dentate gyrus and the CA2-4 subfields of the hippocampus [16].

While fewer studies have examined white matter microstructure, the results appear to be more consistent, with two diffusion tensor imaging studies reporting significant reductions in fractional anisotropy in insomnia within fronto-subcortical tracts, indicating a decline in white matter integrity [34, 35]. Interestingly, such regions have also been implicated in studies of insomnia disorder in younger age groups [36] and studies of poor sleep quality in older adults [37].

Table 1 Clinical studies assessing objective cognitive functioning.

Study (Country)	Demographics			Insomnia			Methods & Results
	N	Age (years)	% Female	Diagnostic Criteria	Duration (years)	PSQI	
Zhang <i>et al.</i> 2018 [11] (China)	I: 34 C: 17	I: 41.1 ± 10.1 C: 41.4 ± 9.9	I: 64 C: 47	DSM-V	≥ 0.5	14.0 [^] [13.0, 16.0]	MoCA-C* , <i>9-Box Maze</i> – ORcM* , SWM* , OWM* , SRM, ORM
Chen <i>et al.</i> 2016 [13] (China)	I: 21 C: 20	I: 41.8 ± 10.4 C: 38.1 ± 10.4	I: 71 C: 65	ICSD-3	≥ 0.5	17.0 [^] [14.0, 19.0]*	<i>9-Box Maze</i> – ORcM* , SWM* , OWM, SRM, ORM
Li <i>et al.</i> 2016 [17] (China)	I: 36 C: 25	I: 40.4 ± 12.36 C: 39.9 ± 12.5	I: 43 C: 47	DSM-IV-TR	≥ 0.5	14.3 ± 2.9	<i>ANT</i> - Accuracy, RT, Alertness, Orientation, Executive*
Fortier-Brochu <i>et al.</i> 2014 [8] (Canada)	I: 25 C: 16	I: 44.0 ± 11.5 C: 42.8 ± 12.9	I: 56 C: 50	DSM-IV / ICD-10	17.3 ± 13.1	N/A	MMSE Attention Composite* : <i>CPT-II</i> – Hit Rate, Hit Rate Block Rate, Omissions, Commissions, Detectability, Perseverations Working Memory Composite: <i>Digit Span</i> - Forward, Backward; PASAT, <i>CVLT-II</i> – Trial 1 Episodic Memory Composite* : <i>CVLT-II</i> – Trial 5, Delayed Recall, Repetitions, Intrusions* Executive Function Composite: <i>Tower</i> - Executive, Violations; <i>Verbal Fluency</i> – Alphabetic, Category, % Set Loss Errors, % Repetition Errors
Liu <i>et al.</i> 2014 [18] (China)	I: 36 C: 26	I: 42.0 ± 11.0 C: 40.5 ± 12.0	I: 58 C: 62	DSM-IV	6.5 ± 6.0	13.6 ± 3.4	<i>ANT</i> – Alertness, Orientation, Executive*
Lovato <i>et al.</i> 2013 [15] (Australia)	I: 49 C: 49	I: 70.0 ± 9.3 C: 69.4 ± 4.8	I: 55 C: 55	Not specified	≥ 0.5	11.7 ± 2.6	<i>Double Span Memory</i> – Objects, Locations, Double
Sivertsen <i>et al.</i> 2013 [9] (Norway)	I: 30 C: 91	T: 64.0 ± 7.6	T: 69	DSM-IV-TR	N/A	N/A	MMSE Processing Speed: <i>CWIT</i> – Reading, Naming; Verbal Fluency – FAS, Category; TMT A Executive Function: <i>CWIT</i> – Inhibition, Inhibition / Switching; FAS Category Switching; Letter Number; TMT B; Coding Memory: <i>CVLT</i> – Learning, Short Delay, Long Delay, Recognition; <i>RCF</i> – Immediate, Delay, Recognition Visual Cognition: WASI Matrix Reasoning, <i>Rey</i> – Copy <i>CDT</i> – Accuracy, RT, Valid RT, Invalid RT, Neutral RT, Nocue RT
Joo <i>et al.</i> 2014 [16] (A) (South Korea)	I: 27 C: 30	I: 51.2 ± 9.6 C: 50.4 ± 7.1	I: 93 C: 93	ICSD-2	8.4 ± 9.1 [≥ 1]	14.9 ± 4.6	Working Memory Composite* ; Executive Function Composite; Verbal Information Processing Composite* ; Verbal Memory Composite* ; Verbal Fluency Composite* ; Visual Memory Composite*
Joo <i>et al.</i> 2013 [10] (A) (South Korea)	I: 27 C: 27	I: 52.3 ± 7.8 C: 51.7 ± 5.4	I: 93 C: 85	ICSD-2	7.6 ± 6.1 [≥ 1]	19.1 ± 4.3	MMSE Attention: <i>Digit Span</i> – Forward, Backward; <i>Corsi</i> – Forward, Backward; TMT – A, B; Digit Symbol* Visuospatial Function: RCF Memory: <i>RCF</i> – Immediate Recall* , Delayed Recall* , Recognition* ; <i>Korean-CVLT</i> – Total, Short Delay, Long Delay, Recognition Language: Korean Boston Naming Test* Executive: <i>COWAT</i> – Animal, Supermarket, Phonemic; <i>Stroop</i> – Word, Color*
Nissen <i>et al.</i> 2011 [14] (Germany)	I: 33 C: 53	I: 46.2 ± 5.1 C: 46.7 ± 4.7	I: 58 C: 60	DSM-IV	N/A	11.7 ± 6.6	<i>Mirror Tracing</i> – Draw Time, Error Count, Error Time; Verbal Memory; Visual Memory; Short-Term Memory; Psychomotor Speed; Alertness; Divided Attention

Table 1 continued

Study (Country)	Demographics			Insomnia			Methods & Results
	N	Age (years)	% Female	Diagnostic Criteria	Duration (years)	PSQI	
Altena <i>et al.</i> 2008 [12] (Netherlands)	I: 25 C: 13	I: 60.6 ± 6.0 C: 60.1 ± 8.3	I: 72 C: 69	DSM-IV	N/A	12.3 ± 3.1	Cognitive Measures – Significant Group Differences in Bold *Reduced Performance in Insomnia Group <i>Simple Vigilance</i> – Lapses; <i>Complex Vigilance</i> – Lapses, False Positives; Complex / Simple Reaction Time Ratio*

Unless otherwise indicated, values are the mean ± SD. ^ denotes P50 [P25, P75] for non-normally distributed variables. (A) indicates overlapping samples.

ANT: Attention Network Task; C: Control Group; CDT: Cued Visual Discrimination Task; COWAT: Controlled Oral Word Association Test; CPT: Conners Continuous Performance Test; CVLT: California Verbal Learning Test; CWIT: Color-Word Interference Test; DSM: Diagnostic and Statistical Manual of Mental Disorders [3, 19, 20]; I: Insomnia Group; ICD: International Classification of Disease [21]; ICSD: International Classification of Sleep Disorders [2, 22]; MoCA-C: Montreal Cognitive Assessment – Chinese-Beijing; MMSE: Mini-Mental State Examination; N/A: Not Applicable; ORcM: Object Recognition Memory; ORM: Object Recognition Memory; OWM: Object Working Memory; PASAT: Paced Auditory Serial Addition Task; RCF: Rey Complex Figure; RT: Reaction Time; SRM: Spatial Recognition Memory; SWM: Spatial Working Memory; T: Total; TMT: Trail Making Test.

Interventional Studies

Although, to the best of our knowledge, there have been no interventional studies examining the effect of treatments for insomnia on the risk of dementia or structural MRI outcomes, a growing literature is exploring whether successful treatment of insomnia has an impact on objective cognitive functioning.

In a study of 77 adults over the age of 60 who met DSM-IV-TR and ICSD-2 criteria for insomnia, Wilckens *et al.* [38] found that a 4-week brief behavioral treatment of insomnia did not improve performance in tests of recall, working memory, or reasoning compared with the provision of sleep information as a control condition. This was despite significant decreases in waking after sleep onset in the treatment group compared with the control group.

In a study of 25 adults meeting the DSM-IV criteria for primary insomnia, a six-week multi-component intervention (including sleep restriction, cognitive behavioral therapy, bright-light therapy, physical activity, and body temperature manipulations) restored reaction time in a test of psychomotor vigilance to a level comparable to that displayed by a control group without insomnia (reducing reaction time in a simple vigilance task, and increasing reaction time in a complex vigilance task) [12].

Finally, in a study of 46 adults over the age of 55 who met the DSM-IV criteria for insomnia, participants were randomized into a 6-week program of CBT-I, a hypnotic treatment group (Zopiclone), or a placebo control group [39]. Across CBT-I and Zopiclone groups, reaction time performance in a vigilance task improved both at post-treatment and at 6-month follow-up assessments. There were no significant group-by-time interactions in reaction time or number of correct responses. Performance on the number of correct responses in the vigilance task worsened significantly in the CBT-I group post-treatment, but not at

follow-up. This final finding likely reflects CBT-I implementing time-in-bed restriction in the early stages of treatment. Indeed, it is consistent with a study of younger adults who met the research criteria for insomnia, in which 4 weeks of sleep restriction therapy was shown to be associated with increases in psychomotor vigilance test lapses within the acute treatment phase, returning to baseline levels by 3-month follow-up [40].

Discussion

We reviewed a range of observational and interventional studies that have investigated the relationship between insomnia and measures of cognitive health in ageing. From the observational studies, the evidence is mixed regarding impaired performance in objective cognitive tests and reduced grey matter volumes. There is limited, emerging evidence suggesting that insomnia is associated with an increased risk of dementia and reduced white matter integrity. From the interventional studies, although the literature is still in its infancy, there is some indication that treatment of insomnia may have an impact on reaction time in vigilance tasks.

Given the variation in results for objective cognitive functioning and grey matter volumes, and the limited number of studies on the risk of dementia or white matter microstructure, it is no surprise that it is challenging to draw strong conclusions on the concordance between different observational approaches. For example, it is not the case that cognitive studies consistently highlight a particular cognitive domain, and MRI studies consistently report structural deficits in networks essential for that cognitive domain. To shed further light on this area, it is encouraging that a growing number of studies are investigating the anatomical substrates of cognitive deficits in

Table 2 Case-control MRI studies examining grey matter volume or white matter microstructure.

	Demographics			Insomnia			Method	Group Differences
	N	Age (years)	% Female	Diagnostic Criteria	Duration (years)	PSQI		
Dai <i>et al.</i> 2018 [32] (China)	I: 39 C: 39	I: 48.9 ± 11.4 C: 47.9 ± 9.2	I: 74 C: 67	ICSD-2	6.5 ± 5.7 [>1]	15.1 ± 2.2	GM: GMV, VBM	No significant differences
Li <i>et al.</i> 2016 [35] (China)	C: 23 I: 30	C: 41.1 ± 10.5 I: 41.6 ± 9.5	I: 57 C: 40	DSM-IV	1.5 ± 1.7	13.4 ± 3.2	WM: Tract Based Spatial Statistics	↓ FA in anterior and posterior limb of internal capsule, anterior and superior corona radiata, superior longitudinal fasciculus, corpus callosum. No significant differences in AxD, RD or MD.
Bumb <i>et al.</i> 2014 [31] (Germany)	I: 23 C: 27	I: 43 ± 7.4 C: 39 ± 13.1	I: 48 C: 59	DSM-IV-TR, ICSD-2	8.6 ± 7.3 [0.5 – 30]	N/A	GM: ROI – Pineal Gland	↓ Pineal gland
Joo <i>et al.</i> 2014 [16] (A) (South Korea)	I: 27 C: 30	I: 51.2 ± 9.6 C: 50.4 ± 7.1	I: 93 C: 93	ICSD-2	8.4 ± 9.1 [≥ 1]	14.9 ± 4.6	GM: ROI –	Hippocampus
↓ Hippocampus								
Spiegelhalder <i>et al.</i> 2014 [34] (B) (Germany)	I: 24 C: 35	I: 42.7 ± 14.5 C: 40.1 ± 9.1	I: 58 C: 57	DSM-IV-TR	12.0 ± 10.9	11.2 ± 2.8	WM: VW	↓ FA in anterior internal capsule
Joo <i>et al.</i> 2013 [10] (A) (South Korea)	I: 27 C: 27	I: 52.3 ± 7.8 C: 51.7 ± 5.4	I: 93 C: 85	ICSD-2	7.6 ± 6.1 [≥ 1]	19.1 ± 4.3	GM: VBM	No significant differences
Spiegelhalder <i>et al.</i> 2013 [33] (B) (Germany)	I: 28 C: 38	I: 43.7 ± 14.2 C: 39.6 ± 8.9	I: 64 C: 55	DSM-IV-TR	12.1 ± 11	10.9 ± 3.0	GM: ROI – Freesurfer Cortical Volumes; VBM	No significant differences
Altena <i>et al.</i> 2010 [30] (Netherlands)	I: 24 C: 13	I: 60.3 ± 6.0 C: 60.2 ± 8.4	I: 71 C: 69	DSM-IV	17.7 ± 15.8 [2.5 – 50]	12.1 ± 3.0	GM: VBM	↓ OFC

Only results after correction for multiple comparisons are presented. Values are the mean ± SD. (A, B) indicates overlapping samples.

↓, reduced in insomnia; ↑, increased in insomnia; AxD, axial diffusivity; C, control group; DLPFC, dorsolateral prefrontal cortex; DSM, Diagnostic and Statistical Manual of Mental Disorders [3, 19, 20]; FA, fractional anisotropy; GM, grey matter; GMV, total grey matter volume; I, insomnia group; ICD, International Classification of Disease [21]; ICSD, International Classification of Sleep Disorders [2, 22]; MD, mean diffusivity; N/A, not applicable; OFC, orbitofrontal cortex; rACC, rostral anterior cingulate cortex; RD, radial diffusivity; ROI, region of interest; VBM, voxel-based morphometry; VW, voxel-wise; WM, white matter.

insomnia within their samples, although the results remain mixed. Clearly, further studies are needed before a consensus can be reached.

Variability in results between studies may not only stem from differences in approach, but also from differences in the demographics of participants (age, gender, and nationality), illness characteristics (diagnosis, duration, severity, and treatment status) and methods (cognitive test or MRI analysis tool). Since a full consideration of every factor that may have influenced the results is outside the scope of

this review, we instead highlight the possible role of diagnostic criteria and the duration of insomnia.

While we limited our review to studies that used recognized diagnostic criteria for insomnia (DSM-IV, DSM-IV-TR, DSM-V, ICD-9, ICD-10, ICSD-2, or ICSD-3), the criteria differ in quantitative thresholds, meaning that insomnia samples are still heterogeneous in nature. Such heterogeneity was illustrated in the results of the America Insomnia Survey, in which insomnia prevalence estimates varied from 4% when based on ICD-10 criteria to

22% when based on DSM-IV-TR criteria [41]. While limiting diagnoses to the most severe cases may be more sensitive in detecting relationships with cognitive outcomes, relevant cases may be missed. Well-powered studies examining different diagnoses and the exact phenotyping of insomnia features (sleep-maintenance *versus* sleep-onset *vs* early-awakening) are warranted. In addition, to reduce sources of heterogeneity, studies that listed a specific co-morbidity as an inclusion criterion were considered outside the scope of this review. However, it is important to note that insomnia is often co-morbid with psychiatric disorders, medical conditions, and/or other sleep disorders [42]. The extent to which such co-morbidities have been considered by research studies varies between approaches. For example, in a recent review that evaluated the impact of CBT-I on cognitive outcomes, insomnia was co-morbid with a physical or mental health condition in the majority of included studies [43]. This is in contrast with the MRI literature, where specific co-morbidities have rarely been examined. Given that the relationship between insomnia and cognitive health may differ depending on the presence and nature of co-morbidities, this is an important area for future research.

Duration of illness may also influence results. While the duration of insomnia was variably reported by case-control studies of cognition, it was consistently included in MRI studies. Across studies assessing grey matter volume, the mean duration of insomnia ranged between 1.5 and 17.7 years, with the shortest duration 0.5 years and longest 50 years. If insomnia causes reductions in grey matter volume, then it follows that increased duration could have cumulative effects on brain structure, and be associated with greater reductions in volume. Certain studies indicate that increased duration of insomnia is associated with reduced hippocampal volume [44], however, others have not found associations between duration and MRI measures after correction for multiple comparisons [10, 16, 30–32]. It is important to note, though, that duration is often poorly defined. For example, in most cases it is unclear whether duration is calculated from symptom onset or first diagnosis, and whether it is based on self-reports or corroborated by others and/or objective measurements. Going forward, a careful consideration of the duration of insomnia and its relation to outcome measures, by both observational and interventional studies, has the potential to yield important insights for the field.

The reviewed literature builds on a substantial literature that suggests that sleep plays a critical role in maintaining cognitive health. Transcriptomic studies have highlighted the protective role of sleep on oligodendrocyte function and myelination [45]. Animal studies indicate that prolonged restriction or disruption of sleep has cumulative effects on the brain, for example leading to reduced

hippocampal cell proliferation, cell survival, and neurogenesis [46]. Meanwhile, in humans, experimental studies have shown that sleep deprivation is associated with significantly reduced performance on tests of attention, working and short-term memory [47], and widespread changes in white matter microstructure [48]. It follows that the reduced quality or quantity of sleep in insomnia may impact on cognitive health.

Symptoms of insomnia in older populations may also be a direct consequence of age- or early neurodegeneration-related changes in networks essential for sleep onset and maintenance, consistent with a neurobiological model of insomnia (Table S1). Indeed, there has been a particular focus on the relationship between sleep and Alzheimer's pathology. For example, pathology studies indicate that the IPA/VLPO neuronal loss in Alzheimer's disease is not significant in age-matched controls [49], and amyloid-precursor protein/amyloid β overproduction causes disrupted sleep in animal models [50]. The relationship between sleep and Alzheimer's pathology is proposed to be bi-directional, though, with sleep disruption also linked to increased production and decrease clearance of amyloid β [50]. In addition, modelling sleep-wake dysregulation in Alzheimer's disease allows for linking its two core pathologies, tauopathy and amyloidopathy [51], in a *bi-directional* relationship between sleep and pathology. Specifically, the presence of early tau pathology in sleep-wake regulating nuclei (Braak stages I/II) [52–54], leads to decreased attenuation of cortical activity during sleep, which in turn promotes subsequent cortical amyloid pathology *via* activity-dependent amyloid deposition [55, 56].

Conclusion

In conclusion, there is mixed evidence for impaired performance in objective cognitive tests and reduced grey matter volumes, and emerging evidence of an increased risk of dementia and reduced white matter integrity. Overall, the heterogeneity could be attributed to different demographics of the participants, illness characteristics, and methods used. Further longitudinal studies are needed to determine whether insomnia is a true risk factor for dementia, and the inclusion of biomarkers and MRI measures would help to understand the underlying mechanisms. Ultimately, intervention studies that assess the effects of insomnia treatment on cognition might help open up new opportunities for the prevention of cognitive decline and dementia in the long run.

Acknowledgements This review was supported in part by the Global Brain Health Institute and Alzheimer's Association (GBHI ALZ-18-

543785, GBHI ALZ UK-19-588605), the National Institute for Health Research Oxford Health Biomedical Research Centre, the Tau Consortium, the American Brain Foundation (AANF-14-ALZ330017), and the National Institute on Aging (1K99AG056598).

Conflict of interest CES reports consulting fees from Jazz Pharmaceuticals.

References

- Patel D, Steinberg J, Patel P. Insomnia in the elderly: A review. *J Clin Sleep Med* 2018, 14: 1017–1024.
- American Academy of Sleep Medicine. The International Classification of Sleep Disorders, 3rd ed (ICSD-3). 2014.
- American Psychiatric A. Diagnostic and Statistical Manual of Mental Disorders. 5th ed. Arlington, VA, 2013.
- Riemann D, Baglioni C, Bassetti C, Bjorvatn B, Dolenc Groselj L, Ellis JG, *et al.* European guideline for the diagnosis and treatment of insomnia. *J Sleep Res* 2017, 26: 675–700.
- Taylor DJ, Lichstein KL, Durrence HH. Insomnia as a health risk factor. *Behav Sleep Med* 2003, 1: 227–247.
- Yaffe K, Falvey CM, Hoang T. Connections between sleep and cognition in older adults. *Lancet Neurol* 2014, 13: 1017–1028.
- Irving K, Hogervorst E, Oliveira D, Kivipelto M. *New Developments in Dementia Prevention Research. State of the Art and Future Possibilities*, 1st ed., Routledge, 2018.
- Fortier-Brochu E, Morin CM. Cognitive impairment in individuals with insomnia: clinical significance and correlates. *Sleep* 2014, 37: 1787–1798.
- Sivertsen B, Hysing M, Wehling E, Pallesen S, Nordhus IH, Espeseth T, *et al.* Neuropsychological performance in older insomniacs. *Neuropsychol Dev Cogn B Aging Neuropsychol Cogn* 2013, 20: 34–48.
- Joo EY, Noh HJ, Kim JS, Koo DL, Kim D, Hwang KJ, *et al.* Brain gray matter deficits in patients with chronic primary insomnia. *Sleep* 2013, 36: 999–1007.
- Zhang P, Tan CW, Chen GH, Ge YJ, Xu J, Xia L, *et al.* Patients with chronic insomnia disorder have increased serum levels of neurofilaments, neuron-specific enolase and S100B: does organic brain damage exist? *Sleep Med* 2018, 48: 163–171.
- Altena E, Van Der Werf YD, Strijers RLM, Van Someren EJ. Sleep loss affects vigilance: effects of chronic insomnia and sleep therapy. *J Sleep Res* 2008, 17: 335–343.
- Chen GH, Xia L, Wang F, Li XW, Jiao CA. Patients with chronic insomnia have selective impairments in memory that are modulated by cortisol. *Psychophysiology* 2016, 53: 1567–1576.
- Nissen C, Kloepfer C, Feige B, Piosczyk H, Spiegelhalder K, Voderholzer U, *et al.* Sleep-related memory consolidation in primary insomnia. *J Sleep Res* 2011, 20: 129–136.
- Lovato N, Lack L, Wright H, Cant M, Humphreys J. Working memory performance of older adults with insomnia. *J Sleep Res* 2013, 22: 251–257.
- Joo EY, Kim H, Suh S, Hong SB. Hippocampal substructural vulnerability to sleep disturbance and cognitive impairment in patients with chronic primary insomnia: magnetic resonance imaging morphometry. *Sleep* 2014, 37: 1189–1198.
- Li Y, Liu H, Weed JG, Ren R, Sun Y, Tan L, *et al.* Deficits in attention performance are associated with insufficiency of slow-wave sleep in insomnia. *Sleep Med* 2016, 24: 124–130.
- Liu H, Wang D, Li Y, Li Z, Zhang Y, Lei F, *et al.* Examination of daytime sleepiness and cognitive performance testing in patients with primary insomnia. *PLoS One* 2014, 9: e100965.
- American Psychiatric Association. *Diagnostic and Statistical Manual of Mental Disorders*. 4th ed., APA Press, Washington DC, 1994.
- American Psychiatric Association. *Diagnostic and Statistical Manual of Mental Disorders*. 4th-TR ed., APA Press, Washington DC, 2000.
- World Health Organization. *ICD-10 Classifications of Mental and Behavioural Disorder: Clinical Descriptions and Diagnostic Guidelines*. Geneva, Switzerland, 1992.
- American Academy of Sleep Medicine. *The International Classification of Sleep Disorders*, 2nd ed. (ICSD-2), Diagnostic and Coding Manual, Westchester, 2005.
- Livingston G, Sommerlad A, Orgeta V, Costafreda SG, Huntley J, Ames D, *et al.* Dementia prevention, intervention, and care. *Lancet* 2017, 390: 2673–2734.
- Barnes DE, Yaffe K. The projected effect of risk factor reduction on Alzheimer's disease prevalence. *Lancet Neurol* 2011, 10: 819–828.
- de Almondes KM, Costa MV, Malloy-Diniz LF, Diniz BS. Insomnia and risk of dementia in older adults: Systematic review and meta-analysis. *J Psychiatr Res* 2016, 77: 109–115.
- Shi L, Chen SJ, Ma MY, Bao YP, Han Y, Wang YM, *et al.* Sleep disturbances increase the risk of dementia: a systematic review and meta-analysis. *Sleep Med Rev* 2018, 40: 4–16.
- Bubu OM, Brannick M, Mortimer J, Umasabor-Bubu O, Sebastião YV, Wen Y, *et al.* Sleep, cognitive impairment, and Alzheimer's disease: A systematic review and meta-analysis. *Sleep* 2017, 40. doi: 10.1093/sleep/zsw032.
- Yaffe K, Nettiksimmons J, Yesavage J, Byers A. Sleep quality and risk of dementia among older male veterans. *Am J Geriatr Psychiatry* 2015, 23: 651–654.
- Chen PL, Lee WJ, Sun WZ, Oyang YJ, Fuh JL. Risk of dementia in patients with insomnia and long-term use of hypnotics: a population-based retrospective cohort study. *PLoS One* 2012, 7: e49113.
- Altena E, Vrenken H, Van Der Werf YD, van den Heuvel OA, Van Someren EJW. Reduced orbitofrontal and parietal gray matter in chronic insomnia: a voxel-based morphometric study. *Biol Psychiatry* 2010, 67: 182–185.
- Bumb JM, Schilling C, Enning F, Haddad L, Paul F, Lederbogen F, *et al.* Pineal gland volume in primary insomnia and healthy controls: a magnetic resonance imaging study. *J Sleep Res* 2014, 23: 276–282.
- Dai XJ, Jiang J, Zhang Z, Nie X, Liu BX, Pei L, *et al.* Plasticity and susceptibility of brain morphometry alterations to insufficient sleep. *Front Psychiatry* 2018, 9: 266.
- Spiegelhalder K, Regen W, Baglioni C, Klöppel S, Abdulkadir A, Hennig J, *et al.* Insomnia does not appear to be associated with substantial structural brain changes. *Sleep* 2013, 36: 731–737.
- Spiegelhalder K, Regen W, Prem M, Baglioni C, Nissen C, Feige B, *et al.* Reduced anterior internal capsule white matter integrity in primary insomnia. *Hum Brain Mapp* 2014, 35: 3431–3438.
- Li S, Tian J, Bauer A, Huang R, Wen H, Li M, *et al.* Reduced integrity of right lateralized white matter in patients with primary insomnia: A diffusion-tensor imaging study. *Radiology* 2016, 280: 520–528.
- Kang JM, Joo SW, Son YD, Kim H, Ko KP, Lee JS, *et al.* Low white-matter integrity between the left thalamus and inferior frontal gyrus in patients with insomnia disorder. *J Psychiatry Neurosci* 2018, 43: 366–374.
- Sexton CE, Zsoldos E, Filippini N, Griffanti L, Winkler A, Mahmood A, *et al.* Associations between self-reported sleep quality and white matter in community-dwelling older adults: A prospective cohort study. *Hum Brain Mapp* 2017, 38: 5465–5473.
- Wilckens KA, Hall MH, Nebes RD, Monk TH, Buysse DJ. Changes in cognitive performance are associated with changes in

- sleep in older adults with insomnia. *Behav Sleep Med* 2016, 14: 295–310.
39. Sivertsen B, Omvik S, Pallesen S, Bjorvatn B, Havik OE, Kvale G, *et al.* Cognitive behavioral therapy vs zopiclone for treatment of chronic primary insomnia in older adults: a randomized controlled trial. *JAMA* 2006, 295: 2851–2858.
 40. Kyle SD, Miller CB, Rogers Z, Siriwardena AN, MacMahon KM, Espie CA. Sleep restriction therapy for insomnia is associated with reduced objective total sleep time, increased daytime somnolence, and objectively impaired vigilance: Implications for the clinical management of insomnia disorder. *Sleep* 2014, 37: 229–237.
 41. Roth T, Coulouvrat C, Hajak G, Lakoma MD, Sampson NA, Shahly V, *et al.* Prevalence and perceived health associated with insomnia based on DSM-IV-TR; International Statistical Classification of Diseases and Related Health Problems, Tenth Revision; and Research Diagnostic Criteria/International Classification of Sleep Disorders, Second Edition Criteria: Results from the America Insomnia Survey. *Biol Psychiatry* 2011, 69: 592–600.
 42. Ohayon MM. Epidemiology of insomnia: what we know and what we still need to learn. *Sleep Med Rev* 2002, 6: 97–111.
 43. Herbert V, Kyle SD, Pratt D. Does cognitive behavioural therapy for insomnia improve cognitive performance? A systematic review and narrative synthesis. *Sleep Med Rev* 2018, 39: 37–51.
 44. Noh HJ, Joo EY, Kim ST, Yoon SM, Koo DL, Kim D, *et al.* The relationship between hippocampal volume and cognition in patients with chronic primary insomnia. *J Clin Neurol* 2012, 8: 130–138.
 45. Bellesi M. Sleep and oligodendrocyte functions. *Curr Sleep Med Rep* 2015, 1: 20–26.
 46. Meerlo P, Mistlberger RE, Jacobs BL, Heller HC, McGinty D. New neurons in the adult brain: the role of sleep and consequences of sleep loss. *Sleep Med Rev* 2009, 13: 187–194.
 47. Lim J, Dinges DF. A meta-analysis of the impact of short-term sleep deprivation on cognitive variables. *Psychol Bull* 2010, 136: 375–389.
 48. Elvsashagen T, Norbom LB, Pedersen PO, Quraishi SH, Bjornerud A, Malt UF, *et al.* Widespread changes in white matter microstructure after a day of waking and sleep deprivation. *PLoS One* 2015, 10: e0127351.
 49. Lim AS, Ellison BA, Wang JL, Yu L, Schneider JA, Buchman AS, *et al.* Sleep is related to neuron numbers in the ventrolateral preoptic/intermediate nucleus in older adults with and without Alzheimer’s disease. *Brain* 2014, 137: 2847–2861.
 50. Holth J, Patel T, Holtzman DM. Sleep in Alzheimer’s disease - Beyond amyloid. *Neurobiol Sleep Circadian Rhythms* 2017, 2: 4–14.
 51. Karageorgiou E, Vossel KA. Brain rhythm attractor breakdown in Alzheimer’s disease: Functional and pathologic implications. *Alzheimers Dement* 2017, 13: 1054–1067.
 52. Ehrenberg AJ, Suemoto CK, França Resende EdP, Petersen C, Leite REP, Rodriguez RD, *et al.* Neuropathologic correlates of psychiatric symptoms in Alzheimer’s disease. *J Alzheimers Dis* 2018, 66: 115–126.
 53. Braak H, Thal DR, Ghebremedhin E, Del Tredici K. Stages of the pathologic process in Alzheimer disease: age categories from 1 to 100 years. *J Neuropathol Exp Neurol* 2011, 70: 960–969.
 54. Grinberg LT, Rüb U, Ferretti REL, Nitrini R, Farfel JM, Polichiso L, *et al.* The dorsal raphe nucleus shows phospho-tau neurofibrillary changes before the transentorhinal region in Alzheimer’s disease. A precocious onset? *Neuropathol Appl Neurobiol* 2009, 35: 406–416.
 55. Roh JH, Huang Y, Bero AW, Kasten T, Stewart FR, Bateman RJ, *et al.* Disruption of the sleep-wake cycle and diurnal fluctuation of β -amyloid in mice with Alzheimer’s disease pathology. *Sci Transl Med* 2012, 4: 150ra122.
 56. Kang JE, Lim MM, Bateman RJ, Lee JJ, Smyth LP, Cirrito JR, *et al.* Amyloid-beta dynamics are regulated by orexin and the sleep-wake cycle. *Science* 2009, 326: 1005–1007.



RESEARCH HIGHLIGHT

More than Scratching the Surface: Recent Progress in Brain Mechanisms Underlying Itch and Scratch

Xu Liu^{1,2} · Xiu-Hua Miao¹ · Tong Liu^{2,3}

Received: 11 January 2019 / Accepted: 2 February 2019 / Published online: 4 March 2019
© Shanghai Institutes for Biological Sciences, CAS 2019

Itch (also called pruritus) is an unpleasant somatosensation that evokes a desire or reflex to scratch in humans and other mammals [1]. Itch is now considered to be a unique sensory modality that is encoded by a labeled line that has genetically distinguishable neurons in the peripheral and central nervous systems [1]. Acute itch evokes scratching that may help to remove potentially harmful irritants from the skin, which is believed to be evolutionarily important for survival. Pathological chronic itch often occurs in patients with inflammatory skin diseases, systemic diseases, and neurological conditions. Importantly, chronic itch causes uncontrollable itch-scratch cycles that induce skin damage, affect sleep, and seriously reduce the quality of life [2]. At present, effective treatment for chronic itch is still lacking, possibly due to limited understanding of the mechanism of itch information-processing in the nervous system. Therefore, elucidation of the molecular, cellular, and circuitry mechanisms of itch will eventually help to develop new effective strategies for the management of chronic itch.

Itch sensation originates from the surface of the skin or mucosa. An itch stimulus is detected by the peripheral

terminals of primary sensory neurons whose cell bodies are located in the dorsal root ganglia and trigeminal ganglia [3]. The central branches of primary sensory neurons, which contain glutamate and neuropeptides, project to the superficial dorsal horn of the spinal cord. In a simplified model, the central terminals of itch sensory neurons that contain the neuropeptide natriuretic polypeptide b (Nppb) make synaptic connections with gastrin-releasing peptide (GRP)-expressing neurons that express the Nppb receptor NPR1 in lamina II of the spinal cord. GRP-expressing neurons release GRP to act on its receptor GRPR, which is expressed in a group of excitatory interneurons expressing vesicular glutamate transporter 2 (VGLUT2). GRPR-expressing neurons excite projection neurons in spinal cord lamina I, which send itch signals to the brain [3]. There are also several groups of itch inhibitory neurons, such as BHLHB5 (basic helix-loop-helix domain-containing protein, class b, 5)-expressing and neuropeptide Y-expressing interneurons, which act on GRPR-expressing neurons or their downstream neurons in the itch pathway to gate itch transmission in the dorsal horn [3]. Thus, there is a complicated gating mechanism for itch transmission in the spinal cord, which may involve distinct population of interneurons, including both excitatory and inhibitory interneurons [4, 5].

After processing in the spinal cord, axons of the itch projection neurons, possibly neurokinin 1 (NK1)-expressing neurons located in superficial lamina I, cross the midline to the contralateral side and join the spinothalamic tract projecting to the thalamus and/or the spinoparabrachial tract projecting to the parabrachial nucleus (PBN) [3], which in turn project into various brain areas. A subpopulation of PBN neurons, which require VGLUT2 for signal transmission, make disynaptic connections with GRPR⁺ neurons in the spinal cord. Positron emission tomography

✉ Xiu-Hua Miao
xiuhua_miao@126.com

✉ Tong Liu
liutong80@suda.edu.cn

¹ The Affiliated Zhangjiagang Hospital of Soochow University, Zhangjiagang 215600, China

² Jiangsu Key Laboratory of Neuropsychiatric Diseases and Institute of Neuroscience, Soochow University, Suzhou 215021, China

³ College of Life Sciences, Yanan University, Yanan 716000, China

and functional magnetic resonance imaging have shown that primary and secondary somatosensory cortex are frequently activated in humans. In addition, other itch-activated areas include the cingulate and prefrontal cortex, amygdala, and limbic systems (possibly involved in emotional processing), as well as premotor, motor, and supplementary motor areas (possibly involved in scratching behavior) [3]. Although non-histaminergic itch induced by cowhage activates distinct brain areas, such as insular cortex, basal ganglia, claustrum, putamen, and thalamic nuclei, both histaminergic and non-histaminergic itch activate similar brain areas. Compared with pain, the precuneus and the posterior cingulate cortex are thought to be itch-specific, although it is still under debate whether there are itch-selective brain areas. Histamine-induced activation of some areas, such as the cingulate and prefrontal cortex, is more robust in chronic itch patients than in healthy individuals, indicating the central sensitization of itch under chronic itch conditions [3]. Nevertheless, our understanding of how itching and scratching are processed under physiological and pathophysiological conditions is still limited.

Like pain, itch-responsive neurons in the spinal cord are significantly affected by descending modulatory pathways from higher brain regions. Serotonergic neurons in the nucleus raphe magnus send descending facilitatory projections to the spinal cord and directly stimulate GRPR⁺ neurons by acting on heterodimers of the 5-hydroxytryptamine (5-HT) 1A and GRP receptors [3]. Noradrenergic neurons in the locus coeruleus send descending inhibitory projections to the spinal cord, possibly *via* α -adrenergic receptors, to enhance the activity of inhibitory interneurons [3]. The periaqueductal gray (PAG), a major endogenous pain modulatory area and controller of morphine analgesia [6], is also activated during itch-induced scratching. Thus, activation of the PAG during scratching is traditionally considered to be correlated with descending itch suppression by opioids [3]. However, the precise neural circuitry of itch processing in the PAG remains unexplored.

In a new paper published in *Neuron*, Gao *et al.* have revealed that tachykinin 1 (Tac1)-expressing (Tac1⁺) neurons located in the PAG facilitate itch-scratch cycles *via* a descending rostral ventromedial medulla (RVM) pathway in mice [7]. First, they reported that neuronal activity in the lateral and ventrolateral PAG (l/vIPAG), reflected by an increased number of *c-fos*⁺ neurons and in extracellular electrophysiological recordings, significantly increases after intradermal injection of pruritogens (such as histamine or chloroquine). Pharmacogenetic inhibition of the l/vIPAG neurons significantly decreases the scratching behavior induced by pruritogens. Gao *et al.* further found that pharmacogenetic suppression of the RVM-projecting

neurons, especially glutamatergic neurons, in the l/vIPAG significantly decreases itch behavior in mice. Thus, activation of glutamatergic PAG neurons promotes itch-scratch cycles *via* a descending RVM pathway in mice.

Next, Gao *et al.* found that ablation of a subpopulation of glutamatergic neurons in the l/vIPAG (Tac1⁺ neurons) significantly decreases the scratching behavior induced by acute and chronic itch in mice. In the mouse cheek model, ablation of Tac1⁺ neurons in the l/vIPAG significantly decreases itch-induced scratching, but not pain-induced wiping. Further, the activity of Tac1⁺ neurons in the l/vIPAG, reflected by fluorescent signal fluctuations, significantly increases during itch-induced scratching, but only slightly increases during pain-induced wiping. Thus, l/vIPAG Tac1⁺ neurons selectively respond to peripheral itch stimuli.

Further, Gao *et al.* showed that pharmacogenetic and optogenetic activation of Tac1⁺ neurons is sufficient to induce robust scratching behavior, which is inhibited by the ablation of spinal GRPR⁺ neurons by intrathecal injection of bombesin-saporin, but not GRPR itself, in mice. Finally, Gao *et al.* found that the scratching behavior induced by activation of l/vIPAG Tac1⁺ neurons is not affected by depletion of spinal 5-HT fibers or pharmacological blockade of spinal 5-HT_{1A} receptors, suggesting that the descending 5-HT projection is not involved in the facilitatory role of l/vIPAG Tac1⁺ neurons in itch transmission. Interestingly, previous work has demonstrated that spinal GRPR⁺ neurons are not involved in chronic mechanical itch in mice [8]. Whether the l/vIPAG Tac1⁺ neurons are involved in mechanical itch processing warrants further investigation. Based on our understanding of the mechanisms underlying itch, we provide a simplified overview of the ascending and descending pathways for itch (Fig. 1).

This work provides important insight into the neural circuitry underlying a descending modulatory pathway of itch sensation in mice. However, it also raises a series of interesting questions. First, under acute itch conditions, scratching is very effective for relieving itch. In contrast, under chronic itch conditions, an itch-scratch-itch cycle occurs [2], suggesting that chronic itch is no longer inhibited by scratching; rather, scratching may promote itch. Do Tac1⁺ neurons in the PAG play a distinct role in acute and chronic itch? Second, given that acute itch can be inhibited by pain or scratching [1], can pain stimuli or scratching itself affect the activity of Tac1⁺ neurons in the PAG? Do Tac1⁺ neurons in the PAG play any role in the inhibition of itch induced by painful stimulation? Third, opioids such as morphine can induce or exacerbate itch sensation in humans and animal models. Given that the PAG is a major area for the action of morphine (such as in analgesia), does morphine have any effect on the activity of Tac1⁺ neurons in the PAG to modulate itch processing?

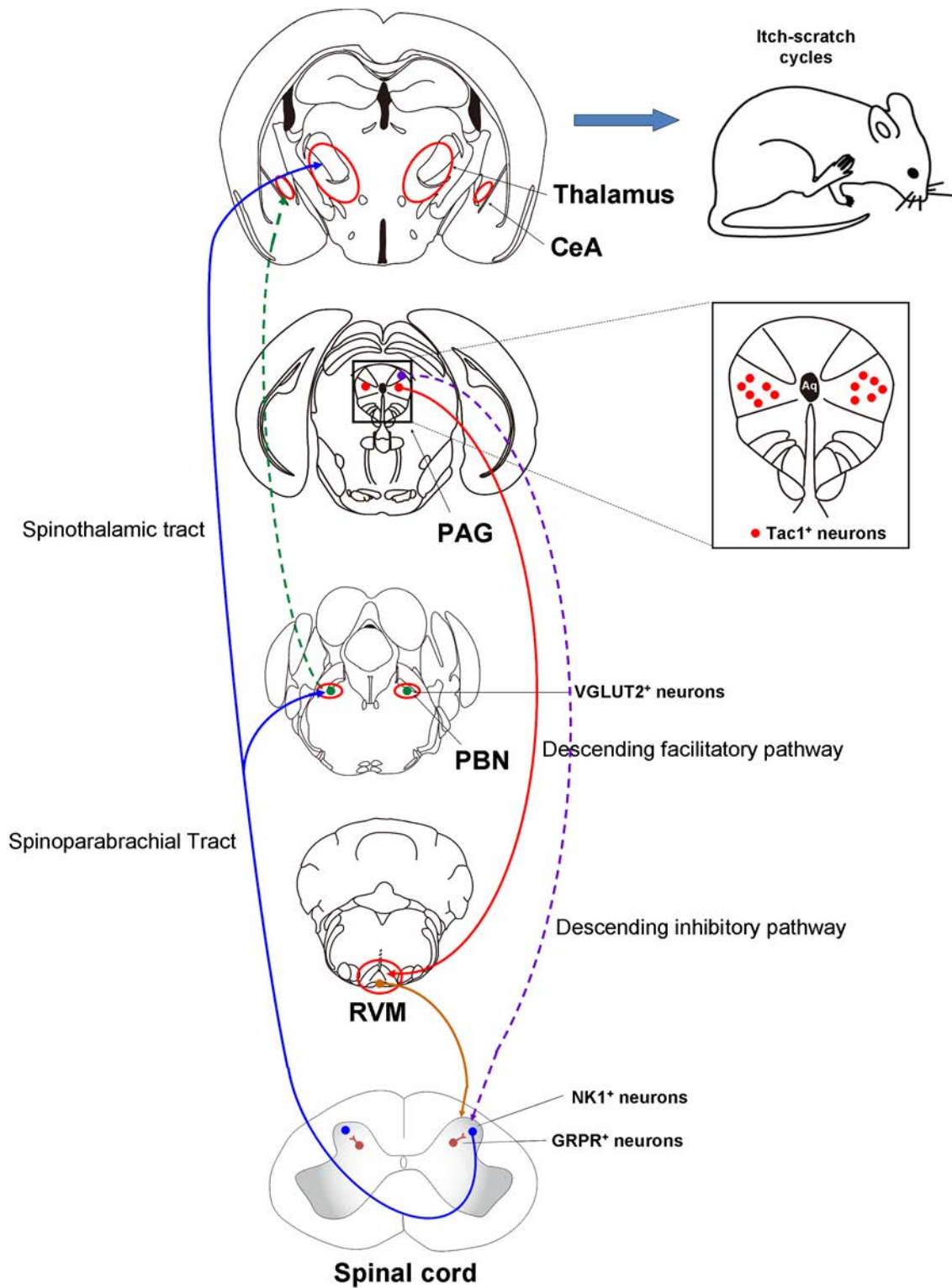


Fig. 1 Overview of the neural circuitry for itch-processing in the central nervous system in mice. CeA, central amygdala; GRPR, gastrin-releasing peptide receptor; NK1, neurokinin 1; PAG,

periaqueductal gray; PBN, parabrachial nucleus; RVM, rostral ventromedial medulla; Tac1, tachykinin 1; VGLUT2, vesicular glutamate transporter 2.

Interestingly, one study has shown that local injection of bombesin, a GRPR ligand, into the PAG reduces scratching behavior followed by immobility in an animal model [9].

Fourth, what is the role of GRP-GRPR signaling in the PAG and its relationship with Tac1⁺ neurons in itch processing? Finally, if the descending 5-HT projection is

not involved in the facilitatory role of PAG Tac1⁺ neurons in itch processing, what transmitter is involved in facilitating the modulation of itch?

Interestingly, grooming is an innate behavior with an evolutionarily-conserved pattern and is frequently used as a measure of repetitive behavior in rodent models of autism spectrum disorder and obsessive compulsive disorder [10]. Gao *et al.* found that activation of PAG Tac1⁺ neurons also evokes robust grooming behavior, and scratching and grooming behaviors are likely mediated by different subsets of these neurons. To further identify the roles of these subpopulations of PAG Tac1⁺ neurons based on their molecular identity or connectivity in distinct functions (such as grooming and scratching) is extremely urgent.

In summary, Gao *et al.* clearly demonstrated that Tac1⁺ neurons in the PAG facilitate the itch-scratching cycle *via* a descending RVM pathway. We also speculate that dysfunction of the descending modulatory system of itch may play a critical role in the development of chronic itch. This has important clinical implications for the discovery of descending neural circuitry to drive the itch-scratching cycle, given that the cycle is a common phenomenon under chronic itch conditions. Thus, this newly identified top-down pathway may provide potential therapeutic targets in the central nervous system for the management of chronic itch

Acknowledgements TL was supported by grants from the National Natural Science Foundation of China (81870874, 31371179, and 81300968) and the Natural Science Foundation of Jiangsu Province, China (BK20170004 and 2015-JY-029). XL was supported by the

Postgraduate Research and Practice Innovation Program of Jiangsu Province, China (KYCX17_2034).

References

1. LaMotte RH, Dong X, Ringkamp M. Sensory neurons and circuits mediating itch. *Nat. Rev. Neurosci.* 2014, 15: 19–31.
2. Yosipovitch G, Bernhard JD. Clinical practice. Chronic pruritus. *N. Engl. J. Med.* 2013, 368: 1625–1634.
3. Dong X, Dong X. Peripheral and Central Mechanisms of Itch. *Neuron* 2018, 98: 482–494.
4. Ji RR. Recent progress in understanding the mechanisms of pain and itch: the second special issue. *Neurosci Bull* 2018, 34: 1–3.
5. Miao X, Huang Y, Liu TT, Guo R, Wang B, Wang XL, *et al.* TNF-alpha/TNFR1 signaling is required for the full expression of acute and chronic itch in mice via peripheral and central mechanisms. *Neurosci Bull* 2018, 34: 42–53.
6. Matthes HW, Maldonado R, Simonin F, Valverde O, Slowe S, Kitchen I, *et al.* Loss of morphine-induced analgesia, reward effect and withdrawal symptoms in mice lacking the mu-opioid-receptor gene. *Nature* 1996, 383: 819–823.
7. Gao ZR, Chen WZ, Liu MZ, Chen XJ, Wan L, Zhang XY, *et al.* Tac1-expressing neurons in the periaqueductal gray facilitate the itch-scratching cycle via descending regulation. *Neuron* 2019, 101: 45–59 e49.
8. Bourane S, Duan B, Koch SC, Dalet A, Britz O, Garcia-Campmany L, *et al.* Gate control of mechanical itch by a subpopulation of spinal cord interneurons. *Science* 2015, 350: 550–554.
9. Spruijt BM, Cools AR, Gispen WH. The periaqueductal gray: a prerequisite for ACTH-induced excessive grooming. *Behav Brain Res* 1986, 20: 19–25.
10. Kalueff AV, Stewart AM, Song C, Berridge KC, Graybiel AM, Fentress JC. Neurobiology of rodent self-grooming and its value for translational neuroscience. *Nat Rev Neurosci* 2016, 17: 45–59.



RESEARCH HIGHLIGHT

Plasma Replacement Therapy for Alzheimer's Disease

Xu-long Ding^{1,2,3} · Peng Lei^{1,2,3}

Received: 7 January 2019 / Accepted: 2 February 2019 / Published online: 20 May 2019
© Shanghai Institutes for Biological Sciences, CAS 2019

Alzheimer's disease (AD) is the most common neurodegenerative disease that affects memory, thinking, behavior, and the ability to perform everyday activities. It has been estimated that more than 35 million people worldwide suffered from AD in 2018 [1], and this figure continues to grow. Unfortunately, no cure or treatment that slows the progression of the disease has been discovered despite extensive efforts from academics and the pharmaceutical industry. Most drug trials for AD have targeted the β -amyloid protein [2], which accumulates in this disease, and the failure of amyloid-based drugs to impact on cognition in people with AD has led to re-questioning of the amyloid hypothesis of AD, and has provided a fresh impetus to explore alternative therapeutic strategies.

Recently, Sha and colleagues [3] performed a randomized clinical trial to test the safety, tolerability, and feasibility of weekly administration of young fresh-frozen plasma (yFFP) to treat patients with mild to moderate AD. The same research group had previously shown that young mouse plasma treatment enhances learning and memory in aged mice [4] and that aged immunodeficient mice treated with human cord plasma have impaired memory [5]. Based on the hypothesis that anti-aging agents in the young blood can provide therapeutic benefits for AD patients, the

authors have now translated these mouse studies into an early clinical trial of 18 patients who were divided into two groups matched for age, sex, baseline Mini-Mental State Examination score, and the apolipoprotein E4 genotype. The first group served as an open-label cohort which included 9 patients, and the patients were informed that treatment with 250 mL yFFP once a week for four weeks was applied. The second group, which also contained 9 patients, participated in a double-blind crossover protocol. Four of the 9 patients in the second group received yFFP once a week for four weeks, followed by a 6-week washout, and then saline was infused once a week for four weeks until the conclusion of the trial. The remaining 5 patients received saline first, followed by washout and yFFP infusion. In baseline and post-yFFP assessments, there were no related serious adverse events and no statistically significant differences were found in the outcomes, including cognitive, functional, and magnetic resonance imaging analyses.

Almost at the same time, Grifols, the largest plasma production company in Europe, also performed a clinical trial for AD using plasma exchange therapy under a different working hypothesis. Grifols had discovered previously that albumin can modify the levels of cerebrospinal fluid (CSF) and plasma amyloid ($A\beta$) 1–42 [6] and that the post-translational nitro-glycated modification state [7] as well as the oxidation state of albumin [8] are significantly increased in AD. They hypothesized that albumin binds to circulating $A\beta$ in plasma and CSF, and this could mobilize $A\beta$ from the brain to the plasma. Therefore, Grifols combined plasmapheresis with albumin, and evaluated the efficacy of plasma exchange using different replacement volumes. They also examined various concentrations of albumin. In a cohort of moderate AD patients, the authors demonstrated a statistically significant

✉ Peng Lei
peng.lei@scu.edu.cn

¹ Department of Neurology and State Key Laboratory of Biotherapy, West China Hospital, Sichuan University, Chengdu 610041, China

² West China School of Basic Medical Sciences and Forensic Medicine, Sichuan University, Chengdu 610041, China

³ Collaborative Innovation Center for Biotherapy, Chengdu 610041, China

reduction of 61% in disease progression from baseline across both primary efficacy endpoints as measured by the AD Assessment Scale—Cognitive and the AD Cooperative Study—Activities of Daily Living scales. These data therefore highlight the potential of plasma exchange as a potential therapeutic strategy for AD.

However, the mechanism underlying how plasma exchange therapy benefits AD patients remains unknown. Tissue inhibitor of metalloproteinases 2 (TIMP2) has been shown by the same group to be a key factor in plasma that reverses senility in aged mice [5]. They showed that systemic injection and shuttling of TIMP2 from the blood into the brain mediates increased synaptic plasticity in the normally-functioning hippocampus, and induces significant improvements in behavior, long-term potentiation, and memory performance in aged mice; however AD mouse models have yet to be investigated. Others have used parabiosis and shown that peripheral A β can enter in the brain to increase the amyloid plaque burden [9], and removal of A β from the blood can reduce brain A β levels in mice [10], which may provide mechanistic insights. Nevertheless, aging is the most critical risk factor for AD [11], and the molecular mechanisms of aging can be clearly distinguished from the pathogenesis of AD [12]. The fact that plasma exchange therapy works in both aging alone, and AD, suggests that it may not be specific strategy for the disease.

Meanwhile, plasma replacement therapy is currently applied to rare, chronic diseases like alpha-1 antitrypsin deficiency, primary immune deficiency diseases, von Willebrand disease, and hemophilia; these patients generally require regular infusions or injections throughout their lives. According to the WHO Global Plasma Status Report, the plasma resource gap exceeds 10,000 tons (The 2016 global status report on blood safety and availability. World Health Organization 2017. <http://www.who.int/iris/handle/10665/254987>). The World Federation of Hemophilia estimates that 70% of patients with hemophilia worldwide are still unable to access any treatment. In this case, if plasma replacement is approved as a therapy for AD, it will face the same challenge as the fetal disorders to allocate the source of blood, and the dilemma of which disease the limited resource should supply.

Overall, the work by Sha and colleagues has added an important avenue to our efforts to cure AD. Further studies and discussions are needed to identify the mechanism of plasma exchange therapy, to investigate its specificity, and to address the ethical concerns related to the low worldwide supply of this human product.

Acknowledgements This highlight was supported by the National Natural Science Foundation of China (81722016), and the R&D Infrastructure and Facility Development Program of Sichuan Province, China (2018TJPT0037).

Conflict of interest The authors declare no conflict of interests.

References

- Patterson, C. World Alzheimer Report 2018. The state of the art of dementia research: new frontiers. An analysis of prevalence, incidence, cost and trends. *Alzheimer's Disease International* 2018.
- Sun BL, Li WW, Zhu C, Jin WS, Zeng F, Liu YH, *et al.* Clinical research on Alzheimer's disease: progress and perspectives. *Neurosci Bull* 2018, 34: 1111–1118.
- Sha SJ, Deutsch GK, Tian L, Richardson K, Coburn M, Gaudioso JL, *et al.* Safety, Tolerability, and feasibility of young plasma infusion in the plasma for Alzheimer symptom amelioration study: a randomized clinical trial. *JAMA Neurol* 2019, 76: 35–40.
- Villeda SA, Plambeck KE, Middeldorp J, Castellano JM, Mosher KI, Luo J, *et al.* Young blood reverses age-related impairments in cognitive function and synaptic plasticity in mice. *Nat Med* 2014, 20: 659–663.
- Castellano JM, Mosher KI, Abbey RJ, McBride AA, James ML, Berdnik D, *et al.* Human umbilical cord plasma proteins revitalize hippocampal function in aged mice. *Nature* 2017, 544: 488–492.
- Boada M, Anaya F, Ortiz P, Olazarán J, Shua-Haim JR, Obisesan TO, *et al.* Efficacy and safety of plasma exchange with 5% albumin to modify cerebrospinal fluid and plasma amyloid-beta concentrations and cognition outcomes in Alzheimer's disease patients: a multicenter, randomized, controlled clinical trial. *J Alzheimers Dis* 2017, 56: 129–143.
- Ramos-Fernandez E, Tajés M, Palomer E, Ill-Raga G, Bosch-Morato M, Guivernau B, *et al.* Posttranslational nitro-glycative modifications of albumin in Alzheimer's disease: implications in cytotoxicity and amyloid-beta peptide aggregation. *J Alzheimers Dis* 2014, 40: 643–657.
- Costa M, Horrillo R, Ortiz AM, Perez A, Mestre A, Ruiz A, *et al.* Increased Albumin oxidation in cerebrospinal fluid and plasma from Alzheimer's disease patients. *J Alzheimers Dis* 2018, 63: 1395–1404.
- Bu XL, Xiang Y, Jin WS, Wang J, Shen LL, Huang ZL, *et al.* Blood-derived amyloid-beta protein induces Alzheimer's disease pathologies. *Mol Psychiatry* 2018, 23: 1948–1956.
- Jin WS, Shen LL, Bu XL, Zhang WW, Chen SH, Huang ZL, *et al.* Peritoneal dialysis reduces amyloid-beta plasma levels in humans and attenuates Alzheimer-associated phenotypes in an APP/PS1 mouse model. *Acta Neuropathol* 2017, 134: 207–220.
- Yu Q, Zhong C. Membrane aging as the real culprit of Alzheimer's disease: modification of a hypothesis. *Neurosci Bull* 2018, 34: 369–381.
- Fjell AM, McEvoy L, Holland D, Dale AM, Walhovd KB. What is normal in normal aging? Effects of aging, amyloid and Alzheimer's disease on the cerebral cortex and the hippocampus. *Prog Neurobiol* 2014, 117: 20–40.



Gut Microbiota and Short Chain Fatty Acids: Influence on the Autonomic Nervous System

Jessica Bruning¹ · Andrew Chapp² · Gregory A. Kaurala³ · Renjun Wang⁴ · Stephen Techtmann³ · Qing-Hui Chen¹

Received: 28 December 2018 / Accepted: 29 April 2019 / Published online: 12 July 2019
© Shanghai Institutes for Biological Sciences, CAS 2019

Reaching across multiple fields of focus, spanning from periodontology to gastroenterology to neurobiology to behavior, interest in the influence of the microbiome in human physiology and pathology has risen over the past few decades. Microbiota co-exist in and on humans forming an evolutionarily symbiotic biological unit, a halobiont, in which disruptions in the relationship can occur through genomic alterations and mutations [1]. The human microbiome consists of bacteria, viruses, fungi, and protozoans that contribute 450 times more genes to this relationship and slightly outnumber human host cells [2, 3]. The bacteria in the gastrointestinal (GI) tract are of the most interest and exist within five phyla: *Bacteroidetes*, *Firmicutes*, *Proteobacteria*, *Actinobacteria*, and *Verrucomicrobia*. Within the *Verrucomicrobia* an interesting bacterium has emerged, *Akkermansia muciniphila*, a mucus-degrading bacterium that influences intestinal permeability [3, 4]. The composition of individual microbiota communities depends on host lifestyle and genetics [1]. Often the *Firmicutes*-to-*Bacteroidetes* ratio is considered a method for measuring the health of a community [2–7] but has not been fully validated in other studies suggesting the measurement of phyla in feces

as a diagnostic tool may not be practical. Malfunction in the GI tract impacts other systems and leads the loss of physiological function, which disrupts the relationship between microbes and host. Gut microbial community disturbances caused by the host lifestyle (antibiotic use, food consumption, and lack of exercise), results in a decrease in diversity and have been linked to cardiovascular diseases, such as hypertension [2, 3, 5, 8], neurodegenerative Parkinson's and Alzheimer's diseases [4, 6], and even obesity [7].

Microbes in the GI tract utilize the food consumed by the host as an energy source and aid in breaking down some foodstuffs, such as fermentable fibers, resistant starches (prebiotics), and some dairy products. Through various metabolic pathways, microbes produce short-chain fatty acids (SCFAs) such as butyric acid, propionic acid, acetic acid and the alpha-hydroxy acid, lactic acid. At physiological pH, these SCFAs exist as conjugate bases; butyrate, acetate, propionate, and lactate (Fig. 1). These SCFAs, particularly butyrate is known to modulate gut functions, such as motility and permeability [3–5, 9, 10] whereas acetate and lactate are absorbed into the circulation and either used or eliminated. The response of human cells to alterations in metabolite concentrations may be regionally specific and influenced by host genomics [1, 8, 10], suggesting the pertinence to investigate microbe populations on the mucosa in various regions of the small intestine and colon. The types of receptors present on specific human cells and the numbers of receptors present alter the downstream effects in response to the presence of SCFAs in a dose-dependent manner (Fig. 1) [8–10]. Little is known about the molecular mechanisms underlying the link between microbial composition, SCFA metabolite concentrations, and overall systemic effects on host physiology. Exploring microbial community composition and associated metabolomic information in normal individuals and those with various diseases may lead to the

✉ Qing-Hui Chen
qinghuic@mtu.edu

¹ Department of Kinesiology and Integrative Physiology, Michigan Technological University, Houghton, MI 49931, USA
² Department of Neuroscience, University of Minnesota, Minneapolis, MN 55455, USA
³ Department of Biological Science, Michigan Technological University, Houghton, MI 49931, USA
⁴ Department of Biotechnology, School of Life Science, Jilin Normal University, Siping 136000, Jilin, China

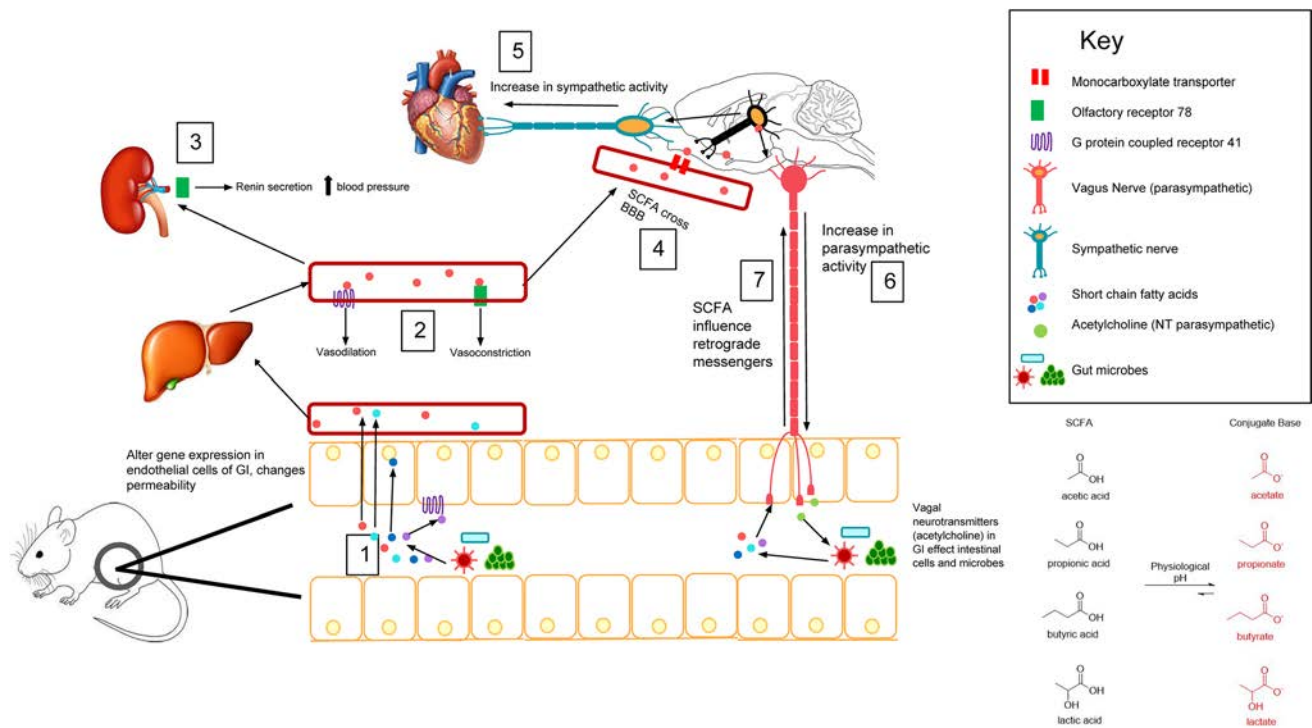


Fig. 1 Physiological effects of short-chain fatty acids (SCFAs) produced by gut microbes on various organs. SCFAs produced by gut bacterial either bind to intestinal endothelial receptors activating various second messenger pathways, pass through cell membranes to influence gene expression, or move through endothelial cells into the portal system (1) to bind to receptors elsewhere. Binding to GPCR 41 receptors in blood vessels induces vasodilation; binding to Olf78 receptors in the blood vessel induces vasoconstriction (2) and renin secretion in the kidney (3); both increase arterial blood pressure

(ABP). Once in the bloodstream, SCFAs can cross the blood brain barrier *via* monocarboxylate transporter (MCTs) (4) and influence various neurons with different receptor expression causing cascading effects, such as increasing sympathetic outflow to increase heart rate (5) and vasoconstriction or by increasing parasympathetic outflow to alter gut motility and the microbes themselves (6). As well as traveling through the blood to the brain, SCFAs can increase the retrograde communication between the gut and the brain, causing downstream effects (7).

development of recognizable biomarkers (host or microbial byproducts) that indicate the possibility of pathology, which hopefully will aid in preventative therapeutic interventions. Understanding the specific receptors to which SCFAs bind and their downstream effects could lead to therapies targeting specific receptors and thus restore gene expression and changes in neuronal signaling. In this insight, we seek to investigate the role of SCFAs produced by resident gut microbes, in regulating the autonomic nervous system and the implications of this regulator role in the development of human pathology.

SCFA Modulation in the Vagus Nerve

Various intraluminal and intramucosal factors can modulate enteric neuronal function, potentially increasing neuronal excitability, which, if occurring over long periods of time alters neuronal morphology, gene expression, and excitability [9, 10]. Most SCFAs present in the plasma are byproducts of bacterial metabolism and act as physiological modulators of the enteric nervous system [8, 9]. The presence of lipids in

the intestines stimulates vagal afferent pathways [9, 10], possibly altering expression in specific brain regions, and increasing parasympathetic output from various brain areas, altering the autonomic influence on the body. SCFAs for example butyrate activate intestinal vagal nerves by directly acting on the terminals in a cholecystinin-independent manner [9], indicating other mechanisms of neurotransmitter release that are currently unknown. In contrast to long-chain fatty acids, SCFAs show a quicker and longer-lasting afferent chemical response, possibly promoting the changes in gene expression. Feeding Sprague–Dawley rats a resistant starch diet increases GI luminal SCFA concentrations and increases acetylcholine synthesis, monocarboxylate transporter 2 receptor expression, neuronal excitability, and histone acetylation [10], displaying the impact microbe SCFAs have on host gene expression. Administration of butyrate increases the proportion of choline acetyltransferase in myenteric neurons, promoting GI motility and contractility [10]. Understanding the underlying mechanisms by which butyrate increases the activity of cholinergic neurons and enhances gut motility could be potential therapeutic targets for individuals suffering from GI dysfunction.

In addition, insulin-resistant rats fed a high-fat diet have increased whole-body acetate turnover and increased fecal and plasma acetate concentrations both of which are accompanied by a rise in parasympathetic activation [7]. The study conducted by Perry and colleagues revealed an acetate-induced increase of parasympathetic vagal stimulation, acutely driving glucose-stimulated insulin secretion through the autonomic activation of pancreatic β -cells. This condition of hyperinsulinemia leads to a fivefold increase in gastrin and a threefold increase in ghrelin, which in turn leads to a dramatic intake of calories resulting in obesity [7]. Understanding the underlying mechanisms by which acetate concentrations influence the autonomic parasympathetic outflow could lead to therapeutics for treating obesity and diabetes. Even though the animal models vary and the downstream effects of increased SCFAs production differ, an increase in SCFA production by gut microbes increases parasympathetic output through the vagus and glossopharyngeal nerves to impact host function. The difference in effects may be attributed to the various transporters/receptors with which SCFAs interact: monocarboxylate transporter (MCTs), G protein-coupled receptors (GPCRs), or olfactory receptors [8, 10]. The expression and localization of these receptors found in specific neurons and/or various regions of the body, or perhaps their concentrations may influence the receptor response and phenotypic output [8, 10–12]. Comprehension of the downstream effects of SCFA-receptor activation and the influence on the autonomic nervous system will lead to novel discoveries in pathophysiology and lead to new approaches in therapeutics and medicine.

SCFA Modulation in the Sympathetic Nervous System

Disruption of the microbiome in disease models in combination with a decrease in intestinal barrier integrity may lead to alterations in SCFA concentrations in the blood. The increase in permeability allows a rise in SCFA concentrations in the blood, leading to enhanced activation of sympathetic nerves by SCFAs [5, 11]. A gain in sympathetic outflow modulates various organ systems, including those of the cardiovascular system controlling heart rate, contractility, vasoconstriction, and renin secretion. Changes in any of these, result in changes in arterial blood pressure (ABP). Interestingly, pre-hypertensive young spontaneous hypertensive rats (SHRs) exhibit a decrease in tight-junction protein expression, which is preceded by an increase in permeability, sympathetic output, and a shift in the gut microbial composition [3, 5]. Measuring individuals assumed at risk of developing hypertension for tight-junction protein gene expression could be used as a biomarker to

determine whether a person is at increased risk of intestinal permeability pathology.

Increasing permeability of the GI allows for higher concentrations of signal molecules, such as SCFAs and cytokines, to reach and cross the blood-brain barrier [8], targeting various regions of the brain and resulting in effects dependent on receptor expression and localization. In SHRs, a shift in the SCFA concentrations stimulates the paraventricular nucleus (PVN) in the hypothalamus, which increases sympathetic signaling to the GI [3, 5]. An increase in autonomic outflow to the GI alters the environment of the GI causing a shift in microbial composition, Yang *et al.* [3] reported a shift to an increase in lactic acid-producing *Firmicutes*. This rise in lactic acid production acts in a positive feedback loop by further increasing PVN sympathetic output, possibly propagating continuous shifts in microbial populations and potentially leading to hypertension.

Microbial dysbiosis is a state in which there is a maladaptation or imbalance in microbial composition. Dysbiosis may induce a shift promoting abnormally high numbers of acetate-producing bacteria. Acetate is the end-product of ethanol/ alcohol metabolism and has a structural homology to glutamate carboxyl terminals [11] with the ability to act in the brain through various mechanisms. When acetate activates N-methyl-D-aspartate receptors (NMDARs) in the central nucleus of the amygdala, sympathetic activity increases resulting in a rise in ABP [11]. In a dose-dependent manner acetate has been shown to induce excitotoxicity in dopaminergic PC12 cells [12] by either binding to NMDARs or entering the cell presumably through MCTs. The opening of NMDARs channels increases cytosolic Ca^{2+} concentrations acting on several second messenger systems. The transport of acetic acid into the cell through MCTs decreases the pH, altering cell functions. These actions point towards upregulation and expression of the pro-inflammatory cytokine tumor necrosis factor alpha and contribute to cell death [12] and possibly contributing to neurodegenerative diseases such as Parkinson's and Alzheimer's. Understanding the pathways through which different SCFAs induce changes in brain signaling and linking the changes in autonomic outflow to adaptations in the microbial population could potentially lead to decreases in sympathetic and parasympathetic output through dietary changes that alter the diversity the gut microbiome selecting for increases or decreases in specific populations.

Influence of SCFAs on Hypertension

The influence of microbial metabolites on hypertension and other cardiopulmonary pathologies is a relatively new focus of study with much still to be discovered. Unraveling the underlying mechanisms by which microbiota secretions

and metabolites act on human cells will impact human health and potentially lead to new methodologies of treatment. According to Koch's third postulate, if microorganisms contribute to disease, then transferring the microorganism to a healthy organism will induce pathogenicity. Using the third postulate as a guide, when normotensive Wistar-Kyoto (WKY) rats receive a fecal microbiota transplant (FMT) from a stroke-prone (SHR), there was an increase in ABP [2]. Along with the rise in ABP, the recipient rats had an increase in SCFA concentrations in the fecal matter accompanied by a shift in microbiome community composition [2], mimicking the diseased microbial configuration.

Microbial composition shifts alter the production of metabolites produced by various bacteria, potentially influencing several systems in the human body. Previous reports using mice, demonstrated that acetate and propionate bind to various GPCRs acting as chemical sensors in the circulatory system and the kidney to play roles in renin secretion and blood flow resistance [8]. Olfactory (Olf) 78 receptors are localized in a subset of smooth muscle cells composing renal artery branches and small resistance vessels associated with the renal juxtaglomerular apparatus, ideal locations for influencing renin secretion and blood flow resistance. Propionate binding to Olf78 receptors induces the release of renin from juxtaglomerular cells in the afferent arterioles, resulting in an increase in ABP. However, if propionate binds to GPCR 41, the ABP drops [1, 8]. Thus, these two receptors are capable of counteracting each other to maintain homeostatic mean arterial pressure in response to varying SCFA concentrations [8]. Building knowledge of the various receptors to which SCFAs bind in different tissues could lead to potential antagonist and agonist drug development to aid in the regulation of ABP.

WKY rats have diverse microbial populations from the major five phyla discussed earlier [2, 3] and when the diversity of the ecosystem decreases it becomes unstable and susceptible to perturbation. Yang *et al.* found that the SCFA concentrations in fecal samples differed depending on the overall microbial composition [3]. SHRs had significantly higher lactate levels associated with diminished acetate and butyrate concentrations than WKY rats. WKY rats that receive a FMT from stroke-prone SHRs show an increase in fecal SCFA acetate, propionate, and butyrate concentrations, which increase above those in WKY and stroke-prone SHRs do not receive FMT [2]. The difference in SCFA concentrations between WKY and SHRs and the shift in SCFA concentrations following FMT of disrupted microbiota into WKY rats are correlated with an increase in *Firmicutes* and decreases in *Bacteroidetes*, *Proteobacteria*, and *Verrucomicrobia* species [2, 3, 5]. It appears that the initial onset of microbial disruption from a

normal composition causes an increase in SCFA production [2, 3, 5], inducing an elevated ABP though an increase in sympathetic outflow. Alterations in microbial communities can modify intestinal permeability, possibly allowing elevated amounts of SCFAs to enter the blood and inducing various physiological responses. An exploration into the mechanisms promoting the growth of various species following initial disruption could lead to potential probiotic and prebiotic therapies to reestablish diversity in the microbial community and restore the balance among species. Several groups have demonstrated a shift in SCFA concentrations and microbial composition in fecal samples [2–7], but there is still a need for exploration into the composition of bacterial populations associated with the mucosal layer throughout the GI. Characterization of various bacterial populations at different sites in the GI may lead to novel discoveries on how the metabolites of bacterial populations influence host cell function.

Influence of SCFAs on Neurodegeneration

Emerging evidence has linked microbial dysbiosis and changes in metabolite production in the GI to neurodegeneration [4, 6]. Several neurodegenerative disorders, such as Parkinson's and Alzheimer's, are associated with the aggregation of proteins in specific regions of the brain, impacting function inducing pathogenicity [4, 6]. Interestingly, aggregation of the protein alpha-synuclein (α Syn) is first seen in the GI of Parkinson's patients [4], suggesting that the pathogenicity spreads from the GI to the CNS through the vagal and glossopharyngeal nerves.

The use of animal models allows researchers to establish various pathways that stimulate the overexpression or aggregation of specific proteins in various brain regions. Fecal samples from individuals with Parkinson's disease (PD) have a lower acetate concentration than those taken from age-matched controls [4]. The administration of Parkinson's patient samples into germ-free mice results in a similar decrease in the relative abundance of acetate in fecal samples [6]. This decrease in acetate could indicate compromised intestinal integrity, allowing more acetate to move from the lumen into the bloodstream to be distributed throughout the body. Exploration of the possible effects of an increase in acetate concentrations in various tissues could lead to discoveries of downstream mechanisms inducing pathogenicity.

Most SCFAs have the capacity to cross the blood-brain barrier via the MCT and affects the central nervous system [6, 7, 10]. SCFA administration in the Thy1- α Syn (alpha-synuclein-overexpressing, ASO) mouse induces an increase in microglia activation in a region-specific manner [6]. Microglia activation is associated with the upregulation

of α Syn aggregation. Microglia in germ-free mice are unable to complete morphological changes in order to induce an inflammatory response [6], showing a correlation between gut microflora secretions and the maintenance of neuronal and glial health. Transplantation of PD fecal samples into ASO mice increases motor impairment [6], suggesting that microbiota contribute to synucleinopathies and progression of the neurodegenerative disorder.

Dysbiosis of bacterial phyla is seen in the GI of individuals with PD in comparison to control samples [4, 6]. Patients with PD display a decrease in *Bacteroidetes* and *Firmicutes* accompanied by an increase in *Proteobacteria*, *Actinobacteria*, and *Verrucomicrobia* species *Akkermansia muciniphila* [4, 6]. Bacterial disruption is associated with several pathologies spanning several systems of the human host however, specific community disruptions and underlying mechanisms of the changes in microbial metabolite production and pathogenicity is still largely unknown.

Conclusions

Over the past two decades, it has been made clear that the composition of the gut microbiome impacts various physiological functions and plays a major role in the development of pathology. Often the *Firmicutes*-to-*Bacteroidetes* ratio is used as a diagnostic tool, but the literature is controversial [2–7] illuminating its insufficiency for clinical use at the current level of understanding. Potential direction of investigation into not only the bacterial composition of fecal matter but also the composition of bacterial populations associated with the mucosal cells of the host could present a more reliable and accurate assessment of microbial communities associated with pathology and health. The varying compositions of microbial communities between pathologies implies a need for future research into microbial diversity in disease states compared to healthy and possible high-risk individuals.

Dysbiosis results in a shift in metabolite production and the concentrations found in the GI, blood plasma, and brain regions. Responses to various SCFAs concentrations may differ regionally [9], depending on receptor expression on resident cells [1, 8], possibly influenced by host genomics [10]. Pathogenicity can change receptor responses to SCFA binding [10]; in normal physiology, binding may cause a reaction that completely opposes the activity induced in a pathogenic state. Investigation into specific regional receptor responses to SCFA binding in normal and pathogenic models will lead to novel discoveries underlying

mechanisms propagating various pathologies, such as hypertension and Parkinson's disease. Distinguishing early biomarkers, tight-junction protein expression and gut microbiota diversity, will aid in the development of therapies targeting prevention of the early onset of cardiovascular diseases and neurodegeneration.

Acknowledgements This insight was supported by Michigan Technological University Portage Health Foundation, America Heart Association (16PRE27780121) and National Natural Science Foundation of China (31871150).

Conflict of interest The authors declare that they have no conflict of interest.

References

- Galla S, Chakraborty Mell B, Vijay-Kumar M, Joe B. Microbiota-host interactions and hypertension. *Physiology (Bethesda)* 2017, 32: 224–233.
- Adnan S, Nelson JW, Ajami NJ, Venna VR, Petrosino JF, Bryan RM Jr, *et al.* Alterations in gut microbiota can elicit hypertension in rats. *Physiol Genomics* 2016, 49: 96–104.
- Yang T, Santisteban MM, Rodriguez V, Li E, Ahmari N, Carvajal JM, *et al.* Gut dysbiosis is linked to hypertension. *Hypertension* 2015, 65: 1331–1340.
- Unger MM, Spiegel J, Dillmann KU, Grundmann D, Philippeit H, Bürmann J, *et al.* Short chain fatty acids and gut microbiota differ between patients with Parkinson's disease and age-matched controls. *Parkinsonism Relat Disord* 2016, 32: 66–72.
- Santisteban MM, Qi Y, Zubcevic J, Kim S, Yang T, Shenoy V, *et al.* Hypertension-linked pathophysiological alterations in the gut. *Circ Res* 2017, 120: 312–323.
- Sampson TR, Debelius JW, Thron T, Janssen S, Shastri GG, Ilhan ZE, *et al.* Gut microbiota regulate motor deficits and neuroinflammation in a model of Parkinson's disease. *Cell* 2016, 167: 1469–1480.
- Perry RJ, Peng L, Barry NA, Cline GW, Zhang D, Cardone RL, *et al.* Acetate mediates a microbiome-brain- β -cell axis to promote metabolic syndrome. *Nature* 2016, 534: 213–217.
- Pluznick J. A novel SCFA receptor, the microbiota, and blood pressure regulation. *Gut Microbes* 2014, 5: 202–207.
- Lal S, Kirkup AJ, Brunson AM, Thompson DG, Grundy D. Vagal afferent responses to fatty acids of different chain length in the rat. *Am J Physiol Gastrointest Liver Physiol* 2001, 281: G907–G915.
- Soret R, Chevalier J, De Coppet P, Poupeau G, Derkinderen P, Segain JP, *et al.* Short-chain fatty acids regulate the enteric neurons and control gastrointestinal motility in rats. *Gastroenterology* 2010, 138: 1772–1782.
- Chapp AD, Gui L, Huber MJ, Liu J, Larson RA, Zhu J, *et al.* Sympathoexcitation and pressor responses induced by ethanol in the central nucleus of amygdala involves activation of NMDA receptors in rats. *Am J Physiol Heart Circ Physiol* 2014, 307: H701–H709.
- Chapp AD, Behnke JE, Driscoll KM, Fan Y, Hoban E, Shan Z, *et al.* Acetate mediates alcohol excitotoxicity in dopaminergic-like PC12 cells. *ACS Chem Neurosci* 2019, 10: 235–245.



NEUROSCIENCE BULLETIN

Impact Factor

4.246

Q2

2018 Journal Citation Report
(Clarivate Analytics, 2019)

NEUROSCIENCE BULLETIN 神经科学通报 (Monthly)

Vol. 36 No. 1 January 15, 2020

Sponsored by: Shanghai Institutes for Biological Sciences, Chinese Academy of Sciences
Chinese Neuroscience Society
Second Military Medical University

Editors-in-Chief: Shumin Duan, Ru-Rong Ji

Edited by: Editorial Board of *Neuroscience Bulletin*

319 Yueyang Road, Building 31 B, Room 405, Shanghai 200031, China

Phone: +86-21-54922863; Fax: +86-21-54922833

E-mail: nsb@sibs.ac.cn; <http://www.neurosci.cn>

Editors: Bin Wei, Xu Jiang, Zhi-Rui Liu

Published by: Shanghai Institutes for Biological Sciences, Chinese Academy of Sciences (320 Yueyang Road, Shanghai)

Printed by: Shanghai Shengtong Times Printing Co., Ltd (A6, No. 2888, Caolang Highway, Jinshan District, Shanghai)

Overseas Distributed by: Springer Nature

Home Distributed by: Local Post Offices

ISSN 1673-7067

CN 31-1975/R

Post Office Code Number: 4-608

Permit of Ad. Number: 3100420130051

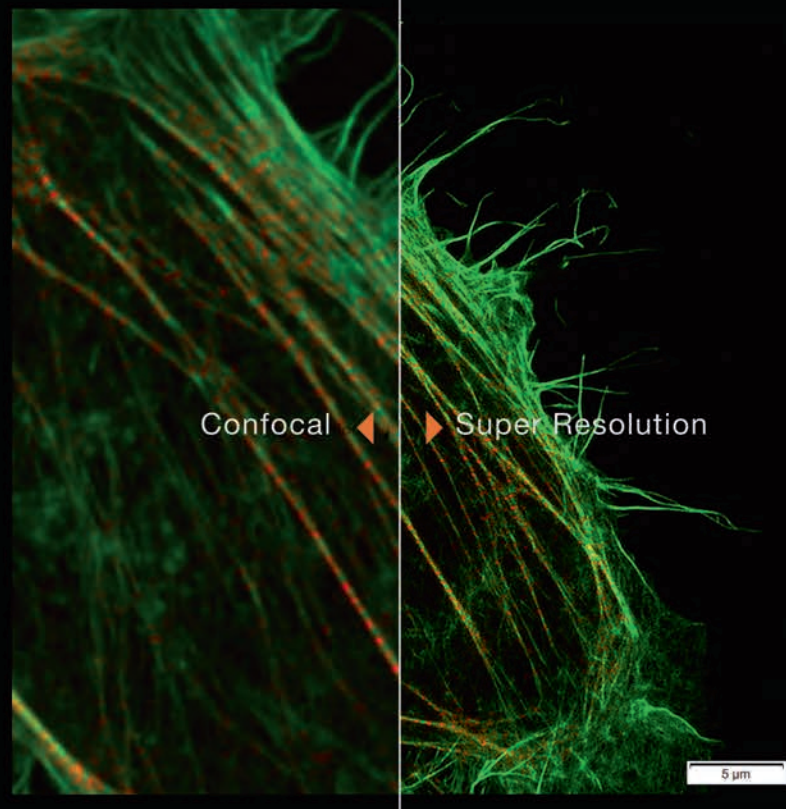
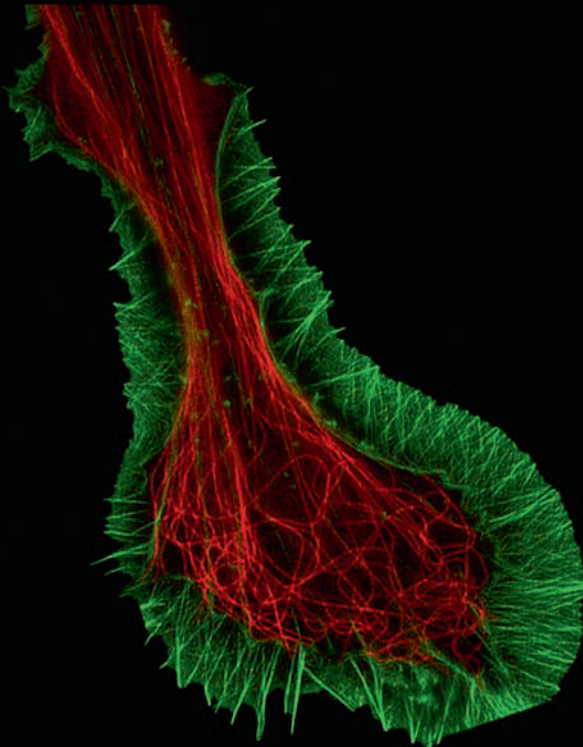
Price: ¥ 100.00

ISSN 1673-7067



兼顾分辨率和速度的

转盘共聚焦活细胞超分辨系统 **SpinSR10**



- 分辨率高达110nm的实时超分辨率成像
- 专有反卷积算法进一步提升图像质量
- 宽视野成像，速度高达 200fps
- 特色硅油物镜可以实现活细胞深层成像
- 宽场、共聚焦、超分辨率模式自由切换
- 功能强大的智能cellSens软件平台



奥林巴斯（北京）销售服务有限公司

北京朝阳区酒仙桥路10号恒通商务园B12C座2F (北京) 010-59756006
 上海市徐汇区淮海中路1010号嘉华中心11楼 (上海) 021-51582084
 广州市环市东路403号广州电子大厦16楼 (广州) 020-61227171

陕西省西安市新城区尚德路85号太平洋保险大厦8F

湖北省武汉市江岸区中山大道1628号武汉天地企业中心5号7楼701单元
 四川省成都市人民南路四段三号来福士广场T1-11楼
 辽宁省沈阳市沈河区友好街10号新地中心1号楼3501室

(西安) 029-87206108

(武汉) 027-82718838

(成都) 028-86703700

(沈阳) 024-23342084